Technische Universität München
TUM School of Engineering and Design

TUM

Vibroacoustic Analysis of Hybrid Steel-Timber Structures with a Focus on Uncertainty and Joints

Bettina Chocholaty

Vollständiger Abdruck der von der TUM School of Engineering and Design der Technischen Universität München zur Erlangung eines

Doktors der Ingenieurwissenschaften (Dr.-Ing.)

genehmigten Dissertation.

Vorsitz: Prof. Dr.-Ing. habil. Fabian Duddeck

Prüfer der Dissertation:
        1. Prof. Dr.-Ing. Steffen Marburg

        2. Prof. Dr.-Ing. Gerhard Müller

Die Dissertation wurde am 27.03.2024 bei der Technischen Universität München eingereicht und durch die TUM School of Engineering and Design am 14.10.2024 angenommen.

Kurzfassung

Mit dem Ziel die Nachhaltigkeit in der Bauindustrie zu verbessern, gibt es vermehrt Bestrebungen, nachwachsende Ressourcen zu verwenden. Hierbei liegt ein besonderer Schwerpunkt auf Holz. Holzdecken sind umweltfreundlicher als beispielsweise Betondecken. Weiterhin erhalten hybride Stahl-Holzdecken zunehmend Aufmerksamkeit, da sie oftmals eine erhöhte Tragfähigkeit im Vergleich zu reinen Holzdecken aufweisen. Bei holzbasierten Decken treten jedoch häufig Beschwerden der Bewohnerinnen und Bewohner über Schwingungen und akustische Probleme auf. Diese Doktorarbeit befasst sich aus diesem Grund mit hybriden Stahl-Holz-Strukturen und untersucht ihr dynamisches Verhalten, insbesondere in Bezug auf die Vibroakustik. Es werden verschiedene Einflussfaktoren auf das dynamische Gesamtverhalten analysiert. Ein Schwerpunkt liegt hierbei auf den Auswirkungen der Verbindungen auf das Gesamtstrukturverhalten. Ein weiterer wichtiger Faktor bei der Untersuchung dieser Strukturen sind die inhärenten Schwankungen des Werkstoffs Holz. Diese mit den Verbindungen- und Materialparametern verbundenen Unsicherheiten erschweren die Vorhersage der dynamischen Reaktion der Deckenstrukturen. In dieser kumulativen Arbeit werden daher experimentelle und numerische Methoden zur Untersuchung des vibroakustischen Verhaltens von hybriden Stahl-Holz-Elementen vorgestellt. Experimentelle Untersuchungen liefern die modalen Eigenschaften von Probekörpern. Zusätzlich wird eine experimentelle Analyse des Einflusses der Verbindungen durchgeführt und das teilweise nichtlineare Verhalten der Strukturen im Zusammenhang mit der Amplitudenabhängigkeit und Beiträgen höherer Ordnung wird in Messungen betrachtet. Weiterhin wird die Bayes'sche Inferenz zur Identifizierung der variierenden Materialeigenschaften von Holz angewendet. Dabei werden die Unsicherheiten in Bezug auf die Materialparameter bestimmt und anschließend in Monte-Carlo-Simulationen verwendet. Hier werden sowohl die Unsicherheiten der Verbindungen als auch der Materialparameter berücksichtigt. Ebenfalls wird die Finite-Elemente-Methode eingesetzt, um die Charakteristika zu bestimmen, welche das Unwohlsein der Bewohnerinnen und Bewohner beeinflussen. Hierbei liegt der Schwerpunkt auf den Schwingungsdosiswerten und Trittschallpegeln für hybride Stahl-Holz-Decken. Trotz der experimentellen Identifikation von Nichtlinearität in Form einer leichten Amplitudenabhängigkeit der Dämpfung und Oberschwingungen höherer Ordnung bei bestimmten Eigenschwingungen wird in dieser Studie das Verhalten der Struktur zur Vereinfachung mithilfe linearer Simulationsmodelle dargestellt, um die Berechnungskomplexität zu verringern. Weiterhin zeigen die Monte-Carlo-Simulationen nicht vernachlässigbare Schwankungsbreiten der Eigenfrequenzen aufgrund der Variabilität von Material- und Verbindungsparametern, was die Relevanz der Berücksichtigung ihrer Unsicherheit unterstreicht. Die Ergebnisse zeigen, dass die derzeitigen Deckenschwingungen die geforderten Grenzwerte für Gebrauchstauglichkeit nicht einhalten. Dies betont die Notwendigkeit weiterer Untersuchungen, welche beispielsweise Maßnahmen zur Verbesserung des Dämpfungsverhaltens beinhalten. Die numerische Studie zu den Trittschalleigenschaften zeigt ein ähnliches Verhalten der simulierten Trittschalldruckpegel mit den Literaturwerten für Beton- und Estrichböden. Zukünftige Studien sollten sich daher mit der experimentellen Validierung dieser Ergebnisse befassen.

Abstract

With the goal of enhancing sustainability, the construction industry is transitioning towards utilizing renewable materials, with a particular emphasis on wood. Wood-based floor structures are environmentally more friendly compared to concrete floors. Therefore, hybrid steel-wood ceilings are also attracting increasing attention due to their often higher load-bearing capacity compared to pure wood ceilings. However, residents often complain about vibrations and acoustic problems with wood-based ceilings. For this reason, this doctoral thesis explores hybrid steel-timber structures, focusing on the dynamic behavior of the structures, specifically in relation to vibroacoustics. To comprehensively address these challenges, this study examines various factors influencing the overall dynamic performance. Here, a special focus lies on the effects of joints between the timber and steel components. Another important factor when investigating these structures is the natural variation of the material wood. These inherent uncertainties associated with joint and material parameters complicate predicting the floor structure's dynamic response. Experimental and numerical methodologies are introduced to analyze the vibroacoustic behavior of hybrid steel-timber elements. Experimental investigations give the modal properties of test specimens. Additionally, the influence of the joints is analyzed experimentally, and the partially nonlinear behavior of the structures is investigated in measurements related to amplitude dependency and higher-order contributions. Bayesian inference is applied to identify the varying timber material properties. Thereby, uncertainties related to material parameters are determined and, subsequently, utilized in Monte Carlo simulations considering both joint and material parameter uncertainties. Additionally, the finite element method is employed to explore characteristics influencing resident discomfort, with a specific focus on vibration dose values and impact sound pressure levels for hybrid steel-timber floors. Despite experimental detection of nonlinearity as a slight amplitude-dependency in damping and higher-order harmonics at certain natural modes, the study linearizes the structure's behavior using linear simulation models to simplify the computations. The Monte Carlo simulations reveal non-negligible ranges of variation in natural frequencies due to material and joint parameters, emphasizing the importance of considering their uncertainty. Furthermore, findings indicate that current floor vibrations do not meet the required serviceability limits, suggesting further investigations. These include measures to enhance inherent damping. The numerical study on impact sound properties shows that the simulated impact sound pressure levels align with literature values for concrete and screed floors. Future studies should deal with an experimental validation of these results.

Danksagung

Diese Arbeit entstand zum Großteil während meiner Zeit am Lehrstuhl für Akustik mobiler Systeme der Technischen Universität München. Mein Dank gilt all den Menschen, die diese Zeit möglich gemacht haben und mir viele schöne, lustige und lehrreiche Momente geschenkt haben.

Ein besonderer Dank gilt meinem Doktorvater Prof. Dr.-Ing. Steffen Marburg für die Unterstützung meines Promotionsvorhabens und das Vertrauen, das er in mich gesteckt hat. Steffen, vielen Dank für Dein offenes Ohr bei Fragen und Diskussionsbedarf sowie den Gestaltungsfreiraum, den Du mir eingeräumt hast.

Besonders bedanken möchte ich mich auch bei Prof. Dr.-Ing. Gerhard Müller. Zum Einen für die Übernahme des Gutachtens dieser Dissertation und zum Anderen für die Einbindung am Lehrstuhl für Baumechanik im Rahmen von Studienarbeiten, als studentische Hilfskraft und als wissenschaftliche Mitarbeiterin. Weiterhin bedanke ich mich für den regen Austausch und die Diskussionen.

Vielen Dank an Prof. Dr.-Ing. Fabian Duddeck für die Übernahme des Prüfungsvorsitzes und die äußerst angenehme Prüfungsatmosphäre.

Ein weiterer großer Dank gilt meinen Kolleginnen und Kollegen beider Lehrstühle, die mich offen und herzlich aufgenommen haben. Vielen Dank für die angenehmen Mittags- und Kaffeepausen, die Feierabendbiere und vieles mehr. Ein besonderer Dank gilt Simone Preuss. Unsere vielen kleinen Unterhaltungen im Arbeitsalltag und außerhalb waren immer eine Freude und eine große Hiilfe. Außerdem möchte ich mich bei Alex Hoppe für seine Unterstützung während einiger fachlicher Krisen bedanken.

Vielen Dank auch an die Kolleginnen des Sekretariats für die administrative und organisatorische Unterstützung während meiner Zeit am Lehrstuhl. Weiterhin möchte ich mich bei der Lehrstuhl-IT bedanken, die mir in vielen Dingen zur Hilfe geeilt ist.

Very special thanks go to Bert Roozen, who supported me a lot with fruitful discussions. Thanks for the successful collaboration.

Meinen Freundinnen und Freunden und meiner Familie, insbesondere Collin Leiber, bin ich zu tiefstem Dank verpflichtet. Vielen Dank an meine Eltern. Ihr habt es mir ermöglicht an diesen Punkt zu kommen. Vielen Dank Collin, dass du immer da warst, um mich aufzubauen, und dass du mir so viel Unterstützung gegeben hast.

Contents

Contents

1 Introduction

In recent years, research on timber as a construction material for buildings received increasing attention due to the rise of engineered wood materials and sustainability concerns in society [1, 2], as wood is a comparably environmentally friendly product. The production of concrete releases eight times more net carbon emissions than lumber does. [3] In this context, studies on hybrid timber-concrete or timber-steel structures are moving into focus [4]. Hybridization aims to use each material optimally such that the hybrid system performs better than a homogeneous structure [5]. In the case of hybridization at the component level, materials are combined for a structural element such as a slab [6], a beam element [7], or for joints [8]. At the building level, the hybrid system is constructed from building elements of different materials, e.g., cross-laminated timber (CLT) panels and steel frames for beams and columns in a hybrid steel-timber (HST) building [5]. The material wood can be represented by orthotropic material behavior, which is described by nine independent elastic constants representing the behavior in three axes: longitudinal (parallel to the fiber), radial (perpendicular to the growth rings in the radial direction), and tangential (perpendicular to the fiber and tangential to the growth rings). This leads to three moduli of elasticity, E_l, E_t, and E_r, three shear moduli, G_{lr}, G_{lt}, and G_{rt}, and three Poisson's ratios, μ_{lr}, μ_{lt}, and μ_{rt}. The remaining material properties follow from the symmetry of the elasticity matrix of the orthotropic material. [9] Unlike timber, steel represents an isotropic material, which uses the interrelated parameters, elasticity modulus E_s, shear modulus G_s, and Poisson's ratio μ_s. Only two out of three are required to fully characterize the elastic behavior of the steel. [10] When combining both materials, wood shows its strength in terms of compressive strength [9]. In completion, steel contributes its high tensile strength. This combination leads to improved load-bearing capacity when the materials are appropriately arranged in a structural element [5]. However, to achieve the best possible environmental compatibility, a simple disassembly of hybrid structures without bonding components is desirable [4]. In terms of fire safety, wooden building elements show advantageous properties if designed with sufficient cross-sections, as a protective layer develops in case of fire that prevents further charring [11]. This layer extends the fire resistance period of a wooden component [11], unlike steel, which quickly loses its strength with increasing temperature [12]. Hence, if designed properly, HST structures can profit from better fire safety than steel-only systems. In addition, wood and hybrid wood structural elements are advantageous when using optimized manufacturing methods for off-site prefabrication [2, 13]. Likewise, wood has a high strength-to-weight ratio [14]. For this reason, wood or hybrid wood buildings are often lighter than other building types, favoring them in terms of seismic activity due to less inertial forces being generated. Another advantage of the low weight relates to fewer geotechnical limitations on the construction site [15].

As high-rise timber buildings and larger spans have recently become more popular, the floors have become more susceptible to vibrations. So even though new products satisfy the design criteria for load-bearing capacity, the criteria for serviceability must also be fulfilled [16]. Otherwise, residents could complain about excessive vibrations [17]. Nonethe-

less, ongoing discussions exist concerning the vibration characteristics and the criteria for acceptable levels of occupant comfort in the context of timber and hybrid timber floors [18, 19]. In addition, the evaluation regarding a standard related to the limit state of vibration serviceability does not necessarily correspond to the perception of residents [20]. Consequently, engineers and researchers do not yet agree on which standard should be applied, especially since disadvantages have been discovered in many of them. Nevertheless, vibration analyses are particularly relevant for wood and hybrid wood structures since, according to a survey, vibrations in wooden structures are more often perceived as disturbing than for, e.g., concrete ceilings [21].

Additionally, lightweight constructions exhibit subpar airborne and impact sound insulation. Noise resulting from impacts within timber structures frequently emerges as a relevant cause of residents' complaints [22]. Ingelaere [23] highlights that wooden structures exhibit superior insulation characteristics within the middle and high-frequency spectrum compared to their heavier counterparts, e.g., those out of concrete. Consequently, investigations often focus on low-frequency impact noise, which is said to be more disturbing and annoying [24]. The overall floor system has to be significantly altered in terms of damping, mass, or stiffness in case of a problematic floor [25]. Consequently, accurate prediction models might prevent changes after the manufacturing of a floor, limiting unnecessary consumption of resources [26, 27]. For impact noise, the typically applied design processes, i.e., using ISO 12354-2 [28] and analytical or empirical approaches [29], have been developed for heavy floors, leading to deviations of the predictions for lightweight structures. So far, theoretical and empirical evaluation methods of bare timber floor impact sound levels are barely available [30]. Hence, there is still a need for an in-depth analysis of the impact sound and vibration characteristics of timber and hybrid timber structures, which is dealt with in this thesis.

1.1 State of the art

The following sections give an overview of the research on HST structures and the vibroacoustics of timber-based floors. Moreover, the commonly applied prediction methods and the inherent uncertainty, which can be dealt with using Bayesian inference and Monte Carlo simulations, are described. Finally, the effects of joints within structures are presented, and the contributions of this thesis to the field of vibroacoustics of HST floors are summarized.

1.1.1 Hybrid steel-timber building elements

Current research on HST building elements covers a wide range of disciplines, whereas load-carrying capacity investigations are the most common. The most popular design features an H-shaped steel beam connected with CLT and LVL panels at the top flange via screws or bolts. Usually, experimental three- or four-point bending tests are employed to assess various structural aspects, such as the load-bearing capacity and maximum

strength. [7, 31–33] In addition, research is conducted on developing empirical formulas, various numerical approaches, including 1-D frame, 2-D continuum-based nonlinear and 3-D Finite Element methods (FEM) [7, 34–38], and analytical models, e.g., the elastic theory of layered beams [39, 40]. By employing the models, the authors conduct a variety of parametric studies to identify critical factors influencing the bending behavior of steel-timber beams, e.g., the type of connector [40], initial imperfection [35], and material nonlinearities [34]. The performed measurements are subsequently utilized to validate the modeling approaches. Moreover, whole floor structures of modular prefabricated steel-timber systems are analyzed experimentally, focusing on, e.g., in-plane stiffness and damage states [41, 42].

Many studies focus on the mechanical processes in relation to statics within joints of HST structures, i.e., beam-to-panel or column-to-beam joints, for example, concerning load-displacement curves and failure modes using push-out tests. Loss et al. explore various fasteners and connection types and analyze the joints' nonlinear behavior experimentally and numerically [42–44]. Another group of authors also conduct various studies on the behavior of joints constructed by different fastener types, and with or without glue [38, 45–48]. Moreover, the energy dissipation capacity and equivalent viscous damping of the joints are identified by experiments with low-cycle high amplitude loading [49]. Furthermore, Chiniforush et al. investigate the long-term behavior and creep coefficient of steel-timber joints by employing analytical, numerical, and experimental methods. Thereby, the authors assess the effect of varying temperature and moisture content of the timber on the structural behavior of the timber, steel, and connectors for a service life of 50 years. [50–55] Some research efforts have also been devoted to fire resistance. The thermo-mechanical response of HST structures when exposed to fire is examined via experimental tests in a furnace. Moreover, one-way coupled numerical analysis is conducted through Computational Fluid Dynamics and FEM software. This way, various cross-sections and connection types are tested. [56–59] However, only a few studies on the seismic performance [60] and on the life cycle assessment [61] exist.

Despite the previous effort, a limited number of studies on the vibrational behavior of HST systems have been performed. Cold-formed steel floors with wood-based particle floor boards are investigated for serviceability criteria by conducting static tests, heel drop tests, and walking tests. These are conducted numerically, in the lab, or in situ to determine deflection limits, natural frequencies, and time-history accelerations [62–66]. Moreover, CLT-steel floors with varying boundary conditions, beam spacing, and beam sizes are investigated by numerical modeling, experimental testing, and analytical considerations to examine their dynamic behavior among others in terms of natural frequency and mode shapes [67–70]. For HST cross-sections consisting of an H-shaped steel beam with a timber panel on top, the authors conduct extensive experimental and numerical studies [71–73]. They perform experimental modal analysis on the steel-timber beams to identify natural frequencies and mode shapes of various setups and calibrate an FE model against those tests. Investigations concerning building code regulations are carried out through the FE model using experimentally determined damping properties. Parametric studies are realized as well, e.g., considering different shear connector types, CLT panel orientations, and dimensions. [71–73] Although low-frequency acoustics are a major con-

cern for lightweight floor structures [30] and research exists on floors using cold-formed steel profiles and oriented-strand board [74], no studies of the building acoustics of hybrid cross-sections made of steel and timber have been performed so far.

Lastly, review articles on steel-timber hybrid structures exist covering a wide range of topics [75–77] and vibrations only [19] showing the great interest of the research community in these systems. Therefore, this thesis deals with the vibrational characteristics of HST structures and conducts a numerical investigation of the impact sound insulation properties of HST floors.

1.1.2 Vibrations and acoustics of timber floors

The rapid construction, impressive strength-to-weight ratio, and lightweight attributes lend favor to timber-based structures. However, the rising pursuit to construct larger spans and taller timber buildings raises concerns about vibrations in floors and similar structural elements. While engineered wood products improve load-bearing capacity, meeting serviceability criteria can still be challenging [16]. As vibrations are a major concern regarding the serviceability of a floor structure, design standards also deal with this issue. Timber floors are often analyzed concerning measures of velocity and acceleration levels of a floor's dynamic response. Here, the root-means-square (RMS) and root-mean quad values are taken into account [78], e.g., for the computation of the Vibration Dose Value (VDV) in BS 6472 [79]. Moreover, response factors, which represent the perceptible level of vibration, are applied as limits to evaluate the performance of a floor [80]. In addition, floor deflection and fundamental frequency are incorporated in the current draft of Eurocode 5 to consider stiffness- and frequency-based criteria [81]. Nevertheless, bearing in mind the different design codes, consent on the usage of various available vibration criteria and limits for HST floors has yet to be achieved. Practitioners frequently rely on various design references to evaluate the vibrations of different types of floors. These include general design guidelines such as the "Design Guide for Footfall Induced Vibration of Structures" (CCIP-016 [82]) and "AISC Design Guide 11" [83], which are commonly applied for evaluating vibration in concrete, steel, and composite floors. Moreover, there are specialized standards tailored to timber structures, such as "Eurocode 5" [84], the "Canadian Wood Council (CWC)" [85], "Canadian Standards Association (CSA O86-19)" [86], the "CLT Handbook"[87], and the "American Engineered Wood Association APA–E710" [88] to address the vibration performance of timber floors. In some cases, researchers also propose consulting "SCI P354" [89] for lightweight cold-formed steel floors, including those featuring timber floorboards [19]. Although still more thorough validation is necessary on steel-timber floors, in their review on vibration assessment methods, Cheraghi-Shirazi et al. [19] conclude that for now, AISC Design 11 [83] and CCIP-016 [82] currently recommend the most suitable approaches for HST floors. Nonetheless, the ongoing discussion about the appropriate design guidelines for HST floors often leads researchers to rely on existing timber-related design standards like Eurocode 5 and the guidelines of the Canadian Wood Council [19], indicating consensus of researchers that HST floors behave to some extent similarly to timber floors. Hence, due to the vast number of studies related to timber floors and, at the same time, a rather limited number related to HST

floors, the relations and issues explored in this section often deal with timber floors while assuming transferability to HST floors. Evaluating existing research on timber and vibration identifies floor vibrations as the most discussed topic [78], hence emphasizing the great interest of the research community.

Low-frequency vibration issues are mainly connected to the interaction with human activities, such as running and walking, potentially leading to excessive vibrations and concerns regarding residents' discomfort. In contrast, high-frequency vibrations lead to effects in the audible frequency spectrum [78]. Although noise and vibration are commonly addressed independently, several authors propose that the primary discomfort encountered within buildings results from a cumulative impact of both [90]. Annoying vibrations occur when the floor structures vibrate in resonance with the walking pace or alternative human activities [78]. Additionally, issues arise concerning the perception of timber floor vibrations due to individual sensitivity and perceived acceptability of vibrations in diverse environments [20]. Another concern relates to the possible wear and deterioration of timber components due to extended exposure to recurrent dynamic loading resulting in fatigue-induced failures and diminished strength and durability of the timber flooring system [91, 92].

Experimental studies in laboratories or in situ and numerical studies are performed to evaluate floor vibrations, identify countermeasures, verify compliance with serviceability guidelines, and improve existing designs. Although numerical methods are increasingly used and thus come into focus, experimental approaches to vibration characterization are still the most commonly used. [78] For the HST structures at hand, no experimental and numerical studies have been performed so far. Therefore, this thesis aims to fill this gap.

As stated before, the discomfort of inhabitants arises due to a combination of vibration and noise events. Hence, the acoustic behavior of timber or hybrid timber floors also accounts for an important factor, especially in the case of impact sound [24, 30]. In general, sound transmission can be airborne, e.g., due to inhabitants talking, or structureborne, e.g., due to residents walking. Consequently, two criteria are taken into account - airborne sound insulation and impact sound insulation - to determine the acoustic performance of a ceiling component. For both of them, the direct sound transmission through the component, as well as the indirect flanking transmission via adjacent components, e.g., walls, are relevant. The evaluation of both is usually carried out through measurements [78] according to the standards ISO 12354-1 [93] and ISO 12354-2 [28]. Single-number quantities that are applied for the acoustic rating of the floor are calculated by employing the rules of ISO 717-2 [94]. The single-number ratings are subsequently compared to the applicable national or international building regulation, e.g., DIN 4109 for Germany [95]. Although airborne noise can be problematic for timber structures, issues due to impact sound transmission are often more prominent [96]. Hence, the focus is repeatedly laid on the impact sound of the floors. In this context, the normalized impact sound pressure level is adopted as the relevant parameter for comparison [97].

Lightweight structures suffer from poor impact sound insulation properties in the low-frequency range [98]. Therefore, it is important to especially consider the frequencies below 100 Hz when dealing with the acoustics of timber and hybrid timber floors. In the case of both, airborne and impact sound insulation, the average sound pressure levels

are usually measured for the frequency range of the one-third octave bands with center frequencies from $100\,\text{Hz}$ to $5000\,\text{Hz}$, which are optionally expanded down to $50\,\text{Hz}$. As measurements are usually performed in ceiling test rigs with transmission and receiving rooms [97, 99], low-frequency acoustic measurements can be challenging, especially for small room sizes due to the long wavelengths of low-frequency sound. Consequently, researchers are working to develop reliable prediction models, especially for low-frequency noise control [100]. Furthermore, it is noted, for example, by Caniato et al. [30] that the acoustic performance varies greatly depending on the flooring and insulation products used, types of timber, construction practices, overall dimensions, and built-up. Here, accurate prediction tools are advantageous over experimental evaluations since parametric studies can be conducted easily. However, this large variability can also cause problems for prediction tools. Differences between in situ and laboratory tests, but also effects of whole systems on individual components, make accurate predictions significantly more difficult [101]. An accurately implemented and tuned prediction model is consequently important to investigate impact sound properties. However, such analyses have not been performed for HST structures before and are therefore done in the scope of this thesis.

1.1.3 Jointed structures and nonlinearities

One factor that largely affects the variability of timber structures is the type of the used joints and their realization. Joints significantly influence a structure's dynamics as they represent one major source of uncertainty. The phenomena occurring in joints mainly depend on the orientation of the transmitted force in the connections, i.e., normal and tangential [102]. Damping more prominently appears in tangentially than normally loaded joints due to "gas-pumping" and friction by relative motion at the interface of components [103]. The asperities in the contact surface experience local microscopic deformations, which include elastic and plastic deformations, potentially inducing micro slip [102]. However, the effects of normal damping increase if a gap appears in the joint, leading to slapping or micro-impacts emerging [104].

To distinguish between micro slip and macro slip in joint connections under tangential load, it is important to note that in the former case, partial slip exists in the contact area, while a larger part of the joint still maintains adherence. As the driving force rises or the normal pressure diminishes, a point is reached where components start moving relative to each other, leading to macro slip. Notably, micro slip and macro slip exhibit nonlinear behavior, and the superposition principle does not apply. Nevertheless, experimental investigations often show an approximately linear behavior of joints when excitation amplitudes are small and macro slip is avoided. [102]

In [105], various factors contributing to nonlinear behaviors in assembled systems are discussed. First, the system's geometry is affected by macro slip under expected excitation levels. Second, coupled modes emerge in the structure's response. Third, the stiffness at the joint interface diminishes, and in the joint interface, damping significantly increases within the micro slip to macro slip transition range before subsequently decreasing. Based on these observations, three phenomena related to joint-induced nonlinearity

are recognized: amplitude-dependent stiffness, amplitude-dependent damping, and the occurrence of nonlinearly coupled modes or higher-order harmonics. To elaborate, if the system's natural frequency changes with increasing load amplitude, it signifies the presence of amplitude-dependent stiffness and possibly amplitude-dependent damping. When loading induces slippage at the joint and the damping ratio shifts due to heightened excitation, amplitude-dependent damping affects the structure's response. Additionally, nonlinearly coupled modes can manifest when the system is driven at one natural frequency, and other modes become prominently excited. This behavior leads to the emergence of multi-harmonic responses. However, it is important to note that while harmonic distortion indicates the engagement of non-smooth nonlinearity near resonance, it does not necessarily imply nonlinear modal interaction. [105] Nonlinearly coupled modes or modal interaction appear when excitation at one resonance frequency results in an unexpectedly large amplitude response in other modes of the studied structure. This situation may arise for commensurate or nearly commensurate natural frequencies. [106, 107]

As an initial categorization approach, the degree of nonlinearity aids in classifying a structure. The assumption of linearity holds if none of the aforementioned phenomena are evident. Weak nonlinearity is indicated when amplitude-dependency is detected, while strong nonlinearity is evident in the system if nonlinearly coupled modes or higher-order harmonics are present alongside amplitude-dependency. [105] Depending on the strength of nonlinearity, different modeling approaches are often employed. Further research also investigates various linear and nonlinear joint models and their suitability. [102] Although previous research on joints of HST structures has been conducted to identify, e.g., load-displacement curves, an investigation of nonlinearities in the dynamic behavior has not been the subject of studies so far and will be dealt with in this thesis.

1.1.4 Prediction tools for vibroacoustics

For the prediction of the vibration performance of timber or hybrid timber floors, experiments account for an important measure to evaluate a floor's vibration behavior. Additionally, calculation tools are applied [80]. A comparative study by Casagrande et al. [108] investigates the commonly employed kinds of methods, their assumptions, simplifications, and acceptability regarding two case studies. The authors' findings are presented below to provide an overview of the prediction tools. Analytical approaches compute specific properties, e.g., the natural frequency, vertical displacement, velocity, and acceleration, via simplified expressions to study the dynamic behavior. For numerical explorations, often, the FEM is applied. This technique can account for the vibrational behavior of the floor in more detail, and moving walking loads are adopted to excite the simulated structure. These approaches can also be used to compute reference parameters, such as maximum deflection, natural frequencies, and mode shapes. With respect to experimental methods, laboratory and in situ tests are performed. Here, modal or walking tests are conducted to compute, e.g., damping properties, natural frequencies, and VDVs. The authors of [108] conclude that analytical procedures are easy-to-use approaches for evaluating a preliminary design. Nevertheless, they are often based on observations from experiments on specific floor structures, limiting the transferability to other floor types. Numerical meth-

ods can represent the behavior more accurately than analytical approaches but constitute a more elaborate methodology, thus necessitating a higher expertise. Experiments are often applied since they provide a reliable evaluation of the vibration performance. [108] However, laboratory tests are costly [109, 110] and require specific equipment and facilities. Moreover, in situ tests are possible only after the construction of the floor, which prohibits preliminary design studies.

The most used method to assess the acoustic characteristics of a building element is to conduct standardized measurements either in situ or in an acoustic laboratory [97, 99, 111]. Often, such measurement results are then used in a subsequent step to estimate the performance of new structures. Moreover, analytical, numerical, and empirical approaches are utilized to approximate the sound transmission loss and impact sound pressure level of floor structures [101]. However, the prediction through such tools sometimes shows considerable deviations from the real behavior [112]. Furthermore, their accuracy diminishes due to a large variety of designs for timber, and thus, hybrid timber floors [101]. Prediction tools for sound transmission vary from analytical formulas to more complex methods. Analytical approaches are developed for single-leaf partitions [113], double-leaf partitions including structural connections [114], and sandwich panels [115]. One example of a more complex method is the transfer matrix method, e.g., in [116], which considers "infinite lateral extent multilayer walls for a particular angle of incidence" [117]. Nevertheless, although beneficial at mid to high frequencies, the transfer matrix method shows suboptimal behavior in the low-frequency range. Here, researchers, e.g., [118], utilize the FEM, which can be applied to structures of unrestrained complexity [117]. Arjunan et al. [119] even expand their study to the entire frequency range (100 - 3150 Hz) relevant to building acoustics. However, the computational effort and limitations of the applicability of FE models in the higher frequency range have to be kept in mind, thus facilitating research related to hybrid methods, e.g., a hybrid FE-TMM [120], a modal-based TMM [121], and a hybrid SEA-FE [122] approach. Moreover, the statistical energy analysis is applied to study the airborne sound transmission [123]. Recent studies by Bader et al. [101, 124] proposed a new technique by applying artificial neural networks.

When considering impact sound, i.e., sound radiation from floor structures under loading of a tapping machine [125], in addition to the structure and the sound radiation into the receiving room, an adequate prediction of the impact load itself is required. This prediction is especially challenging for lightweight floor structures since the interaction of the floor and the tapping machine hammers shows considerable impact on the load due to the tapping machine's and the overall structural behavior [126]. Brunskog et al. [126] thus established a model that incorporates the interaction for the case of a lumped model. More recent studies, e.g., [100], used the approach by Brunskog et al. for investigations using FEM.

In practice, there often exists a disparity between FEM predictions and actual test outcomes, mainly related to model form errors and approximation errors, which are both forms of either epistemic or aleatoric uncertainty [127]. To mitigate these disparities, a process known as model updating or model calibration involving the iterative adjustment of model parameters is often employed. This iterative approach decreases approximation errors and strengthens the model's reliability and precision. The process entails

determining model parameters by minimizing a specific objective function tailored to the problem. [128] Various methodologies have been proposed for this purpose, e.g., genetic algorithms [129], or Bayesian optimization [130, 131].

1.1.5 Uncertainty and Bayesian inference applied to timber structures

The challenge of precisely understanding the behavior of timber-based structures, which are subject to various uncertainties, often leads researchers to favor experimental investigations over simulated ones. In practical scenarios, when the prediction of the response of a vibroacoustic system is required, mechanical modeling is typically involved. Here, two distinct sources of uncertainty are introduced: model uncertainties and data uncertainties. Model uncertainties pertain to the applicability of a model to the specific problem at hand, representing a form of epistemic error. On the other hand, data uncertainties are a type of aleatoric error linked to the parameters of the system, such as geometrical attributes, boundary conditions, or material properties. Addressing data uncertainties can be accomplished by incorporating random quantities, such as random variables or stochastic fields, into the parameters within the prediction tool. [105, 132]

In engineering practice, these uncertainties are often addressed using safety factors, which result in conservative designs [133]. To enhance efficiency, recent research on reliable predictions for building elements has shifted its focus towards considering data uncertainties rather than relying on safety factors. For example, recent studies on stochastic analyses of wooden floors, including CLT slabs [134] and floors made of wood beams and particle boards [135], employ the Monte Carlo method to account for the randomness of material properties and determine the vibroacoustic response of the floor within confidence intervals. The random material parameters are determined by calibrating FE models to match eigenfrequencies obtained from experimental modal analyses [134, 135]. Alternatively, more sophisticated objectives could be achieved by incorporating prior information on elastic constants within a Bayesian framework [136]. Previous research has applied Bayesian inference to laminated, orthotropic materials like engineered wood products, e.g., for general thin orthotropic laminates [137], thick orthotropic laminated plates [136], laminated timber beams [138], and CLT structures [139]. These studies utilize different types of tests and data, such as static deflection tests, natural frequencies, or frequency response data, to determine material properties. Within this thesis, an uncertainty quantification related to the vibrational behavior of the HST structures is performed to investigate the effects of input parameter uncertainty. Such analyses have not been conducted so far for HST structures.

1.2 Contributions and accomplishments

This cumulative thesis contributes to the field of vibroacoustics of HST structures, addressing the issues highlighted in the Introduction. Therefore, three peer-reviewed publications build the basis of this work, introducing numerical and experimental approaches that investigate the overall dynamic behavior of the structures. The major accomplishments can be briefly summarized as follows:

- Paper A [140] deals with experimental investigations related to modal properties of HST systems. Moreover, nonlinearities due to joints are detected by considering amplitude-dependency and higher-order harmonics.

- In Paper B [141], a Monte Carlo simulation is employed to quantify the uncertainty in the modal properties of the HST building elements. Uncertainties related to timber materials are analyzed using Bayesian Inference.

- Paper C [142] characterizes HST floors in a vibroacoustic sense by numerically computing VDV and impact sound pressure levels. The adopted FE model is based on a calibrated model and experimental investigations on small-scale test specimens.

2 Investigations of hybrid steel-timber structures

First, the HST structures under investigation are described in section 2.1. Afterward, information based on the experimental studies performed on the HST elements is given in section 2.2. Finally, the numerical approaches utilized for the investigations on the HST systems are elucidated in section 2.3.

2.1 Objects of investigation

This thesis deals with a specific kind of HST structure. The top and bottom LVL plates represent the chords of the HST element. A trapezoidal steel core is placed between them. Due to manufacturing reasons, two types of joints are applied to connect the individual components: steel-timber and timber-steel joints. The labels of the joints refer to the sequence in which the components are joined together. In the case of the steel-timber joint, the fastener is first driven through the steel and then into the wooden plate. For a timber-steel joint, the assembly is carried out the other way around. As a fastener, either screws or nails are employed. Timber-steel joints are solely built by screws, whereas steel-timber joints are manufactured by either, depending on the test sample.
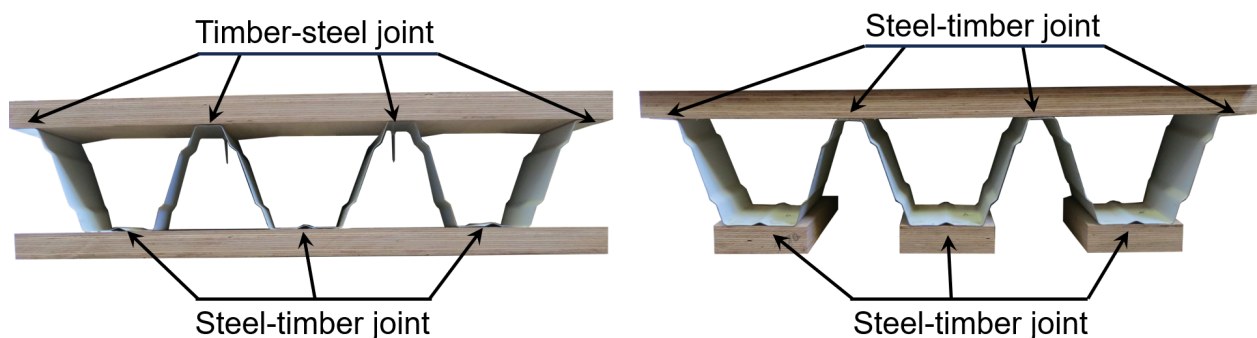

Figure 1: HST cross-section types: closed (left) and open cross-section (right).

A variety of test specimens is analyzed within the appended publications. These specimens differ by dimensions, e.g., steel frame thickness, fastener type, e.g., the diameter of the screw, type of timber material, e.g., LVL made from beech or spruce and pine, and the cross-section type, i.e., open and closed. The difference between open and closed cross-sections becomes apparent when looking at the lower layer of the HST element. A continuous LVL panel is attached to the steel core for closed configurations, whereas individual LVL planks constitute the lower chord for open cases. Examples of both cross-section types are displayed in Fig. 1.

The structures are to be analyzed for future use as a floor structure, requiring investigations regarding vibration and acoustic characteristics, as elucidated in the Introduction. Consequently, the methods described in the following sections deal with experimental and numerical approaches to this purpose.

2.2 Experimental studies

Ewins [143] mentions a threefold motivation to conduct experimental vibration studies. First, one can assess the kind and magnitude of structural vibration responses. Second, models and prediction tools are validated, and third, structural parameters, e.g., natural frequencies and damping properties, are determined. For the latter item, experimental modal analysis is usually conducted. [143]

2.2.1 Experimental modal analysis

For experimental modal analysis, the tested structure is driven to vibrate by a known excitation, often in the form of white or pseudo-random noise. At the same time, the vibration levels are recorded, e.g., as surface velocities or accelerations, to identify natural frequencies, modal damping, and mode shapes. [143] Unlike natural frequencies and damping properties, analyzing mode shapes requires spatial information, meaning vibration measurement data has to be recorded at distributed observation points on the structure. To this aim, the approach of laser Doppler vibrometry has gained popularity over the last decades. Due to the possibility of easily relocating the laser beam by optical devices, there is no need to, e.g., attach many accelerometers to the test specimen. [144] In general, a time signal is measured by a respective device. Filters, such as antialiasing filters, are subsequently applied to the time signal, which is then windowed by, e.g., a rectangular or Hanning function to reduce leakage effects. Finally, a Fast Fourier Transformation (FFT) is applied to compute the frequency response functions (FRF) of the investigated structure. Modal parameters are then extracted by adopting mathematical algorithms, such as polynomial curve fitting. [145]

Experimental modal analysis is conducted within the scope of Paper A. Based on this, model updating is performed in Paper C as described in section 2.3.2. Moreover, the acquired data is utilized in Paper B.

2.2.2 Experimental nonlinearity detection

As elucidated in the Introduction, amplitude-dependent stiffness and damping properties, nonlinearly coupled modes, and higher-order harmonics represent indicators of prevalent nonlinearity in the structure's response.

Amplitude-dependent stiffness and damping values are studied by investigating FRFs and the respective modal data while exciting the structure at varying force levels [105]. If the
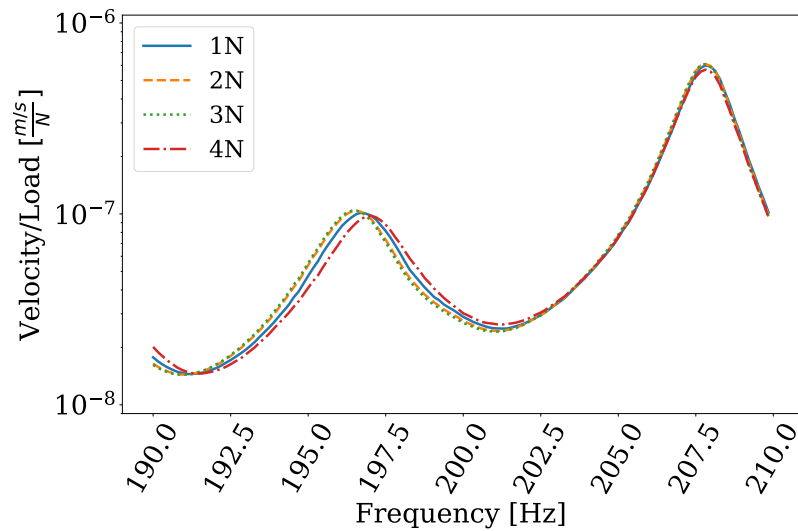
Figure 2: Example FRFs for varying load levels, i.e., 1N, 2N, 3N, and 4N

resonance peaks in the transfer functions or the respective natural frequencies shift to lower or higher frequencies for altered excitation levels, amplitude-dependent stiffness is present in the structure. In cases where the vibration amplitude at the resonances or the modal damping values change due to adapted loads, one detects amplitude-dependent damping. An example is plotted in Fig. 2, where both effects are illustrated for the left peak. The left peak shows a slightly reduced peak amplitude and a slight shift in resonance frequency to higher values. The right peak around $208\,\mathrm{Hz}$ reveals no frequency shift, and a negligible decrease in vibration levels is visible.

A different approach is conducted if higher-order contributions are to be detected. The test specimens are excited by sine-sweep loading, whereas the excitation frequency ranges vary within specified limits. The sweeping time must be chosen carefully so the structure can vibrate at the defined excitation frequencies. In this case, the acquired time data is not directly processed by an FFT. Instead, the frequency spectra are represented over time in spectrograms. Here, the abscissa displays the time dependence, and the ordinate refers to frequency dependency. [146] A notably high-amplitude response at higher-order modes for excitation at a specific resonance frequency indicates nonlinearly coupled modes or modal interaction [106, 107].

Fig. 3 depicts two example spectrograms, one plot with and one without higher-order contribution. For the left plot of Fig. 3, a low excitation level is chosen, and, thus, the structural response is only visible at the excitation frequencies, i.e., between 50 and 100 Hz, indicating linearity. In the case of the right plot of Fig. 3, a higher load level is applied, leading to structural responses at the excitation frequencies and multiples of these, hence indicating higher-order contributions and nonlinearity. Furthermore, the effects of impurities of the excitation's input sine wave must be considered [147].

The approaches described for nonlinearity detection are applied in Paper A.
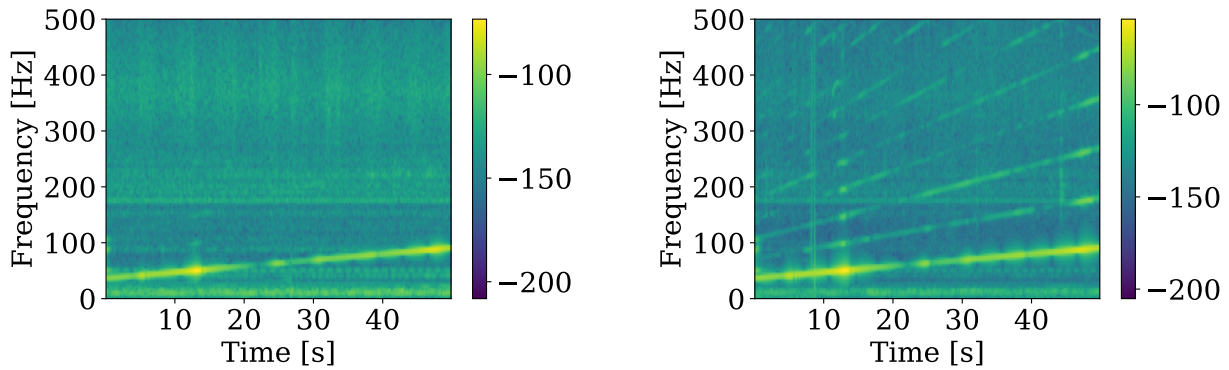
Figure 3: Example spectrograms without (left) and with (right) higher-order contributions

2.3 Numerical methods

Related to the modeling approaches, orthotropic, as opposed to isotropic material behavior, is explained since timber structures are the subject of investigation in all appended studies. This material behavior is presented together with some details on the applied damping concepts. Moreover, the FEM is briefly introduced while presenting commonly used damping and fastener models, which have been applied in the appended publications. Modal analysis and time-harmonic are conducted as deterministic analysis types. This is followed by the introduction of the Rayleigh-Ritz method for moderately thick orthotropic plates. Besides, stochastic approaches using Monte Carlo simulations and Latin Hypercube sampling are presented. Afterward, elaborations on model calibration succeed, followed by elucidations on the Bayesian inference method. Finally, the approaches used for the vibroacoustic validation of the HST floors, i.e., VDV and impact sound computations, are described in the section on post-processing.

FEM is used in all three appended publications. Its probabilistic version is applied to HST structures in Paper B. Additionally, the Bayesian inference and Rayleigh-Ritz method are applied to the case of the investigated LVL plates. Paper C employs model calibration together with FEM to compute the vibroacoustic characteristics described in the section Post-processing.

2.3.1 Modeling approaches

As timber represents an anisotropic material, the applied material model is described first. Subsequently, the two types of numerical models utilized for the analysis of the HST structures, i.e., FEM and the Rayleigh-Ritz method, are elucidated. Additionally, uncertainty quantification related to timber material properties and joint parameters is conducted in this work using probabilistic analysis, which is described at the end of this subsection.

Material behavior

In the scope of this work, elastic material behavior is assumed, which can be described by Hooke's law of elasticity. Grimsel [148] introduces a proportionality between stress σ_{kl} and strain tensor ε_{ij} as

$$\varepsilon_{ij} = J_{ijkl}\sigma_{kl}. \tag{2.1}$$

by establishing a set of proportionality factors J_{ijkl}. Due to the reciprocity of shear stresses, stress and strain tensors are symmetric. Hence, the components of the elasticity tensor of the first two pairs of indices are equal [148]

$$J_{ijkl} = J_{jikl} = J_{ijlk} = J_{jilk}, \tag{2.2}$$

where the i, j, k, l vary from 1 to 3. Moreover, due to the assumption of the existence of an elastic potential, the interchangeability of the index pairs follows [148]

$$J_{ijkl} = J_{klij}. \tag{2.3}$$

Consequently, of the original $3^4 = 81$ components, only 21 are independent of each other, which leads to the Voigt matrix formulation

$$
\begin{pmatrix} \varepsilon_1 \\ \varepsilon_2 \\ \varepsilon_3 \\ \gamma_{23} \\ \gamma_{13} \\ \gamma_{12} \end{pmatrix} =
\begin{bmatrix}
s_{11} & s_{12} & s_{13} & s_{14} & s_{15} & s_{16} \\
s_{21} & s_{22} & s_{23} & s_{24} & s_{25} & s_{26} \\
s_{31} & s_{32} & s_{33} & s_{34} & s_{35} & s_{36} \\
s_{41} & s_{42} & s_{43} & s_{44} & s_{45} & s_{46} \\
s_{51} & s_{52} & s_{53} & s_{54} & s_{55} & s_{56} \\
s_{61} & s_{62} & s_{63} & s_{64} & s_{65} & s_{66}
\end{bmatrix}
\begin{pmatrix} \sigma_1 \\ \sigma_2 \\ \sigma_3 \\ \tau_{23} \\ \tau_{13} \\ \tau_{12} \end{pmatrix}, \tag{2.4}
$$

where the matrix is symmetric, i.e., $s_{ij} = s_{ji}$ [148]. Using this description, general anisotropic, linear elastic material behavior can be defined. In the case of isotropic material behavior, only two non-zero components in the elasticity tensor exist due to symmetry axes in the material. [149] The following elasticity matrix $\mathbf{D} = \mathbf{s}^{-1}$ is gained [149]:

$$
\mathbf{D} =
\begin{bmatrix}
D_{11} & D_{12} & D_{12} & 0 & 0 & 0 \\
 & D_{11} & D_{12} & 0 & 0 & 0 \\
 & & D_{11} & 0 & 0 & 0 \\
 & & & \frac{D_{11}-D_{12}}{2} & 0 & 0 \\
 & \text{sym} & & & \frac{D_{11}-D_{12}}{2} & 0 \\
 & & & & & \frac{D_{11}-D_{12}}{2}
\end{bmatrix}. \tag{2.5}
$$

For orthotropic materials, due to the symmetric condition of the elasticity matrix of the overall twelve entries, only nine entries in the elasticity matrix are independent and non-

zero [149]:

$$\mathbf{D} = \begin{bmatrix} D_{11} & D_{12} & D_{13} & 0 & 0 & 0 \\ & D_{22} & D_{23} & 0 & 0 & 0 \\ & & D_{33} & 0 & 0 & 0 \\ & & & D_{44} & 0 & 0 \\ & \text{sym} & & & D_{55} & 0 \\ & & & & & D_{66} \end{bmatrix}. \tag{2.6}$$

In this case, two orthogonal symmetry planes intercept the coordinate axes [149]. For wood, often orthotropic material behavior is assumed since wood shows three main axes, i.e., longitudinal l, tangential t, and radial r [148]. Locally, the engineering properties moduli of elasticity E_i, shear moduli G_{ij}, and Poisson's ratios v_{ij} are related to the factors of eq. (2.4) as follows [148]

$$E_t = 1/s_{11}; \quad G_{rt} = 1/s_{44}; \quad v_{tl} = -\frac{s_{12}}{s_{22}}. \tag{2.7}$$

All other entries of the elasticity matrix can be computed analogously [148]. Together with the structure's geometry, the elasticity matrix contributes to the stiffness matrix K, whereas the material's density influences the mass matrix M defined in section 2.3.1 [150].

Damping theories All real-world structures inherit some kind of damping. Consequently, amplitudes of vibration do not continue with the same magnitude infinitely but decrease and come to an end after some time. Damping can occur due to many factors, such as internal friction in the material or effects due to surrounding fluids. Hence, different types of damping are defined, i.e., structural, viscous, and coulomb damping. Structural or hysteretic damping is related to frictional effects within the materials. [151] Using the damping coefficient g, the structural damping force is computed as [152]

$$F_0 = \frac{g}{\pi \omega} \dot{u}. \tag{2.8}$$

Here, $\dot{u}$ denotes the structure's velocity, and ω represents the circular frequency. Coulomb damping, or dry friction, arises when a structure moves on a dry surface or two structures move relative to each other. Here, the damping force results as [151]

$$F_0 = \mu N, \tag{2.9}$$

with the normal force N of the moving structure on the surface and the coefficient of friction μ.

Viscous damping is assumed to be proportional to the velocity and emerges in vibrating systems immersed in fluids [151], for dashpots, and hydraulic dampers [152]. The respective damping force is given as [151]

$$F_0 = c\dot{u} \tag{2.10}$$

using the viscous damping coefficient c. Often, the loss factor is utilized to describe damping. It is defined as [153]

$$\eta = \frac{c|\omega|}{k},\qquad(2.11)$$

with the stiffness k. A frequency-dependent viscous damping coefficient $c(\omega)$ can be stated as [153]

$$c(\omega) = \frac{k\eta(\omega)}{|\omega|}.\qquad(2.12)$$

Finite element modeling

Simulations represent a physical relation as a mathematical model, which numerical methods such as the FEM approximate. The solution of interest is subsequently taken from the approximation. However, errors are introduced within simulations, i.e., model form and approximation errors. In the FEM, objects of investigation are represented by an assembly of finite elements, such as beams, plates, shells, and solids. [127] An exemplary FE model is visualized in Fig. 4.
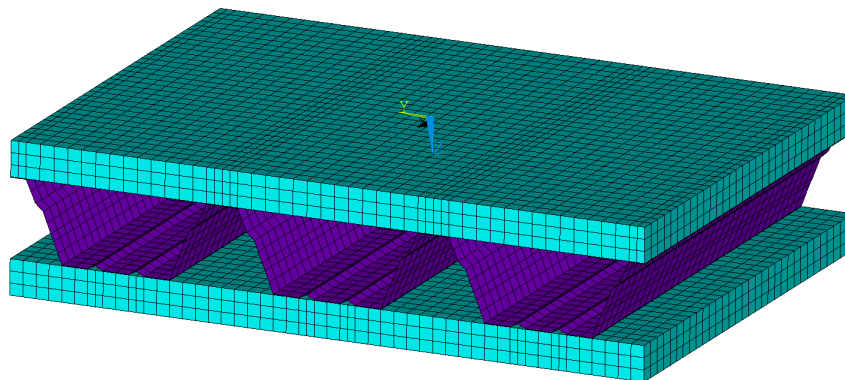

Figure 4: Exemplary mesh of an FE model of an HST element. Steel parts are colored in purple. Timber components are plotted in cyan.

The respective equations that describe a problem are solved at the nodes of the elements, and the solution within the elements is found using the nodal solution and the elements' respective shape functions, e.g., quadratic or linear. [127]

Regarding its dynamic behavior in 3D, a node of a corresponding element can perform six possible movements, i.e., it has six degrees of freedom (DOFs) - three translations, i.e., in x-, y-, and z-direction, in the case of a cartesian coordinate system, and three rotations around the respective coordinate axes. [151] These deformations can be identified through the equations of motion, e.g., for the forced vibration of a single DOF system [151]:

$$m\ddot{u}(t) + c\dot{u}(t) + ku = F(t),\qquad(2.13)$$

with the mass m, the damping c, the stiffness k, the displacement function $u(t)$, and the loading function $F(t)$ depending on time. $\ddot{u}$ and $\dot{u}$ denote the twofold and single derivatives

with respect to time. [151] When considering a complete structure, a system matrix is assembled from the elements' system of equations, which leads to stiffness **K**, mass **M**, and damping matrices **C** instead of scalar values [151]:

$$\mathbf{M\ddot{u}}(t) + \mathbf{C\dot{u}}(t) + \mathbf{Ku} = \mathbf{F}(t), \tag{2.14}$$

with the force vector $\mathbf{F}(t)$ and the vector of displacements $\mathbf{u}(t)$. The matrix dimensions correspond to the number of DOFs n_{dof}, i.e., the matrices **M**, **C**, and **K** have the dimension $n_{\text{dof}} \times n_{\text{dof}}$ and the vectors **u** and **F** are of the size $n_{\text{dof}} \times 1$. The displacement vector consists of the nodal solutions regarding the respective DOFs, which is used to compute the overall vibration response within the finite elements by the shape functions. [151]

Modeling of damping   The mass and stiffness matrices of eq. (2.14) are constructed using the defined material behavior and properties (section 2.3.1). The last missing part of eq. (2.14) represents the damping matrix. When assuming a time-harmonic excitation, the following relation is established from eq. (2.13) [153]:

$$[-m\omega^2 + \mathrm{i}\omega c(\omega) + k]\bar{u}(\mathrm{i}\omega) = \bar{F}(\mathrm{i}\omega), \tag{2.15}$$

where the displacement $\bar{u}(\mathrm{i}\omega)$ and the force $\bar{F}(\mathrm{i}\omega)$ are given in the frequency domain. However, due to causality principles, physical limitations must be considered. Therefore, to establish damping by applying eq. (2.12) leads to

$$[-m\omega^2 + k(1 + \mathrm{i}\eta(\omega)sgn(\omega))]\bar{u}(\mathrm{i}\omega) = \bar{F}(\mathrm{i}\omega), \tag{2.16}$$

with $\mathrm{sgn}()$ representing the signum function. [153] The viscous damping describes a material or structural damping with a dependency on the velocity or displacement. This is achieved by introducing a complex stiffness or, in the case of a material, a complex elasticity modulus, for example. The damping ratio follows as $D = \eta/2$. [154]

Challenges in theoretically or experimentally identifying damping still remain, resulting in simplified approaches to represent damping within a structure [151]. Hence, another favorable damping approach in the context of multi-DOF systems has been established, called Rayleigh damping [155]. Here, the damping matrix is assumed to be proportionally dependent on the mass and stiffness matrix [154]:

$$\mathbf{C} = \alpha\mathbf{M} + \beta\mathbf{K}, \tag{2.17}$$

where the individual entries on the diagonal of the damping matrix result as $C_{ii} = \alpha + \beta\omega_i^2$. Here, ω_i^2 represents the circular natural frequencies of the investigated structure. In this case, the modal damping ratios equal

$$D_i = \frac{1}{2}\left(\frac{\alpha}{\omega_i} + \beta\omega_i\right), \tag{2.18}$$

where α is the mass and β the stiffness matrix multiplier [154]. Hence, when conducting modal analysis, a modal damping ratio can be defined [156].

Joint modeling   Joint models can be categorized based on the dimension regarding their extension. Lumped models, also known as 0-D models, assume no spatial extension and are suitable when the joint's size is small related to the structure's dimensions and the contact area stays constant. The 0-D models are applicable as long as the smallest considered wavelength is larger than the joint's patch size. For cases where the contact area shows nearly constant conditions in one direction, line models (1-D) can be utilized. Alternatively, when local differences within the entire joint patch need to be considered, interface models (2-D) are employed. Moreover, joint models can be categorized based on the linearity of their behavior. However, experimental investigations often show an approximately linear behavior of joints when excitation amplitudes are small and macroslip is avoided. [102] Hence, regularly, the structural behavior is equivalently linearized. When comparing nonlinear and linearized system matrices, only some matrix entries are changed since nonlinearity occurs only at some positions in the structure. [157]

Joint models are realized in different ways in the FEM. On the one hand, a surface-by-surface implementation is possible with the help of zero-thickness or thin-layer elements, which accounts for 2-D models. On the other hand, node-to-node or node-to-surface elements are applicable, representing 0-D models and a hybrid 0-to-2-D option. [102]

A balance between detailed representations of joint kinematics and the computational resources needed to predict the dynamic structural responses seems favorable [158]. Calibrated node-to-node joint models based on linear springs [159] and damper elements [157] are easily implemented in an FE model. The commercial FE software ANSYS offers various implementations of such elements with the COMBIN-series, whereas the COMBIN14 element represents the easiest implementation. It consists of a linear spring with constant k and a damper with the coefficient c, which acts as a uniaxial tension-compression component with longitudinal and torsional capabilities. [160] The element's damping is included in the form of damping coefficients as part of the structural damping matrix, where the damping force is given as, e.g., [156]

$$F_x = -c\frac{\mathrm{d}}{\mathrm{d}t}u_x. \tag{2.19}$$

The joint's spring stiffness directly contributes to the system's stiffness matrix [156]. These uniaxial elements are applied to connect the individual structural components in the required DOF directions (Fig. 5).

When combining a one-dimensional element with a 3D FE model, issues regarding non-physical singularities of stresses are involved. To overcome those complications, whole-joint kinematics are introduced, which couple the contact areas surrounding a bolt as two rigid surfaces connected by a single element. [161] Different implementations of such an option are conceivable.

A combination of surface-to-surface contact via thin-layer or zero-thickness elements, which are defined by a constitutive matrix, and a node-to-node contact via spring elements represents the "MPC184 General Joint Element". Here, relative displacements and rotations between the connected nodes are possible if not prohibited by defined con-
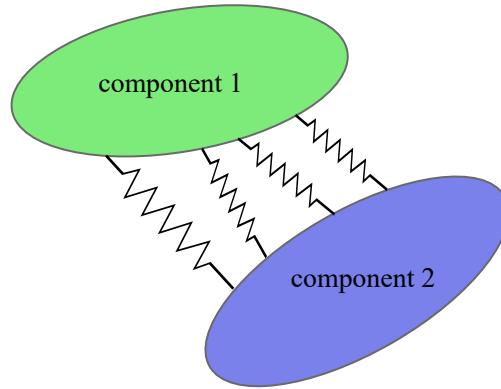
Figure 5: Structural components are coupled via uniaxial springs in the respective DOF directions.

straints. [160] Their behavior is specified by a general stiffness matrix with 21 independent entries [160]:

$$
d_{\text{joint}} = \begin{bmatrix} d_{11} & d_{12} & d_{13} & d_{14} & d_{15} & d_{16} \\ & d_{22} & d_{23} & d_{24} & d_{25} & d_{26} \\ & & d_{33} & d_{34} & d_{35} & d_{36} \\ & & & d_{44} & d_{45} & d_{46} \\ & \text{sym.} & & & d_{55} & d_{56} \\ & & & & & d_{66} \end{bmatrix}.
\tag{2.20}
$$

The first three indices refer to the relative displacements in the element's local x-, y-, and z-direction, whereas the latter three indices assign the rotational DOF directions [160].

Modal analysis   Once all structural components, i.e., timber plates, steel frame, and joints, are represented in the model, analyses can be conducted, e.g., modal analysis. For an unloaded, undamped structure, i.e., considering the undamped free vibrations of a structure, the force vector is set to zero, i.e., $\mathbf{F}(t) = 0$, and the following equation of motion is given [162]:

$$
\mathbf{M}\ddot{\mathbf{u}}(t) + \mathbf{K}\mathbf{u}(t) = \mathbf{0}.
\tag{2.21}
$$

A harmonic displacement form [162]

$$
\mathbf{u} = \mathbf{a} \cos \omega t
\tag{2.22}
$$

is assumed for the free vibrations of a linear system with the vector of the amplitudes of motion $\mathbf{a}$. Subsequently, by inserting eq. (2.22) into eq. (2.21) and factoring out the cosine term, an eigenvalue problem is established [162]:

$$
(\mathbf{K} - \omega_i^2 \mathbf{M})\mathbf{a} = \mathbf{0}.
\tag{2.23}
$$

The nontrivial solution to this problem gives the circular natural frequencies ω_i and the eigenvectors $\mathbf{a}$ corresponding to the eigenvalues, i.e., the natural frequencies. These are the mode shapes of the system and can be arranged in the modal matrix of the system $[\boldsymbol{\Phi}]$. [162]

Time-harmonic analysis For time-harmonic analysis, it is assumed that linear structures perform steady-state vibrations at the frequencies of interest $f \in \mathbf{f}\,[\mathrm{Hz}]$ [162]. The structural response can be found by solving the general equation of motion in eq. (2.13) while introducing a harmonic, i.e., sine or cosine function, excitation of a structure as

$$\mathbf{F} = \mathbf{F}_{\mathrm{max}} \exp\{\mathrm{i}\Psi\} \exp\{\mathrm{i}\Omega t\}, \tag{2.24}$$

with the force amplitude $\mathbf{F}_{\mathrm{max}}$, the applied circular frequency $\Omega = 2\pi f$, and the force phase shift Ψ [162].

Moreover, a harmonic displacement description as

$$\mathbf{u} = \mathbf{u}_{\mathrm{max}} \exp\{\mathrm{i}\vartheta\} \exp\{\mathrm{i}\Omega t\} \tag{2.25}$$

is utilized with the displacement amplitudes $\mathbf{u}_{\mathrm{max}}$ and the displacement phases ϑ [162].

Subsequently, a reformulated equation of motion is established by inserting eq. (2.24) and eq. (2.25) into eq. (2.13) as [162]

$$(-\Omega^2 \mathbf{M} + \mathrm{i}\Omega \mathbf{C} + \mathbf{K})\mathbf{u}_{\mathrm{max}} \exp\{\mathrm{i}\vartheta\} \exp\{\mathrm{i}\Omega t\} = \mathbf{F}_{\mathrm{max}} \exp\{\mathrm{i}\Psi\} \exp\{\mathrm{i}\Omega t\}. \tag{2.26}$$

By solving this equation, the complex displacement vector $\mathbf{u}$ at the respective frequencies $f \in \mathbf{f}\,[\mathrm{Hz}]$ is found [162].

Rayleigh Ritz approach for modal data related to orthotropic moderately thick plates

For some assessments, many model evaluations and hybrid methodologies, e.g., commercial FE software and a programming environment, are required. This necessitates a computationally faster model. Hence, additionally, to the commercially implemented FEM, a Rayleigh-Ritz approach is applicable.

The often-used classical plate theory assumes thin plate structures and does not consider transverse shear deformation effects. This can lead to wrong predictions of buckling loads and natural frequencies when the theory is applied to thicker plates. [163] The term "thick plate" relates to the ratio of plate thickness and considered wavelengths. Applying the first-order shear deformation theory of Mindlin presents a remedy for this [164] and builds the basis for the following derivations.

Wood is usually simulated as an orthotropic material due to its anatomy (sec. 2.3.1) [148]. Moreover, vibration measurements (sec. 2.2) are often conducted with hanging supports

to simulate free boundary conditions [143]. Therefore, a Rayleigh-Ritz method for orthotropic Mindlin-Plates with free supports is introduced [163, 165].

The energy functionals for the strain and kinetic energy of the plate are computed by incorporating the constitutive equations specific to a moderately thick orthotropic plate with the length l_t, width b_t, and thickness h. In order to fulfill the boundary conditions, trigonometric basis functions are employed as follows [165]

$$\varphi_m(x) = \begin{cases} \cos(\lambda_m x) & m \geq 0 \\ \sin(\lambda_m x) & m < 0 \end{cases}, \qquad \lambda_m = m\pi/l_t, \tag{2.27}$$

$$\varphi_n(y) = \begin{cases} \cos(\lambda_n y) & n \geq 0 \\ \sin(\lambda_n y) & n < 0 \end{cases}, \qquad \lambda_n = n\pi/b_t, \tag{2.28}$$

$$\tag{2.29}$$

to define the displacements w and rotations ψ_i of the plates as [165]

$$\psi_x(x,y) = \sum_{m=-2}^{\infty} \sum_{n=-2}^{\infty} A_{mn}\varphi_m(x)\varphi_n(y), \tag{2.30}$$

$$\psi_y(x,y) = \sum_{m=-2}^{\infty} \sum_{n=-2}^{\infty} B_{mn}\varphi_m(x)\varphi_n(y), \tag{2.31}$$

$$w(x,y) = \sum_{m=-2}^{\infty} \sum_{n=-2}^{\infty} C_{mn}\varphi_m(x)\varphi_n(y). \tag{2.32}$$

The deformation functions rely on the coefficients A_{mn}, B_{mn}, and C_{mn} to describe the potential and kinetic energies, U and T, and build the Lagrangian expression [165].

The Lagrangian is calculated as [163]

$$L = T - U. \tag{2.33}$$

Here, the strain energy is computed as [163]

$$U = \iint_A \left\{ D_{11}\left(\frac{\partial \psi_x}{\partial x}\right)^2 + D_{22}\left(\frac{\partial \psi_y}{\partial y}\right)^2 + (\mu_{xy}D_{11} + \mu_{yx}D_{22})\frac{\partial \psi_x}{\partial x}\frac{\partial \psi_y}{\partial y} + \right.$$
$$\left. D_{xy}\left(\frac{\partial \psi_x}{\partial y} + \frac{\partial \psi_y}{\partial x}\right)^2 + \kappa G_{xz}h\left(\psi_x + \frac{\partial w}{\partial x}\right)^2 + \kappa G_{yz}h\left(\frac{\partial w}{\partial y}\right)^2 \right\} \mathrm{dxdy} \tag{2.34}$$

considering the flexural rigidities of the plate [163]

$$D_{11} = \frac{E_x h^3}{12(1 - v_{xy}v_{yx})}, \tag{2.35}$$

$$D_{12} = \frac{v_{xy}E_x h^3}{12(1 - v_{xy}v_{yx})}, \tag{2.36}$$

$$D_{21} = \frac{\nu_{yx} E_y h^3}{12(1 - \nu_{xy}\nu_{yx})}, \tag{2.37}$$

$$D_{22} = \frac{E_y h^3}{12(1 - \nu_{xy}\nu_{yx})}, \tag{2.38}$$

$$D_{xy} = \frac{G_{xy} h^3}{12}. \tag{2.39}$$

Furthermore, the total kinetic energy is calculated as [163]

$$T = \frac{\rho h \omega^2}{2} \iint_A [w^2 + h^2(\psi_x^2 + \psi_y^2)/12] \mathrm{dxdy}. \tag{2.40}$$

The Lagrangian expression is derived with respect to the coefficients and, subsequently, minimized. Therefore, it is summarized in matrix form as [163]

$$(\mathbf{K} - \omega^2 \mathbf{M})\mathbf{E}_c = 0, \tag{2.41}$$

with the stiffness matrix $\mathbf{K}$, the mass matrix $\mathbf{M}$, the natural frequencies $\mathbf{f} = \omega/(2\pi)$ and the coefficient matrix [165]

$$\mathbf{E}_c = \left\{ \begin{array}{cccc} A_{-2,-2} & A_{-2,-1} & ... & A_{M,N} \\ B_{-2,-2} & B_{-2,-1} & ... & B_{M,N} \\ C_{-2,-2} & C_{-2,-1} & ... & C_{M,N} \end{array} \right\}^T, \tag{2.42}$$

where the truncation order $M = 8$ and $N = 8$ is applied.

Probabilistic analysis

Various uncertainties are inherent when analyzing structures, such as the stiffness of supports [166], joints [167], and irregularities in material data, especially in wood, due to natural growth, knots, and changing fiber directions [9, 168]. Probabilistic analysis is performed to assess the influence of the parameter uncertainties on the response of engineering structures. Here, often the FEM is utilized as a deterministic analysis tool, but it is applied in a stochastic context within the Monte Carlo simulation approach. Probabilistic design parameters undergo sampling, and a series of deterministic computations are executed to yield insights into the distribution or specific statistics of response parameters. While this approach is accurate, straightforward, and widely applicable, its popularity is tempered by its high computational cost. Hence, for deterministic executions, computational advantages can be gained from the use of commercial code. Moreover, efficient sampling techniques, e.g., stratified sampling and Latin hypercube sampling, decrease the necessary computational resources significantly. [169]

For Monte Carlo simulations, design parameters, e.g., moduli of elasticity, can be represented as random fields depending on the spatial variable x. The design parameters can

be regarded as random variables if assumed to be homogeneous over the spatial domain. [169]

Realizations are created in accordance with the statistics of the random fields or random variables within the Monte Carlo method. Subsequently, for each of the considered variables k_{MC}, i.e., stochastic input parameters, n_{MC} independent Gaussian distributed random numbers ζ_{MC} with mean zero and variance of one are generated and saved in the matrix $\mathbf{R}$ of size $n_{MC} \times k_{MC}$. [169] Then, a Cholesky decomposition of the target covariance matrix $\mathbf{C}$ of size $k_{MC} \times k_{MC}$ is computed as [169]

$$\mathbf{L}\mathbf{L}^T = \mathbf{C}, \tag{2.43}$$

with the lower triangular matrix $\mathbf{L}$. Next, an $n_{MC} \times k_{MC}$ matrix $\mathbf{U}$ of Gaussian random numbers with zero mean and a covariance corresponding to the target matrix is estimated [169]:

$$\mathbf{U} = \mathbf{R}\mathbf{L}^T. \tag{2.44}$$

The vector of mean values $\mathbf{m} \in \mathbb{R}^{1 \times k_{MC}}$ is added to each row in the matrix $\mathbf{U}$ to attain the target mean values. Latin hypercube sampling decreases the number of samples required to explore the target statistics. Here, the samples are distributed over the whole sampling space. When reducing the dimensionality of the problem to two instead of k_{MC}, a Latin square is given if only one sample in each row and column is taken. This concept is expanded to a general number of dimensions for a Latin hypercube. This way, the risk of leaving parts of the sample space unexplored is decreased. [169]

The probabilistic analysis using Monte Carlo simulations and Latin hypercube sampling investigates the uncertainty of the system by propagating the random design parameters through the simulation model [135].

The uncertainty of model input parameters can be taken from measurement data by, e.g., calibrating an FE model and its parameters until the target error lies below a threshold. This procedure can be repeated for several experiments on seemingly similar structures to provide a set of calibrated model parameters. Subsequently, mean and variance are computed from the dataset to represent the uncertainty of the input properties. Errors and uncertainties related to the model, such as those arising from the model itself, the considered boundary conditions, or excitation, are not taken into account here. Only interspecimen and, to some extent, measurement uncertainty are incorporated by conducting measurements on similar specimens. Since this approach requires iteratively performing an FE simulation and adjusting the model input parameters, it can be seen as an iterative, i.e., a model updating approach. As an example, this technique has been applied to identify timber material properties in [135].

2.3.2 Model calibration and parameter optimization

Even though advanced FE techniques for structural analysis are readily available, a notable disparity in practical applications between analytical or numerical predictions and actual test results often exists. Adjustments to modeling assumptions and parameters are made until the correlation between predictions and experimental outcomes meets practical requirements. Traditionally, this involves a trial-and-error process, which generally proves to be time-consuming and may be impractical in certain situations. Consequently, computational procedures have been established to calibrate model parameters utilizing experimental data. Specifically, modal data, such as natural frequencies and mode shapes derived from measured frequency response data, are widely used as an objective for adjusting model parameters. [128]

When applying FEM to model a physical system, idealization errors, such as model simplifications, discretization errors, e.g., too coarse of an FE mesh, and errors related to model parameters, e.g., material parameters, are introduced. The goal of every structural analysis is to minimize all three error types within the model.

Model updating

Often, an iterative process, also known as model updating, is employed to reduce the error due to parameter estimates [128]. Therefore, a residual related to the discrepancy between predicted and measured structural behavior is established [128]:

$$\varepsilon = z_m - z(\boldsymbol{\theta}), \tag{2.45}$$

with the measured quantities z_m, here, natural frequencies and modes, and the predictions $z(\boldsymbol{\theta})$ dependent on the parameter set $\boldsymbol{\theta}$.

The procedure of model updating is affected by the parametrization of the problem, as updating a large number of parameters might lead to an almost perfect agreement while losing physical insight. Moreover, only outputs sensitive to the chosen updating parameters should be accounted for.

When applying the FEM to perform model updating, an optimization problem based on an objective function in terms of the residual (eq. (2.45)) is formulated. The objective functions often depend on modal data, i.e., natural frequencies and modes. Two approaches are commonly applied to incorporate frequencies and modes in the objective. [129]

First, single-objective functions are employed, which include weightings of terms related to frequencies and terms related to mode shapes [129]:

$$e(\boldsymbol{\theta}) = w_f \left(\sum_i^{n_f} r_{if}^2 \right)^{1/2} + w_m \left(\sum_i^{n_m} r_{im}^2 \right)^{1/2}, \tag{2.46}$$

with the frequency weighting factor w_f, the residual of frequencies r_{if}, the number of considered frequencies n_f, the mode weighting factor w_m, the residual related to modes

r_{im}, and the number of considered modes n_m. The weightings are selected to represent the degree of uncertainty associated with the measured quantities. Hence, natural frequencies are often weighted more than the modes since they are identified more easily. However, the choice of weightings is initially unclear and is usually found by trial and error. [129]

Second, to overcome the challenge of choosing appropriate weightings, multi-objective functions are utilized, which consist of the same terms as the single-objective function but do not require any weights [129]:

$$\min e(\boldsymbol{\theta}) = \min(e_1(\boldsymbol{\theta}) \& e_2(\boldsymbol{\theta})) = \begin{cases} e_1(\boldsymbol{\theta}) = \left(\Sigma_i^{n_f} r_{if}^2\right)^{1/2} \\ e_2(\boldsymbol{\theta}) = \left(\Sigma_i^{n_m} r_{im}^2\right)^{1/2} \end{cases}. \tag{2.47}$$

Here, one tries to identify the optimal solution in the Pareto optimal front [129]. For conflicting objectives, a single optimal solution is not attainable. Rather, a set of alternative solutions known as Pareto optimal solutions exist. These solutions are considered optimal because, within the parameter space, no other solutions outperform them when all objectives are taken into account. [170] To identify the best solution, it is essential to establish a sensible criterion. In problems framed within the FE model updating context with two sub-objective functions, i.e., bi-criterion problems, an additional constraint is typically imposed, which aims to achieve effective compromises or "trade-offs" between conflicting objective functions in an optimal fashion. [129]

The objective related to frequencies often takes the form [71]

$$e_1(\boldsymbol{\theta}) = \sum_i^{n_f} \alpha_i \left(\frac{f_{\mathsf{exp},i} - f_i(\boldsymbol{\theta})}{f_{\mathsf{exp},i}} \right), \tag{2.48}$$

with the optional individual frequency weighting α_i, the measured natural frequencies $\mathbf{f}_{\mathsf{exp}}$, the number of considered frequencies n_f, and the computed natural frequencies $\mathbf{f}(\boldsymbol{\theta})$ depending on the model parameters $\boldsymbol{\theta}$.

The objective function related to mode shapes is given as [71]

$$e_2(\boldsymbol{\theta}) = \sum_{i=1}^{n_m} \left(\frac{1 - \mathsf{MAC}_i}{\mathsf{MAC}_i} \right)^2, \tag{2.49}$$

with the experimentally determined and numerically predicted natural modes, Φ_{exp} and $\Phi(\boldsymbol{\theta})$. Usually, the Modal Assurance Criterion MAC is calculated as [171]

$$\mathsf{MAC}_i = \frac{|\Phi_{\mathsf{exp},i}^T \Phi_i(\boldsymbol{\theta})|^2}{(\Phi_{\mathsf{exp},i}^T \Phi_{\mathsf{exp},i})(\Phi_i(\boldsymbol{\theta})^T \Phi_i(\boldsymbol{\theta}))}. \tag{2.50}$$

To minimize the objective functions, various optimization approaches, e.g., genetic algorithms, particle swarm optimization, and Bayesian approaches, are applied [129].

Bayesian inference

A common strategy to estimate material parameters while considering the uncertainty related to the parameters is the so-called Bayesian inference. In this context, probabilities associated with uncertain material input parameters in a simulation model are determined. The approach involves updating prior information on model parameters, such as in this thesis the material properties of timber, by integrating experimentally determined data. This enhances the level of confidence in the probability distribution of the material parameters. [172]

The probabilistic model of uncertain material parameters denoted as the posterior probability [172]

$$p(\boldsymbol{\theta}|\mathbf{f}_{\text{exp}}) \propto p(\mathbf{f}_{\text{exp}}|\boldsymbol{\theta})p(\boldsymbol{\theta}), \tag{2.51}$$

is established using Bayes' rule with the uncertain parameters $\boldsymbol{\theta}$, the measured data $\mathbf{f}_{\text{exp}}$, the prior probability of an uncertain parameter $p(\boldsymbol{\theta})$, and the likelihood $p(\mathbf{f}_{\text{exp}}|\boldsymbol{\theta})$. The denominator in Bayes' formula serves as a normalization of the probabilities and is often left out, as in eq. (2.51) [172].

Within the context of vibroacoustics, the relevant measured data $\mathbf{f}_{\text{exp}}$ often consists of natural frequencies obtained by experimental modal analysis (sec. 2.2.1). The uncertain material parameters $\boldsymbol{\theta}$ serve as inputs to a forward model $\mathbf{f}_t(\boldsymbol{\theta})$, which is a Rayleigh-Ritz approach in this work (sec. 2.3.1). The forward model, along with the measurement data, is employed to estimate the likelihood. A computationally efficient forward model is preferably chosen since many model evaluations are necessary for Bayesian inference if Markov Chain Monte Carlo methods are employed. [172]

The initial probabilities, also known as priors, comprise the beliefs regarding the uncertain parameters before incorporating measurement data [172]. Prior predictive checks can be performed to verify that the prior probabilities represent physically meaningful ranges of values. Here, it is determined whether the forward model represents the actual data. The prior predictive checks are essential if a complex problem with little data is studied since, in this case, the priors exert a strong effect on the posterior probabilities. Hence, a prior predictive distribution is evaluated by drawing values from it, assuming the model represents the physical behavior accurately. The similarity of the observed data with the prior predictive distributions is then checked. [173]

To ascertain the posterior densities in light of the measurement data $\mathbf{f}_{\text{exp}}$, the likelihood $p(\mathbf{f}_{\text{exp}}|\boldsymbol{\theta})$ is integrated with the prior probabilities $p(\boldsymbol{\theta})$. Thus, the likelihood assesses the probability of obtaining a specific measurement result given a particular material parameterization $\boldsymbol{\theta}$. The mean of the distribution μ relates to the actual measured natural frequencies $\mathbf{f}_{\text{exp}}$, while the standard deviation σ refers to the measurement noise. [174] When describing the problem related to the measurement data and model parameters while the mean is connected to the model parameter, the residual error is assumed to have a zero mean $\mu_{\text{lik}} = 0$ and is given as [174]

$$\varepsilon_i = f_{\text{exp},i} - f_{t,i}(\boldsymbol{\theta}), \tag{2.52}$$

with $f_{\text{exp},i}$ being one of the $1 \leq i \leq n_f$ measured datasets. Subsequently, through maximizing entropy, the probability of the residual error [174]

$$p(\varepsilon_i | \boldsymbol{\theta}, \mathbf{f}_t(\boldsymbol{\theta}), \sigma_{\text{lik},i}, \mu_{\text{lik}} = 0) = \frac{1}{\sqrt{2\pi}\sigma_{\text{lik},i}} \exp\left\{ -\frac{\varepsilon_i^2}{2\sigma_{\text{lik},i}^2} \right\}, \tag{2.53}$$

is found, given the forward model $\mathbf{f}_t(\boldsymbol{\theta})$, the model parameters $\boldsymbol{\theta}$, and the standard deviation $\sigma_{\text{lik},i}$. It is crucial for the employed forward model $\mathbf{f}_t(\boldsymbol{\theta})$ to accurately reproduce the experimental data [174].

The probability associated with each data point corresponds to the probability of the residual error at that specific data point $p(\mathbf{f}_{\text{exp}} | \boldsymbol{\theta}, \mathbf{f}_t(\boldsymbol{\theta}), \sigma_{\text{lik}}) = p(\varepsilon | \boldsymbol{\theta}, \mathbf{f}_t(\boldsymbol{\theta}), \sigma_{\text{lik}})$ [174]. Consequently, the overall likelihood function is calculated as the joint probability of all data points [174]

$$p(\mathbf{f}_{\text{exp}} | \boldsymbol{\theta}, \mathbf{f}_t(\boldsymbol{\theta}), \sigma_{\text{lik},1}, \sigma_{\text{lik},2}, ..., \sigma_{\text{lik},n_f}) = p(\varepsilon_1, \varepsilon_2, ..., \varepsilon_{n_f} | \boldsymbol{\theta}, \mathbf{f}_t(\boldsymbol{\theta}), \sigma_{\text{lik},1}, \sigma_{\text{lik},2}, ..., \sigma_{\text{lik},n_f}). \tag{2.54}$$

Given that the noise is consistent across most measurements in typical experiments, it is presumed that $\sigma_{\text{lik}} = \sigma_{\text{lik},i}$ for all $1 \leq i \leq n_f$, where n_f equals the number of experimentally identified natural frequencies [174]. Moreover, following the principle of maximum entropy, the individual measurements are logically considered independent, resulting in the joint probability as follows [174]:

$$p(\mathbf{f}_{\text{exp}} | \boldsymbol{\theta}, \mathbf{f}_t(\boldsymbol{\theta}), \sigma_{\text{lik}}) = \prod_i^{n_f} \frac{1}{\sqrt{2\pi}\sigma_{\text{lik}}} \exp\left\{ -\frac{\varepsilon_i^2}{2\sigma_{\text{lik}}^2} \right\}. \tag{2.55}$$

Furthermore, more than one specimen, i.e., $n_r \geq 1$, is examined to account for the repeatability of measurements. As a result, the scalar values in the residual error in eq. (2.52) transform into vectors with a length of n_r: $\varepsilon_i = \mathbf{f}_{\text{exp},i} - \mathbf{f}_{t,i}(\boldsymbol{\theta})$.

Marginalization is applied to the joint probability, if the hyperparameters are not of specific interest, to estimate a likelihood without the standard deviation σ_{lik} [174]:

$$\begin{aligned} p(\mathbf{f}_{\text{exp}} | \boldsymbol{\theta}, \mathbf{f}_t(\boldsymbol{\theta})) &= \int p(\mathbf{f}_{\text{exp}}, \sigma_{\text{lik}} | \boldsymbol{\theta}, \mathbf{f}_t(\boldsymbol{\theta})) \mathrm{d}\sigma_{\text{lik}} \\ &= \int p(\mathbf{f}_{\text{exp}} | \boldsymbol{\theta}, \mathbf{f}_t(\boldsymbol{\theta}), \sigma_{\text{lik}}) p(\sigma_{\text{lik}} | \boldsymbol{\theta}, \mathbf{f}_t(\boldsymbol{\theta})) \mathrm{d}\sigma_{\text{lik}}. \end{aligned} \tag{2.56}$$

For the marginal distribution $p(\sigma_{\text{lik}} | \boldsymbol{\theta}, \mathbf{f}_t(\boldsymbol{\theta}))$, Jeffrey's prior

$$p(\sigma_{\text{lik}} | \boldsymbol{\theta}, \mathbf{f}_t(\boldsymbol{\theta})) = \frac{1}{\sigma_{\text{lik}}}. \tag{2.57}$$

is assigned employing the principle of maximum entropy [174].

Then, the integration from eq. (2.56) is executed with the limits $\sigma_{\text{lik}} \in [0, \infty)$ leading to a marginalized likelihood that can be represented by a Student's t-distribution [174]

$$p(\mathbf{f}_{\text{exp}}|\boldsymbol{\theta}, \mathbf{f}_t(\boldsymbol{\theta})) = \frac{\Gamma(n_f/2)}{2} \left(\pi \sum_{i=1}^{n_f} \varepsilon_i^2 \right)^{-n_f/2}, \tag{2.58}$$

where $\Gamma(...)$ denotes the standard gamma function. The experiments conducted on individual specimens $j \in n_r$ are incorporated by aggregating the error regarding those data points as [174]

$$p(\mathbf{f}_{\text{exp}}|\boldsymbol{\theta}, \mathbf{f}_t(\boldsymbol{\theta})) = \frac{\Gamma(n_f/2)}{2} \left(\pi \sum_{i=1}^{n_f} \sum_{j=1}^{n_r} \varepsilon_{ji}^2 \right)^{-n_f/2}, \tag{2.59}$$

where $\varepsilon_{ji} = f_{\text{exp},ji} - f_{t,ji}(\boldsymbol{\theta})$.

Once the likelihood function is established, the priors are checked, and the forward model is implemented in the framework, the posterior distribution is constructed by eq. (2.51). Here, methods to explore these probabilities are applied since analytical solutions for the posterior seldom exist, as in the case of conjugacy. Therefore, Markov Chain Monte Carlo sampling methods, which compute samples for each likelihood evaluation from the model, are utilized. [172] One example of a Markov Chain Monte Carlo sampler is the so-called Sequential Monte Carlo (SMC) sampler. Multimodal posterior probabilities are handled more easily with this approach, as the sampler is less prone to becoming trapped in local minima than traditional Markov Chain Monte Carlo methods. This challenge is addressed by incorporating the concept of tempering, where the number of states of a physical system is based on the system's temperature. The system remains within a single state for zero Kelvin, whereas all possible states are equally likely obtained for an infinite temperature. [175] This concept is incorporated in Bayes' theorem by adding the parameter β, the inverse temperature or tempering parameter, to eq. (2.51) [175]:

$$p(\boldsymbol{\theta}|\mathbf{f}_{\text{exp}})_\beta = p(\mathbf{f}_{\text{exp}}|\boldsymbol{\theta})^\beta p(\boldsymbol{\theta}). \tag{2.60}$$

In the case of $\beta = 0$, $p(\mathbf{f}_{\text{exp}}|\boldsymbol{\theta})^\beta = 1$, which leads to the tempered posterior $p(\boldsymbol{\theta}|\mathbf{f}_{\text{exp}})_\beta$ resembling the prior $p(\boldsymbol{\theta})$. On the contrary, if $\beta = 1$, the tempered posterior equals the actual full posterior. The SMC algorithm starts by sampling from the prior since it is easier than sampling from the posterior. Subsequently, by slowly increasing the value of β, the sampler moves to the more complex posterior distribution. Hence, the sampling proceeds iteratively until the tempering parameter β lies above a value of one. These steps are conducted for a provided number of n_c chains. Moreover, within SMC, resampling takes place by replacing samples with a low probability by samples with a higher probability. The number of steps the algorithm needs to easily transition from one stage to another is determined internally based on the difficulty of the problem while also considering computational resources. [175]

When sampling within the Bayesian inference framework would lead to high computational effort, a first approximation of the posterior's mean values can also be gained by

applying maximum likelihood or maximum a-posteriori estimation. Both approaches are based on the likelihood function in eq. (2.59) and Bayes' formula in eq. (2.51). Generally, the maximum likelihood estimate represents the posterior mode for a noninformative or improper prior. For other types of priors, a maximum a-posteriori estimation is performed to obtain a guess on the posterior mode without requiring extensive model evaluations. [172, 176]

2.3.3 Post-processing

Once the needed model parameters are found and calibrated, the simulation model is built, and the analysis of the HST structures follows.

Computation of the vibration dose value

As stated in section 1.1.2, currently, AISC Design 11 [83] and CCIP-016 [82] appear to be the most reasonable design guides to be applied to HST floors. The codes rely on the evaluation of VDVs, which are either estimated based on numerically or experimentally determined vibration responses of floors. The numerical approach is elucidated in the following.

Floor structures with natural frequencies exceeding $4\,\mathrm{Hz}$ are analyzed employing the impulse response calculation steps as outlined in the following [82, 83, 89]:

1. Modes Φ_m and natural frequencies f_m up to two times the fundamental frequency f_0 for $m \in n_m$

2. Effective footfall impulse: $I_{\mathrm{eff},m} = 54 \cdot f_w^{1.43} / f_m^{1.30}$
   - $f_w = 1.8\,\mathrm{Hz}$ maximum walking frequency

3. Peak velocity in each mode m: $\hat{v}_m = \Phi_{e,m}\Phi_{r,m}I_{\mathrm{eff},m}/\hat{m}_m$
   - $\Phi_{e,m}$ the value of the mode shape m at the excitation position
   - $\Phi_{r,m}$ the value of the mode shape m at the receiving position
   - $\hat{m}_m$ the modal mass of mode m

4. Velocity response in each mode over the period of one footfall T:
   $v_m(t) = \hat{v}_m \exp\{(-2\pi f_m \zeta t)\} \sin(2\pi f_m t)$
   - $\hat{v}_m$ modal velocity magnitude
   - ζ as the modal damping ratio

5. Total response to each footfall: $v(t) = \sum_{m=1}^{n_m} v_m(t) \cdot w_m$
   - w_m weighting taken from [79] as suggested in [82]

6. For a time-harmonic analysis: total response to each footfall transformed from velocity to acceleration by $\hat{a} = (-i\omega)\hat{v}$

7. Root-mean-square (RMS) response evaluated over one footfall:
$$a_{\text{w,RMS}} = \sqrt{\frac{1}{T_f} \int_0^{T_f} a(t)^2 dt}$$

For continuous vibrations, the response factor is computed using the acceleration time history. However, in the case of intermittent vibration, which occurs more frequently for floors, the VDV is the preferred quantity for evaluating the vibration serviceability of a floor structure. [83] It is defined as [83]

$$\text{VDV} = \left(\int_0^{T_f} a^4(t) dt \right)^{1/4} = 0.68 \cdot a_{\text{w,rms}} (n_{\text{day/night}} T_{\text{single}})^{1/4}, \tag{2.61}$$

where $a_{\text{w,rms}}$ denotes the RMS-acceleration response from above, and $n_{\text{day}} = 32$ and $n_{\text{night}} = 16$ represent the occurrences of floor crossings during day and night. The time of a floor crossing is computed as

$$T_{\text{single}} = \frac{d_{\text{floor}}}{v_{\text{step}}} = \frac{\sqrt{(l^2 + b^2)}}{(1.67 f_w^2 - 4.83 f_w + 4.50)}, \tag{2.62}$$

with l and b being the width and length of the investigated floor structure.

Thus, by FE modal analysis, the fundamental frequency f_0, the natural frequencies f_m, and respective modal masses $\hat{m}_m$ of modes up to two times the fundamental frequency are calculated. The modal damping ratios are determined based on vibration measurements or are given by recommendations of design guides, e.g., 1% in Eurocode 5 [84].

Calculation of impact sound levels

The created FE model of the HST floors is also utilized for impact sound investigations. Here, a numerical implementation of the standardized tapping machine is applied as an excitation.

Tapping machine loading   In the standard ISO 10140-5 [125], the tapping machine is established as an excitation source for impact sound measurements. Consequently, in the case of FE simulations, the tapping machine load is implemented as a force to estimate impact sound pressure levels numerically. The details on determining this force in the frequency domain are given below.

As illustrated by Brunskog et al. [126], a floor structure is represented by a general frequency-dependent driving point impedance Z_{dp}. The applied hammer impact force $\mathfrak{f}_0(t) = F_0 \delta(t)$ using the dirac impulse $\delta(t)$ is Fourier transformed to result in the frequency-dependent force $\mathfrak{f}_0(\omega) = \mathscr{F}\{\mathfrak{f}_0(t); \omega\} = \mathscr{F}\{F_0 \delta(t); \omega\} = F_0$, which lies between $2M_0 v_0$ for elastic impacts and $M_0 v_0$ for plastic impacts. Here, $M_0 = 0.5\,\text{kg}$ denotes the weight of a hammer and $v_0 = 0.886\,\text{m/s}$ equals the initial hammer velocity. [126] As a first estimate, the geometric mean $\sqrt{2} M_0 v_0$ can be considered [177]. Subsequently, the spectrum of the continuing impact is computed as [126]

$$\mathfrak{f}_1'(\omega) = \frac{\mathfrak{f}_0}{1 + i\omega M_0/Z_{\mathsf{dp}}}, \tag{2.63}$$

and the corresponding force in time $\mathfrak{f}_1'(t)$ is found by an inverse Fourier transform. After applying the time of the zero crossing of the hammer impact $t_{\mathsf{cut}} = \{\min t | t > 0, \mathfrak{f}_1'(t) = 0\}$ to the force in time, the force spectrum $F_1(\omega)$ is determined by a Fourier transform. Lastly, the application of the Fourier series components $F_n = F_1(nf_h)f_h$ with the frequency $f_h = 1/T_h$ and period $T_h = 0.5\,\mathsf{s}$ for each of the five hammers as an excitation of the floor structure follows. [126]

Moreover, using the the local Z_{L} and global impedance Z_{G}, the driving-force impedance of the floor is estimated as [100]

$$Z_{\mathsf{dp}} = \frac{Z_{\mathsf{G}}(\omega)Z_{\mathsf{L}}(\omega)}{Z_{\mathsf{G}}(\omega) + Z_{\mathsf{L}}(\omega)}, \tag{2.64}$$

since it is required for eq. (2.63). For the computation of the global impedance [100]

$$Z_{\mathsf{G}}(\omega) = \frac{-iK_{\mathsf{dyn},jj}(\omega)}{\omega}, \tag{2.65}$$

the dynamic stiffness of the floor [100]

$$K_{\mathsf{dyn},jj}(\omega) = -\omega^2 M_{jj} + K_{jj}(1 + ig) \tag{2.66}$$

is retrieved from the numerical model at the DOF of the impact j. Hence, the mass M_{jj} and stiffness K_{jj} matrix entries and a material damping coefficient g of the material at the contact surface of the hammer and structure are ascertained [100].

The local impedance corresponds to [100]

$$Z_{\mathsf{L}}(\omega) = \frac{2Er_h}{i\omega(1+\nu)(1-\nu)}, \tag{2.67}$$

where r_h denotes the hammer radius, $\nu = \sqrt{\nu_{xy} \cdot \nu_{yx}}$ represents the Poisson's ratio, and $E = \sqrt{E_x \cdot E_y}$ denotes the elasticity modulus of the respective material.

The force is determined by utilizing the presented relations and, subsequently, applied to the FE model of the investigated floor structure in a time-harmonic analysis in the frequency range of interest. The FE simulation solves the system of equations, as exemplarily specified in sec. 2.3.1, and the quantities of interest, i.e., structural displacements and velocities, are found.

Commonly, the normalized impact sound pressure levels as ratings are compared to minimum reference levels in current design codes for acoustic requirements in buildings, e.g., DIN4109 in Germany [95]. Therefore, a transition of the acquired structural velocities to sound power values is performed by the commonly employed Rayleigh integral [178].

Subsequently, the computed sound power is converted to sound pressure and the corresponding normalized impact sound pressure levels.

Conversion to sound power In order to compute the radiated sound power, details on the computation of sound fields due to structural vibrations are given. If a vibrating structure is in contact with a fluid, the fluid is displaced at the fluid-structure interface, thus generating sound. The deformation of a small element on the vibrating surface leads to a displacement of the adjacent fluid volume part. When superposition is assumed to be applicable, the overall sound field is established considering the summed contributions of small surface elements. [178] The sound pressure $p(r,t)$ produced by a uniformly, radially, harmonically pulsating sphere of radius a_s at circular frequency ω in the free field reads as [178]

$$p(r,t) = \frac{1}{1+\mathrm{i}ka_s} \frac{\mathrm{i}\omega\rho_0\tilde{Q}}{4\pi r} \exp\{\mathrm{i}[\omega t - k(r-a_s)]\}, \tag{2.68}$$

with the air density $\rho_0 = 343\,\mathrm{m/s}$, the wave number k, the radial distance from the sphere's center r, the complex amplitude of the source's volume velocity $\tilde{Q}$, and the complex amplitude of volume acceleration $i\omega\tilde{Q}$. In the case of a small source dimension compared to the investigated wavelength, i.e., $ka_s \ll 1$, a "monopole source" is analyzed, and eq. (2.68) changes to [178]

$$p(r,t) = \frac{\mathrm{i}\omega\rho_0\tilde{Q}}{4\pi r} \exp\{\mathrm{i}[\omega t - kr]\}, \tag{2.69}$$

where $\exp\{-\mathrm{i}kr\}/4\pi r$ is often referred to as "Green's function".

Considering an infinite and rigid plane surface on which an elementary volume source operates, one observes $\tilde{Q}/2$ on one side of the panel. At the same time, the pressure is computed by eq. (2.69) [178]. If a small piston vibrates on the plane surface, the normal surface velocity is defined as [178]

$$v_n(t) = \tilde{v}_n \exp\{\mathrm{i}\omega t\}, \tag{2.70}$$

and it is stated that $\tilde{Q} = 2\tilde{v}_n\delta S$. Thus, eq. (2.69) is reformulated as [178]

$$p(r,t) = \frac{\mathrm{i}\omega\rho_0 2\tilde{v}_n\delta S}{4\pi r} \exp\{\mathrm{i}[\omega t - kr]\}, \tag{2.71}$$

with the element's surface area δS. Here, infinitesimally small sources are assumed, which is valid until very close to the source area if the dimension of the source area d complies with the limit $kd \ll 1$ [178]. When summing or integrating over the small sources, eq. (2.71) is valid for infinitely extended plane surfaces [178] and results in the formulation established by Lord Rayleigh [179]:

$$p(\mathbf{r},t) = \frac{\mathrm{i}\omega\rho_0}{2\pi}\exp\{\mathrm{i}\omega t\}\int_S \frac{\tilde{v}_n(\mathbf{r}_s)\exp\{-\mathrm{i}kR\}}{R}dS, \tag{2.72}$$

with the position of the observation point $\mathbf{r}$, the position of the element $\mathbf{r}_s$, and the magnitude of the difference of both vectors $R = |\mathbf{r} - \mathbf{r}_s|$. The formula is often applied to evaluate the radiation from vibrating planes and baffled pistons [178].

The sound intensity is then obtained from the time-averaged product of sound pressure and particle velocity by [178]

$$\bar{I}(\mathbf{r}) = \frac{1}{T}\int_0^T p(\mathbf{r},t)v(\mathbf{r},t)dt, \tag{2.73}$$

with T being a suitable length of time to assess the mean intensity value. In the case of a far field, the sound intensity is radially directed due to the particle velocity and pressure being radially directed and in phase. Thus, the sound intensity is calculated by the product of radial velocity $\tilde{v}_r$ and sound pressure. [178] If a harmonic vibration is considered, the particle velocity is given as $\tilde{p}(\mathbf{r},\omega)/(\rho_0 c)$ with the wave velocity c, and the sound intensity results as [178]

$$\bar{I}(\mathbf{r}) = \frac{1}{2}\mathrm{Re}\{\tilde{p}^*(\mathbf{r},\omega)\tilde{v}_r(\mathbf{r},\omega)\} = \frac{|\tilde{p}(\mathbf{r},\omega)|^2}{2\rho_0 c}. \tag{2.74}$$

Subsequently, the radiated sound power is calculated by an integral of the far-field intensity over the hemispherical surface centered on the radiating panel [178]:

$$\bar{P} = \int_S \bar{I}(\mathbf{r},\omega)dS. \tag{2.75}$$

If the formulation is adapted for a grid of R_e elementary radiators while assuming time-harmonic motion, the velocities of the elements and sound pressure values are collected in vectors [178]:

$$\tilde{\mathbf{v}}_e = [\tilde{v}_1\,\tilde{v}_2\,...\tilde{v}_{R_e}]^T \tag{2.76}$$

and

$$\tilde{\mathbf{p}}_e = [\tilde{p}_1\,\tilde{p}_2\,...\tilde{p}_{R_e}]^T. \tag{2.77}$$

By choosing elements that are small with respect to acoustic and structural wavelengths, the radiated sound power is obtained as the sum of the elements' radiated sound powers by [178]

$$\bar{P}(\omega) = \sum_{e=1}^{R_e}\frac{1}{2}A_e\mathrm{Re}\{\tilde{v}_e^*\tilde{p}_e\} = \frac{S}{2R_e}\mathrm{Re}\{\tilde{\mathbf{v}}_e^H\tilde{\mathbf{p}}_e\}, \tag{2.78}$$

with the element's area A_e and the overall panel area S. The pressure of each element is computed by [178]

$$\tilde{p}_e(x_l, y_l) = \frac{i\omega\rho_0 A_e \exp\{-ikR_{lj}\}}{2\pi R_{lj}} \tilde{v}_e(x_j, y_j), \tag{2.79}$$

with the distance between the centers of the lth and j^{th} element R_{lj}. This relation can be assembled in the symmetric impedance matrix $[\tilde{\mathbf{Z}}]$ with the entries [178]

$$\tilde{Z}_{lj}(\omega) = \frac{i\omega\rho_0 A_e}{2\pi R_{lj}} \exp\{-ikR_{lj}\}, \tag{2.80}$$

so the sound power is obtained by [178]

$$\bar{P}(\omega) = \frac{S}{2R_e} \text{Re}\{\tilde{\mathbf{v}}_e[\tilde{\mathbf{Z}}]\tilde{\mathbf{v}}_e\}. \tag{2.81}$$

Transition to normalized impact sound pressure level   Subsequently, the sound power level L_w is determined from the sound power as

$$L_W = 10\log_{10}(P/10^{-12}). \tag{2.82}$$

From the equidistant frequency data, third-octave band data is computed. Then, the relations from [180] are applied to retrieve sound pressure levels from sound power levels by

$$L_p = L_W - \left\{ 10\log\left(\frac{A}{A_0}\right) + 4.34\frac{A}{S} + 10\log\left(1 + \frac{cS}{8Vf}\right) + C_1 + C_2 - 6 \right\}, \tag{2.83}$$

with the equivalent absorption surface $A\,[\text{m}^2]$ of the room given as

$$A = \frac{55.26V}{cT_{60}}, \tag{2.84}$$

and using

- T_{60} the reverberation time of the investigated room
- V the respective room volume
- $A_0 = 1\,[\text{m}^2]$ the reference surface
- S the overall surface of the room
- $f\,[\text{Hz}]$ the center frequency of third-octaves
- $C_1 = -10\log\left(\frac{p_s}{p_{s,0}}\right) + 5\log\left[\frac{273.15+\Theta}{\Theta_0}\right]$ and

- $C_2 = -10\log\left(\frac{p_s}{p_{s,0}}\right) + 15\log\left[\frac{273.15+\Theta}{\Theta_1}\right]$ correction terms with
  - $p_{s,0} = 101.325\,\text{kPa}$ the static air pressure
  - $p_s\,[\text{kPa}]$ the static air pressure in the investigated room
  - $\Theta\,[\text{K}]$ the air temperature in the room
  - $\Theta_0 = 314\,\text{K}$ and $\Theta_1 = 296\,\text{K}$ the reference temperatures.

Finally, the normalized impact sound pressure level is obtained by [97]

$$L_n = L_p + 10\log\left(\frac{A}{10\,\text{m}^2}\right). \tag{2.85}$$

3 Summary of Appended Publications

This chapter summarizes the publications Paper A [140], Paper B [141], and Paper C [142]. The key aspects, results, and the authors' individual contributions are highlighted. Reprints of the full texts are provided in Appendix A.

3.1 Paper A

Vibroacoustic response of steel-timber composite elements

Bettina Chocholaty, Nicolaas Bernardus Roozen, Marcus Maeder, Steffen Marburg

Summary In this work, HST elements are investigated experimentally and numerically in terms of vibroacoustics. Here, the influence of the joints on the overall structural dynamics is of interest, which is especially relevant since assembled systems often reveal prominent nonlinear behavior due to their joints [105]. This study aims to comprehensively investigate the influence of various properties on the dynamics of HST elements. These investigations include exploring dimensions, fasteners, joint types, and other pertinent factors. Another focus lies on detecting nonlinearities in the system, particularly concerning amplitude-dependent stiffness and damping, higher-order contributions, and the presence of nonlinearly coupled modes. Therefore, vibration measurements with varying load levels are performed using random excitation types or sine-sweep loading. The results are analyzed by applying EMA or by visualization in spectrograms. Overall, 12 test samples are studied to evaluate the influence of various parameters, e.g., dimensions and LVL material type. Moreover, a manually calibrated FE model is used in a time-harmonic analysis to numerically investigate the vibroacoustics of the HST elements.

Comparing the measurement results of assemblies of different configurations reveals the anticipated impact of geometric parameters, e.g., component thickness, on the first natural frequency of the system — an essential criterion for assessing floor vibrations in terms of serviceability. Among others, thicker steel sheets contribute to higher natural frequencies and increased damping. This effect is enhanced by thicker timber plates, albeit being subject to potential manufacturing uncertainties. The choice of fastener type is equally crucial, as it affects the structure's stiffness. The two cross-section types, one with a single-component lower chord, i.e., the closed configuration, and another with a partitioned lower chord, i.e., the open configuration, significantly influence the two lowest structural modes. Due to the less stiff behavior of the open cross-section, the decision to opt for an open configuration should be made carefully, always considering the floor's lowest natural frequency. Comparisons with existing steel-timber elements reveal higher natural frequencies of the proposed structure, which are deemed more favorable due to the human perception of low-frequency vibrations as unpleasant. The damping behavior

is influenced by geometric parameters, the fastener type, and joint tightness. Nevertheless, it needs to be kept in mind that the prediction of damping in structures is complex and subject to uncertainties.

The conducted observations on nonlinearity primarily highlight the occurrence of higher harmonics in responses, as there is no evidence of amplitude-dependent stiffness, and only slight amplitude-dependent damping is identified. Notably, amplitude-dependent damping is detected when forces induce micro-slip in joints, and higher harmonics are often found near nodal lines with high rotational deformations. Furthermore, configurations with less stiff characteristics, such as higher steel frames and thin steel sheets in open configurations, result in a more pronounced contribution of higher harmonics. Consequently, exploring nonlinearities seems to be a critical aspect of studies on steel-timber composite structures.

A reasonably good correspondence of the response of the calibrated FE model using the measured data is achieved with a linear FE model as an initial proof-of-concept. However, future work may involve a more complex model incorporating nonlinearity and higher harmonics, possibly using the Harmonic Balance Method. Additionally, the current manual calibration of the model suggests the need for automatic optimization to obtain more accurate parameters.

Contribution   Bettina Chocholaty contributed to the conceptualization and methodology of the experimental and numerical study. Bettina Chocholaty and Nicolaas Bernardus Roozen contributed to the conceptualization and methodology of nonlinearity detection. Bettina Chocholaty and Marcus Maeder conceptualized the measurement setup. Bettina Chocholaty carried out the measurements and code implementation for the measurement data post-processing. Bettina Chocholaty conducted the FE simulations and prepared the draft of the manuscript. Bettina Chocholaty and Nicolaas Bernardus Roozen contributed to the discussion of the results. All authors provided critical feedback and approved the final version of the manuscript.

Reference   Chocholaty, B., Roozen, N. B., Maeder, M., & Marburg, S. (2022). Vibroacoustic response of steel-timber composite elements. *Engineering Structures, 271*, 114911. https://doi.org/10.1016/j.engstruct.2022.114911.

3.2 Paper B

Vibration response of a hybrid steel-timber building element with uncertain material and joint parameters

Bettina Chocholaty, Martin Eser, Karl-Alexander Hoppe, Daotong Wang, Steffen Marburg

Summary In view of economic viability and environmental sustainability, material-efficient designs of building elements receive increasing attention. Hereof, reliable prediction tools for designing HST floors regarding vibrations aim at rendering experimental campaigns less important, thus requiring less experimental prototyping while saving resources [181]. Due to model and data uncertainties inherent to prediction tools [132] and small variations of seemingly similar building elements, safety factors are commonly applied in the design process of building elements in engineering practice [133]. However, over the last few years, alternative research has investigated the benefit of employing approaches that consider data uncertainties within the prediction tools. Monte Carlo methods are adopted to perform a stochastic analysis of building elements, e.g., wooden floors. Thereby, the randomness of assembly or component uncertainties related to materials and joints is taken into account. [134, 135]

Accordingly, in this appended publication, a probabilistic FE analysis of an HST building element is conducted using the Monte Carlo method. Here, the effect of timber material and joint parameter uncertainties is propagated to the vibration response of the HST structure. The material uncertainties are represented by posterior distributions found by Bayesian inference. The required measurement data for the Bayesian inference is collected from EMA on small-scale LVL plates. Moreover, the forward model necessary to evaluate the likelihood is built upon a Rayleigh-Ritz approach for orthotropic plates. The uncertainty related to the joints of the HST specimen is considered by taking coefficients of variation from the literature and performing a maximum a-posteriori estimation to assess the mean values for the joints. Here, experimental modal data and an FE model of the HST element are utilized. Subsequently, the probabilistic analysis is conducted by considering the identified probabilities of LVL material and joint properties. Furthermore, Latin hypercube sampling is applied to allow for an efficient evaluation of the parameter space. Finally, ranges for the natural frequencies of the HST specimen are computed in the form of percentiles and compared to the measured quantities.

The approach based on Bayesian inference allows the identification of narrower posterior probabilities than the prior knowledge suggested. This, in turn, implies abated uncertainty of LVL material properties after accounting for measurement data. Moreover, the identified posterior means deviate from the material data provided by the manufacturer, highlighting the relevance of considering the material variability at hand in component designs. The probabilistic analysis reveals significant ranges for some of the investigated natural frequencies, especially regarding the 5th and 95th percentiles. Hence, the importance of accounting for data uncertainty in structural designs is emphasized, particularly

in view of enhanced resource efficiency. Finally, it is observed that only the first measured natural frequency lies within the range obtained by the probabilistic analysis of the HST element. Thus, further investigations seem reasonable, especially dealing with the joints of the HST structure, e.g., by applying Bayesian inference to infer the unknown joint properties or testing different joint modeling approaches.

Contribution   Bettina Chocholaty, Martin Eser, and Karl-Alexander Hoppe contributed to the conceptualization and methodology of Bayesian inference. Bettina Chocholaty conceptualized the analyses for uncertainty quantification. Bettina Chocholaty conducted the numerical simulations and the measurements. Bettina Chocholaty prepared the FE model. Daotong Wang carried out the code implementation of the forward model. Bettina Chocholaty implemented the remaining code and prepared the draft of the manuscript. Bettina Chocholaty and Steffen Marburg contributed to the discussion of the results. All authors provided critical feedback and approved the final version of the manuscript.

Reference   Chocholaty, B., Eser, M., Hoppe, K.-A., Wang, D., & Marburg, S. (2023). Vibration response of a hybrid steel-timber building element with uncertain material and joint parameters. *Archives of civil and mechanical engineering, 24(1)*, 22. `https://doi.org/10.1007/s43452-023-00819-z`.

3.3 Paper C

Vibration and impact sound properties of hybrid steel-timber floor structures

Bettina Chocholaty, Nicolaas Bernardus Roozen, Karl-Alexander Hoppe, Marcus Maeder, Steffen Marburg

Summary   When dealing with lightweight floors, such as wood or hybrid wood, a higher susceptibility to annoying vibrations is often observed, being even more pronounced for large-scale and lean constructions [17, 20]. Therefore, due to the likely exceedance of permissible vibration limits and the potential discomfort with wooden floors, investigating the vibration performance of wood-based floors proves to be important [21]. Moreover, timber-based floors tend to show critical behavior regarding impact sound characteristics [182]. Evaluation of the vibroacoustic performance of floors relies primarily on laboratory testing. However, especially if conducted in certified testing facilities, these tests are often time-consuming and costly. [109, 110] A remedy to this is provided by using FE models [181] if the simulations are adequately calibrated [128].

Thus, within this work, the impact sound and vibration serviceability characteristics are studied numerically to verify the applicability of the HST elements as floor structures in buildings. First, the unknown fastener parameters of the utilized FE model are calibrated by considering experimental modal data. However, due to spatial limitations, no vibration measurements have been performed on full-scale HST floor specimens. Hence, small-scale HST specimens are tested. Their natural frequencies and mode shapes are estimated and used to calibrate the simulation. The calibration is carried out by applying multi-objective optimization. Then, the FE model is adapted to represent the full-scale HST floor specimens using the calibrated fastener parameters. Based on this model, vibration limits and impact sound criteria are evaluated. Here, the VDVs for different configurations are considered. Again, two types of cross-sections, an open and closed setting, are investigated. As described before, the cross-sections mainly differ by the construction of the lower structural layer, being either one continuous or many separate LVL boards. Moreover, fully clamped or free support conditions are applied to the FE model since the actual boundary conditions are not known due to missing full-scale in-situ tests. This way, a potential range of the vibration response is computed as the actual support conditions will fall within the range of clamped to free supports. Thus, FE modal analysis is carried out to identify natural frequencies, modal masses, and mode shapes for the computation of VDVs. Additionally, a numerical version of the commonly used tapping machine for impact sound tests is implemented and applied as an excitation to the floor configurations in the FE model. Time-harmonic analyses are conducted to yield the vibration response of the HST floors due to tapping machine loading in the required frequency range. Subsequently, the Rayleigh integral is employed to compute sound power values. Finally, the sound power is transformed to normalized impact sound pressure levels.

The VDVs calculated for the HST floors are compared to commonly considered limit values, leading to the overall rating of "adverse comments possible". Hence, there is still

a need to improve the vibration response by carefully adding distributed mass or further investigating the damping properties of the floors. Comparing the two types of cross-sections reveals only minor differences regarding normalized impact sound pressure levels, barely recommending one type over the other. The influence of free or clamped support conditions is mainly observable in the low-frequency range, similar to what could be expected. Moreover, a comparison of the normalized impact sound pressure level of the HST floors to floors built from concrete and screed is made, yielding a somewhat comparative behavior. Thus, although it has to be kept in mind that the FE results are based on modeling assumptions regarding the fastener parameters, the floor damping behavior, and the support conditions, the HST floors seem to be competitive with commonly employed floors. This implies that they could be regarded as advantageous in terms of weight and sustainability.

So far, the study assumes the transferability of the model calibrated on small-scale specimens to full-scale floor structures. However, this conjecture has to be validated in future studies while considering appropriate in-situ support conditions. Moreover, additional structural components, e.g., floating floors, are not yet considered in the FE model and will also influence the impact sound behavior of the HST floors. Future studies should deal with these topics.

Contribution Bettina Chocholaty, Nicolaas Bernardus Roozen, and Marcus Maeder conceptualized the study. Bettina Chocholaty, Nicolaas Bernardus Roozen, Karl-Alexander Hoppe, and Steffen Marburg contributed to the methodology. Bettina Chocholaty carried out the code implementations and conducted the FE simulations. Bettina Chocholaty prepared the draft of the manuscript. Bettina Chocholaty, Nicolaas Bernardus Roozen, and Karl-Alexander Hoppe contributed to the discussion of the results. All authors provided critical feedback and approved the final version of the manuscript.

Reference Chocholaty, B., Roozen, N. B., Hoppe, K.-A., Maeder, M., & Marburg, S. (2024). Vibration and impact sound properties of hybrid steel-timber floor structures. *Acta Acustica, 8(11)*, 1-18, https://doi.org/10.1051/aacus/2024001.

4 Discussion and Conclusions

4.1 Contribution and discussion of this research

This cumulative thesis deals with the vibrational and acoustic characteristics of HST structures. The structures have top and bottom LVL layers with a corrugated steel core. Key aspects explored include the effects of the structure's joints on its overall behavior, the influence of uncertainties in joint and material properties, and the potential use of HST structures as floor elements.

The analyses conducted in Paper A revealed that joints induce nonlinear effects in the structure's response. While initial linear modeling approaches may be suitable, the study suggests that nonlinear modeling might be necessary to fully capture the joint's effects. The comparison of the measurement results with an experimental modal analysis in literature conducted on HST elements made of CLT and an H-shaped steel beam indicates higher natural frequencies for the first couple of modes for the currently investigated HST elements. In Paper B, Bayesian inference that identifies LVL material properties provides reasonable estimates. Moreover, considering uncertainties in material properties and joint stiffness values results in significant variations in the natural frequencies of HST building elements. Nevertheless, some discrepancies between measured and simulated natural frequencies remain, which might be attributed to manufacturing uncertainties and modeling inaccuracies. The subsequent study in Paper C improves the model, achieving a good match of natural frequencies and modes through deterministic model calibration. However, challenges still remain due to the complexity of the structure and unaccounted effects in joints. Vibration serviceability analysis indicates relatively high VDVs, necessitating further studies on damping, support conditions, and other factors. Comparable studies in previous research, such as Hassanieh et al.'s [73] work on HST floors, showed the suitability of HST floors for some but not all kinds of buildings. Additionally, Owolabi et al.'s [69] experiments on U-shaped steel with Cross-Laminated Timber (CLT) provided valuable insights by considering subjective vibration evaluation. A subjective vibration evaluation is also a possible next step for the LVL-steel floors investigated in this thesis. To the best of the authors' knowledge, no impact sound evaluations on such types of floors have been conducted yet. Therefore, no valid comparison of the performed impact sound study can be drawn.

The comprehensive exploration of LVL and trapezoidal steel structures allows for insightful comparisons with commonly used CLT-steel structures. Furthermore, the uncertainty quantification on HST elements offers implications for developing prediction tools for such structures. The initial estimates of vibration serviceability and impact sound characteristics highlight the potential suitability of HST structures in residential and commercial buildings, presenting a sustainable alternative to concrete floors. Notably, the study extends prior research by addressing impact sound.

4.2 Limitations

Advances in modeling engineering structures always rely on assumptions and an abstraction of reality. Therefore, they only represent a replica of real-world behavior being subject to uncertainties and errors. Although accurate modeling selection and calibration improve the accuracy, deviations related to reality will remain. Adequate material modeling regarding the appropriate selection of material parameter values especially improves the model accuracy. [132] Furthermore, for heterogeneous materials such as wood [183], more refined, localized models can improve the prediction quality, e.g., on lamella-basis [184]. Further, adequate modeling of joints still poses challenges to engineers and researchers since joints induce complex behavior in a structure. A linear simulation approach based on linear element types might not be elaborate enough, and an advanced approach, e.g., using an Iwan-type model, would be beneficial for the studies of HST systems. [102] Moreover, FE simulations have limitations, as their accuracy depends on the discretization. This is especially true for higher frequencies, where smaller elements are required to accurately describe a structure's response [185]. However, for large structures, simulations with small elements lead to very costly and time-consuming computations. Hence, one has to weigh the benefits and drawbacks of simulation approaches when deciding which simplifications and assumptions are acceptable.

Another important aspect to remember regarding simulation and modeling is the transferability of the computed results. One may find an accurate prediction via a calibrated FE model for a specific test specimen. However, a slight variation in the test specimen or its support conditions may require an adapted FE model, thus limiting the validity of the simulation results.

Some limitations also exist related to vibration measurements. In most experiments, some type and extent of measurement errors are introduced, even if conducted with precision and care [186]. For example, a slightly skewed load application could introduce horizontal forces in the test specimen, although only vertical ones have been asked for. Moreover, the position of accelerometers or scan points can influence the measurement quality since some positions on the structure might be better suited than others, e.g., in the context of spatial aliasing. [143] How samples are supported also strongly affects the measured response [187]. Measurement engineers often try to achieve supports similar to free boundary conditions of simulations by using rubber bands or soft airbags [188]. This is done since free supports are deemed to be established more easily than, e.g., simply supported boundaries. However, even if attached with care, these supports may unintentionally influence the damping or stiffness of the investigated structure.

The repeatability and reproducibility of measurement results are also of major concern related to established supports and applied excitation. [143] Often, repeatability is not as easily guaranteed as expected. This is also a major concern in nonlinearity detection. Nonlinearity is often induced by frictional effects in joints. However, friction strongly depends on the current contact status, which is significantly influenced by the current state of assembly. [189] Hence, different results might be obtained if the structure is dis- and subsequently reassembled. Consequently, the repeatability of measurements poses a great challenge to vibrational experiments. Finally, a limitation of the conducted experi-

mental studies is given by the effect of friction between components degrading over time due to cycles of loading and unloading during the service life of the structure [105], which has not been assessed so far.

4.2.1 Future work

With regard to the limitations explained before, the following ideas emerge for future research.

Parametric study on the impact sound insulation properties: As of now, the impact sound computations have been conducted using a single excitation position. One next step could be to consider a variety of loading positions to evaluate the effect on the normalized impact sound pressure level. Furthermore, a larger variety of HST floors could be investigated regarding impact sound in a parametric study. This includes but is not limited to variations of the used LVL material type, the height of the floor, or similar factors. In the parametric studies, the frequency range of interest for impact sound properties ranges up to more than 3000 Hz. At the same time, floor structures with minimum requirements for their dimensions have to be investigated. This leads to large FE models that require large computational effort. Hence, as another extension of the current research, model order reduction approaches could be applied to make the above-elucidated analyses more feasible.

Uncertainty quantification related to VDVs and impact sound characteristics: Similar to investigating the effects of uncertain material and joint parameters on the modal characteristics of the HST elements, uncertainty quantification for VDVs and normalized impact sound characteristics can be performed. This way, slight variations in the assembly of HST floors are incorporated in the uncertain parameters, and their effect on the vibroacoustic response is assessed. The aforementioned model order reduction is also a feasible tool for these investigations.

Elaborate measurement campaign on HST structures: In an extensive experimental campaign, many factors could be investigated. The repeatability of the vibration measurements could be quantified by studying the effect of slightly varying measurement setups, as well as dis- and reassembly. Moreover, varying torques in the fasteners and different contact pressures in the joints could be investigated in future experiments. Lastly, a long-term experimental study on the friction effects for loading and unloading cycles could be of interest.

Investigations on damping of LVL material and HST structures: As the VDVs of the HST elements range within the possibility of adverse comments from residents, a more elaborate study of the damping properties could be beneficial. On the one hand, the material damping inherent to LVL, especially regarding frequency-dependency, might be of interest. On the other hand, the overall damping properties of HST floors are a relevant research objective, e.g., considering in-situ support conditions. This might give insight into how to improve the behavior of the HST floors related to vibration serviceability.

Influence of additional structural components on HST floors: For built-in situations, additional structural components, such as floating floors and suspended ceilings, are ap-

plied to floor structures. These components could improve the impact sound insulation properties of the HST floors. However, their effects remain unexplored so far and might be analyzed in future research, both numerically and experimentally.

4.3 Closing remarks

This thesis has taken a step toward the vibroacoustic characterization of HST elements for use in residential or commercial buildings. To this aim, a thorough experimental investigation has been performed to construct a reliable numerical prediction tool. Although the experimental validation of full-size HST floor structures regarding vibrations and impact sound still needs to be performed, a first estimate of the related properties has been computed numerically. Moreover, the implementation of a probabilistic model represents a base for further investigations on uncertainty within the behavior of HST structures. The gained insights on the vibroacoustic behavior of LVL-corrugated steel structures offer a variety of future research possibilities through which new knowledge can be acquired. In summary, this comprehensive investigation of HST structures has led to a deeper understanding of their vibrational behavior, identified key challenges, and highlighted their potential as a sustainable alternative in construction.

Bibliography

[1] R. Brandner, G. Flatscher, A. Ringhofer, G. Schickhofer, and A. Thiel, "Cross laminated timber (clt): overview and development," *European Journal of Wood and Wood Products*, vol. 74, pp. 331–351, 2016. https://doi.org/10.1007/s00107-015-0999-5.

[2] M. Izzi, D. Casagrande, S. Bezzi, D. Pasca, M. Follesa, and R. Tomasi, "Seismic behaviour of cross-laminated timber structures: A state-of-the-art review," *Engineering Structures*, vol. 170, pp. 42–52, 2018. https://doi.org/10.1016/j.engstruct.2018.05.060.

[3] R. H. Falk, "Wood as a sustainable building material," in *Wood handbook: wood as an engineering material* (R. J. Ross, ed.), pp. 1 1–1 6, Madison USA: Forest Products Laboratory, 2010. https://doi.org/10.2737/FPL-GTR-190.

[4] M. Fujita, J. Sakai, H. Oda, and M. Iwata, "Building system for a composite steel-timber structure," *Steel Construction*, vol. 7, no. 3, pp. 183–187, 2014. https://doi.org/10.1002/stco.201410032.

[5] C. Loss, M. Piazza, and R. Zandonini, "Experimental tests of cross-laminated timber floors to be used in timber-steel hybrid structures," in *Proceedings of WCTE 2014 conference*, pp. 53 1–53 8, 2014.

[6] N. Keipour, H. R. Valipour, and M. A. Bradford, "Steel-timber composite beam-to-column joints: Effect of connections between timber slabs," *Journal of Constructional Steel Research*, vol. 151, pp. 132–145, 2018. https://doi.org/10.1016/j.jcsr.2018.09.019.

[7] A. Hassanieh, H. R. Valipour, and M. A. Bradford, "Experimental and numerical study of steel-timber composite (stc) beams," *Journal of Constructional Steel Research*, vol. 122, pp. 367–378, 2016. https://doi.org/10.1016/j.jcsr.2016.04.005.

[8] T. Smith, S. Pampanin, A. Buchanan, and M. Fragiacomo, "Feasibility and detailing of post-tensioned timber buildings for seismic areas," in *Proceedings of 2008 NZSEE Conference*, 2008.

[9] D. E. Kretschmann, "Mechanical properties of wood," in *Wood handbook: wood as an engineering material* (R. J. Ross, ed.), pp. 5 1–5 46, Madison USA: Forest Products Laboratory, 2010. https://doi.org/10.2737/FPL-GTR-190.

[10] P. M. Mariano and L. Galano, *Fundamentals of the Mechanics of Solids*. Boston: Birkhäuser, 2015. https://doi.org/10.1007/978-1-4939-3133-0.

[11] R. H. White and M. A. Dietenberger, "Fire safety of wood construction," in *Wood handbook: wood as an engineering material* (R. J. Ross, ed.), pp. 18 1–18 22, Madison USA: Forest Products Laboratory, 2010. https://doi.org/10.2737/FPL-GTR-190.

[12] A. H. Buchanan and A. K. Abu, *Structural design for fire safety*. Chichester: John Wiley & Sons, second ed., 2017. https://doi.org/10.1002/9781118700402.

[13] L. De Geetere and B. Ingelaere, "A new building acoustical concept for lightweight timber frame constructions," in *INTER-NOISE and NOISE-CON Congress and Conference Proceedings*, vol. 249, pp. 5928–5935, 2014.

[14] M. C. Wiemann, "Characteristics and availability of commercially important woods," in *Wood handbook: wood as an engineering material* (R. J. Ross, ed.), pp. 2 1–2 45, Madison USA: Forest Products Laboratory, 2010. https://doi.org/10.2737/FPL-GTR-190.

[15] H. Karampour, F. Piran, A. Faircloth, N. Talebian, and D. Miller, "Vibration of timber and hybrid floors: A review of methods of measurement, analysis, and design," *Buildings*, vol. 13, no. 7, p. 1756, 2023. https://doi.org/10.3390/buildings13071756.

[16] J. D. Dolan, T. M. Murray, J. R. Johnson, D. Runte, and B. C. Shue, "Preventing annoying wood floor vibrations," *Journal of Structural Engineering*, vol. 125, no. 1, pp. 19–24, 1999. https://doi.org/10.1061/(ASCE)0733-9445(1999)125:1(19).

[17] J. Weckendorf, G. Hafeez, G. Doudak, and I. Smith, "Floor vibration serviceability problems in wood light-frame buildings," *Journal of Performance of Constructed Facilities*, vol. 28, no. 6, p. A4014003, 2014. https://doi.org/10.1061/(ASCE)CF.1943-5509.0000538.

[18] J. Weckendorf, T. Toratti, I. Smith, and T. Tannert, "Vibration serviceability performance of timber floors," *European Journal of Wood and Wood Products*, vol. 74, pp. 353–367, 2016. https://doi.org/10.1007/s00107-015-0976-z.

[19] N. Cheraghi-Shirazi, K. Crews, and S. Malek, "Review of vibration assessment methods for steel-timber composite floors," *Buildings*, vol. 12, no. 12, p. 2061, 2022. https://doi.org/10.3390/buildings12122061.

[20] J. Negreira, A. Trollé, K. Jarnerö, L.-G. Sjökvist, and D. Bard, "Psycho-vibratory evaluation of timber floors–towards the determination of design indicators of vibration acceptability and vibration annoyance," *Journal of Sound and Vibration*, vol. 340, pp. 383–408, 2015. http://dx.doi.org/10.1016/j.jsv.2014.12.001.

[21] A. Pavic, "Results of IStructE 2015 survey of practitioners on vibration serviceability," in *Proceedings of the SECED 2019 conference: Earthquake Risk and Engineering towards a Resilient World*, pp. 1–8, 2019.

[22] F. Ljunggren, C. Simmons, and K. Hagberg, "Correlation between sound insulation and occupants' perception–proposal of alternative single number rating of impact sound," *Applied Acoustics*, vol. 85, pp. 57–68, 2014. https://doi.org/10.1016/j.apacoust.2014.04.003.

[23] B. Ingelaere, "Acoustic design of lightweight timber frame constructions," in *COST Action FP0702. Net-Acoustics for Timber based lightweight buildings and element*, pp. 1–110, COST European Cooperation in Science and Technology, 2012.

[24] F. Ljunggren, C. Simmons, and R. Öqvist, "Correlation between sound insulation and occupants' perception–proposal of alternative single number rating of impact sound, part II," *Applied Acoustics*, vol. 123, pp. 143–151, 2017. https://doi.org/10.1016/j.apacoust.2017.03.014.

[25] M. Sanayei, N. Zhao, P. Maurya, J. A. Moore, J. A. Zapfe, and E. M. Hines, "Prediction and mitigation of building floor vibrations using a blocking floor," *Journal of Structural Engineering*, vol. 138, no. 10, pp. 1181–1192, 2012. https://doi.org/10.1061/(asce)st.1943-541x.0000557.

[26] M. Vorländer, "Building acoustics: from prediction models to auralization," in *Proceedings of Acoustics - First Australasian Conference*, pp. 15–22, 2006.

[27] L. Li, T. Qu, Y. Liu, R. Y. Zhong, G. Xu, H. Sun, Y. Gao, B. Lei, C. Mao, Y. Pan, *et al.*, "Sustainability assessment of intelligent manufacturing supported by digital twin," *IEEE Access*, vol. 8, pp. 174988–175008, 2020. https://doi.org/10.1109/access.2020.3026541.

[28] "DIN EN ISO 12354-2 - Building acoustics - Estimation of acoustic performance of buildings from the performance of elements - Part 2: Impact sound insulation between rooms," Standard, European Committee for Standardization, Belgium, Brussels, Nov 2017. https://doi.org/10.31030/2625099.

[29] L. Cremer and M. Heckl, *Abstrahlung von Körperschall*. Berlin: Springer, second ed., 1996. https://doi.org/10.1007/978-3-662-08182-2.

[30] M. Caniato, F. Bettarello, P. Fausti, A. Ferluga, L. Marsich, and C. Schmid, "Impact sound of timber floors in sustainable buildings," *Building and Environment*, vol. 120, pp. 110–122, 2017. https://doi.org/10.1016/j.buildenv.2017.05.015.

[31] M. Fujita and M. Iwata, "Bending test of the composite steel-timber beam," *Applied Mechanics and Materials*, vol. 351, pp. 415–421, 2013. https://doi.org/10.4028/www.scientific.net/amm.351-352.415.

[32] A. Hassanieh, H. R. Valipour, and M. A. Bradford, "Load-slip behaviour of steel-cross laminated timber (clt) composite connections," *Journal of Constructional Steel Research*, vol. 122, pp. 110–121, 2016. https://doi.org/10.1016/j.jcsr.2016.03.008.

[33] R. Liu, J. Liu, Z. Wu, L. Chen, and J. Wang, "A study on the influence of bolt arrangement parameters on the bending behavior of timber–steel composite (tsc) beams," *Buildings*, vol. 12, no. 11, p. 2013, 2022. https://doi.org/10.3390/buildings12112013.

[34] P. Kyvelou, L. Gardner, and D. A. Nethercot, "Finite element modelling of composite cold-formed steel flooring systems," *Engineering Structures*, vol. 158, pp. 28–42, 2018. https://doi.org/10.1016/j.engstruct.2017.12.024.

[35] Y. Gao, F. Xu, X. Meng, Y. Zhang, and H. Yang, "Experimental and numerical study on the lateral torsional buckling of full-scale steel-timber composite beams," *Advances in Structural Engineering*, vol. 25, no. 3, pp. 522–540, 2022. https://doi.org/10.1177/13694332211057263.

[36] Y. Zhao, Y. Yuan, C.-L. Wang, and S. Meng, "Experimental and finite element analysis of flexural performance of steel-timber composite beams connected by hybrid-anchored screws," *Engineering Structures*, vol. 292, p. 116503, 2023. https://doi.org/10.1016/j.engstruct.2023.116503.

[37] K. Okutu, B. Davison, and J. Carr, "CLT-steel composite slimfloor construction: An investigation of mechanical behaviour using finite element software," in *Proceedings of EUROSTEEL 2017*, vol. 1, pp. 4447–4456, Wiley Online Library, 2017. https://doi.org/10.1002/cepa.504.

[38] A. Hassanieh, H. R. Valipour, and M. A. Bradford, "Composite connections between clt slab and steel beam: Experiments and empirical models," *Journal of Constructional Steel Research*, vol. 138, pp. 823–836, 2017. https://doi.org/10.1016/j.jcsr.2017.09.002.

[39] A. Aspila, M. Heinisuo, K. Mela, M. Malaska, and S. Pajunen, "Elastic design of steel-timber composite beams," *Wood Material Science & Engineering*, vol. 17, no. 4, pp. 243–252, 2022. https://doi.org/10.1080/17480272.2022.2093128.

[40] M. Heinisuo, K. Mela, S. Pajunen, and M. Malaska, "New steel-timber composite beam, nordic system," in *Proceedings of XII Congresso de Contruçao Metálica e Mista*, vol. 3, pp. 193–202, Wiley Online Library, 2019. https://doi.org/10.1002/cepa.1194.

[41] C. Loss and A. Frangi, "Experimental investigation on in-plane stiffness and strength of innovative steel-timber hybrid floor diaphragms," *Engineering Structures*, vol. 138, pp. 229–244, 2017. https://doi.org/10.1016/j.engstruct.2017.02.032.

[42] C. Loss, M. Piazza, and R. Zandonini, "Connections for steel–timber hybrid prefabricated buildings. part II: Innovative modular structures," *Construction and Building Materials*, vol. 122, pp. 796–808, 2016. https://doi.org/10.1016/j.conbuildmat.2015.12.001.

[43] C. Loss, M. Piazza, and R. Zandonini, "Connections for steel–timber hybrid prefabricated buildings. part I: Experimental tests," *Construction and Building Materials*, vol. 122, pp. 781–795, 2016. https://doi.org/10.1016/j.conbuildmat.2015.12.002.

[44] C. Loss and B. Davison, "Innovative composite steel-timber floors with prefabricated modular components," *Engineering Structures*, vol. 132, pp. 695–713, 2017. https://doi.org/10.1016/j.engstruct.2016.11.062.

[45] M. A. Bradford, A. Hassanieh, H. R. Valipour, and S. J. Foster, "Sustainable steel-timber joints for framed structures," *Procedia Engineering*, vol. 172, pp. 2–12, 2017. https://doi.org/10.1016/j.proeng.2017.02.011.

[46] A. Hassanieh, H. R. Valipour, and M. A. Bradford, "Experimental and analytical behaviour of steel-timber composite connections," *Construction and Building Materials*, vol. 118, pp. 63–75, 2016. https://doi.org/10.1016/j.conbuildmat.2016.05.052.

[47] A. Ataei, A. A. Chiniforush, M. A. Bradford, H. R. Valipour, and T. D. Ngo, "Behaviour of embedded bolted shear connectors in steel-timber composite beams subjected to cyclic loading," *Journal of Building Engineering*, vol. 54, p. 104581, 2022.

[48] A. Hassanieh, H. R. Valipour, and M. A. Bradford, "Bolt shear connectors in grout pockets: Finite element modelling and parametric study," *Construction and Building Materials*, vol. 176, pp. 179–192, 2018.

[49] A. Ataei, A. A. Chiniforush, M. A. Bradford, and H. R. Valipour, "Cyclic behaviour of bolt and screw shear connectors in steel-timber composite (stc) beams," *Journal of Constructional Steel Research*, vol. 161, pp. 328–340, 2019. https://doi.org/10.1016/j.jcsr.2019.05.048.

[50] A. A. Chiniforush, H. R. Valipour, and A. Akbarnezhad, "Long-term coupled analysis of steel-timber composite (stc) beams," *Construction and Building Materials*, vol. 278, p. 122348, 2021. https://doi.org/10.1016/j.conbuildmat.2021.122348.

[51] A. A. Chiniforush, H. R. Valipour, M. A. Bradford, and A. Akbarnezhad, "Long-term behaviour of steel-timber composite (stc) shear connections," *Engineering Structures*, vol. 196, p. 109356, 2019. https://doi.org/10.1016/j.engstruct.2019.109356.

[52] A. A. Chiniforush, H. R. Valipour, M. A. Bradford, and A. A. Nezhad, "Experimental and theoretical investigation of long-term performance of steel-timber composite beams," *Engineering Structures*, vol. 249, p. 113314, 2021.

[53] A. A. Chiniforush, A. Akbarnezhad, and S. Malek, "Time-dependent deflection measurement for steel-timber composite (stc) flooring system," in *Proceedings of the International Conference on Advances in Experimental Structural Engineering*, pp. 1–11, 2020.

[54] A. A. Chiniforush, A. Akbarnezhad, H. R. Valipour, and M. Bradford, "Long-term behavior of steel-clt connections," in *Proceedings of World Conference on Timber Engeneering*, 2018.

[55] A. A. Chiniforush, H. Valipour, A. Akbarnezhad, and M. Bradford, "Steel-timber composite (stc) beams: Numerical simulation of long-term behaviour," in *Proceedings of EUROSTEEL 2017*, vol. 1, pp. 2051–2059, Wiley Online Library, 2017. https://doi.org/10.1002/cepa.250.

[56] M. G. Dellepiani, G. R. Munoz, S. J. Yanez, C. F. Guzmán, E. I. S. Flores, and J. C. Pina, "Numerical study of the thermo-mechanical behavior of steel–timber structures exposed to fire," *Journal of Building Engineering*, vol. 65, p. 105758, 2023. https://doi.org/10.1016/j.jobe.2022.105758.

[57] A. O. Akotuah, S. G. Ali, J. Erochko, X. Zhang, and G. V. Hadjisophocleous, "Study of the fire performance of hybrid steel-timber connections with full-scale tests and finite element modelling," in *Proceedings of the International Conference in Dubrovnik*, pp. 251–256, 2015. https://doi.org/10.14311/asfe.2015.039.

[58] B. Izumi, A. Tani, N. Toba, K. Nakashima, M. Koshihara, T. Yamanashi, M. Kohno, and W. Winter, "Fire performances of timber-cold formed thin steel plate composite beam," in *Proceedings of the World Conference on Timber Engineering*, Vienna University of Technology, 2016.

[59] Z. Liu, B. Zhang, H. Jia, and T. Kilpatrick, "Numerical analysis of flexural performances of composite steel-timber beams under fire conditions," *Journal of Civil Engineering and Construction*, vol. 12, no. 3, pp. 167–185, 2023. https://doi.org/10.32732/jcec.2023.12.3.167.

[60] F. Chen, Z. Li, M. He, Y. Wang, Z. Shu, and G. He, "Seismic performance of self-centering steel-timber hybrid shear wall structures," *Journal of Building Engineering*, vol. 43, p. 102530, 2021. https://doi.org/10.1016/j.jobe.2021.102530.

[61] A. A. Chiniforush, A. Akbarnezhad, H. R. Valipour, and J. Xiao, "Energy implications of using steel-timber composite (stc) elements in buildings," *Energy and Buildings*, vol. 176, pp. 203–215, 2018. https://doi.org/10.1016/j.enbuild.2018.07.038.

[62] C. A. Kraus, *Floor vibration design criterion for cold-formed C-Shaped supported residential floor systems*. PhD thesis, Virginia Tech, 1997.

[63] R. Parnell, B. W. Davis, and L. Xu, "Vibration performance of lightweight cold-formed steel floors," *Journal of Structural Engineering*, vol. 136, no. 6, pp. 645–653, 2010.

[64] L. Xu and F. M. Tangorra, "Experimental investigation of lightweight residential floors supported by cold-formed steel c-shape joists," *Journal of constructional steel research*, vol. 63, no. 3, pp. 422–435, 2007. https://doi.org/10.1016/j.jcsr.2006.05.010.

[65] L. Xu, "Floor vibration in lightweight cold-formed steel framing," *Advances in Structural Engineering*, vol. 14, no. 4, pp. 659–672, 2011. https://doi.org/10.1260/1369-4332.14.4.659.

[66] S. Al Hunaity, H. Far, and A. Saleh, "Vibration behaviour of cold formed steel and particleboard composite flooring systems," *Steel and Composite Structures: an international journal*, vol. 43, no. 3, pp. 403–417, 2022. https://doi.org/10.12989/scs.2022.43.3.403.

[67] H. Huang, Y. Gao, and W.-S. Chang, "Human-induced vibration of cross-laminated timber (clt) floor under different boundary conditions," *Engineering Structures*, vol. 204, p. 110016, 2020. https://doi.org/10.1016/j.engstruct.2019.110016.

[68] C. Wang, W.-S. Chang, W. Yan, and H. Huang, "Predicting the human-induced vibration of cross laminated timber floor under multi-person loadings," *Structures*, vol. 29, pp. 65–78, 2021. https://doi.org/10.1016/j.istruc.2020.10.074.

[69] D. Owolabi, C. Loss, and J. Zhou, "Vibration properties and serviceability performance of a modular cross-laminated timber-steel composite floor system," *Journal of Structural Engineering*, vol. 149, no. 12, p. 04023171, 2023. https://doi.org/10.1061/jsendh.steng-12587.

[70] A. Aloisio, D. P. Pasca, D. Owolabi, and C. Loss, "Vibration serviceability of hybrid clt-steel composite floors based on experimental and numerical investigations using random walk models," *Engineering Structures*, vol. 304, p. 117600, 2024. https://doi.org/10.1016/j.engstruct.2024.117600.

[71] A. A. Chiniforush, M. M. Alamdari, U. Dackermann, H. R. Valipour, and A. Akbarnezhad, "Vibration behaviour of steel-timber composite floors, part (1): Experimental & numerical investigation," *Journal of Constructional Steel Research*, vol. 161, pp. 244–257, 2019. https://doi.org/10.1016/j.jcsr.2019.07.007.

[72] A. A. Chiniforush, A. Akbarnezhad, H. Valipour, and U. Dackermann, "Dynamic response of steel-timber composite (stc) beams," in *Proceedings of the 24th International Congress of Sound and Vibration*, 2017.

[73] A. Hassanieh, A. A. Chiniforush, H. R. Valipour, and M. A. Bradford, "Vibration behaviour of steel-timber composite floors, part (2): evaluation of human-induced vibrations," *Journal of Constructional Steel Research*, vol. 158, pp. 156–170, 2019. https://doi.org/10.1016/j.jcsr.2019.03.026.

[74] M. Fuente, S. Arines, P. Elguezabal, M. Pérez, and M. J. de Rozas, "Industrialized lightweight floors for multi-storey dwellings in spain," in *Proceedings of Forum Acusticum*, pp. 1665–1668, 2011.

[75] S. Pastori, E. S. Mazzucchelli, and M. Wallhagen, "Hybrid timber-based structures: A state of the art review," *Construction and Building Materials*, vol. 359, p. 129505, 2022. https://doi.org/10.1016/j.conbuildmat.2022.129505.

[76] R. Pimentel, R. Simões, and L. S. da Silva, "Demountable steel-clt composite floors for net-zero carbon buildings: State of the art and design principles," in *Proceedings of XIII Congresso de Contruçao Metálica e Mista*, vol. 5, pp. 184–195, Wiley Online Library, 2022. https://doi.org/10.1002/cepa.1713.

[77] F. Y. Moritani, C. E. J. Martins, and A. M. P. G. Dias, "A literature review on cold-formed steel-timber composite structures," *BioResources*, vol. 16, no. 4, p. 8489, 2021. https://doi.org/10.15376/biores.16.4.moritani.

[78] A. Aloisio, D. P. Pasca, Y. De Santis, T. Hillberger, P. F. Giordano, M. M. Rosso, R. Tomasi, M. P. Limongelli, and C. Bedon, "Vibration issues in timber structures: A state-of-the-art review," *Journal of Building Engineering*, p. 107098, 2023. https://doi.org/10.1016/j.jobe.2023.107098.

[79] "BS 6472-1 - Guide to evaluation of human exposure to vibration in buildings - Part 1: Vibration sources other than blasting," Standard, British Standards Insitution, London, UK, Jun 2008. https://doi.org/10.3403/19971044U.

[80] "ISO 10137 2007(E) - Bases for design of structures - Serviceability of buildings and walkways against vibrations," Standard, International Organization for Standardization, Geneva, Switzerland, Nov 2007.

[81] W. Schirén and T. Swahn, "Vibrations in residential timber floors - A comparison between the current and the revised Eurocode 5," in *Proceedings of the 25. Internationales Holzbau-Forum IHF*, vol. 25, pp. 23–34, 2019.

[82] M. R. Willford and P. Young, *A design guide for footfall induced vibration of structures*. London, UK: Concrete Society for The Concrete Centre, 2007.

[83] T. Murray, D. Allen, E. Ungar, and D. Davis, *Vibrations of Steel-Framed Structural Systems Due to Human Activity: AISC Design Guide 11*. Chicago, USA: American Institute of Steel Construction, second ed., 2016.

[84] "DIN EN 1995 1-1 - Eurocode 5: Design of timber structures, Part 1-1: General - Common rules and rules for buildings," Standard, European Committee for Standardization, Brussels, Belgium, Dez 2010. https://dx.doi.org/10.31030/1722665.

[85] Canadian Wood Council, "Development of design procedures for vibration controlled spans using engineered wood members," tech. rep., Canadian Construction Materials Centre, Ottawa, ON, Canada, 1997.

[86] "CSA O86-19: Engineering design in wood.," Standard, Canadian Standards Association, Toronto, Canada, Nov 2019.

[87] E. Karacabeyli and S. Gagnon, *Canadian CLT handbook*. Vancouver, Canada: FPinnovation, 2019.

[88] "E710 - Minimizing floor vibration by design and retrofit," Technical note, APA - The Engineered Wood Association, Tacoma, USA, 2004.

[89] A. L. Smith, S. J. Hicks, and P. J. Devine, *Design of floors for vibration: A new approach*. Ascot, Berkshire, UK: Steel Construction Institute, 2007.

[90] K. Nering, A. Kowalska-Koczwara, and K. Stypuła, "Annoyance based vibro-acoustic comfort evaluation of as summation of stimuli annoyance in the context of human exposure to noise and vibration in buildings," *Sustainability*, vol. 12, no. 23, p. 9876, 2020. https://doi.org/10.3390/su12239876.

[91] G. H. Kyanka, "Fatigue properties of wood and wood composites," *International Journal of Fracture*, vol. 16, pp. 609–616, 1980. https://doi.org/10.1007/bf02265220.

[92] M. Chaplain, Z. Nafa, and M. Guenfoud, "Damage of glulam beams under cyclic torsion: Experiments and modelling," in *Damage and Fracture Mechanics: Failure Analysis of Engineering Materials and Structures* (T. Boukharouba, M. Elboujdaini, and G. Pluvinage, eds.), pp. 349–356, Springer Science & Business Media, 2009. https://doi.org/10.1007/978-90-481-2669-9_37.

[93] "DIN EN ISO 12354-1 - Building acoustics - Estimation of acoustic performance of buildings from the performance of elements - Part 1: Airborne sound insulation between rooms," Standard, European Committee for Standardization, Belgium, Brussels, Nov 2017. https://doi.org/10.31030/2625097.

[94] "DIN EN ISO 717-2 - Rating of sound insulation in buildings and of building elements - Part 2: Impact sound insulation," Standard, European Committee for Standardization, Brussels, Belgium, May 2021. https://dx.doi.org/10.31030/3201675.

[95] "DIN 4109-1 - Schallschutz im Hochbau - Teil 1: Mindestanforderungen," Standard, Deutsches Institut für Normung e.V., Berlin, Jan 2018. https://dx.doi.org/10.31030/2764537.

[96] A. Jayalath, S. Navaratnam, T. Gunawardena, P. Mendis, and L. Aye, "Airborne and impact sound performance of modern lightweight timber buildings in the australian construction industry," *Case Studies in Construction Materials*, vol. 15, p. e00632, 2021. https://doi.org/10.1016/j.cscm.2021.e00632.

[97] "DIN EN ISO 10140-3 - Acoustics - Laboratory measurement of sound insulation of building elements - Part 3: Measurements of impact sound insulation," Standard, European Committee for Standardization, Brussels, Belgium, Sep 2021. https://dx.doi.org/10.31030/3237068.

[98] P. Sipari, "Sound insulation of multi-storey houses—a summary of finnish impact sound insulation results," *Building Acoustics*, vol. 7, no. 1, pp. 15–30, 2000. https://doi.org/10.1260/1351010001501471.

[99] "DIN EN ISO 10140-2 - Acoustics - Laboratory measurement of sound insulation of building elements - Part 2: Measurements of airborne sound insulation," Standard, European Committee for Standardization, Brussels, Belgium, Sep 2021. https://dx.doi.org/10.31030/3237066.

[100] P. Wang, C. Van hoorickx, G. Lombaert, and E. Reynders, "Numerical prediction and experimental validation of impact sound radiation by timber joist floors," *Applied Acoustics*, vol. 162, p. 107182, 2020. https://doi.org/10.1016/j.apacoust.2019.107182.

[101] M. Bader Eddin, S. Ménard, D. Bard Hagberg, J.-L. Kouyoumji, and N.-G. Vardaxis, "Prediction of sound insulation using artificial neural networks — Part I: Lightweight wooden floor structures," *Acoustics*, vol. 4, no. 1, pp. 203–226, 2022. https://doi.org/10.3390/acoustics4010013.

[102] S. Bograd, P. Reuss, A. Schmidt, L. Gaul, and M. Mayer, "Modeling the dynamics of mechanical joints," *Mechanical Systems and Signal Processing*, vol. 25, no. 8, pp. 2801–2826, 2011. https://doi.org/10.1016/j.ymssp.2011.01.010.

[103] "VDI 3830 - Damping of materials and members," Guideline, VDI - Association of German Engineers, Duesseldorf, Germany, Aug 2004.

[104] X. Ma, L. Bergman, and A. Vakakis, "Identification of bolted joints through laser vibrometry," *Journal of Sound and Vibration*, vol. 246, no. 3, pp. 441–460, 2001. https://doi.org/10.1006/jsvi.2001.3573.

[105] M. R. W. Brake, *The mechanics of jointed structures: recent research and open challenges for developing predictive models for structural dynamics*. Cham: Springer, 2018. https://doi.org/10.1007/978-3-319-56818-8.

[106] S. A. Nayfeh and A. H. Nayfeh, "Nonlinear interactions between two widely spaced modes — external excitation," *International Journal of Bifurcation and Chaos*, vol. 3, no. 02, pp. 417–427, 1993. https://doi.org/10.1142/S0218127493000301.

[107] K. Oh and A. H. Nayfeh, "Nonlinear combination resonances in cantilever composite plates," *Nonlinear Dynamics*, vol. 11, no. 2, pp. 143–169, 1996. https://doi.org/10.1007/BF00044999.

[108] D. Casagrande, I. Giongo, F. Pederzolli, A. Franciosi, and M. Piazza, "Analytical, numerical and experimental assessment of vibration performance in timber floors," *Engineering Structures*, vol. 168, pp. 748–758, 2018. https://doi.org/10.1016/j.engstruct.2018.05.020.

[109] L. Godinho, R. Masgalos, A. Pereira, and F. Branco, "On the use of a small-sized acoustic chamber for the analysis of impact sound reduction by floor coverings," *Noise Control Engineering Journal*, vol. 58, no. 6, pp. 658–668, 2010. https://doi.org/10.3397/1.3484866.

[110] F. G. Branco and L. Godinho, "On the use of lightweight mortars for the minimization of impact sound transmission," *Construction and Building Materials*, vol. 45, pp. 184–191, 2013. https://doi.org/10.1016/j.conbuildmat.2013.04.001.

[111] "DIN EN ISO 10140-1 - Acoustics - Laboratory measurement of sound insulation of building elements - Part 1: Application rules for specific products," Standard, European Committee for Standardization, Brussels, Belgium, Sep 2021. `https://dx.doi.org/10.31030/3238584`.

[112] V. Hongisto *et al.*, *Airborne sound insulation of wall structures: measurement and prediction methods*. PhD thesis, Helsinki University of Technology, 2000.

[113] J. L. Davy, "Predicting the sound insulation of single leaf walls: Extension of cremer's model," *The Journal of the Acoustical Society of America*, vol. 126, no. 4, pp. 1871–1877, 2009. `https://doi.org/10.1121/1.3206582`.

[114] V. Hongisto, "Sound insulation of double panels-comparison of existing prediction models," *Acta acustica united with acustica*, vol. 92, no. 1, pp. 61–78, 2006.

[115] V. D'Alessandro, G. Petrone, F. Franco, and S. De Rosa, "A review of the vibroacoustics of sandwich panels: Models and experiments," *Journal of Sandwich Structures & Materials*, vol. 15, no. 5, pp. 541–582, 2013. `https://doi.org/10.1177/1099636213490588`.

[116] T. E. Vigran, "Sound transmission in multilayered structures–introducing finite structural connections in the transfer matrix method," *Applied Acoustics*, vol. 71, no. 1, pp. 39–44, 2010. `https://doi.org/10.1016/j.apacoust.2009.07.005`.

[117] A. Santoni, J. L. Davy, P. Fausti, and P. Bonfiglio, "A review of the different approaches to predict the sound transmission loss of building partitions," *Building Acoustics*, vol. 27, no. 3, pp. 253–279, 2020. `https://doi.org/10.1177/1351010x20911599`.

[118] S. P. S. Maluski and B. M. Gibbs, "Application of a finite-element model to low-frequency sound insulation in dwellings," *The Journal of the Acoustical Society of America*, vol. 108, no. 4, pp. 1741–1751, 2000. `https://doi.org/10.1121/1.1310355`.

[119] A. Arjunan, C. J. Wang, K. Yahiaoui, D. J. Mynors, T. Morgan, V. B. Nguyen, and M. English, "Development of a 3D finite element acoustic model to predict the sound reduction index of stud based double-leaf walls," *Journal of Sound and Vibration*, vol. 333, no. 23, pp. 6140–6155, 2014. `https://doi.org/10.1016/j.jsv.2014.06.032`.

[120] L. Alimonti, N. Atalla, A. Berry, and F. Sgard, "Assessment of a hybrid finite element-transfer matrix model for flat structures with homogeneous acoustic treatments," *The Journal of the Acoustical Society of America*, vol. 135, no. 5, pp. 2694–2705, 2014. `https://doi.org/10.1121/1.4871355`.

[121] D. Rhazi and N. Atalla, "Acoustic and vibration response of a structure with added noise control treatment under various excitations," *The Journal of the Acoustical Society of America*, vol. 135, no. 2, pp. 693–704, 2014. `https://doi.org/10.1121/1.4861361`.

[122] J. C. E. Van den Wyngaert, M. Schevenels, and E. P. B. Reynders, "Predicting the sound insulation of finite double-leaf walls with a flexible frame," *Applied Acoustics*, vol. 141, pp. 93–105, 2018. https://doi.org/10.1016/j.apacoust.2018.06.020.

[123] C. Churchill and C. Hopkins, "Prediction of airborne sound transmission across a timber–concrete composite floor using statistical energy analysis," *Applied Acoustics*, vol. 110, pp. 145–159, 2016. url-https://doi.org/10.1016/j.apacoust.2016.03.031.

[124] M. Bader Eddin, N.-G. Vardaxis, S. Ménard, D. Bard Hagberg, and J.-L. Kouyoumji, "Prediction of sound insulation using artificial neural networks — part II: Lightweight wooden façade structures," *Applied Sciences*, vol. 12, no. 14, p. 6983, 2022. https://doi.org/10.3390/app12146983.

[125] "DIN EN ISO 10140-5 - Acoustics - Laboratory measurement of sound insulation of building elements - Part 5: Requirements for test facilities and equipment," Standard, European Committee for Standardization, Brussels, Belgium, Sep 2021. https://doi.org/10.31030/3237462.

[126] J. Brunskog and P. Hammer, "The interaction between the ISO tapping machine and lightweight floors," *Acta Acustica united with Acustica*, vol. 89, no. 2, pp. 296–308, 2003.

[127] B. Szabó and I. Babuška, *Finite Element Analysis: Method, Verification and Validation*. Hoboken, USA: John Wiley & Sons, second ed., 2021. https://doi.org/10.1002/9781119426479.

[128] J. E. Mottershead, M. Link, M. I. Friswell, and C. Schedlinski, "Model updating," in *Handbook of Experimental Structural Dynamics* (R. Allemang and P. Avitabile, eds.), pp. 1–53, New York, USA: Springer, 2021. https://doi.org/10.1007/978-1-4939-6503-8_18-1.

[129] S. Ereiz, I. Duvnjak, and J. F. Jiménez-Alonso, "Review of finite element model updating methods for structural applications," *Structures*, vol. 41, pp. 684–723, 2022. https://doi.org/10.1016/j.istruc.2022.05.041.

[130] B. Shahriari, K. Swersky, Z. Wang, R. P. Adams, and N. De Freitas, "Taking the human out of the loop: A review of bayesian optimization," *Proceedings of the IEEE*, vol. 104, no. 1, pp. 148–175, 2015. https://doi.org/10.1109/JPROC.2015.2494218.

[131] S. Tao, A. Van Beek, D. W. Apley, and W. Chen, "Multi-model bayesian optimization for simulation-based design," *Journal of Mechanical Design*, vol. 143, no. 11, 2021. https://doi.org/10.1115/1.4050738.

[132] C. Soize, "A comprehensive overview of a non-parametric probabilistic approach of model uncertainties for predictive models in structural dynamics," *Journal of Sound and Vibration*, vol. 288, no. 3, pp. 623–652, 2005. https://doi.org/10.1016/j.jsv.2005.07.009.

[133] F. Gant, P. Rouch, and L. Champaney, "Updating of uncertain joint models using the lack-of-knowledge theory," *Computers & Structures*, vol. 128, pp. 128–135, 2013. https://doi.org/10.1016/j.compstruc.2013.06.013.

[134] C. Qian, S. Ménard, D. Bard, and J. Negreira, "Development of a vibroacoustic stochastic finite element prediction tool for a clt floor," *Applied Sciences*, vol. 9, no. 6, p. 1106, 2019. https://doi.org/10.3390/app9061106.

[135] P. Persson and O. Flodén, "Effect of material parameter variability on vibroacoustic response in wood floors," *Applied Acoustics*, vol. 146, pp. 38–49, 2019. https://doi.org/10.1016/j.apacoust.2018.10.034.

[136] F. Daghia, S. de Miranda, F. Ubertini, and E. Viola, "Estimation of elastic constants of thick laminated plates within a bayesian framework," *Composite Structures*, vol. 80, no. 3, pp. 461–473, 2007. https://doi.org/10.1016/j.compstruct.2006.06.030.

[137] C. Gogu, R. Haftka, R. Le Riche, J. Molimard, A. Vautrin, and B. Sankar, "Bayesian statistical identification of orthotropic elastic constants accounting for measurement and modeling errors," in *50th AIAA/ASME/ASCE/AHS/ASC Structures, Structural Dynamics, and Materials Conference*, p. 2258, 2009. https://doi.org/10.2514/6.2009-2258.

[138] L. Melzerová, T. Janda, M. Šejnoha, and J. Šejnoha, "FEM models of glued laminated timber beams enhanced by bayesian updating of elastic moduli," *International Journal of Civil and Environmental Engineering*, vol. 9, no. 5, pp. 692–698, 2015. https://doi.org/10.5281/zenodo.1100296.

[139] F. Schneider, I. Papaioannou, D. Straub, C. Winter, and G. Müller, "Bayesian parameter updating in linear structural dynamics with frequency transformed data using rational surrogate models," *Mechanical Systems and Signal Processing*, vol. 166, p. 108407, 2022. /10.1016/j.ymssp.2021.108407.

[140] B. Chocholaty, N. B. Roozen, M. Maeder, and S. Marburg, "Vibroacoustic response of steel–timber composite elements," *Engineering Structures*, vol. 271, p. 114911, 2022. https://doi.org/10.1016/j.engstruct.2022.114911.

[141] B. Chocholaty, M. Eser, K.-A. Hoppe, D. Wang, and S. Marburg, "Vibration response of a hybrid steel–timber building element with uncertain material and joint parameters," *Archives of Civil and Mechanical Engineering*, vol. 24, no. 1, p. 22, 2023. https://doi.org/10.1007/s43452-023-00819-z.

[142] B. Chocholaty, N. B. Roozen, K.-A. Hoppe, M. Maeder, and S. Marburg, "Vibration and impact sound properties of hybrid steel-timber floor structures," *Acta Acustica*, vol. 8, no. 11, pp. 1–18, 2024. https://doi.org/10.1051/aacus/2024001.

[143] D. J. Ewins, *Modal testing: theory, practice and application*. Baldock, UK: Research Studies Press Ltd., second ed., 2000.

[144] S. J. Rothberg, M. S. Allen, P. Castellini, D. Di Maio, J. J. J. Dirckx, D. J. Ewins, B. J. Halkon, P. Muyshondt, N. Paone, T. Ryan, H. Steger, E. P. Tomasini, S. Vanlanduit, and J. F. Vignola, "An international review of laser Doppler vibrometry: Making light work of vibration measurement," *Optics and Lasers in Engineering*, vol. 99, pp. 11–22, 2017. https://doi.org/10.1016/j.optlaseng.2016.10.023.

[145] P. Avitabile, "Experimental modal analysis," *Sound and vibration*, vol. 35, no. 1, pp. 20–31, 2001.

[146] J.-P. Noël, L. Renson, and G. Kerschen, "Complex dynamics of a nonlinear aerospace structure: experimental identification and modal interactions," *Journal of Sound and Vibration*, vol. 333, no. 12, pp. 2588–2607, 2014. https://doi.org/10.1016/j.jsv.2014.01.024.

[147] J.-P. Noel and G. Kerschen, "Nonlinear system identification in structural dynamics: 10 more years of progress," *Mechanical Systems and Signal Processing*, vol. 83, pp. 2–35, 2017. http://dx.doi.org/10.1016/j.ymssp.2016.07.020.

[148] M. Grimsel, *Mechanisches Verhalten von Holz: Struktur-und Parameteridentifikation eines anisotropen Werkstoffes*. Dresden: web-Univ.-Verlag, 1999.

[149] H. Altenbach, *Kontinuumsmechanik: Einführung in die materialunabhängigen und materialabhängigen Gleichungen*. Heidelberg: Springer Berlin, second ed., 2012. https://doi.org/10.1007/978-3-642-24119-2.

[150] O. C. Zienkiewicz, R. L. Taylor, and D. Fox, *The finite element method for solid and structural mechanics*. Elsevier, seventh ed., 2014. https://doi.org/10.1016/C2009-0-26332-X.

[151] M. Mukhopadhyay, *Structural Dynamics*. Cham: Springer, 2021. https://doi.org/10.1007/978-3-030-69674-0.

[152] A. Nilsson and B. Liu, *Vibro-Acoustics, Volume 1*. Berlin: Springer, second ed., 2015. https://doi.org/10.1007/978-3-662-47807-3.

[153] S. Adhikari, *Structural dynamic analysis with generalized damping models: analysis*. Hoboken, USA: John Wiley & Sons, 2014. https://doi.org/10.1002/9781118572023.

[154] A. Rabold, *Anwendung der Finite Elemente Methode auf die Trittschallberechnung*. PhD thesis, Technische Universität München, 2010.

[155] J. W. S. B. Rayleigh, *The theory of sound*, vol. 1. London: Macmillan, 1877.

[156] ANSYS, "ANSYS Theory Reference." https://www.caee.utexas.edu/prof/kallivokas/teaching/ANSYS_examples/ansys56theory.pdf. Accessed: 2023-11-10.

[157] Z. Shen, X. Liu, C. Zang, and S. Hu, "Bayesian uncertainty identification of model parameters for the jointed structures with nonlinearity," *Shock and Vibration*, vol. 2021, 2021. https://doi.org/10.1155/2021/2638995.

[158] R. Lacayo, L. Pesaresi, J. Groß, D. Fochler, J. Armand, L. Salles, C. Schwingshackl, M. Allen, and M. Brake, "Nonlinear modeling of structures with bolted joints: a comparison of two approaches based on a time-domain and frequency-domain solver," *Mechanical Systems and Signal Processing*, vol. 114, pp. 413–438, 2019. https://doi.org/10.1016/j.ymssp.2018.05.033.

[159] F. Gant, P. Rouch, F. Louf, and L. Champaney, "Definition and updating of simplified models of joint stiffness," *International Journal of Solids and Structures*, vol. 48, no. 5, pp. 775–784, 2011. https://doi.org/10.1016/j.ijsolstr.2010.11.011.

[160] ANSYS, "ANSYS Element Reference." https://www.mm.bme.hu/~gyebro/files/vem/ansys_14_element_reference.pdf. Accessed: 2023-11-13.

[161] D. J. Segalman, D. L. Gregory, M. J. Starr, B. R. Resor, M. D. Jew, J. P. Lauffer, and N. M. Ames, "Handbook on dynamics of jointed structures," tech. rep., Sandia National Laboratories, Albuquerque, 2009. https://doi.org/10.2172/1028891.

[162] P. Mario and H. K. Young, *Structural dynamics: Theory and computation*. Cham: Spinger, sixth ed., 2019. https://doi.org/10.1007/978-3-319-94743-3.

[163] Q. Wang, D. Shi, and X. Shi, "A modified solution for the free vibration analysis of moderately thick orthotropic rectangular plates with general boundary conditions, internal line supports and resting on elastic foundation," *Meccanica*, vol. 51, pp. 1985–2017, 2016. https://doi.org/10.1007/s11012-015-0345-3.

[164] R. D. Mindlin, "Influence of rotatory inertia and shear on flexural motions of isotropic, elastic plates," *Journal Of Applied Mechanics*, vol. 18, no. 1, pp. 31–38, 1951. https://doi.org/10.1115/1.4010217.

[165] D. Shi, Z. Zhuang, and T. Zhang, "Free vibration analysis of orthotropic rectangular mindlin plates with general elastic boundary conditions," in *INTER-NOISE and NOISE-CON Congress and Conference Proceedings*, vol. 249, pp. 1477–1485, 2014.

[166] L. V. Andersen, C. Frier, and L. Pedersen, "Probabilistic analysis of modal properties for floor systems with uncertain support conditions," in *Dynamics of Civil Structures, Volume 2: Proceedings of the 36th IMAC, A Conference and Exposition on Structural Dynamics 2018* (S. Pakzad, ed.), pp. 67–75, Springer, 2019. https://doi.org/10.1007/978-3-319-74421-6_10.

[167] R. A. Ibrahim and C. L. Pettit, "Uncertainties and dynamic problems of bolted joints and other fasteners," *Journal of Sound and Vibration*, vol. 279, no. 3-5, pp. 857–936, 2005. https://doi.org/10.1016/j.jsv.2003.11.064.

[168] M. Johansson and S. Ormarsson, "Influence of growth stresses and material properties on distortion of sawn timber–numerical investigation," *Annals of Forest Science*, vol. 66, no. 6, pp. 1–10, 2009. `https//doi:10.1051/forest/2009045`.

[169] A. M. J. Olsson and G. E. Sandberg, "Latin hypercube sampling for stochastic finite element analysis," *Journal of Engineering Mechanics*, vol. 128, no. 1, pp. 121–125, 2002. `https://doi.org/10.1061/(asce)0733-9399(2002)128:1(121)`.

[170] K. Christodoulou, E. Ntotsios, C. Papadimitriou, and P. Panetsos, "Structural model updating and prediction variability using pareto optimal models," *Computer Methods in Applied Mechanics and Engineering*, vol. 198, no. 1, pp. 138–149, 2008. `https://doi.org/10.1016/j.cma.2008.04.010`.

[171] R. J. Allemang, "The modal assurance criterion – twenty years of use and abuse," *Sound and vibration*, vol. 37, no. 8, pp. 14–23, 2003.

[172] A. Gelman, J. B. Carlin, H. S. Stern, D. B. Dunson, A. Vehtari, and D. B. Rubin, *Bayesian Data Analysis*. New York: Chapman and Hall/CRC, third ed., 2013. `https://doi.org/10.1201/b16018`.

[173] R. van de Schoot, S. Depaoli, R. King, B. Kramer, K. Märtens, M. G. Tadesse, M. Vannucci, A. Gelman, D. Veen, J. Willemsen, and C. Yau, "Bayesian statistics and modelling," *Nature Reviews Methods Primers*, vol. 1, no. 1, p. 1, 2021. `https://doi.org/10.1038/s43586-020-00001-2`.

[174] N. Xiang, "Model-based bayesian analysis in acoustics—a tutorial," *The Journal of the Acoustical Society of America*, vol. 148, no. 2, pp. 1101–1120, 2020. `/10.1121/10.0001731`.

[175] O. Martin, *Bayesian Analysis with Python: Introduction to statistical modeling and probabilistic programming using PyMC3 and ArviZ*. Birmingham: Packt Publishing Ltd, second ed., 2018.

[176] J.-L. Gauvain and C.-H. Lee, "Maximum a posteriori estimation for multivariate gaussian mixture observations of markov chains," *IEEE transactions on speech and audio processing*, vol. 2, no. 2, pp. 291–298, 1994. `/10.1109/89.279278`.

[177] J. Lietzén, J. Miettinen, M. Kylliäinen, and S. Pajunen, "Impact force excitation generated by an iso tapping machine on wooden floors," *Applied Acoustics*, vol. 175, p. 107821, 2021. `https://doi.org/10.1016/j.apacoust.2020.107821`.

[178] F. J. Fahy and P. Gardonio, *Sound and structural vibration: radiation, transmission and response*. Elsevier, second ed., 2007. `https://doi.org/10.1016/B978-0-12-373633-8.X5000-5`.

[179] J. W. S. B. Rayleigh, *The theory of sound*, vol. 2. London: Macmillan, second ed., 1896.

[180] "DIN EN ISO 3741 - Acoustics - Determination of sound power levels and sound energy levels of noise sources using sound pressure - Precision methods for reverberation test rooms," Standard, European Committee for Standardization, Brussels, Belgium, Jan 2011. https://doi.org/10.31030/1642422.

[181] D. E. Post and R. P. Kendall, *Creating and using virtual prototyping software: Principles and practices*. Addison-Wesley Professional, 2021.

[182] N.-G. Vardaxis, D. Bard Hagberg, and J. Dahlström, "Evaluating laboratory measurements for sound insulation of cross-laminated timber (CLT) floors: Configurations in lightweight buildings," *Applied Sciences*, vol. 12, no. 15, p. 7642, 2022. https://doi.org/10.3390/app12157642.

[183] V. Bucur, *Acoustics of wood*. Heidelberg: Springer, second ed., 2006. https://doi.org/10.1007/3-540-30594-7.

[184] V. Sebera, L. Muszyński, J. Tippner, M. Noyel, T. Pisaneschi, and B. Sundberg, "FE analysis of CLT panel subjected to torsion and verified by DIC," *Materials and Structures*, vol. 48, pp. 451–459, 2015. https://doi.org/10.1617/s11527-013-0195-1.

[185] P. Langer, M. Maeder, C. Guist, M. Krause, and S. Marburg, "More than six elements per wavelength: The practical use of structural finite element models and their accuracy in comparison with experimental results," *Journal of Computational Acoustics*, vol. 25, no. 04, p. 1750025, 2017. https://doi.org/10.1142/s0218396x17500254.

[186] C. Sujatha, *Vibration, Acoustics and Strain Measurement: Theory and Experiments*. Cham: Springer Nature, 2023. https://doi.org/10.1007/978-3-031-03968-3.

[187] C. A. Geweth, S. K. Baydoun, F. Saati, K. Sepahvand, and S. Marburg, "Effect of boundary conditions in the experimental determination of structural damping," *Mechanical Systems and Signal Processing*, vol. 146, p. 107052, 2021. https://doi.org/10.1016/j.ymssp.2020.107052.

[188] S. Perinpanayagam and D. J. Ewins, "Free-free, fixed or other test boundary conditions for the best modal test," in *Proceedings of the 21st international modal analysis conference (IMAC-XXI)*, 2003. https://api.semanticscholar.org/CorpusID:13979253.

[189] C. W. Schwingshackl, E. P. Petrov, and D. J. Ewins, "Measured and estimated friction interface parameters in a nonlinear dynamic analysis," *Mechanical Systems and Signal Processing*, vol. 28, pp. 574–584, 2012. https://doi.org/10.1016/j.ymssp.2011.10.005.
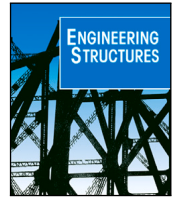
A Appended Publications

A.1 Paper A

Vibroacoustic response of steel-timber composite elements

Bettina Chocholaty, Nicolaas Bernardus Roozen, Marcus Maeder, Steffen Marburg

Vibroacoustic response of steel–timber composite elements

B. Chocholaty [a],[*], N.B. Roozen [b],[a], M. Maeder [a], S. Marburg [a]

[a] *Chair of Vibroacoustics of Vehicles and Machines, Technical University of Munich, Boltzmannstr. 15, Garching b. München, 85748, Germany*
[b] *Laboratory of Acoustics, Soft Matter and Biophysics, Katholieke Universiteit Leuven, Celestijnenlaan 200D, Leuven, 3001, Belgium*

ARTICLE INFO

ABSTRACT

With the increasing demand for sustainable construction and, at the same time, for larger spans in buildings and high-rise buildings, composite timber structures are gaining more attention, and steel–timber hybrid elements offer a promising approach. Therefore, this study analyzes a novel steel–timber composite floor structure experimentally and numerically. The investigations focus on the vibrational behavior of the structures while considering nonlinearities due to frictional effects in joints. First, eigenfrequencies, damping properties, and consequently, the vibrational characteristics of the systems are determined. Then, detection of nonlinearity follows, investigating amplitude-dependent stiffness and damping and the occurrence of higher harmonics. Results reveal nonlinearities indicated by the occurrence of higher-order harmonics and slight amplitude-dependent damping. Furthermore, the influence of parameters, such as steel thickness and fastener type, on the vibrational behavior of the structures is investigated, comparing specimens of various configurations. Finally, the experimental results validate a linear Finite Element model using the commercial software ANSYS as a first approach despite the nonlinearities that occurred during the measurements. Nonetheless, further investigations could deal with nonlinear models to get more detailed insight.

1. Introduction

Replacing concrete and structural steel with wood-engineered products saves greenhouse gas emissions such as carbon dioxide emissions, increasing sustainability [3,4]. Furthermore, fast construction, high strength-to-weight ratio, and lightweight characteristics favor buildings made of timber. However, the increasing demand for larger spans and high-rise timber buildings leads to higher susceptibility of floors and similar building elements to vibrations. Therefore, although the design criteria concerning load-bearing capacity are fulfilled due to new engineered-wood products, the serviceability criteria might not be met [5]. In this case, occupants note excessive vibrations in terms of annoyance [6]. Moreover, lightweight structures show poor sound insulation properties for both airborne and impact sound. The typically low mass per unit area of those building elements leads to high sound transmission [7].

Current research in wooden structures focuses increasingly on composite structures to overcome drawbacks in wooden materials such as impermanence and limited application. Initial advances for combining timber and steel deal with columns built from steel cross-sections surrounded by wooden materials for use as a column in buildings [8]. Further researchers proposed beam and floor elements constructed from structural steel and engineered wood products. Those investigations consider different sections for the steel, such as omega-shaped cold-formed steel, U-shaped sections, C-shaped cold-formed steel, welded steel beams, or H-shaped beams. Moreover, different engineered wood products are investigated: cross-laminated timber (CLT) and laminated veneer lumber (LVL). Static load bearing capacities [9], load–slip curves, and failure modes of joints [10] are analyzed for various types and combinations of steel and wood elements. Experimental and numerical tests on prototypes highlight the advantages of such composite steel–timber systems compared to typical construction materials in the related articles [11,12]. In [13], the authors study static nonlinearities due to connectors, geometry, and interface conditions. The first approach toward vibrational characterization of steel–timber floor systems has been recently made in [2,14].

Consequently, steel–timber composite structures of various configurations are analyzed in the literature. Investigations deal with different steel sections, wooden materials, and the arrangement of components. Nonetheless, structures constructed by a corrugated steel core with a top and bottom chord made of LVL plates have not been studied so far. Furthermore, most works investigate static properties on the joint level or the overall floor structure. However, studies considering vibrational effects of the structures are rare, and no detailed investigation of the dynamic behavior of the joints has been conducted so far.

Joints significantly influence the dynamics of a structure. In [15], several reasons are given for nonlinearities in an assembled system. First, under expected excitation levels, macro-slip influences the system's geometry. Second, coupled modes appear in the structure's response. Third, the stiffness in the joint's interface becomes smaller, and, finally, in the jointed interface, the damping rises significantly in the regime of micro-slip until macro-slip, then it decreases. Based on this, three phenomena concerning joint-related nonlinearity are identified, i.e., amplitude-dependent stiffness, amplitude-dependent damping, and occurrence of nonlinearly coupled modes or higher-order harmonics. First, if the natural frequency of the system changes as the load amplitude increases, amplitude-dependent stiffness exists. Second, if the loading is sufficient to cause slippage in the joint and the damping ratio changes due to increased excitation amplitude, amplitude-dependent damping also influences the structure's response. Third, if the system is excited at one natural frequency and other modes are strongly activated, nonlinearly coupled modes exist in the structure. This condition is indicated by multi-harmonic responses. However, harmonic distortion suggests the activation of non-smooth nonlinearity in the neighborhood of the resonance but not necessarily nonlinear modal interaction [15]. Nonlinearly coupled modes or modal interaction only occur if an excitation at one resonance frequency leads to a surprisingly large-amplitude response at other modes of the investigated structure. This might be the case for commensurate or nearly commensurate natural frequencies [16,17].

As a first approach, the strength of nonlinearity helps to classify a structure. Linearity is assumed if none of the above-described phenomena is revealed. Weak nonlinearity exists if amplitude-dependency is observed. Strong nonlinearity is revealed in the system if nonlinearly coupled modes or higher-order harmonics appear additionally to the amplitude-dependency [15]. Different modeling approaches are used depending on the strength of nonlinearity. Several joint models and their applicability are investigated in [18]. A popular linear modeling approach also used in the context of this study is the Finite Element (FE) analysis. In the case of wood–steel composite structures, it should also be noted that wood components often have a greater thickness than, for example, steel components. For this reason, it is in general appropriate to use, e.g., volumetric elements or higher order shear deformation elements when modeling timber structures with finite element methods [19,20]. Additionally, experimental validation of the used models is of great importance. Modal data such as eigenfrequencies and eigenmodes are often used in this context [21].

This article deals with a steel–timber composite structure and its vibrational behavior. The investigated sandwich structure consists of two LVL plates and a corrugated steel core which is a new design for this type of structure. Furthermore, the focus lies on the influence of the joints on the overall vibroacoustics. To the best of our knowledge, no studies on the dynamic behavior of building elements made of LVL and corrugated steel exist in literature. Further, no detailed study on the influence of the joints and the thereby introduced nonlinearity on the structural dynamics of steel–timber composite structures has been conducted. This paper aims to fill this gap by performing a comprehensive investigation of the vibrations of the proposed element. Experimental as well as numerical investigations are presented. Based on the results, insights are subsequently gained regarding the influencing parameters and their applicability for steel–timber composites.

The article is organized as follows. Section 2 explains the experimental program and numerical simulations. In Section 3, the results of experiments and numerical modeling are presented together with a discussion of the results. Finally, Section 4 concludes this study and discusses ideas for future work.

2. Investigations on steel–timber composite elements

This section presents and discusses the conducted experimental and numerical investigations. First, the steel–timber composite element is introduced. The experimental setups and investigations follow. Finally, the numerical approach for validation is described.

2.1. Steel–timber composite element

The investigated steel–timber composite sandwich elements consist of top and bottom chord LVL plates and a corrugated steel frame as the core (Fig. 1). The two different investigated cross-section types differ mainly in the lower chord. The closed configuration includes a continuous lower wooden panel (Fig. 1(b)), while the open one is divided into individual wooden boards at the bottom chord (Fig. 1(a)).

Furthermore, the connection between the components is realized either with a steel–timber or timber–steel joint. The open configuration only uses steel–timber joints. On the contrary, the closed cross-section is constructed by a timber–steel joint in the upper connection and a steel–timber joint in the lower one (Fig. 1(b)). For the steel–timber joint, a screw or nail is first driven through the steel sheet and, subsequently, into the LVL component. In the case of the timber–steel joint, a screw is first driven through the LVL and then through the steel component. However, problems can arise for the latter joint since the connection between the LVL board and steel sheet lacks pretension. This results in a deformation of the steel component just before drilling through, leading to a remaining gap between steel and timber. Therefore, the connection becomes weaker than for the steel–timber joint. The influence of the joint configuration and other parameters are investigated by experimentally analyzing various combinations of timber material, system dimensions, and fastener types. Subsequently, a numerical study is conducted to validate the measurements.

2.2. Experimental setup and investigations

Measurements are performed on samples with varying parameters in two different settings. First, smaller size samples are investigated in the vibrational laboratory at the *Technical University of Munich* (TUM). Second, further measurements on larger test specimens are performed at the chair of *Timber Structures and Building Construction* at *Karlsruhe Institute of Technology* (KIT).

2.2.1. Objectives and specimen details

The experiments aim to measure transfer functions. Subsequently, modal parameters are derived by employing an experimental modal analysis. See Ewins [22] for deeper insight into the topic of experimental modal analysis. In addition, numerical studies, which are further discussed in Section 2.3, are validated using this data.

As described in the introduction (Section 1), jointed structures are prone to nonlinearities influencing the vibrational behavior, e.g., due to effects of friction [23]. The experiments focus on identifying nonlinearities and determining whether they should be taken into account. In order to conduct realistic tests, attention is paid to the maximum resulting vibration amplitudes. The amplitudes are chosen as reasonable limits of the application as a floor structure. In [24], standard impact sound levels are given for raw ceilings as a function of the area-related mass. Since the graph provided in [24] stops at $100 \, \mathrm{kg/m^2}$ with $95 \, \mathrm{dB}$ and the investigated structures have less than $100 \, \mathrm{kg/m^2}$, $100 - 110 \, \mathrm{dB}$ was selected as a limit, including a small safety margin.

Detecting nonlinearity concentrates on three aspects: amplitude-dependent stiffness, amplitude-dependent damping, and the appearance of higher harmonics in the structure's response.

Vibration measurements are conducted on the samples listed in the appendix in Table A.1 to investigate the vibroacoustic behavior of the steel–timber composite structure. The tested specimens vary with respect to the dimensions of the overall structure, dimensions of the components, material properties, overall configuration, and type of fastener. The different fasteners are summarized in Table 1.
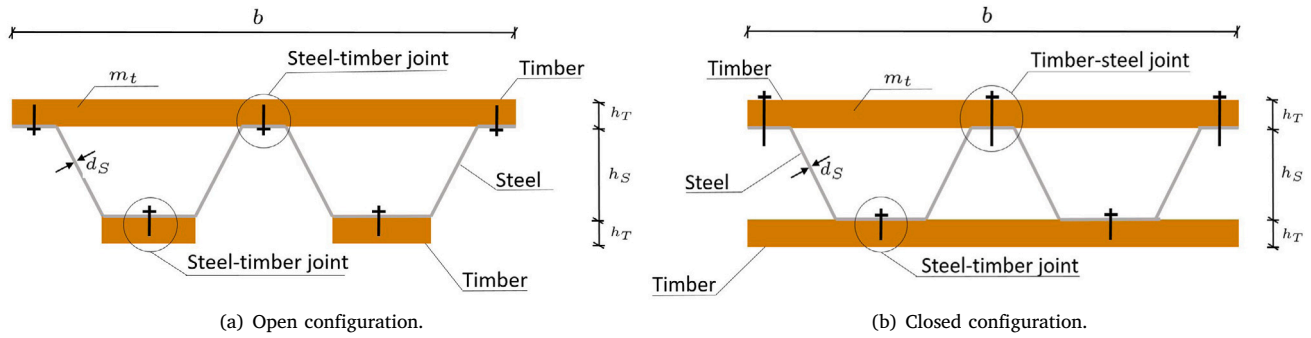
(a) Open configuration.

(b) Closed configuration.

Fig. 1. Cross-section of open (left) and closed (right) steel–timber composite element.

Table 1
Fastener types used to assemble steel–timber elements.

Fastener	Description (manufacturer)	Picture
SBS1	Screw 4.2 × 38 (Rothoblaas)	
BS1	Screw 6.0 × 64 (SFS)	
HS2	Screw 5.0 × 40 (SFS)	
Re	Screw 6.0 × 90 (Reisser)	
Re*	Screw 6.0 × 90 (Reisser) (adapted tip)	
StNa	Nail	Unpublished prototype

2.2.2. Measurement setup

The specimens are excited using a B&K,[1] modal exciter type 4824 together with a stinger. The stinger is added in order to reduce any transferred moments. Subsequently, the force transducer (B&K Force Transducer Deltatron Type 8230) connects the stinger to the structure. On the opposite surface of the specimens, a scanning Laser Doppler Vibrometer PSV-500.[2] (LDV) measures the structural vibrations. The shaker applies the excitation force to the lower chord for closed specimens while measuring the surface velocities on the upper chord through the LDV, as displayed in Figs. 2(a), 2(b), 3(a) and 3(c) For the open configurations, the force transducer is attached to the upper timber chord, and the vibration measurements are conducted on the lower side of the structure (Figs. 3(b) and 3(c)).

Hanging support is chosen for the measurement to avoid in-plane stresses influencing the structural response due to gravitational effects [25]. Depending on the sample size, two different ways of suspension are realized at TUM and KIT. At TUM, rubber bands hold the smaller samples in place, whereas heavy-duty slings and a crane are utilized at KIT to support the larger structures. Exemplary setups are visualized in two figures (Figs. 2 and 3). Slight shear stress might have been introduced by the supports at KIT in contrast to TUM due to the three-point support of the slings. This might lead to slightly higher natural frequencies at KIT. Additionally, rubber bands exhibit more damping than slings which could lead to smaller vibration amplitudes at TUM as opposed to KIT. However, a comparison of the mode shape (1,1) (Figs. 6 and 7) for specimens tested at TUM, respectively KIT, showed similar vibration amplitudes at supported and unsupported

corners of the samples. Therefore, the influence of the suspension seems negligible.

First, to measure the transfer functions between the force transducer signal and the vibration signal at each scanning point, white noise and pseudo-random noise serve as the excitation signal for measurement at TUM and KIT, respectively. All signal channels are windowed using a Hanning window. Depending on the circumstances, such as the geometry, the number of scan points is chosen between $n_{sp} = 60 - 275$. At each measurement point, 25 time windows are recorded and transferred to the frequency domain through the Fast Fourier Transformation (FFT). Again, due to the circumstances, different sampling rates f_{smp} as well as frequency resolutions of Δf are determined. The sampling rate f_{smp} and frequency resolution of Δf range between $f_{smp} = 0.8 - 5\,\text{kHz}$ and $\Delta f = 0.16 - 0.39\,\text{Hz}$, respectively. The resulting 25 transfer functions are averaged in the complex plane to improve the signal-to-noise-ratio (SNR). Furthermore, the force level is altered to investigate the amplitude-dependent nonlinearities as $F_k \cong k \cdot F_0$ with $k = 1, 2, 3, 4$, where the approximation is based on the root-mean-square (RMS) values within the stochastic force excitation signal.

In contrast to the small structures, the larger specimens analyzed at KIT are excited using a higher force level due to the larger mass of the complete structure. The applied force is given as $F_l \cong l \cdot F_0$ with $l = 1, 5, 10$.

To identify force levels F_k and F_l, preliminary measurements utilizing a sine-sweep loading investigated the maximum surface velocity levels. Here, the measurements are set in such way that for $k = 4$ and $l = 10$ the maximum resulting surface velocity amplitudes remains within a range of $100\,\text{dB} – 110\,\text{dB}$ with the corresponding reference of $0\,\text{dB} = 5 \cdot 10^{-8}\,\text{m/s}$. An explanation for the choice of this limit is given in Section 2.2.1. The identified load levels are further used for all measurements of this sample type.

Furthermore, the samples are excited by a sine sweep loading approximately at the first three eigenfrequencies. Comparable load levels as before are used. Depending on the circumstances, the scan point number $n_{SP} = 60 - 253$, the sampling rate $f_{smp} = 1 - 2\,\text{kHz}$ and the time resolution $\Delta t = 0.5 - 1\,\text{ms}$ are chosen. The velocity and force data collected in the time domain are then converted to the frequency domain and represented in a spectrogram.

Measurements at TUM — two-component assembly:

The designed floor structure consists of three components, i.e., two timber plates and a steel frame. However, as a first step, an assembly built by the lower LVL chord and the steel frame only is studied experimentally to identify the effect of the joints in the structure. This procedure is applied to specimens $V1a$, $V2a$, $V3a$, and $V4a$ (Table A.1).

Measurements at TUM and KIT — three-component assembly:

Next, investigations on a complete assembly consisting of three components, i.e., bottom LVL chord, steel frame, and top LVL chord, are performed. Three different groups are distinguished herein. The samples tested at KIT measure $3.5\,\text{m}$ in length, the specimens tested at TUM only $0.6\,\text{m}$. The tests at KIT are conducted on closed and

(a) Scan setup using rubber bands for suspension. A LDV is used to measure surface velocities on the specimen.

(b) Shaker setup: a stinger in combination with a force transducer is used to apply an excitation to the specimen.
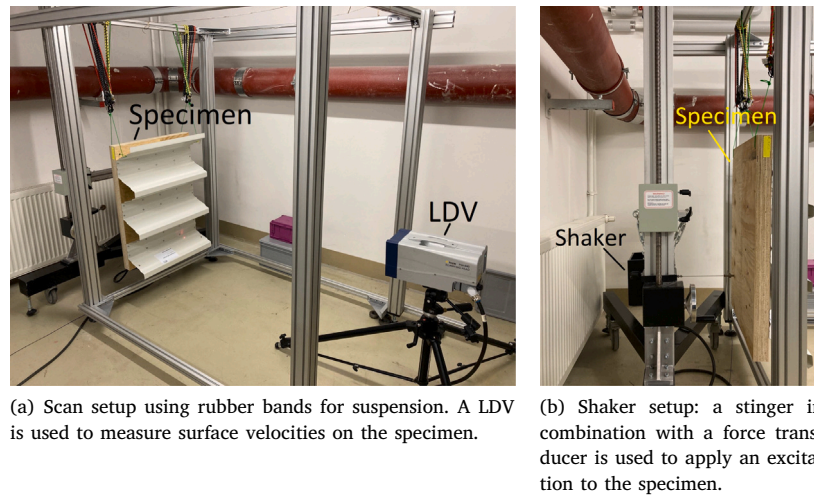
Fig. 2. Measurement configurations at TUM.

(a) Scan of upper chord for closed configurations via LDV. The suspension is realized using heavy-duty slings.

(b) Scan of lower chord for open configurations via LDV. The suspension is realized using heavy-duty slings.

(c) Shaker setup for lower or upper chord: a stinger in combination with a force transducer is used to apply an excitation on the specimen.
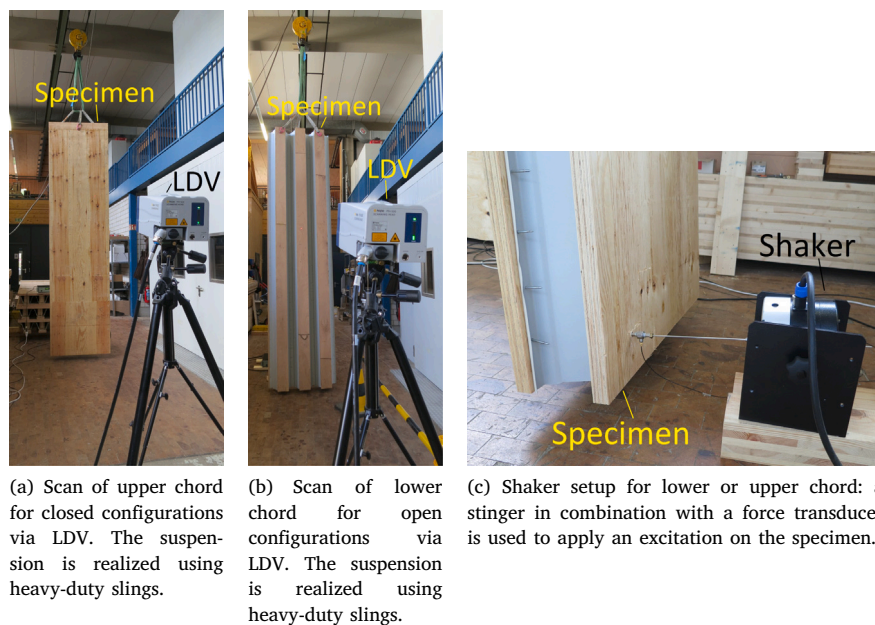
Fig. 3. Measurement configurations at KIT.

open structures. The groups consequently are *small, closed samples* (TUM), i.e., $V1b$, $V2b$, $V3b$, and $V4b$, *long, closed samples* (closed samples measured at KIT), $V7$ and $V8$, and *long, open samples* (open configurations measured at KIT), i.e., $V9$ and $V10$. A complete list of all configurations and the corresponding labeling is presented in the appendix (Table A.1).

2.3. Numerical simulation using finite element analysis

Within the scope of this work, a simulation model is built employing FE analysis. The following section discusses the FE model used to represent the steel–timber element.

2.3.1. Objectives

Experiments often account for the most work- and cost-intensive part of the design process of products and structures, e.g., cars and buildings. Therefore, simulation techniques such as the FE method are applied to reduce this effort by shifting first-stage developments into

the virtual environment. The response of different structural configurations is computed with little effort using a parametric simulation model since no test specimens and, consequently, no manufacturing is necessary. Furthermore, by means of a model, the proposed building element will be verified for application in commercial and residential buildings in the context of acoustics and vibrations in future studies.

2.3.2. Components

All FE simulations are conducted using the commercial software *ANSYS*.[3] by means of the intern programming language *Mechanical APDL* The simulation model has three essential components similar to the real structure: an upper chord built from an LVL plate, a steel frame in the middle, and a lower LVL chord. The wooden parts are modeled with hexahedral elements (SOLID186), for which orthotropic material properties are assumed. On the contrary, the steel frame is represented

---

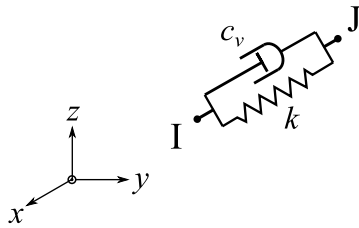[3] ANSYS, Inc., https://www.ansys.com

Fig. 4. Spring–damper element used to connect the translational DOFs of nodes related to joints [1].

by shell elements (SHELL281) with isotropic material properties. All elements use quadratic trial functions. For all components, a mesh size of approximately 0.03 m is used. For components that prohibit such mesh sizes due to smaller dimensions, the mesh size is adapted accordingly. This leads in the example of Section 3.2 to an overall number of DOFs of approximately 97,000.

As specified in the introduction (Section 1), different types of joint models exist in the literature. For simplicity, an element with a displacement-proportional spring and a velocity-proportional damper is implemented to represent the joint behavior within the FE model. See Yang and Park for deeper insight [26] into the model. At the positions of the screws or nails in the structure, the translational degrees of freedom (DOFs) of the timber plate and steel frame are connected by these spring–damper elements (COMBIN14 [1]) in all three directions, i.e., x-, y- and z-direction. A representative picture of the element is displayed in Fig. 4.

Exemplarily, a full FE model is provided for better understanding (Fig. 5).

The geometric dimensions of the structure remain fixed from the start corresponding to the measurement samples.

For the steel material properties, i.e., elasticity modulus, shear modulus, and density, values are given in [27]. Nevertheless, the stiffness and density differ from wood product to wood product, so non-identical material parameters are assumed for different products. Although manufacturers provide material properties to some extent, those are mainly valid for static analysis. Consequently, to analyze structural dynamics, material properties have to be deduced from the static properties for higher frequencies, or individual vibration measurements on the wooden components only have to be conducted.

In this study, two types of LVL, i.e., *Steico LVL X*[4] (NLVL) [28] and *Baubuche*[5] (BB) [29] are used. For NLVL, measurements on separate plates are performed to identify the properties listed in Table 2. Similar to the measurement setup in Section 2.2.2, experimental modal analysis is performed on suspended LVL plates to identify the modal parameters such as eigenfrequencies and mode shapes. By solving a subsequent inverse problem, the material properties of NLVL are calibrated. On the contrary, for BB (Table 3), the material properties are calibrated using the more complex assembly model described above. Furthermore, to the authors' best knowledge, appropriate parameters for the joint elements are missing in the literature and, therefore, are calibrated manually utilizing modal information derived from the measurements. For the example investigated in Section 3.2, the identified spring stiffnesses and damping constants in horizontal (x, y) (k_{hor}, c_{hor}) and vertical (z) (k_{ver}, c_{ver}) directions are also listed (Table 3).

Finally, time-harmonic analyses are conducted to validate the numerical model, consisting of joints, LVL plates, and steel parts, concerning the experiments. Therefore, the frequency range of interest is adapted in correspondence with the experiments, which is in the case

---

[4] Softwood LVL by STEICO SE, D-85622 Feldkirchen, Germany
[5] Hardwood LVL by Pollmeier Massivholz, D-99831 Amt Creuzburg, Germany

Table 2
Material properties of NLVL and steel.

Steel	Literature data [27]	
E	$2.1 \cdot 10^{11}$ N/m²	
v	0.3	
ρ	7850 kg/m³	
ζ	$1 \cdot 10^{-4}$	

NLVL	Manufacturer's data [28]	Fitted properties
E_x	$10.6 \cdot 10^9$	$11.9 \cdot 10^9$ N/m²
E_y	$2.5 \cdot 10^9$	$25.1 \cdot 10^8$ N/m²
E_z	–	$25.1 \cdot 10^8$ N/m²
G_{xy}	$1.5 \cdot 10^8$	$7.3 \cdot 10^8$ N/m²
G_{xz}	–	$6.9 \cdot 10^8$ N/m²
G_{yz}	–	$5.0 \cdot 10^7$ N/m²
v_{xy}	–	0.42
v_{xz}	–	0.42
v_{yz}	–	0.42
ρ	530	660 kg/m³
ζ	–	0.01

Table 3
Material properties of BB and joint parameters.

BB	Manufacturer's data [29]	Fitted properties
E_x	$12.8 \cdot 10^9$	$29.6 \cdot 10^{10}$ N/m²
E_y	$2.0 \cdot 10^9$	$28.1 \cdot 10^8$ N/m²
E_z	–	$40.2 \cdot 10^7$ N/m²
G_{xy}	$4.3 \cdot 10^8$	$62.1 \cdot 10^8$ N/m²
G_{xz}	–	$39.3 \cdot 10^8$ N/m²
G_{xy}	–	$28.1 \cdot 10^7$ N/m²
v_{xy}	–	0.42
v_{xz}	–	0.42
v_{yz}	–	0.42
ρ	800	820 kg/m³
ζ	–	0.01

Screws/nails	Fitted properties
Stiffness k_{hor}	$4.0 \cdot 10^6$ N/m
Stiffness k_{ver}	$4.5 \cdot 10^5$ N/m
Damping c_{hor}	750 N s/m
Damping c_{ver}	750 N s/m

of the example of Section 3.2 $f_{harmonic} = 10 - 310$ Hz. Here, a frequency resolution of $\Delta f = 1.0$ Hz is used. The boundary conditions are adapted to simulate the suspension in the measurements by using soft springs. Also, the loading is chosen according to the experiments.

3. Results

Results from experimental and numerical investigations are presented in the following.

3.1. Experimental results

First, the experimental results are described. Some of the mode shapes observed for measurements at TUM and KIT are plotted in Fig. 6 and Fig. 7, respectively.

In the case of Fig. 7, the plots are split into two parts since the measurements on the structure at KIT have to be done in two parts due to the size of the structure. The two parts are combined by the LDV's software via stitching. Still, a visual break remains in the plots.

Furthermore, modes of similar shapes appeared more often than once for some specimens, e.g., mode shape (0,2)* (see Table C.1, Table C.4 and Fig. 6). The assembly process can lead to inaccuracies in mounting conditions and uncertainties, e.g., concerning the symmetry of specimens. Moreover, not clearly identifiable mode shapes occur in the experimental modal analysis. Such an 'unclear' mode represents a mode shape that cannot be attributed to a comparable mode and is visualized in Fig. 6.
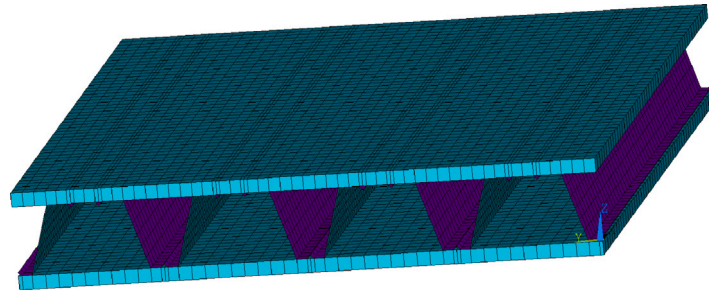
Fig. 5. Three-dimensional sketch of exemplary FE model of steel–timber structure.
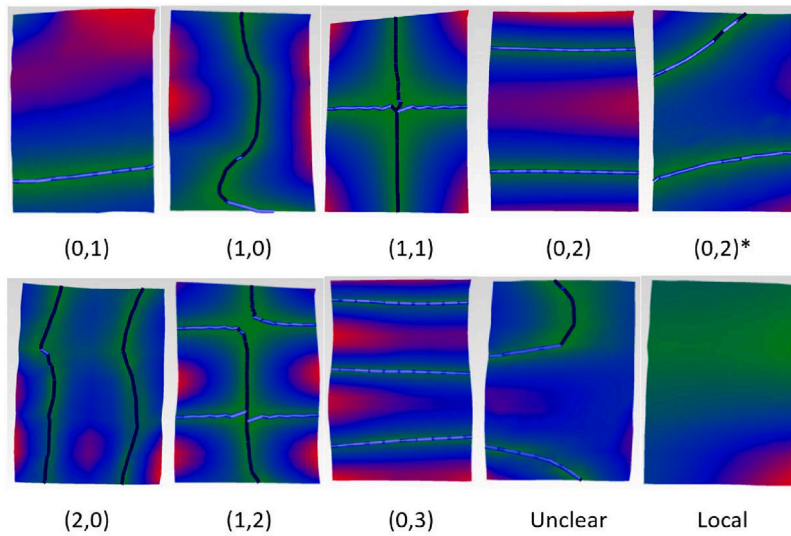

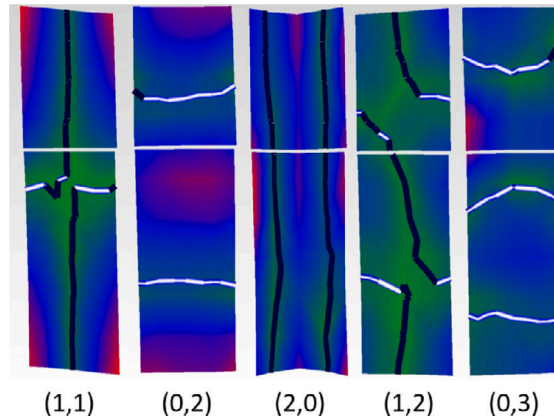**Fig. 6.** Exemplary mode shapes observed for measurements at TUM.

Fig. 7. Exemplary mode shapes observed for measurements at KIT.

Additionally, for two-component assemblies, local modes appear where only steel frame parts vibrate, and for three-component assemblies, when single corners move independently from the rest of the structure ('local' mode in Fig. 6). Also, due to the specimens' geometric properties, the top and bottom chords of the three-component assemblies, in some cases, vibrate separately, i.e., modes (0,1) and (1,0). For mode (0,1), the top LVL plate rotates independently of the lower chord around the lateral axis and, for mode (1,0), around the longitudinal axis (Fig. 6).

The experiments at TUM are conducted for four load levels (load factor (LF) 1 to 4) for investigations concerning amplitude-dependency.

The median value and standard deviation for the eigenfrequencies at the four load levels are calculated. The median instead of the mean is chosen to minimize the effect of outliers. Both statistical parameters are given in Table C.1 in Appendix C. Additionally, Table C.2 lists the median value and standard deviation of the loss factors identified for the assemblies. Last, Table C.4 summarizes the results obtained for the sine sweep measurements at TUM to investigate the contributions of higher-order harmonics.

At KIT, essentially the same experiments as at TUM are performed. The measurements help to identify eigenfrequencies, loss factors, and

higher harmonics in the structural response. Table C.3 lists the results for eigenfrequencies and loss factors, again considering median values and standard deviations, whereas Table C.5 summarizes the investigations for higher harmonics.

3.1.1. Comparison between assemblies

This section contrasts the results of samples of various configurations (refer to Table A.1 for the specimens' details). In this way, influences of several parameters, e.g., geometry, are identified. The following comparisons use the median values from Table C.1.

First of all, the investigation deals with the specimens' dynamic stiffness and modal mass effects by means of the identified eigenfrequencies. Furthermore, the damping behavior is analyzed by comparing identified loss factors. Nonetheless, uncertainties in identifying the above-mentioned characteristics exist, especially related to damping.

The following influential parameters are identified: steel thickness (comparison of $d_s = 0.75$ mm to $d_s = 1.25$ mm) together with fastener type (SBS1 to HS2 (two-component assembly — denoted by 'a' in Table A.1) and SBS1/BS1 to HS2/Re (three-component assembly — denoted by 'b' in Table A.1)), steel height ($h_s = 0.100$ m to $h_s = 0.155$ m) together with LVL plate thickness ($h_t = 0.045$ mm to $h_t = 0.055$ mm), LVL material type (BB to LVL), timber–steel joints (two-component assemblies to three-component assemblies), and open/closed configurations.

Higher eigenfrequencies result from stiffer specimens due to thicker steel sheets, higher steel frames, thicker LVL plates, or the transition from two-component assemblies to three-component assemblies. However, although the material type BB is stiffer in a static sense, comparing the two LVL types does not show increasing eigenfrequencies. The reason lies in the higher effective masses due to a higher density of BB as opposed to NLVL. Furthermore, other effects counteract the stiffening mentioned above. For the lateral bending mode of an open specimen, the effective added mass due to thicker steel is more prominent than the introduced effective stiffness. Moreover, the timber–steel joint, compared to the steel–timber joint (refer to Fig. 1 for the joint types), introduces less stiffness into the structure. Among others, this is seen by comparing two-component to three-component assemblies. Besides, for thicker steel sheets as well as higher steel frames together with thicker LVL plates, tight connections, i.e., tight timber–steel joints, become more complex. Thicker steel sheets are a possible reason since they resist more to a screw to be drilled through. Furthermore, thicker LVL plates foster uncertainties in the joint such as skewed screw angles. Additionally, higher steel frames show more flexibility. That is why the steel bends more under the tip of the screw to be drilled through. The resulting gap might remain after the finished manufacturing. Similar softening effects due to the timber–steel joint can also be observed by comparing open and closed cross-sections. Whereas the lateral bending mode shows increased eigenfrequencies for the closed setup, the eigenfrequency in the case of the first longitudinal bending mode decreases. The first fact results from the obviously less stiff lower chord in the open setup. However, the latter stems from the stiffer steel–timber joint used twice in the open configuration but only once together with a softer timber–steel joint in the closed configuration. Consequently, some influential parameters counteract the intuition that stiff structures, at first sight, lead to higher eigenfrequencies.

Concerning damping properties, larger contact areas result in higher damping in the specimen, whereas larger remaining gaps in a connection reduce the damping. Samples with thicker steel sheets thereby show higher damping since the steel is less bent around the fastener and, consequently, remains in place, which goes along with larger contact surfaces. Furthermore, samples with weaker timber–steel joints, such as higher steel frames and thicker LVL plates, contain larger remaining gaps, which results in less damping due to smaller contact surfaces. This is again supported by the comparison of open to closed setups. Higher damping occurs in the open cross-sections since the tighter steel–timber joint is used twice instead of once together with a timber–steel joint.

Figs. 8(a) and 8(b) show the deviation concerning the mean value for the eigenfrequencies and damping values for the measurements at TUM. Depicted are boxplots. For each mode, e.g., (1,1), the eigenfrequencies of all tested assemblies at load factor 1 are normalized by the mean value of those eigenfrequencies. From this, the boxplots are created showing the median value (red line), lower and upper quantile (lower and upper bound of the box), whiskers (lower and upper end of the black line), and outliers (black circles). For the cross-assembly comparison, the quantile values lie within the same range for all modes, except for mode (2,0), where it is smaller than for the other modes. However, the whiskers for modes (1,1) and (0,2) are the largest for the TUM assemblies, indicating more significant variability. For the loss factor, quantiles for modes (0,2), (1,2), and (0,3) reveal the largest value and lie within the same range. Nevertheless, mode (1,2) indicates the most considerable variability in damping since it shows the largest whiskers. So mode (1,2) seems to be quite sensitive to changes concerning damping, whereas mode (1,1) is primarily influenced in the case of the eigenfrequencies.

Fig. 9(a) illustrates the boxplot considering the eigenfrequencies of samples tested at KIT. Here, the lateral bending mode (2,0) shows by far the most significant variation. This phenomenon is logical since open and closed configurations are compared. The reduced stiffness in the lateral direction for open in contrast to the closed samples leads to significant differences in the eigenfrequencies.

Finally, Fig. 9(b) presents boxplots of the loss factors identified for the specimens measured at KIT. The damping values of mode shape (1,1) vary the most for the cross-assembly comparison. In this case, closed configurations lead to higher damping than the open samples due to the effects within the closed configurations' timber–steel joints. These phenomena are activated when the structure vibrates in mode shape (1,1). Further, more considerable differences occur for the modes (1,2) and (0,3), which coincides with the previous results.

Comparison with previously studied steel–timber-structures:

The eigenfrequencies determined in this study are compared with values from a reference article to evaluate the vibrational characteristics of the proposed elements. In Hassanieh et al. [2], the authors identify dynamic characteristics of steel–timber beams made of a CLT slab connected to an H-steel profile below by modal testing. They investigate 3 m long and 1 m wide beams. Since those dimensions match the ones from the specimens measured at KIT quite well, their results are used for comparison. However, in the reference study, the specimens have been simply supported in the test, whereas in this study, a free boundary condition is simulated by the suspension. Consequently, the mode shapes are not easily compared. However, the first torsional mode shapes and the first bending modes, which look alike, are contrasted in Table 4. In this table, *H1* to *H6* denote samples tested in Hassanieh et al. [2].

As can be seen, the herein proposed steel–timber element shows higher eigenfrequencies for all modes except for the second bending mode. Here, only *V10* can compete. Higher frequencies are advantageous since low natural frequencies of ceiling structures cause increased disturbance to residents. Furthermore, floor vibrations are critical in the lower frequency range around the first eigenfrequency concerning the serviceability criteria of floors. In this range, the proposed element performs much better.

3.1.2. Weakly nonlinear behavior — Amplitude-dependent stiffness and damping

Tables C.1 and C.2 depict the eigenfrequencies, respectively loss factors, for each assembly for all load levels by considering the standard deviations given. The standard deviation thereby shows the variations due to changes in excitation amplitude.

Hardly any differences in the eigenfrequencies are observed for varying load levels. All except for one eigenfrequency revealed a standard deviation of less than 1 Hz. Consequently, no amplitude-dependent stiffness could be identified.
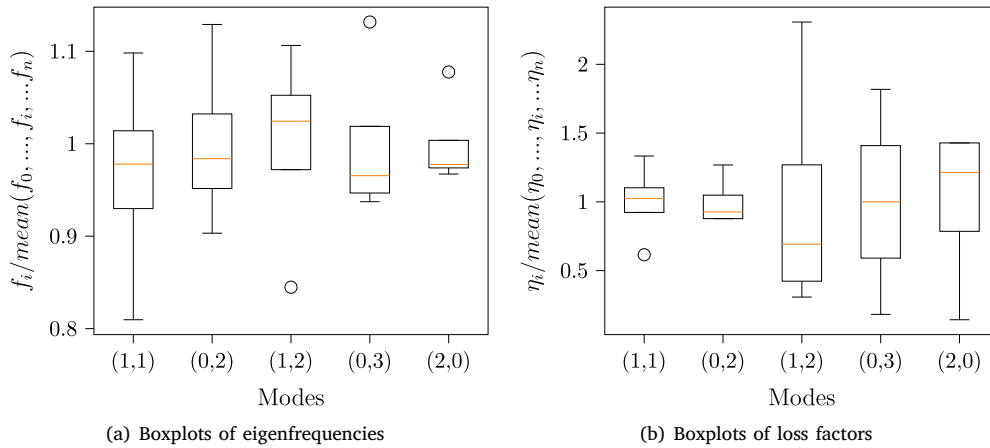
(a) Boxplots of eigenfrequencies

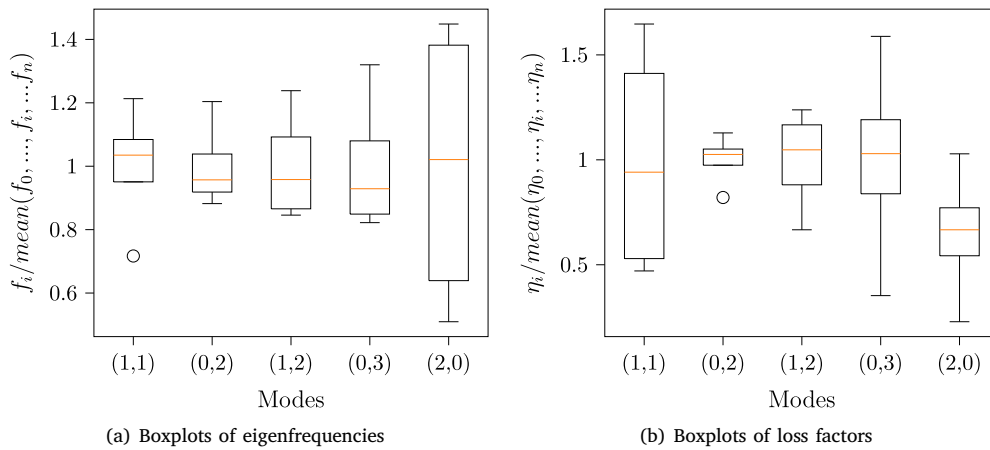(b) Boxplots of loss factors

Fig. 8. Cross-assembly comparison at observed modes of eigenfrequencies f_i and loss factors η_i for all specimens $i = 1, \ldots, n$ measured at TUM: values at load factor 1 f_i or η_i are normalized by the cross-assembly mean value $mean(f_0, \ldots, f_i, \ldots, f_n)$ or $mean(\eta_0, \ldots, \eta_i, \ldots, \eta_n)$.

(a) Boxplots of eigenfrequencies

(b) Boxplots of loss factors

Fig. 9. Cross-assembly comparison at observed modes of eigenfrequencies f_i and loss factors η_i for all specimens $i = 1, \ldots, n$ measured at KIT: values at load factor 1 f_i or η_i are normalized by the cross-assembly mean value $mean(f_0, \ldots, f_i, \ldots, f_n)$ or $mean(\eta_0, \ldots, \eta_i, \ldots, \eta_n)$.

Table 4
Eigenfrequencies [Hz] of specimens tested in Hassanieh et al. [2] (*H1* to *H6*) and tested at KIT (*V7* to *V10*) for selected modes.

Mode	H1	H2	H3	H4	H5	H6	V7	V8	V9	V10
1st torsion	10.5	10.6	10.2	6.7	6.8	–	57	48	34	49
2nd torsion	63.5	58.3	67.4	–	56.4	61.4	77	79	94	112
1st bending	24.2	24.7	24.7	17.2	21.4	24.5	71	64	67	87
2nd bending	–	114.4	107.3	86.6	100.5	102.6	88	85	–	136

On the contrary, more variations are visible for the loss factors. In the case of the loss factors, the ratio of standard deviation to median value is additionally computed to validate the differences across load levels relatively. Table C.2 also lists those ratios which are compared to the signal-to-noise ratio of the measurement. If the ratio due to variation of load amplitude exceeds the signal-to-noise ratio, it is marked in bold letters in the respective table. In this case, the differences are considered significant, indicating amplitude-dependent damping.

From these investigations, it becomes evident that the lower-order mode shapes, (1,1), (0,2), and (2,0), seem to initiate amplitude-dependency more often than the higher-order modes, (1,2) and (0,3). Local modes also often reveal amplitude-dependent loss factors, which might be due to locally high vibration amplitudes leading to nonlinearity.

Furthermore, samples with thinner steel sheets show more amplitude-dependent damping effects than their counterparts with thicker steel. Thinner steel sheets allow more local vibrational behavior due to less stiffness, leading to more complex behavior and consequently nonlinearity in the joints. Furthermore, it is noted that samples of an open cross-section, especially *V9* with the thinner steel, show more amplitude-dependent behavior than closed cross-sections. Consequently, open configurations also foster nonlinearity. The results further reveal that the fastener types BS1 and SBS1 induce more amplitude-dependency than Re and HS2. However, this tendency is not observed for the two-component assembly counterparts, which means the fastener type BS1 of the timber–steel joint and not SBS1 of the steel–timber joint initiates nonlinearity. The two-piece thread of Re might be the reason since it allows for a tighter connection and thus more contact area (see Table 1).

Joint damping mainly increases at sufficiently high load levels due to the initiation of micro-slip in the joints' interface. However, damping decreases again once the state of macro-slip is reached in the joints.

Table 5
Loss factors identified for exemplary modes for measurements at TUM and KIT.

Mode	Specimen	Load Factor (LF)	Frequency [Hz]	Loss factors [–]
(2,0)	V8	1	107.2	0.0047
		2		0.0054
		3		0.0059
(1,1)	V2a	1	137.9	0.0116
		2		0.0113
		3		0.0111
		4		0.0109
(2,0)	V3b	1	666.1	0.0013
		2		0.0010
		3		0.0050
		4		0.0050
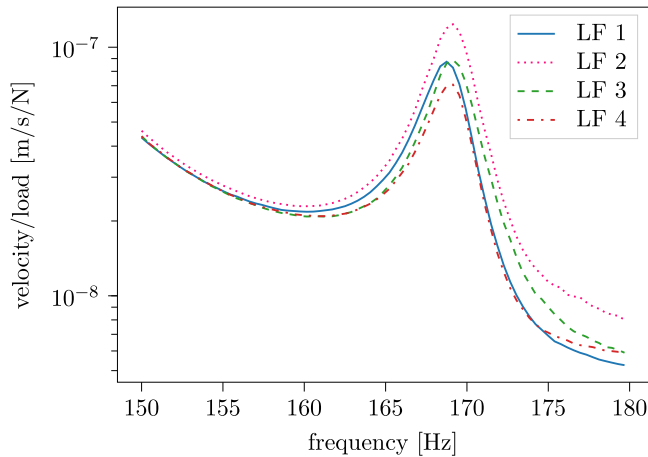
Fig. 10. FRF of *V2b* around resonance frequency 168 Hz at mode (0,2)*. Curves for four load levels are depicted (LF 1 to 4). Changes of resonance frequency and loss factors are observed.

About one-third of the observed modes show increased loss factors for increased load amplitudes, probably due to the initiation of micro-slip in the interface. Moreover, the loss factors reveal mixed tendencies with increasing load levels for almost half of the observed cases. Here, the complexity of the joint's interface conditions introduces behavior that cannot be interpreted easily. This effect is caused by joints getting stuck temporarily at some excitation amplitudes and being rereleased at higher load levels, resulting in further micro-slip. For the remaining modes, the damping values decrease. Again, joints get stuck or are at a state of macro-slip. However, macro-slip occurs only for high vibration amplitudes that are probably not reached in this study. Examples for all three cases are given in Table 5, i.e., increasing loss factors for mode (2,0) of *V8*, decreasing loss factors for mode (1,1) *V2a* and unclear tendencies for mode (2,0) *V3b*.

Slight changes in resonance frequencies and loss factors due to increased load amplitudes can also be visualized in the spatially averaged frequency response function (FRF). Fig. 10 plots the observed peak related to mode (0,2)* for specimen *V2b* in the frequency range 150 Hz to 180 Hz. No clear trend toward an increase or decrease is observed according to Table 5. The same unclear effect is also visible in the figure.

Fig. 11 again depicts boxplots. The standard deviation for one sample at all load levels for each mode is calculated as a data basis (given in Table C.2). Then, those standard deviations are collected for one mode across all assemblies and presented in a boxplot. Here, a high median value indicates larger susceptibility of a mode to amplitude-dependency in damping. For the measurements at TUM, modes (2,0), (0,3), and (1,2) show the highest median. On the contrary, for specimens measured at KIT, the loss factors gained for mode (1,1) differ the most due to excitation variation. Those observations correspond quite well with the ones from the cross-assembly comparison (Section 3.1.1).

The variations of the loss factor in the cross-assembly comparison are also the largest for modes (1,2), (0,3), and (2,0) at TUM and mode (1,1) at KIT. Consequently, those modes for the small samples at TUM and the larger ones at KIT are sensitive to geometric changes but also to nonlinear effects. All in all, an amplitude-dependent damping behavior is observable, especially for specific modes.

3.1.3. Strongly nonlinear behavior — higher harmonics

As described in Section 2.2.2, the system is excited by a swept sinusoidal loading to identify higher harmonics in the structure's response. The frequency range of excitation approximately covers the first three identified eigenfrequencies. The acquired time data is Fourier transformed and visualized in a spectrogram.

The abscissa and ordinate of the spectrogram represent time information and frequency content, respectively. In the case of linear structural behavior at low force levels (e.g., LF 1), the structure's response, e.g., in the spectrogram for LF 1 at scan point 7 of the sample *V2b* (see Fig. 12(a)), only shows contributions at the frequency of excitation. Since the frequency of excitation is swept from 120 Hz to 175 Hz, the peak of the structure's fundamental response also appears at those rising frequencies. Fig. 12(b) shows an exemplary spectrogram of the same sample *V2b* and scan point for LF 4. As can be seen, the most decisive contribution of the structure's response appears at the excitation frequency. However, also contributions at multiples of these fundamental frequencies, i.e., higher harmonics, are visible. Nevertheless, higher harmonics might also occur due to impurities of the input sine wave [30]. In Noël and Kerschen [30], those impurities are characterized by a difference in the higher harmonics' contributions to the maximum amplitude of less than 40 dB. Further, the detection of significant harmonics due to nonlinearity ranges from 20 to 40 dB difference compared to the maximum velocity amplitude. For 40 dB, a ratio of $r = 1/10^{40/20} = 1 \cdot 10^{-2}$ is computed. This ratio is taken as a minimum limit for the presence of higher-order harmonics in the following studies, i.e., medium-level nonlinearity. A level of 20 dB is used as a limit for stronger nonlinearity, i.e., high nonlinearity level, which corresponds to a ratio of $r = 1/10^{20/20} = 1 \cdot 10^{-1}$. Contributions of higher harmonics leading to a difference of more than 40 dB indicate low-level nonlinearity.

By means of the spectrograms (see Fig. 12(b) as an example) major contributions of higher harmonics are sought in the vicinity of structural resonances by visual inspection. For these cases, the frequency data of the spectrogram is plotted for the specific point in time (see Fig. 12(d) as an example). The peak velocities at fundamental and multiple higher frequencies are identified more easily in this plot. For the example of Fig. 12(d), the frequencies f_i respectively velocity magnitudes v_i for the peaks are $f_0 \approx 168$ Hz resp. $v_0 \approx 7.9 \cdot 10^{-5}$ m/s, $f_1 \approx 336$ Hz resp. $v_1 \approx 9.2 \cdot 10^{-6}$ m/s, $f_2 \approx 504$ Hz resp. $v_2 \approx 1.2 \cdot 10^{-5}$ m/s and $f_3 \approx 672$ Hz resp. $v_3 \approx 6.7 \cdot 10^{-7}$ m/s.

As a measure for nonlinearity, the fundamental peak amplitude v_0 of the structure's velocity is compared to the second highest peak $max(v_i)$ (i = 1,...,n, multiple peaks). The ratio of the amplitude peak values is calculated by $r_{ampl} = max(v_i)/v_0$ and compared to the differences described above of 20 dB and 40 dB. For the example of Figs. 12(b) and 12(d), one computes the ratio $r_{ampl} = 9.2 \cdot 10^{-6}/7.9 \cdot 10^{-5} = 1.2 \cdot 10^{-1} > 1 \cdot 10^{-1}$, which indicates a high level of nonlinearity for scan point 7.

In Fig. 12(c), the frequency spectrum of the same point in time as for Fig. 12(d) is plotted but for load factor 1 instead of 4. However, for lower loading, no significant higher harmonics are visible, only measurement noise. Consequently, the structure still behaves linearly for LF 1.

Since, for this example, the frequency 168 Hz approximately corresponds to mode (0,2)* according to Table C.1 and a high nonlinearity level is detected, a bold entry is added to Table C.4 for this mode shape. Table C.4 also lists the position and number of scan points revealing high or medium nonlinearity levels. Similarly, results for the measurements at KIT are summarized in Table C.5.
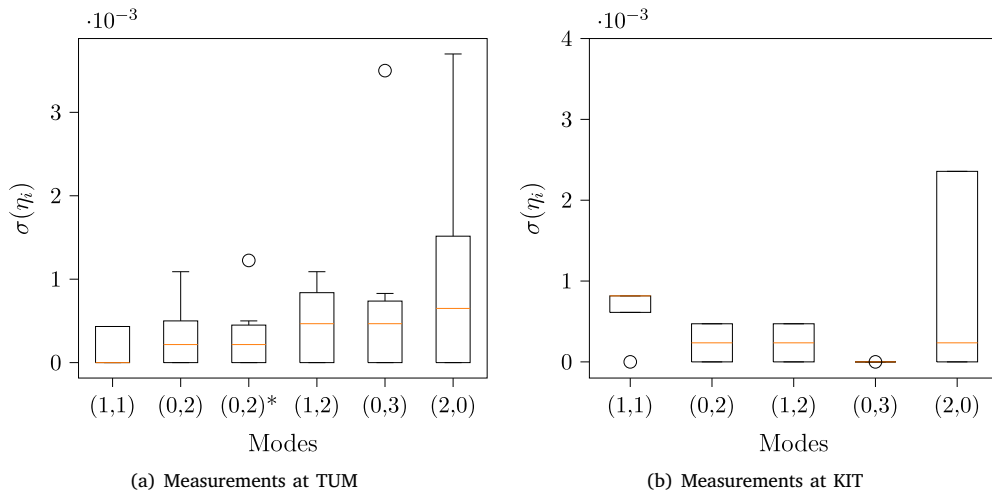
(a) Measurements at TUM

(b) Measurements at KIT

Fig. 11. Comparison of standard deviations of loss factors $\sigma(\eta_i)$ due to load variation (LF 1 to 4) in boxplots.

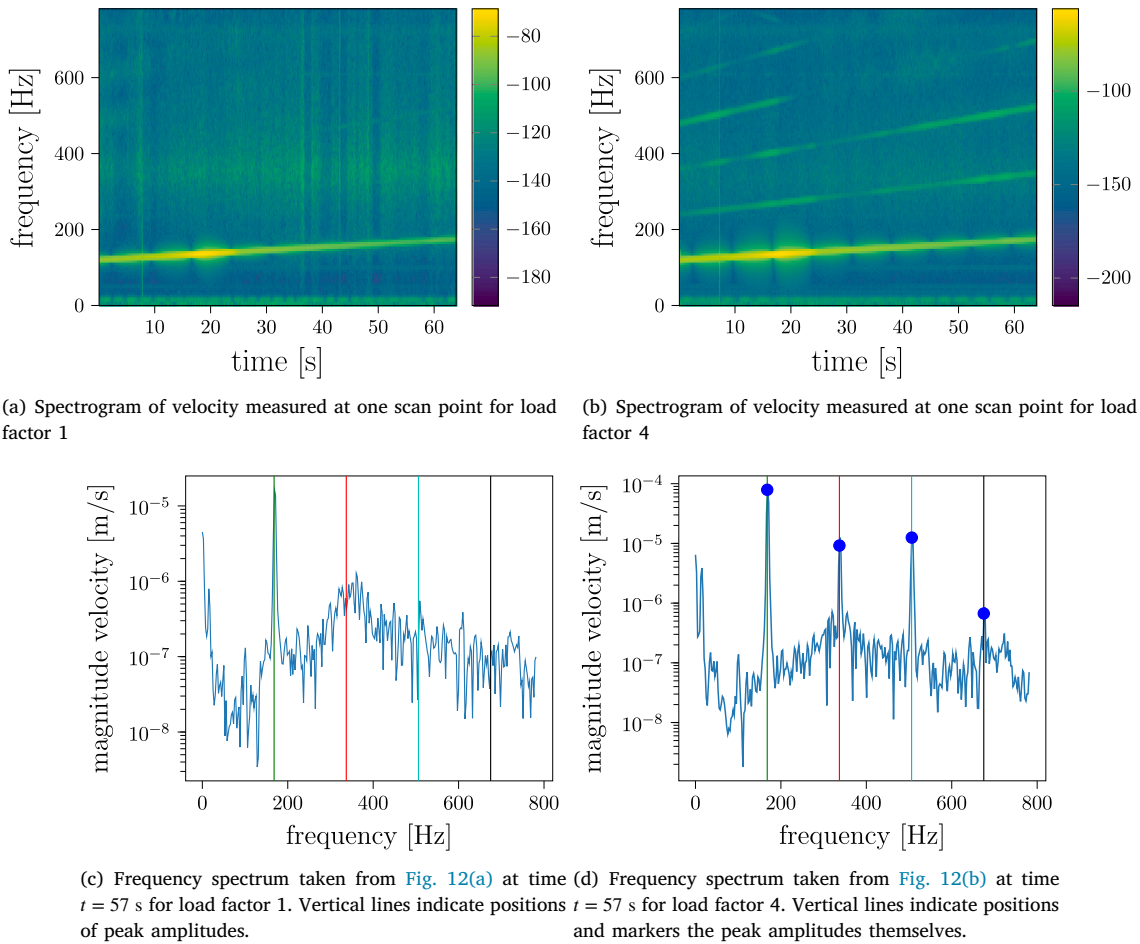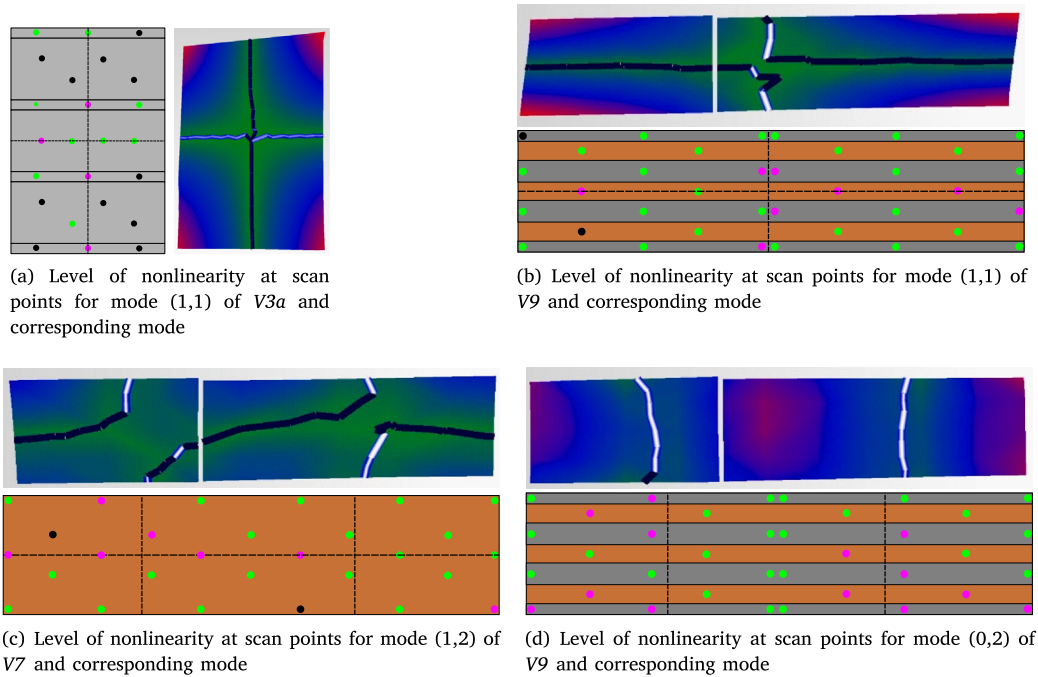(a) Spectrogram of velocity measured at one scan point for load factor 1

(b) Spectrogram of velocity measured at one scan point for load factor 4

(c) Frequency spectrum taken from Fig. 12(a) at time $t = 57$ s for load factor 1. Vertical lines indicate positions of peak amplitudes.

(d) Frequency spectrum taken from Fig. 12(b) at time $t = 57$ s for load factor 4. Vertical lines indicate positions and markers the peak amplitudes themselves.

Fig. 12. Identification of higher harmonics for a measurement on specimen *V2b* for sine-sweep excitation from 120 Hz to 175 Hz: The load levels LF 1 (12(a), 12(c)) and LF 4 (12(b), 12(d)) are depicted. The acquired velocity time data is Fourier transformed and visualized in spectrograms (12(a), 12(b)). Spectrogram levels are given in dB (ref. 0 dB = 1 m/s). At $t = 50$ s the frequency spectrum is plotted to visualize higher harmonics' contributions (12(c), 12(d)).

For the experiments performed at TUM, two-component specimens with high steel frames show the most locations with high nonlinearity levels for most observed mode shapes. The high steel frame that is only fixed at the lower chord is free to vibrate at the upper steel chord. This leads to higher vibration amplitudes and, therefore, more nonlinear behavior. For the three-component assemblies at TUM, the specimens using the fastener type BS1 and SBS1 show noticeable nonlinear behavior, probably due to tighter contacts and, consequently, more friction in the joints. Moreover, the sample tested at KIT with an open cross-section and thin steel sheets shows substantial contributions of higher

(a) Level of nonlinearity at scan points for mode (1,1) of *V3a* and corresponding mode

(b) Level of nonlinearity at scan points for mode (1,1) of *V9* and corresponding mode

(c) Level of nonlinearity at scan points for mode (1,2) of *V7* and corresponding mode

(d) Level of nonlinearity at scan points for mode (0,2) of *V9* and corresponding mode

Fig. 13. Examples of scan points with low (black markers), medium (green markers), and high (pink markers) levels of nonlinearity. Scan points with high nonlinearity levels lie close to the nodal lines (dashed lines in plots). (For interpretation of the references to color in this figure legend, the reader is referred to the web version of this article.)

harmonics at most observed modes at most locations for the measurements. The nonlinear effects seem reasonable for this specimen since the open configuration combined with the thin steel frame does not suppress a larger movement of the separate lower wooden chords. The timber boards can vibrate more freely, fostering nonlinear behavior.

Considering the two tables, Tables C.4 and C.5, the results reveal that contributions of higher harmonics appeared for all observed modes. However, they appear more often or stronger for some samples and modes. Further, it is noted that the scan points where higher harmonics were measured often are located close to nodal lines of a mode shape, especially for mode (1,1). Figs. 13(a) and 13(b) visualize the locations where a low, medium, and high level of nonlinearity was detected for mode (1,1) for *V3a* and *V9*, respectively. Although the translational displacements close to nodal lines are small, the rotational deformations are larger. This might be why the structures behave more nonlinearly close to nodal lines. Similar phenomena are observed in Figs. 13(c) and 13(d) for mode shape (1,2) and mode (0,2) of *V7*.

Also, the local or unclear modes often show a higher level of nonlinearity. Due to inherent nonlinear behavior such as frictional effects, modes might be hard to identify clearly, which explains the more significant contributions of higher harmonics at those modes. For the local modes, small parts of the samples vibrate strongly, e.g., the upper chords of the sample *V1b*, leading to nonlinearity in the specimen's response.

Further, within this study, amplitude-dependency at modes is often related to significant contributions of higher harmonics at that same mode. An example is given in the following and shown in Fig. 10, 12(b), and 12(d). Fig. 10 depicts the FRFs at the four load levels. Differences in damping for varying excitation amplitudes are visible in the plot close to the resonance frequency of approximately 168 Hz. Contributions to the structural response apart from the frequency, where it was excited, are observed, looking at the spectrogram in Fig. 12(b). The frequency of $f_e = 168$ Hz is excited approximately at $t = 50$ s. Fig. 12(d) plots the velocity data at $t = 50$ s over the frequency. Here, responses at multiples of f_e, i.e., $f_{r,1} = 336$ Hz and $f_{r,2} = 504$ Hz, are also noticeable.

Exemplarily, similar results are also observed for mode (1,1) of *V7*. Here, the FRFs (see Fig. 14(a)) show some amplitude-dependency for

the resonance at approximately 57 Hz. This frequency is excited in the sine-sweep measurements at $t = 8$ s. For this point in time, contributions of higher harmonics are visible in the spectrogram (see Fig. 14(b)). The frequency spectrum at $t = 8$ s is visualized in Fig. 14(c) and supports the previous assumptions of the occurrence of significant higher-order harmonics. Nevertheless, a peak close to 0 Hz appears in the spectrum due to the measurements being slightly noisy in the lower frequencies.

In addition to the sole occurrence of higher harmonics, the effect of modal interaction is also seen for some of the specimen. For the mode (0,2)* of *V2b* at $f_0 \cong 168$ Hz, larger contributions of higher harmonics are identified above for the frequencies $f_1 \cong 336$ Hz, $f_2 \cong 504$ Hz and $f_3 \cong 672$ Hz (see Fig. 12). Interestingly, at or close to those frequencies, eigenfrequencies of *V2b* occur, i.e., at $f_{r,1} \cong 337$ Hz, $f_{r,2} \cong 500$ Hz and $f_{r,3} \cong 653$ Hz. However, the mode shapes related to those frequencies are not very clear (Fig. 15). This is why they are not mentioned in Table C.1. Since those modes are activated strongly by an excitation at the resonance frequency of $f_0 \cong 168$ Hz, nonlinear modal interaction for commensurate resonances is indicated.

In addition, uncertainties in the manufacturing process, such as slightly different drilling angles or arrangement of the components relative to each other, are inevitable. However, the test specimens at TUM and KIT were assembled by different people with different professional backgrounds, and nonetheless, friction effects occurred in samples at both test rigs. The influence of manufacturing is therefore still relevant, but not such that it can completely suppress friction effects. As previously observed, friction has an effect on the structural vibrations, but, at the same time, these effects can decrease over time due to loading cycles. Therefore, further long-term investigations dealing with the time-evolving influence of loading and unloading cycles on the friction between components should be conducted in the future but are outside the scope of this work.

3.2. Numerical results

As mentioned in Section 2.3.2, the created FE model will be used in future studies for parametric and acoustic investigations.
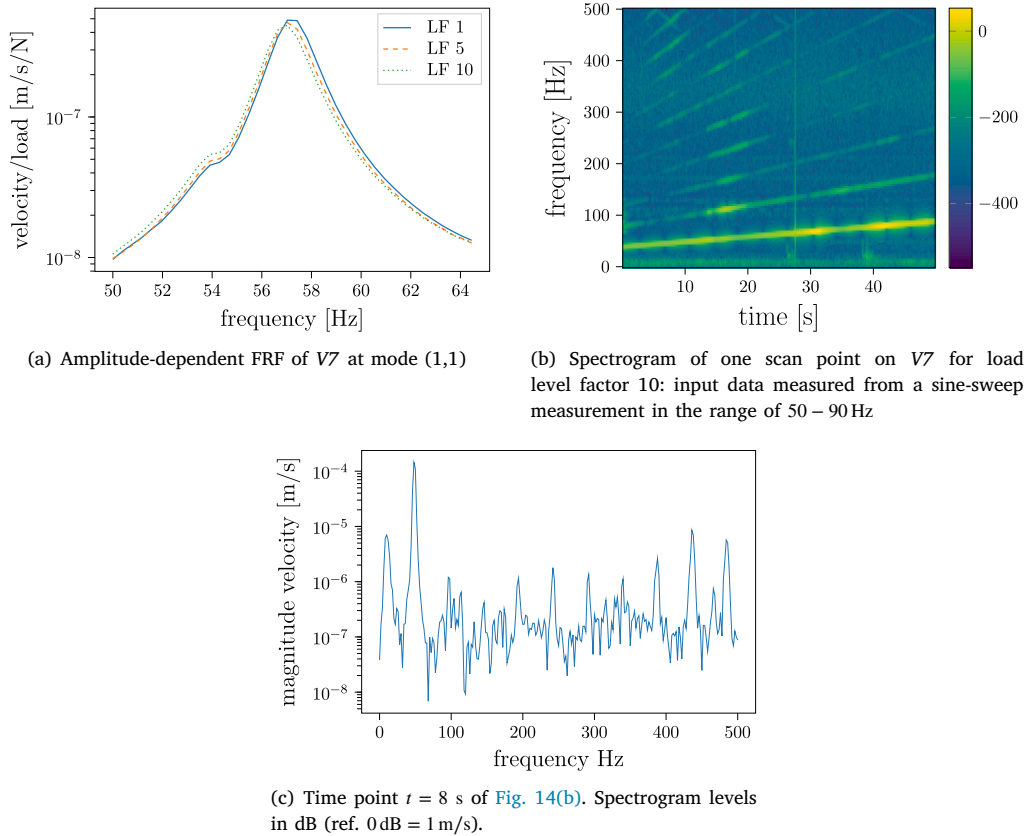
(a) Amplitude-dependent FRF of *V7* at mode (1,1)

(b) Spectrogram of one scan point on *V7* for load level factor 10: input data measured from a sine-sweep measurement in the range of $50 - 90$ Hz

(c) Time point $t = 8$ s of Fig. 14(b). Spectrogram levels in dB (ref. 0 dB $= 1$ m/s).

Fig. 14. Relation between amplitude-dependent FRF and occurrence of higher-order harmonics: Slight amplitude-dependency is visible in 14(a) for $f = 57$ Hz. At this frequency, higher harmonics are observable in the spectrogram 14(b). The frequency spectrum at this point in time of the sweep supports this observation.

(a) $f_{r,1} \approx 337$ Hz

(b) $f_{r,2} \approx 500$ Hz

(c) $f_{r,3} \approx 653$ Hz
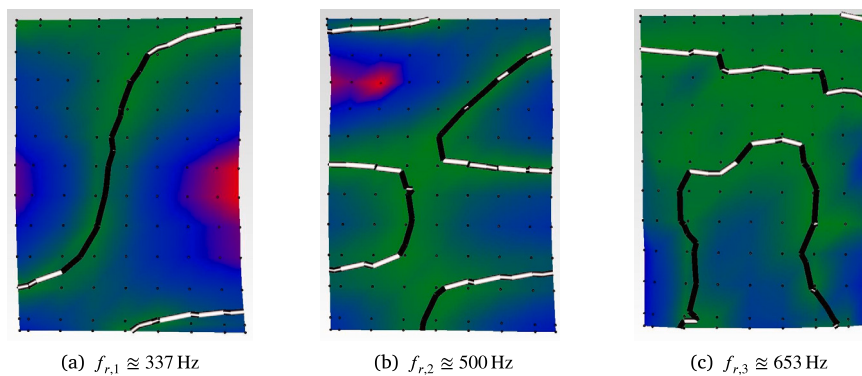
Fig. 15. Modes of *V2b* are found at multiples of the eigenfrequency $f_0 \approx 168$ Hz for mode (0,2)*. For those multiple frequencies large contributions of higher harmonics are found in Fig. 12. Nonlinear modal interaction is indicated.

The validation of the simulation model is described in the following. The comparison of measurements and simulations used harmonic analysis in ANSYS. Herein, the frequency range of observation ($f_{obs} = 10$ Hz ... 310 Hz), loading position (lower right corner), and boundary conditions (free) are adapted according to the conditions in the measurements. Experimental tests conducted at KIT serve as the basis for the validation. Since a free-free boundary condition is the goal of the hanging configuration but is difficult to achieve as an ideal in the experiments, springs are attached to the FE model. As stated in Section 2.3, the material properties of the wooden components, as well as the parameters for the joints' simulation model, had to be identified to generate a suitable model. Due to the structure's complexity, a perfect fit of measurement and FE simulation data is hardly possible.

Hence, the goal is to match the eigenfrequency of the mode (1,1) and the peak amplitude of spatially averaged FRF data at this frequency. Furthermore, the sound power level generated by the vibrating floor elements is compared. The sound power level is calculated based on the velocities measured or computed on the structure's surface away from the load employing the Rayleigh integral [31,32]. Although the Rayleigh integral assumes baffled boundaries, it is deemed appropriate here for a comparison. Similar studies were also conducted by Sharma et al. [33] using sound power levels and baffled supports.

Further details on the simulations, such as material properties used and the application of the Rayleigh integral, are given in Appendix B.

Figs. 16(a) and 16(b) depict the spatially averaged FRF and sound power level data for the measurement and simulation of *V9*. The
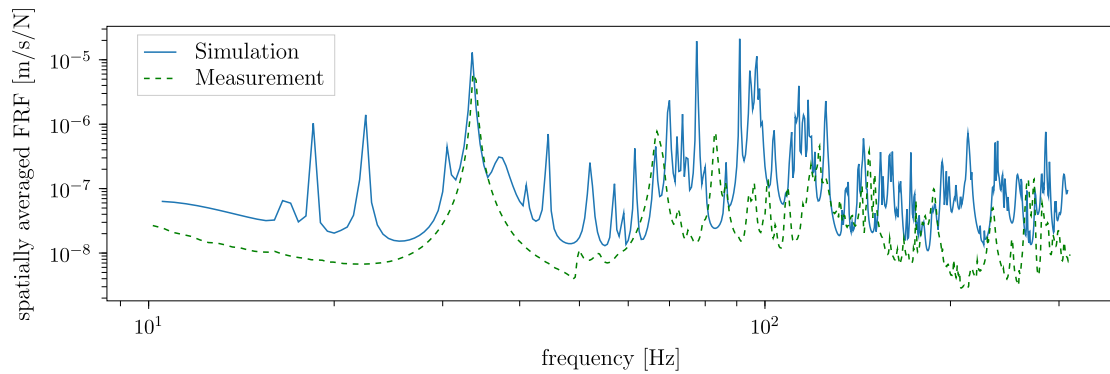
(a) Spatially averaged FRFs: data from FE simulation and measurement is compared.
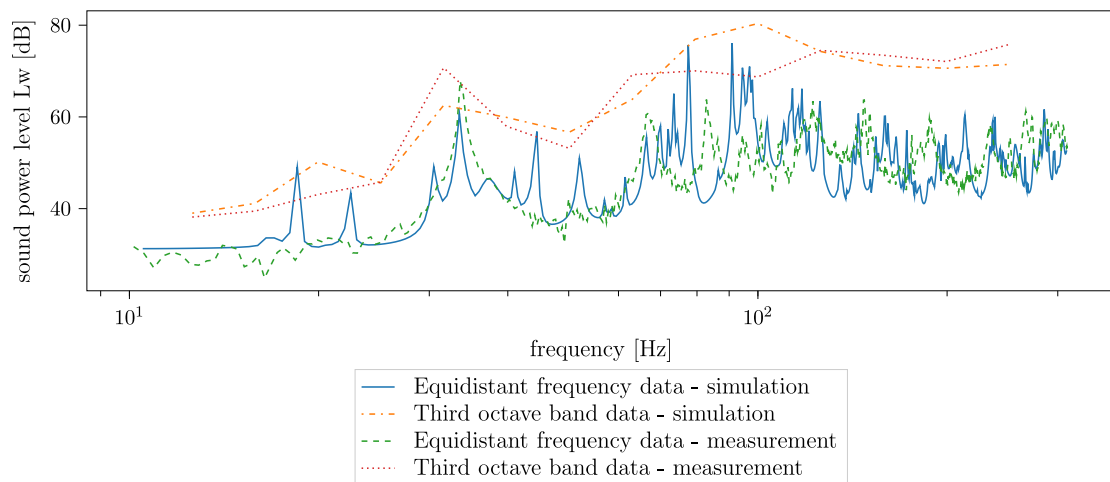
(b) Sound power levels: data from FE simulation and measurement is compared. Equidistant frequency and third octave band data is plotted for comparison.

Fig. 16. Validation of FE simulation with measurements at specimen *V9* by means of spatially averaged FRFs (see Fig. 16(a)) and sound power levels (see Fig. 16(b)).

eigenfrequency for (1,1) is located at approximately $f_{(1,1)} = 34\,\text{Hz}$ for the sample. As can be seen, the fit of spatially averaged data (Fig. 16(a)) looks quite good around this frequency. Two peaks appear below $f_{(1,1)}$ for the simulation but not for the measurement. However, they are about one order of magnitude smaller in amplitude. Those lower peaks represent local vibrations of the lower chords of the specimen, which do not show up in the measurements, probably due to higher damping. Additional higher peaks are visible at about 100 Hz, but the modal density is already quite high at these frequencies, making a good fit difficult. The sound power level depicted in Fig. 16(b) reveals deviations between measurement and simulation at similar frequencies as the spatially averaged case. Furthermore, third-octave band data, computed from the equidistant frequency data, show similar differences in Fig. 16(b). However, the numerical model meets the overall trend well.

The conclusions described above (Section 3.1) from the experimental results reveal the influence of higher harmonics on the structure's response. On the contrary, amplitude-dependency seems not as crucial since only slight amplitude-dependent damping occurs. Furthermore, the numerical validation shows good agreement between the linear simulation model and the measurement results, especially around the eigenfrequency of the mode (1,1). Consequently, a linear FE model is adequate for the investigated structure as a first estimate, although nonlinear behavior exists to some extent.

4. Conclusion and outlook

The comparison of assemblies of various configurations shows the expected influence of geometrical parameters, such as the thickness of components. Positive, increasing effects on the first natural frequency of the system would be desirable since it is the critical frequency that is considered for the serviceability criteria of floor vibrations. Assemblies with thicker steel sheets often lead to higher eigenfrequencies and loss factors. Thicker steel frames are less deflected during vibration and therefore stay in contact with the timber plate, which causes frictional effects and thus damping. Thicker timber plates also increase eigenfrequencies. However, the manufacturing uncertainties accumulate as well in this case. Furthermore, other influential parameters such as the type of fastener are also essential since they can reverse the stiffening effects due to softer connections. The two types of cross-sections, i.e., with a one-component lower chord (closed configuration) or with a split lower chord (open configuration), lead to significant differences for modes (2,0) and (1,1). Those are the lowest two and, therefore, most relevant modes. Consequently, the choice of an open configuration has to be made carefully, always considering the lowest natural frequency of the floor.

A comparison with already existing and analyzed steel–timber elements shows better performance of the proposed structure concerning the serviceability aspect. The observed larger eigenfrequencies are beneficial since low-frequency vibrations tend to be rated as unpleasant by humans.

The damping behavior is also influenced by geometrical parameters but mainly by the fastener type and tightness of joints. Unfortunately, the prediction of damping in a structure is complex, introducing uncertainties.

Observations concerning nonlinearity basically show the occurrence of higher harmonics in the responses since no amplitude-dependent stiffness, and only slight amplitude-dependent damping are discovered. Amplitude-dependent damping occurs once the forces in the structure become sufficient to induce micro-slip in the joints. Higher harmonics are often detected close to nodal lines where rotational deformations are high. Additionally, samples of softer configurations such as high steel frames for two-component assemblies and thin steel sheets for open configurations lead to more contributions of higher harmonics. Hence, considering nonlinearities is a crucial aspect that should be investigated in future studies on steel–timber composite structures.

However, since the fitted FE simulation model coincides well with the measured response, the linear FE model seems adequate as a first approach. A more complex model considering nonlinearity including higher harmonics, e.g., using the Harmonic Balance Method [34,35], can be adapted in future work. Moreover, the current model is only fitted manually, so the next step would be to identify an optimization problem to find more accurate parameters for the model. With this model, sound insulation properties can be determined in future studies.

CRediT authorship contribution statement

B. Chocholaty: Conceptualization, Methodology, Software, Data curation, Validation, Formal analysis, Visualization, Writing – original draft, Writing – review & editing. **N.B. Roozen:** Conceptualization, Methodology, Validation, Writing – review, Supervision. **M. Maeder:** Data curation, Writing – review & editing, Supervision. **S. Marburg:** Funding acquisition, Resources, Supervision, Writing – review.

Declaration of competing interest

The authors declare that they have no known competing financial interests or personal relationships that could have appeared to influence the work reported in this paper.

Data availability

Data will be made available on request.

Acknowledgments

Funding

Appendix A. Properties of test samples

The following table (Table A.1) lists the properties of specimens tested at TUM and KIT considering geometry, materials, fasteners, and configuration type.

Appendix B. Simulation model

Supplementary information on the Rayleigh Integral computation:

In Section 3.2, the sound power level was calculated using the Rayleigh integral. However, a further calculation step was necessary in the case of open configurations. Here, the requirement of a planar radiating surface is not fulfilled. Therefore, the velocity data of the lower side of the upper chord (marked in blue in Fig. B.17) was first moved virtually to the lower side of the lower chord (marked in green in Fig. B.17). Consequently, the phase of the signal was shifted by:

$$\phi_{add} = \frac{2\pi \Delta z}{\lambda} \tag{B.1}$$

with $\lambda = c_{air}/f_{excit}$ the wavelength, c_{air} the wave velocity of air, f_{excit} the excitation frequency, and Δz being the difference between the position on the lower side of the upper chord and the lower side of the lower chord (Fig. B.17). The amplitude of the signal was not modified.

Appendix C. Statistic evaluation

The following tables, Table C.1, Table C.2, and Table C.3, list the median and standard deviation computed from eigenfrequencies and loss factors for the measurements at TUM and KIT at varying load levels.

Furthermore, a criterion is established to distinguish between changes in loss factors due to measurement uncertainties and changes due to nonlinearity. The signal-to-noise ratio is computed from the measured coherence of a specimen in the frequency range of a mode. In the next step, the signal-to-noise ratio is compared to the ratio of the standard deviation to the median given in Table C.2. If the ratio due to load variation is larger than the signal-to-noise ratio, the values of the ratio are marked with bold letters in the corresponding entry of Table C.2. This procedure shows that the measurement uncertainties were too large for some modes so that no certain assumption is made concerning the amplitude-dependency. An example is the mode (0,2) of *V4a*. Here, the signal-to-noise ratio at load level 3 was $snr_{LF3,V4a,(0,2)} = 42.2\%$. At the same time, the loss factor at LF 3 $\eta_{LF3,V4a,(0,2)} = 0.0021$ caused the larger standard deviation $\eta_{std} = 0.0005$ compared to the median value of $\eta_{median} = 0.0030$. Consequently, the computed ratio concerning load variation represents no significant amplitude-dependency for this mode shape. Furthermore, a standard deviation to median ratio concerning the loss factor of less than 1% was considered negligible and will not be considered any further.

Tables C.4 and C.5 list results concerning the occurrence of higher harmonics. The procedure explained in Section 3.1 uses velocity data presented in a spectrogram. The plots of frequency content at specific points in time (e.g., Fig. 12(d)) serve as a basis for the following definitions.

As a measure of nonlinearity, the fundamental peak amplitude v_0 of the structure's velocity at a specific point in time is compared to the second highest peak $max(v_i)$ (i = 1,...,n, multiple peaks). The ratio of the amplitude peak values is calculated by $r_{ampl} = max(v_i)/v_0$ and compared to the differences of 20 dB and 40 dB described in Section 3.1. If the ratio is smaller than $r_{limit} = 1 \cdot 10^{-2}$ (corresponding to a difference of more than 40 dB), no or a low nonlinearity level is assumed, and no entry is added to Table C.4. This limit coincides with the observations from [30], as stated before. For a high level of nonlinearity, the ratio should be $r_{ampl} > 1 \cdot 10^{-1}$ (corresponding to a difference of less than 20 dB). In the table, this is highlighted by bold letters. A medium nonlinearity level is reached for $1 \cdot 10^{-2} < r_{ampl} < 1 \cdot 10^{-1}$. In this case, the entry in the table uses non-bold letters. The label *no data* is added to the table if no data is observed for the specified mode. This is the case

Table A.1

Test samples at TUM (V1a to V4b) and KIT (V7 to V9). Parameters: length l, width b, and thickness h_T of test specimen, material of timber plates m_t as Nadel-LVL X (NLVL) or Baubuche Typ Q (BB), thickness d_S and height h_S of steel frame, configuration type c_t, fastener type — lower l_{ft} & upper connection f_{st}.

Sample	l [m]	b [m]	h_T [m]	m_t	d_S [m]	h_S [m]	c_t	u_{ft}	l_{ft}
V1a	0.6	0.825	0.045	NLVL	$0.75 \cdot 10^{-3}$	0.100	closed	–	SBS1
V2a	0.6	0.825	0.045	NLVL	$1.25 \cdot 10^{-3}$	0.100	closed	–	HS2
V3a	0.6	0.840	0.055	NLVL	$0.75 \cdot 10^{-3}$	0.155	closed	–	HS2
V4a	0.6	0.840	0.055	NLVL	$1.25 \cdot 10^{-3}$	0.155	closed	–	SBS1
V1b	0.6	0.825	0.045	NLVL	$0.75 \cdot 10^{-3}$	0.100	closed	BS1	SBS1
V2b	0.6	0.825	0.045	NLVL	$1.25 \cdot 10^{-3}$	0.100	closed	Re	HS2
V3b	0.6	0.840	0.055	NLVL	$0.75 \cdot 10^{-3}$	0.155	closed	Re	HS2
V4b	0.6	0.840	0.055	NLVL	$1.25 \cdot 10^{-3}$	0.155	closed	BS1	SBS1
V7	3.5	0.900	0.039	NLVL	$0.75 \cdot 10^{-3}$	0.155	closed	Re*	StNa
V8	3.5	0.900	0.040	BB	$0.75 \cdot 10^{-3}$	0.155	closed	Re*	StNa
V9	3.5	0.900	0.040	BB	$0.75 \cdot 10^{-3}$	0.155	open	StNa	StNa
V10	3.5	0.900	0.040	BB	$1.25 \cdot 10^{-3}$	0.155	open	StNa	StNa
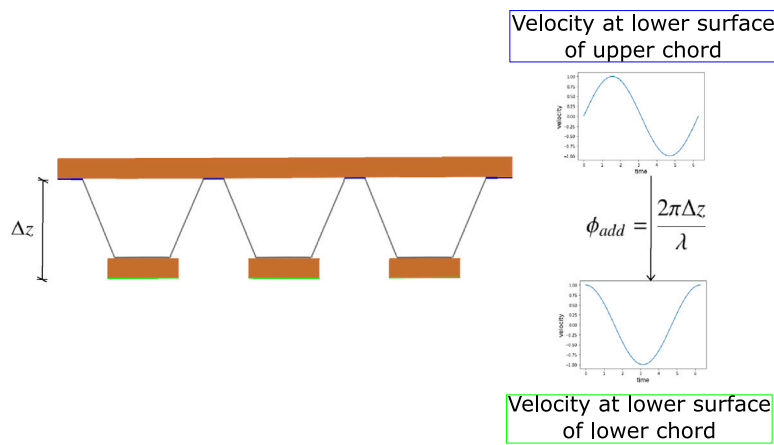
Fig. B.17. Phase shift added to surface velocities computed at lower surface of upper chord.. (For interpretation of the references to color in this figure legend, the reader is referred to the web version of this article.)

Table C.1

Eigenfrequencies [Hz] of test samples (for details, refer to Table A.1) for observed modes for four load factors (LF)—median values $\tilde{f}$ and standard deviations σ.

Mode	V1a	V2a	V3a	V4a	V1b	V2b	V3b	V4b
1,1	108.5 ± 0.02	137.9 ± 0.04	125.3 ± 0.15	144.4 ± 0.85	122.8 ± 0.10	137.1 ± 0.03	100.9 ± 0.04	120.7 ± 0.05
0,2	134.6 ± 0.06	126.2 ± 0.31	166.6 ± 0.57	175.4 ± 0.14	150.0 ± 0.07	140.3 ± 0.05	174.6 ± 0.16	155.5 ± 0.05
0,2*	*no data*	161.1 ± 0.44	*no data*	150.9 ± 0.31	196.9 ± 0.14	169.3 ± 0.19	*no data*	204.2 ± 0.03
1,2	173.3 ± 0.56	194.5 ± 0.11	329.4 ± 0.27	285.7 ± 0.20	352.8 ± 0.47	360.5 ± 0.16	293.6 ± 0.01	384.8 ± 0.23
0,3	297.7 ± 0.35	296.6 ± 0.14	178.8 ± 0.28	273.9 ± 0.07	298.7 ± 0.09	303.4 ± 0.14	312.8 ± 0.12	361.0 ± 0.26
2,0	*no data*	*no data*	*no data*	*no data*	663.2 ± 0.41	731.8 ± 0.42	666.1 ± 0.56	657.5 ± 0.44
0,1	*no data*	*no data*	*no data*	*no data*	184.2 ± 0.02	*no data*	111.7 ± 0.03	*no data*
1,0	*no data*	*no data*	*no data*	*no data*	*no data*	*no data*	131.1 ± 0.01	181.4 ± 0.06
Local/unclear	*no data*	178.8 ± 0.03	156.1 ± 0.07	117.8 ± 0.05	207.9 ± 0.03	*no data*	*no data*	111.3 ± 0.04

if this mode is not excited within the observed frequency range. The number and locations of nonlinearity and its level are also investigated. The term *irregular locations* means that nonlinearity is present at some points but not many positions on the structure. *Many locations* means more than half of the observed positions indicate nonlinear behavior, whereas, for *most locations*, this applied to all locations except for a small number. In the case of the label *concentrated locations*, all observation points in a limited region vibrate nonlinearly.

Table C.2

Loss factor [–] of test samples (for details refer to Table A.1) for observed modes for four load levels — measurements at TUM: median values $\tilde{\eta}$ and standard deviations σ are given. $\tilde{\eta} \pm \sigma$. The ratio of standard deviation to median value is listed in [%]. Ratios larger than the signal-to-noise ratio are marked with bold letters.

Mode	V1a	V2a	V3a	V4a	V1b	V2b	V3b	V4b
1,1	0.0072 ± 0.0008 **11.6**	0.0112 ± 0.0003 **2.4**	0.0088 ± 0.0001 **1.5**	0.0104 ± 0.0003 **3.1**	0.0108 ± 0.0001 0.5	0.0102 ± 0.0000 0.2	0.0061 ± 0.0000 0.7	0.0133 ± 0.0032 **24.2**
0,2	0.0058 ± 0.0006 **11.1**	0.0104 ± 0.0001 0.7	0.0035 ± 0.0000 **1.2**	0.0030 ± 0.0005 17.4	0.0104 ± 0.0000 0.1	0.0088 ± 0.0001 1.4	0.0094 ± 0.0006 **5.9**	0.0134 ± 0.0007 3.9
0,2*	*no data*	0.0065 ± 0.0012 **5.7**	*no data*	0.0085 ± 0.0003 **3.8**	0.0075 ± 0.0001 **1.6**	0.0092 ± 0.0007 **9.1**	*no data*	0.0031 ± 0.0002 **4.9**
1,2	0.0093 ± 0.0013 **14.2**	0.0038 ± 0.0001 2.5	0.0045 ± 0.0001 1.5	0.0062 ± 0.0000 0.7	0.0154 ± 0.0008 **6.1**	0.0053 ± 0.0001 2.5	0.0022 ± 0.0001 3.8	0.0067 ± 0.0001 1.7
0,3	0.0099 ± 0.0013 **12.7**	0.0090 ± 0.0005 **7.0**	0.0054 ± 0.0000 0.9	0.0035 ± 0.0001 3.0	0.0040 ± 0.0000 1.2	0.0103 ± 0.0002 **1.6**	0.0015 ± 0.0006 **39.5**	0.0080 ± 0.0008 **3.6**
2,0	*no data*	*no data*	*no data*	*no data*	0.0059 ± 0.0015 **25.6**	0.0098 ± 0.0048 **48.3**	0.0032 ± 0.0022 **70.0**	0.0097 ± 0.0014 **16.5**
0,1	*no data*	*no data*	*no data*	*no data*	0.0053 ± 0.0000 0.6	*no data*	0.0059 ± 0.0001 2.0	*no data*
1,0	*no data*	*no data*	*no data*	*no data*	*no data*	*no data*	0.0030 ± 0.0000 0.8	0.0029 ± 0.0009 **35.2**
Local /unclear	*no data*	0.0023 ± 0.0001 2.8	0.0061 ± 0.0002 **3.1**	0.0025 ± 0.0001 5.8	0.0046 ± 0.0000 **1.1**	*no data*	*no data*	0.0073 ± 0.0002 **3.9**

Table C.3

Eigenfrequencies [Hz] and loss factors [–] of test samples (for details refer to Table A.1) for lowest modes for three load levels — measurements at KIT: median values and standard deviations are given. $\tilde{\eta} \pm \sigma$. The ratio of standard deviation to median value is listed in [%]. Ratios larger than the signal-to-noise ratio are marked with bold letters.

Mode	V7 f [Hz]	V8 f [Hz]	V9 f [Hz]	V10 f [Hz]	V7 η [–]	V8 η [–]	V9 η [–]	V10 η [–]
(1,1)	57.1 ± 0.14	48.4 ± 0.10	33.7 ± 0.09	49.0 ± 0.02	0.0180 ± 0.0008 **4.6**	0.0224 ± 0.0012 **5.4**	0.0070 ± 0.0009 **12.8**	0.0067 ± 0.0002 **3.2**
(0,2)	70.9 ± 0.07	63.6 ± 0.05	66.9 ± 0.08	86.8 ± 0.03	0.0082 ± 0.0001 1.0	0.0114 ± 0.0001 0.9	0.0110 ± 0.0006 **5.6**	0.0098 ± 0.0001 0.8
(0,2)	*no data*	76.7 ± 0.02	*no data*	*no data*	*no data*	0.0077 ± 0.0001 0.9	*no data*	*no data*
(2,0)	113.9 ± 0.07	107.2 ± 0.06	52.9 ± 0.67	40.0 ± 0.07	0.0088 ± 0.0004 **4.7**	0.0054 ± 0.0006 **10.9**	0.0171 ± 0.0025 **14.4**	0.0048 ± 0.0003 1.4
(2,0)	*no data*	*no data*	72.1 ± 0.14	68.1 ± 0.03	*no data*	*no data*	0.0092 ± 0.0004 **4.5**	0.0067 ± 0.0001 0.1
(1,2)	76.5 ± 1.18	78.8 ± 0.06	94.1 ± 0.19	93.7 ± 0.19	0.0132 ± 0.0024 **18.1**	0.0106 ± 0.0002 1.5	0.0074 ± 0.0004 **6.0**	0.0071 ± 0.019 **27.4**
(0,3)	88.3 ± 0.10	84.7 ± 0.02	*no data*	136.4 ± 0.50	0.0090 ± 0.0001 1.0	0.0062 ± 0.0001 1.0	*no data*	0.0037 ± 0.0011 **36.2**
(0,2)+(1,1)	*no data*	*no data*	49.6 ± 0.12	*no data*	*no data*	*no data*	0.0082 ± 0.0002 1.4	*no data*
(2,0)+(1,1)	*no data*	*no data*	*no data*	77.1 ± 0.09	*no data*	*no data*	*no data*	0.0064 ± 0.0002 **3.7**
(0,2)+(1,2)	81.5 ± 0.37	68.1 ± 0.03	*no data*	*no data*	0.0153 ± 0.0011 **7.0**	0.0178 ± 0.0004 0.0	*no data*	*no data*
Local	54.2 ± 0.49	55.9 ± 0.05	82.8 ± 0.20	62.8 ± 0.01	0.0083 ± 0.0025 **30.4**	0.0182 ± 0.0009 **4.8**	0.0057 ± 0.0002 **4.0**	0.0052 ± 0.0002 0.4

Table C.4

Nonlinearity levels for sine sweep tests for samples measured at TUM. Displayed is the ratio between vibration amplitudes at the excitation frequency and the second highest peak of the higher harmonics. Bold letters — ratio smaller than $1 \cdot 10^{-1}$ (high level of nonlinearity); normal letters — ratio smaller than $1 \cdot 10^{-2}$ and larger than $1 \cdot 10^{-1}$ (medium level of nonlinearity); blank — ratio larger than $1 \cdot 10^{-2}$ (small or no level of nonlinearity). Irregular locations — il; concentrated locations — cl; most locations — ml; many locations — mal.

Mode	V1a	V2a	V3a	V4a	V1b	V2b	V3b	V4b
(1,1)	il	il	**il**/cl	**il**/mal	**il**/ml	**il**/il	il	**il**/il
(0,2)	il/cl		mal/**il**/cl	**il**/ml	il	cl	ml	il
(0,2)*	*no data*	**ml**/il	*no data*	**cl**/ ml	**cl**/ml	**il**/ml	*no data*	**il**/il
(1,2)	**il/cl**	mal	*no data*	*no data*	*no data*	*no data*	*no data*	il
(0,3)	*no data*	*no data*	**il**/il	*no data*	*no data*	*no data*	*no data*	*no data*
(0,1)	*no data*	*no data*	*no data*	*no data*	**il**/mal	*no data*	**il**/ml	*no data*
(1,0)	*no data*	*no data*	*no data*	*no data*	*no data*	*no data*	**il**/ml	**mal**/ml
Local	*no data*	mal	**il**/ml	**ml**/ml	cl	*no data*	*no data*	*no data*

Table C.5

Nonlinearity levels for sine sweep tests for test samples — measurements at KIT are given. Displayed is the ratio between vibration amplitudes at the excitation frequency and the second highest peak of the higher harmonics. Bold letters — ratio smaller than $1 \cdot 10^{-1}$ (high level of nonlinearity); normal letters — ratio smaller than $1 \cdot 10^{-2}$ and larger than $1 \cdot 10^{-1}$ (medium level of nonlinearity); blank — ratio larger than $1 \cdot 10^{-2}$ (small or no level of nonlinearity). Irregular locations — il; concentrated locations — cl; most locations — ml; many locations — mal.

Mode	V7	V8	V9	V10
(1,1)	**il**/ml	**il**/il	**il**/ml	**il**/il
(0,2)	**il**/ml	**il**/mal	**il**/ml	**il**/ml
(0,2)	*no data*	**il**/ml	*no data*	*no data*
(2,0)	*no data*	*no data*	**il**/ml	**il**/il
(2,0)	*no data*	*no data*	*no data*	ml
(1,2)	**il**/ml	**il**/ml	*no data*	*no data*
(0,2)+(1,2)	ml	**il**/ml	*no data*	*no data*
(0,2)+(1,1)	*no data*	*no data*	**il**/ml	*no data*
(2,0)+(1,1)	*no data*	*no data*	*no data*	ml
(0,3)	**il**/ml	**il**/ml	*no data*	*no data*
Local/unclear	**il**/mal	**il**/mal	**il**/ml	**il**/ml

References

[1] ANSYS. ANSYS element library. 2022, https://ansyshelp.ansys.com/account/secured?returnurl=/Views/Secured/corp/v221/en/. Accessed: 2022-01-24.

[2] Hassanieh A, Chiniforush AA, Valipour HR, Bradford MA. Vibration behaviour of steel-timber composite floors, part (2): evaluation of human-induced vibrations. J Construct Steel Res 2019;158:156–70. http://dx.doi.org/10.1016/j.jcsr.2019.03.026.

[3] Buchanan AH, Levine SB. Wood-based building materials and atmospheric carbon emissions. Environ Sci Policy 1999;2(6):427–37. http://dx.doi.org/10.1016/S1462-9011(99)00038-6.

[4] Gerilla GP, Teknomo K, Hokao K. An environmental assessment of wood and steel reinforced concrete housing construction. Build Environ 2007;42(7):2778–84. http://dx.doi.org/10.1016/j.buildenv.2006.07.021.

[5] Dolan JD, Murray TM, Johnson JR, Runte D, Shue B. Preventing annoying wood floor vibrations. J Struct Eng 1999;125(1):19–24. http://dx.doi.org/10.1061/(ASCE)0733-9445(1999)125:1(19).

[6] Weckendorf J, Hafeez G, Doudak G, Smith I. Floor vibration serviceability problems in wood light-frame buildings. J Perform Constr Facil 2014;28(6):A4014003. http://dx.doi.org/10.1061/(ASCE)CF.1943-5509.0000538.

[7] Proenca M, Neves e Sousa A, Garrido M, Correia JR. Acoustic performance of composite sandwich panels for building floors: Experimental tests and numerical-analytical simulation. J Build Eng 2020;32:101751. http://dx.doi.org/10.1016/j.jobe.2020.101751.

[8] Fujita M, Sakai J, Oda H, Iwata M. Building system for a composite steel-timber structure. Steel Constr 2014;7(3):183–7. http://dx.doi.org/10.1002/stco.201410032.

[9] Loss C, Piazza M, Zandonini R. Experimental tests of cross-laminated timber floors to be used in timber-steel hybrid structures. In: Proceedings of WCTE 2014 conference. Quebec, Canada, August. 2014.

[10] Hassanieh A, Valipour HR, Bradford MA. Experimental and analytical behaviour of steel-timber composite connections. Constr Build Mater 2016;118:63–75. http://dx.doi.org/10.1016/j.conbuildmat.2016.05.052.

[11] Loss C, Piazza M, Zandonini R. Connections for steel–timber hybrid prefabricated buildings. Part I: Experimental tests. Constr Build Mater 2016;122:781–95. http://dx.doi.org/10.1016/j.conbuildmat.2015.12.002.

[12] Loss C, Piazza M, Zandonini R. Connections for steel–timber hybrid prefabricated buildings. Part II: Innovative modular structures. Constr Build Mater 2016;122:796–808. http://dx.doi.org/10.1016/j.conbuildmat.2015.12.001.

[13] Hassanieh A, Valipour HR, Bradford MA, Sandhaas C. Modelling of steel-timber composite connections: Validation of finite element model and parametric study. Eng Struct 2017;138:35–49. http://dx.doi.org/10.1016/j.engstruct.2017.02.016.

[14] Chiniforush AA, Alamdari MM, Dackermann U, Valipour HR, Akbarnezhad A. Vibration behaviour of steel-timber composite floors, part (1): Experimental & numerical investigation. J Construct Steel Res 2019;161:244–57. http://dx.doi.org/10.1016/j.jcsr.2019.07.007.

[15] Brake MR. The mechanics of jointed structures: Recent research and open challenges for developing predictive models for structural dynamics. Cham: Springer; 2018, http://dx.doi.org/10.1007/978-3-319-56818-8.

[16] Oh K, Nayfeh AH. Nonlinear combination resonances in cantilever composite plates. Nonlinear Dynam 1996;11(2):143–69. http://dx.doi.org/10.1007/BF00044999.

[17] Nayfeh SA, Nayfeh AH. Nonlinear interactions between two widely spaced modes—external excitation. Int J Bifurcation Chaos 1993;3(02):417–27. http://dx.doi.org/10.1142/S0218127493000301.

[18] Bograd S, Reuss P, Schmidt A, Gaul L, Mayer M. Modeling the dynamics of mechanical joints. Mech Syst Signal Process 2011;25(8):2801–26. http://dx.doi.org/10.1016/j.ymssp.2011.01.010.

[19] Sharma N, Mahapatra TR, Panda SK. Hygrothermal effect on vibroacoustic behaviour of higher-order sandwich panel structure with laminated composite face sheets. Eng Struct 2019;197:109355.

[20] Winter C, Buchschmid M, Müller G. Modeling of orthotropic plates out of cross laminated timber in the mid and high frequency range. Procedia Eng 2017;199:1392–7.

[21] Sharma N, Mahapatra TR, Panda SK, Hirwani CK. Acoustic radiation and frequency response of higher-order shear deformable multilayered composite doubly curved shell panel–an experimental validation. Appl Acoust 2018;133:38–51.

[22] Ewins DJ. Modal testing - theory, practice and application. New York: John Wiley & Sons; 2009.

[23] Weisheit K, Marburg S. Squeak noise prediction for systems with dry friction damping. In: SAE technical paper series. SAE International; 2018, http://dx.doi.org/10.4271/2018-01-1483.

[24] Knauf. Schallschutz mit Knauf. 2022, https://www.knauf.de/profi/meta/suche/index.php?q=ermittlung+im+eingebauten+zustand. Accessed: 2022-04-01.

[25] Kiesel T, Langer P, Marburg S. Numerical study on the effect of gravity on modal analysis of thin-walled structures. Acta Acust United Acust 2019;105(3):545–54. http://dx.doi.org/10.3813/AAA.919335.

[26] Yang K-T, Park Y-s. Joint structural parameter identification using a subset of frequency response function measurements. Mech Syst Signal Process 1993;7(6):509–30. http://dx.doi.org/10.1006/mssp.1993.1030.

[27] Andrej A. Schneider: Bautabellen Für Ingenieure, vol. 21. Bundesanzeiger Verlag; 2014, http://dx.doi.org/10.1002/best.201190039.

[28] STEICO. Konstruktionsheft von STEICO zu LVL/Furnierschichtholz. 2021, https://www.steico.com/de/downloads/dokumente/produkte-allgemeines. (Accessed: 2021-01-19).

[29] Pollmeier. Leistungserklärung einer Platte in Baubuche. 2022, https://www.pollmeier.com/de/produkte/ueber-baubuche/baubuche-platte. Accessed: 2022-01-19.

[30] Noel J-P, Kerschen G. Nonlinear system identification in structural dynamics: 10 more years of progress. Mech Syst Signal Process 2017;83:2–35. http://dx.doi.org/10.1016/j.ymssp.2016.07.020.

[31] Fritze D, Marburg S, Hardtke H-J. Estimation of radiated sound power: A case study on common approximation methods. Acta Acust United Acust 2009;95(5):833–42. http://dx.doi.org/10.3813/AAA.918214.

[32] Klaerner M, Wuehrl M, Kroll L, Marburg S. FEA-based methods for optimising structure-borne sound radiation. Mech Syst Signal Process 2017;89:37–47. http://dx.doi.org/10.1016/j.ymssp.2016.07.019.

[33] Sharma N, Mahapatra TR, Panda SK. Vibro-acoustic behaviour of shear deformable laminated composite flat panel using BEM and the higher order shear deformation theory. Compos Struct 2017;180:116–29.

[34] Krack M, Gross J. Harmonic balance for nonlinear vibration problems, vol. 1. Cham: Springer; 2019, http://dx.doi.org/10.1007/978-3-030-14023-6.

[35] Utzig L, Weisheit K, Maeder M, Marburg S. Quantitative prediction of rattle noise: An experimentally validated approach using the harmonic balance method. Mech Syst Signal Process 2022;167:108592. http://dx.doi.org/10.1016/j.ymssp.2021.108592.

A.2 Paper B

Vibration response of a hybrid steel-timber building element with uncertain material and joint parameters

Bettina Chocholaty, Martin Eser, Karl-Alexander Hoppe, Daotong Wang, Steffen Marburg

ORIGINAL ARTICLE

Vibration response of a hybrid steel–timber building element with uncertain material and joint parameters

Bettina Chocholaty[1] · Martin Eser[1] · Karl-Alexander Hoppe[1] · Daotong Wang[1] · Steffen Marburg[1]

Abstract

The design of building elements is usually done conservatively by considering safety factors. However, more efficient designs are gaining interest for economic and sustainability reasons. Hence, an adequate prediction tool can improve the design of building elements. Probabilistic modeling, for example, Monte Carlo simulations, represents a remedy to this by examining uncertainties in a structure through uncertain input parameters. In this work, a Monte Carlo simulation is performed to quantify the uncertainty in the modal properties of a hybrid steel–timber building element. The material properties of the timber material and the stiffness of the structural joints are considered uncertain inputs. The probabilistic properties of the timber material are evaluated utilizing Bayesian inference instead of the usually applied empirical methods. Using these inferred timber material properties leads to a good match of simulated and measured natural frequencies of the timber components. These parameters are utilized together with the joints' uncertain inputs in the Monte Carlo simulation of the hybrid steel–timber building element. The results show a significant span for the identified eigenfrequencies, which proves the relevance of probabilistic analyses for the vibration characteristics of building elements.

Keywords Hybrid steel–timber elements · Monte Carlo simulation · Vibrations · Bayesian inference

1 Introduction

Hybrid wood structures combined with steel or concrete are moving into the focus of wood construction research, especially in the topic of vibrations [1]. Human activities, e.g., walking or jogging, can significantly influence the design of hybrid steel–timber floor elements in terms of vibrations [2]. In the design process of floor structures related to vibrations, calculations or certified measurements are required [3]. However, analytical calculations become challenging for complex cross-sections, emphasizing the need to develop reliable, advanced prediction tools for vibrations of compounded structures, such as hybrid steel–timber building elements. These predictive models prove to be relevant, especially for material-efficient designs in the context of

economic efficiency and sustainability, since without predictive tools, various prototypes have to be tested experimentally [4].

The vibroacoustic behavior of hybrid steel–timber floors has already been studied experimentally and numerically [2, 5, 6]. A steel–timber beam made of a Cross-Laminated-Timber (CLT) panel and an H-shaped steel profile has been investigated concerning natural frequencies, mode shapes, modal damping ratios, and acceleration response. A finite element (FE) model has been updated to match the results from experimental analyses [6]. The same structure has been analyzed concerning vibration serviceability in [2]. A different structure has been studied in [5]. Here, the authors have investigated the vibrational behavior of a structure made of top and bottom laminated veneer lumber (LVL) panels and a trapezoidal steel web.

In practice, the response prediction of a vibroacoustic system is generally performed through mechanical modeling, which introduces data and model uncertainties. Model uncertainties relate to the applicability of a model to the specific problem at hand and represent a type of epistemic error. On the other hand, data uncertainties constitute a type of aleatoric error and are related to the parameters of a

---

✉ Bettina Chocholaty
   bettina.chocholaty@tum.de

1 Chair of Vibroacoustics of Vehicles and Machines,
   Department of Engineering Physics and Computation,
   TUM School of Engineering and Design, Technical
   University of Munich, Boltzmannstraße 15,
   85748 Garching bei München, Germany

system, e.g., geometrical parameters, boundary conditions, or material properties. Data uncertainties can be considered by using random quantities, e.g., random variables or stochastic fields, for the parameters in the prediction tool [7, 8]. However, in engineering practice, those uncertainties are often accounted for through safety factors [9] leading to conservative designs.

To develop more efficient designs, research on reliable predictions for building elements focuses increasingly on considering data uncertainties instead of safety factors. Recent studies on the stochastic analyses of wooden floors, i.e., a CLT slab [10] and a floor made of wood beams and particle boards [11], use the Monte Carlo (MC) method to include the randomness of the components' material properties and to determine the vibroacoustic response of the floor in confidence intervals. The random material parameter inputs are found by calibrating FE models to match eigenfrequencies from an experimental modal analysis. In [11], this has been done by determining the mean and standard deviation for the material parameters from 62 measurements on wooden beams. In [10], using a random elasticity tensor built from initial values from the literature, the best combination of material parameters in the FE model is sought to calibrate the model with results from an experimental modal analysis. Furthermore, non-Gaussian uncertain parameters of ash wood are identified using generalized polynomial chaos expansions and experimental modal data by solving a stochastic inverse problem in [12, 13].

Another approach to identifying unknown, uncertain parameters based on experiments and modeling is Bayesian inference. Former research has exploited Bayesian inference for laminated, orthotropic materials such as engineered wood products, i.e., for general thin orthotropic laminates [14], thick orthotropic laminated plates [15], laminated timber beams [16], and CLT [17]. The studies either use static deflection tests [16], simulated and experimentally determined natural frequencies [14, 15] or frequency response data of a linear dynamic model and measurements [17] to determine the material properties.

Prior investigations into the uncertainty quantification of building elements have predominantly relied on deterministic methods for identifying material properties through model calibration using experimental data [10, 11]. Alternatively, some studies have considered Bayesian inference to incorporate prior information on elastic constants, as exemplified by [15]. Notably, these Bayesian inference studies on engineered wood materials focus solely on inferring material properties without integrating them into subsequent analyses. Consequently, a critical gap emerges in connecting these approaches. In this study, this gap is filled by applying a novel combination of both methodologies to address the vibrational behavior of a hybrid steel-timber building element. This research concentrates on the quantification of uncertainty in the vibroacoustic behavior of this hybrid structure, focusing on the variability of modal properties. The approach adopted encompasses two main phases, detailed in Sect. 2 and Sect. 3. First, Bayesian inference is applied to establish probabilistic representations of timber material properties, incorporating the inherent variability found in real-world scenarios. These probabilistic representations serve as the foundation for the subsequent phase, where a probabilistic model is developed to predict the vibroacoustic response of the hybrid structure, as discussed in Sect. 3. The outcomes of these interconnected phases undergo thorough analysis and discussion in Sect. 4.

In summary, this article introduces a novel combination of two distinct methodologies applied for the first time to the examination of a hybrid steel–timber building element. This research contributes to the field of uncertainty quantification in vibrational behavior, yielding valuable insights into the dynamic variations of modal properties while leveraging more efficient structural designs.

2 Materials and methods

This study aims to quantify uncertainty for the vibroacoustic behavior of a hybrid steel–timber building element, which has been previously studied in terms of vibroacoustics in [5]. The variability of the natural frequencies of the element due to uncertain inputs is analyzed. The overall workflow is visualized in Fig. 1. In Sect. 2.1, the vibrational behavior of the hybrid steel–timber building element is evaluated experimentally and numerically. The stiffness of the joints and the material properties of the timber are assigned to be uncertain inputs. For the latter, the approach of Bayesian inference is applied to characterize the uncertainty in Sect. 2.2. For the former, the parameters are identified by maximum a posteriori (MAP) estimation, and their variation is based on literature references (Sect. 2.3). Finally, the numerical model and these uncertain inputs are used in a probabilistic analysis in Sect. 2.4.

2.1 Experimental and numerical investigations on the hybrid steel–timber element

The investigated hybrid structure utilizes LVL panels as top and bottom planking and a trapezoidal steel web. Fasteners connect the individual components. An overview of the concept is given in Fig. 1. The dimensions of the samples are depicted in Fig. 1 and listed in Table 1.

An FE model is created for the probabilistic analysis as described in Sect. 2.1.2 and is validated by vibration measurements (Sect. 2.1.1).
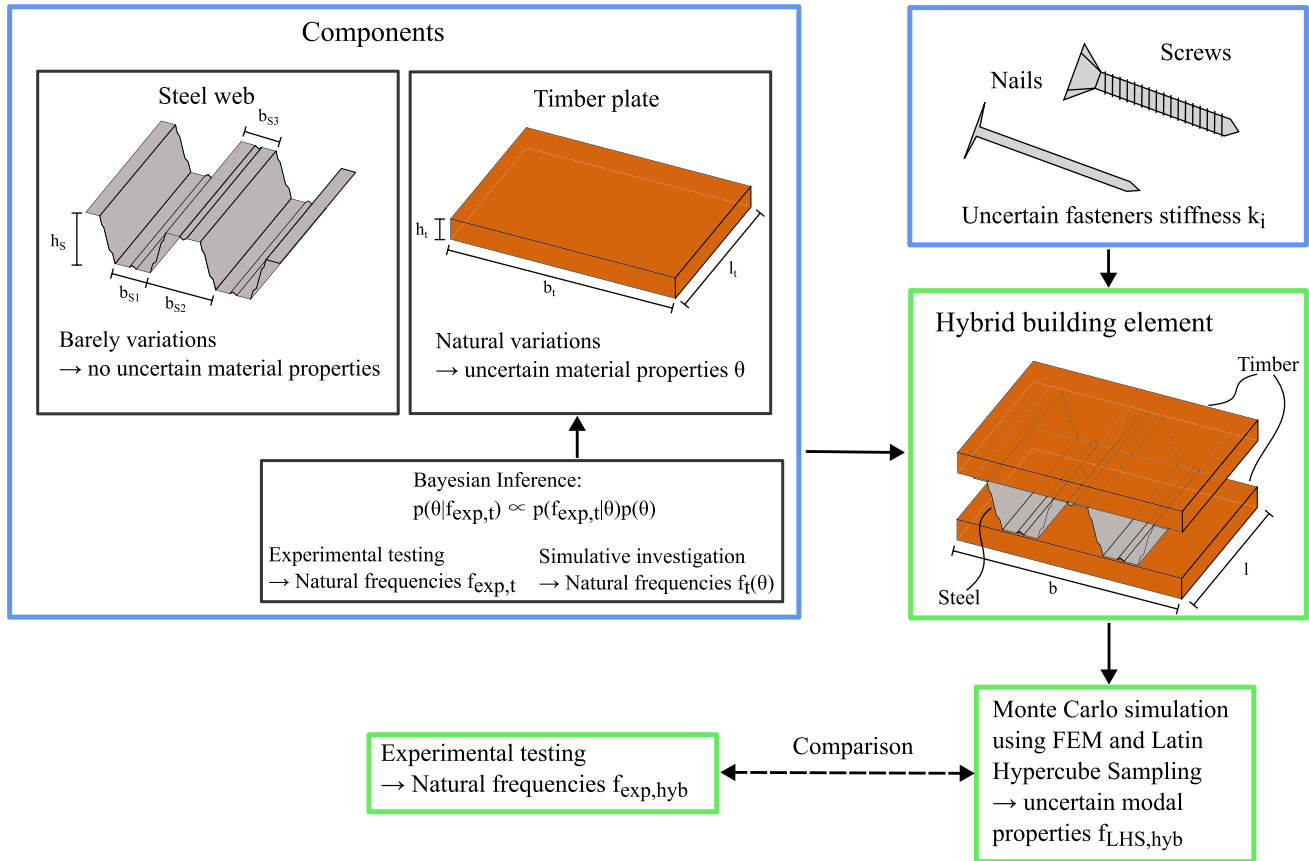
Fig. 1 Overview of methodological approach

Table 1 Geometric properties of the hybrid steel–timber test sample (refer to Fig. 1 for the parameter definition)

l [m]	b [m]	h_t [m]	d_s [m]	h_s [m]	b_{s1} [m]	b_{s2} [m]	b_{s3} [m]
3.5	0.900	0.039	$0.75 \cdot 10^{-3}$	0.155	0.110	0.170	0.04

2.1.1 Measurements on the hybrid element

The following paragraph briefly describes the measurement setup and procedure. More details are available in [5]. Measurements of vibration on the hybrid steel–timber element are carried out (Fig. 2). A B &K[1] modal exciter type 4284 applies a pseudo-random excitation on the structure by a stinger. Heavy-duty slings support the specimen. Hanging supports are chosen in the measurements to exclude influences from uncertain boundary conditions, since unconstrained supports are less challenging to realize adequately [18]. Furthermore, a B &K force transducer Deltatron Type 8230 measures the applied force. The vibrations of the specimens' surface are identified by a scanning Laser Doppler Vibrometer PSV-500 (LDV)[2] at an evenly distributed grid

---

[1] Hottinger Brüel & Kjær GmbH, D-64293 Darmstadt, Germany.

[2] Polytec GmbH, D-76337 Waldbronn, Germany.
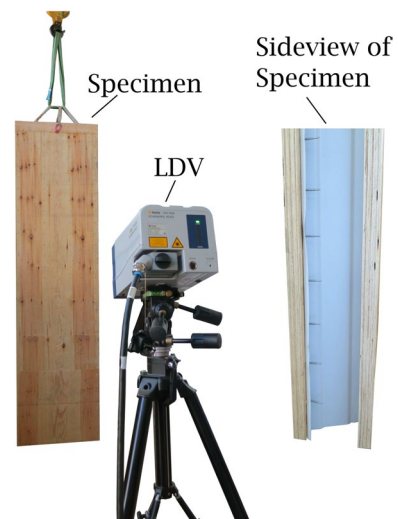
Fig. 2 Measurement setup for the hybrid element
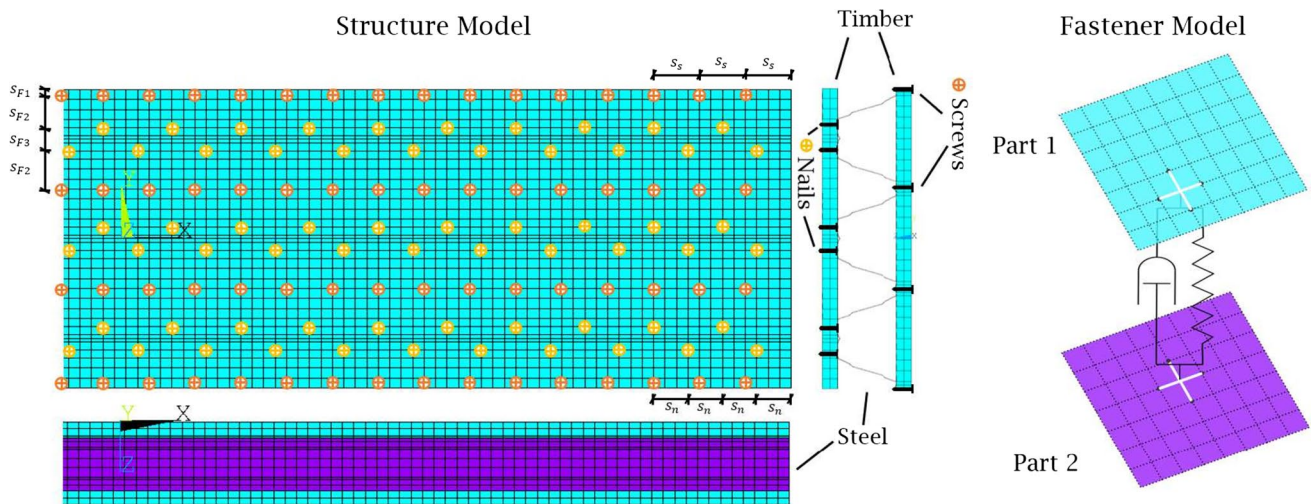
Fig. 3 Finite element model of the hybrid steel–timber element: structural model is depicted on the left and the fastener model on the right

of locations on the structure. For each scan point, a Fourier transform is utilized to transform the determined time data. Subsequently, the frequency response functions are calculated by means of the measured force and velocity signals. The Polytec system software applies a rectangular window to the signals.

The first five eigenfrequencies of the hybrid structure $f_{\text{exp,hyb}}$ are identified by an experimental modal analysis [18].

2.1.2 Finite element model

The commercial software ANSYS [19] is used to simulate the vibrational behavior of the hybrid structure. The FE representation of the steel–timber structure is visualized in Fig. 3. The lower and upper wooden panels are modeled by orthotropic and hexahedral elements (SOLID186) with quadratic shape functions. The steel web is meshed by isotropic, quadratic shell elements (SHELL281). The fasteners are simulated by parallel spring and damper elements (COMBIN14) applied for all translational degrees of freedom (DOFs) of nodes related to fasteners (as in, e.g., [20]). The adjacent nodes of a fastener are rigidly coupled in terms of translational DOFs (Fig. 3). In longitudinal direction, the screws are placed with $s_s = 0.12$ m and the nails with $s_n = 0.09$ m. The transversal fastener distances are given as $s_{F1} = 0.010$ m, $s_{F2} = 0.103$ m and $s_{F3} = 0.055$ m. The used mesh size is approximately $l_{\text{ele}} = 0.03$ m for the timber components and $l_{\text{ele}} = 0.02$ m for the steel parts. Those element sizes are chosen as a good compromise between geometrical constraints and the rule of thumb to use six to eight quadratic elements per wavelength [21]. The boundary conditions in the simulations are modeled as free supports to adopt the measurement setup.

The influence of input parameter uncertainties on the natural frequencies of the building element is of interest. Therefore, modal analysis is conducted in ANSYS. The five structural mode shapes $f_{\text{FE,hyb}}$ matching the experimentally determined ones are computed.

The FE model uses material properties for the steel and timber components, as well as joint and geometric parameters as inputs. The geometrical inputs for the hybrid specimen are given in Table 1. Uncertainties from geometrical parameters are assumed to be negligible. Ballast [22] states manufacturing tolerances of approximately 0.1%, which is below the uncertainties for, e.g., joints in structures, as stated in Sect. 2.3.

For the steel profile, the elasticity modulus E_s, the shear modulus G_s, the Poisson ratio ν_s, and the density ρ_s as provided by [23] are utilized (Table 2). Since LVL is an orthotropic material, the elasticity moduli, $E_{x,0}$, $E_{y,0}$, and $E_{z,0}$, the shear moduli, $G_{xy,0}$, $G_{xz,0}$, and $G_{yz,0}$, the Poisson ratios, $\nu_{xy,0}$, $\nu_{xz,0}$, and $\nu_{yz,0}$, and the density ρ_0 as given by the manufacturer [24] are used (Table 3).

Since wood is a naturally grown material, variations in the material occur. In [25], the authors state a coefficient of variation (CoV) of 0.13 for the bending modulus of elasticity for timber, which is high compared to CoV = 0.03 of the elasticity modulus of structural steel given in [25]. Hence, the LVL but not the steel material properties are assigned to be uncertain inputs. Details on how the probabilities of the LVL material properties are obtained are given in Sect. 2.2.

Table 2 Steel material properties [23]

E_s [N/m^2]	G_s [N/m^2]	ν_s [-]	ρ_s [kg/m^3]
$2.1 \cdot 10^{11}$	$8.1 \cdot 10^{11}$	0.3	7850

Table 3 LVL material properties θ_0 [24]

$E_{x,0}$ [N/m²]	$E_{y,0}$ [N/m²]	$E_{z,0}$ [N/m²]	$G_{xy,0}$ [N/m²]	$G_{xz,0}$ [N/m²]	$G_{yz,0}$ [N/m²]	$\nu_{xy,0}$ [-]	$\nu_{xz,0}$ [-]	$\nu_{yz,0}$ [-]	ρ_0 [kg/m³]
$1.06 \cdot 10^{10}$	$2.50 \cdot 10^9$	$3.00 \cdot 10^8$	$6.00 \cdot 10^8$	$1.50 \cdot 10^8$	$1.50 \cdot 10^8$	0.59	0.59	0.36	530

2.2 Inverse characterization of LVL material properties by Bayesian inference

The characterization of uncertain timber material properties is done using Bayesian inference, since the method provides a good framework for such an identification. This approach is described in more detail in the following section.

The probabilities for the uncertain LVL material input parameters of the simulation model for the hybrid steel–timber structure are identified by Bayesian inference. In this method, prior information on the probability of the model parameters, i.e., the material properties of the LVL, is updated by incorporating experimentally measured data to strengthen the degree of belief in the probability of the material parameters.

The probability model of the uncertain material parameters, i.e., the posterior probabilities $p(\theta|\mathbf{f}_{\exp})$, is fitted employing Bayes' rule [26]

$$p(\theta|\mathbf{f}_{\exp}) \propto p(\mathbf{f}_{\exp}|\theta)p(\theta), \tag{1}$$

with the uncertain parameters θ, the measured data $\mathbf{f}_{\exp}$, the prior probabilities of uncertain parameters $p(\theta)$, and the likelihood $p(\mathbf{f}_{\exp}|\theta)$. The denominator in Bayes' formula only normalizes the probabilities, which is why it is omitted here [26]. The measured data $\mathbf{f}_{\exp}$ are represented by seven natural frequencies determined from vibrational experiments on timber panels made of LVL $\mathbf{f}_{\exp,t}$ via experimental modal analysis. The uncertain material parameters θ constitute the inputs to the used forward model $\mathbf{f}_t(\theta)$, which is based on a Rayleigh–Ritz approach (Sect. 2.2.3). The forward model is utilized together with the measurement data to evaluate the likelihood (Sect. 2.2.1).

2.2.1 Likelihood

The likelihood $p(\mathbf{f}_{\exp,t}|\theta)$ is combined with the prior probabilities $p(\theta)$ to explore the posterior densities given the measurement data $\mathbf{f}_{\exp,t}$. Hence, it evaluates the probability that a certain measurement is obtained given a specific material parameterization θ. The mean of the distribution represents the de facto measured natural frequencies $\mathbf{f}_{\exp,t}$, and the standard deviation relates to the measurement noise. The likelihood function is computed by maximizing the entropy and considering it for discrete variables by means of a residual error $\epsilon_i = f_{\exp,t,i} - f_{t,i}(\theta)$ [27]

$$p(\epsilon_i|\theta, \mathbf{f}_t(\theta), \sigma_{\mathrm{lik},i}, \mu_{\mathrm{lik}} = 0) = \frac{1}{\sqrt{2\pi}\sigma_{\mathrm{lik},i}} \exp\left(-\frac{\epsilon_i^2}{2\sigma_{\mathrm{lik},i}^2}\right), \tag{2}$$

where $f_{\exp,i}$ represents one of the $1 \le i \le N_f$ measured datasets. The used forward model $\mathbf{f}_t(\theta)$ should be able to reproduce the experimental data well.

The probability regarding each data point equals the probability of the residual error at each data point. Hence, the overall likelihood function is computed as the joint probability of all data points [27]

$$p(\mathbf{f}_{\exp,t}|\theta, f_t(\theta), \sigma_{\mathrm{lik},1}, \sigma_{\mathrm{lik},2}, ..., \sigma_{\mathrm{lik},N_f})$$
$$= p(\epsilon_1, \epsilon_2, ..., \epsilon_{N_f}|\theta, \mathbf{f}_t(\theta), \sigma_{\mathrm{lik},1}, \sigma_{\mathrm{lik},2}, ..., \sigma_{\mathrm{lik},N_f}). \tag{3}$$

Since the noise is the same for each measurement in most experiments, it is assumed that $\sigma_{\mathrm{lik}} = \sigma_{\mathrm{lik},i}$ for all $1 \le i \le N_f$. $N_f = 7$ represents the number of measured frequencies. Furthermore, as justified by the principle of maximum entropy, the individual measurements are logically independent, which leads to the joint probability as [27]

$$p(\mathbf{f}_{\exp,t}|\theta, f_t(\theta), \sigma_{\mathrm{lik}}) = \prod_i^{N_f} \frac{1}{\sqrt{2\pi}\sigma_{\mathrm{lik}}} \exp\left(-\frac{\epsilon_i^2}{2\sigma_{\mathrm{lik}}^2}\right). \tag{4}$$

Additionally, to consider the repeatability of the measurements, 12 specimens $N_r = 12$ are investigated. Consequently, the scalar values in the residual error $\epsilon_i = \mathbf{f}_{\exp,t,i} - \mathbf{f}_{t,i}(\theta)$ become vectors with the length N_r.

Since the hyperparameter σ_{lik} is not of particular interest in this study, marginalization is used on the joint probability to compute a likelihood probability without the standard deviation σ_{lik} [27]

$$p(\mathbf{f}_{\exp,t}|\theta, \mathbf{f}_t(\theta)) = \int p(\mathbf{f}_{\exp,t}, \sigma_{\mathrm{lik}}|\theta, \mathbf{f}_t(\theta))d\sigma_{\mathrm{lik}}$$
$$= \int p(\mathbf{f}_{\exp,t}|\theta, \mathbf{f}_t(\theta), \sigma_{\mathrm{lik}})p(\sigma_{\mathrm{lik}}|\theta, \mathbf{f}_t(\theta))d\sigma_{\mathrm{lik}}. \tag{5}$$

Using the principle of maximum entropy, the Jeffreys' prior is assigned for the marginal distribution $p(\sigma_{\mathrm{lik}}|\theta, \mathbf{f}_t(\theta))$ [27]

$$p(\sigma_{\mathrm{lik}}|\theta, \mathbf{f}_t(\theta)) = \frac{1}{\sigma_{\mathrm{lik}}}. \tag{6}$$
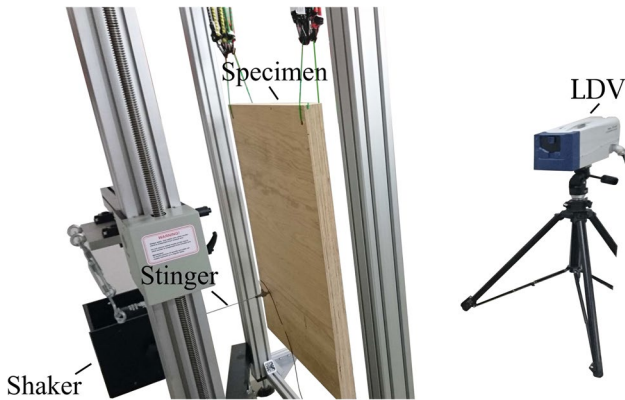
Fig. 4 Measurement setup for the components

Table 4 Dimensions of LVL samples

Label	Thickness h_t [m]	Width b_t [m]	Length l_t [m]
H451-H454	0.045	0.825	0.6
H551-H554	0.055	0.840	0.6
H651-H654	0.065	0.750	0.6

Subsequently, the integral from Eq. (5) is performed using the limits $\sigma_{\text{lik}} \in [0, \infty)$ resulting in a marginalized likelihood in the form of a student's t-distribution

$$p(\mathbf{f}_{\text{exp},t}|\boldsymbol{\theta}, \mathbf{f}_t(\boldsymbol{\theta})) = \frac{\Gamma(N_f/2)}{2}\left(\pi \sum_{i=1}^{N_f} \epsilon_i^2\right)^{-N_f/2}, \tag{7}$$
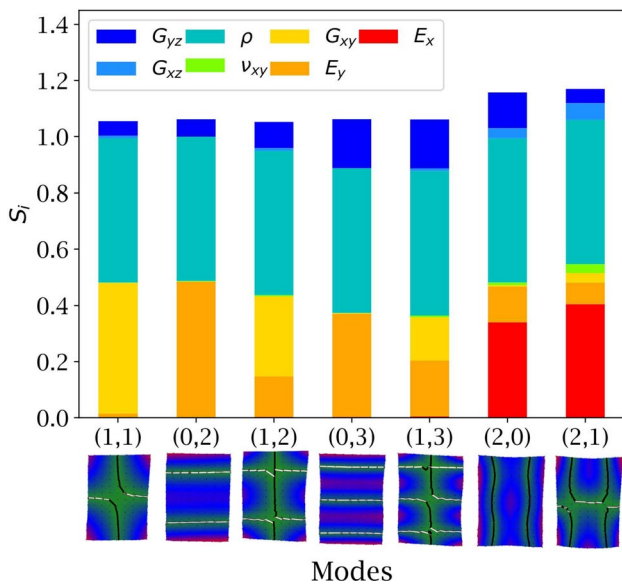
Fig. 5 Sensitivities S_i for an LVL plate with thickness $h = 4.5$ cm for the seven lowest eigenfrequencies

with the standard gamma function $\Gamma(...)$. The individual specimens' experiments are taken into account by summing the error also w.r.t. those data points

$$p(\mathbf{f}_{\text{exp},t}|\boldsymbol{\theta}, \mathbf{f}_t(\boldsymbol{\theta})) = \frac{\Gamma(N_f/2)}{2}\left(\pi \sum_{i=1}^{N_f} \sum_{j=1}^{N_r} \epsilon_{ji}^2\right)^{-N_f/2}, \tag{8}$$

where $\epsilon_{ji} = f_{\text{exp},t,ji} - f_{t,ji}(\boldsymbol{\theta})$.

2.2.2 Vibration measurements on timber panels

The experimental data are acquired by performing vibration measurements on the individual components, i.e., 12 LVL panels ($N_r = 12$). The components' measurements are established similarly to the experiments on the hybrid element (Sect. 2.1.1). A white-noise excitation is applied to the structure by the stinger. Furthermore, the sample is supported by rubber slings. The respective test setup is visualized in Fig. 4.

The first seven eigenfrequencies $f_{\text{exp},t}$ of the 12 LVL plates are identified by an experimental modal analysis [18] and are visualized below the abscissa in Fig. 5. The dimensions of the samples, i.e., length l_t, width b_t, and thickness h_t, are given in Table 4. Four samples of three different geometries are used in the experiments, i.e., H45i with a thickness of $h_t = 45$ mm, H55i with a thickness of $h_t = 55$ mm, and H65i with a thickness of $h_t = 65$ mm. The fiber direction of the LVL is aligned with the shorter side length l_t.

2.2.3 Forward model: Rayleigh–Ritz approach

A forward model is necessary to evaluate the likelihood. Here, many evaluations are required, which is why, instead of an FE approach, a computationally faster model is used. Due to its anatomy, wood is often modeled as an orthotropic material. Hence, a Rayleigh–Ritz method for orthotropic Mindlin plates with free supports is implemented [28]. In the Rayleigh–Ritz method, energy functionals for the strain and kinetic energy of the plate are calculated by considering the constitutive equations of an orthotropic Mindlin plate (details are given in the appendix). To satisfy the boundary conditions, the following trigonometric basis functions:

$$\phi_m(x) = \begin{cases} \cos(\lambda_m x) & m \geq 0 \\ \sin(\lambda_m x) & m < 0 \end{cases} \quad \lambda_m = m\pi/l_t \tag{9}$$

$$\phi_n(y) = \begin{cases} \cos(\lambda_n y) & n \geq 0 \\ \sin(\lambda_n y) & n < 0 \end{cases} \quad \lambda_n = n\pi/b_t \tag{10}$$

are utilized to describe the displacements w and rotations ψ_i of the plates

$$\psi_x(x, y) = \sum_{m=-2}^{\infty} \sum_{n=-2}^{\infty} A_{mn}\phi_m(x)\phi_n(y), \qquad (11)$$

$$\psi_y(x, y) = \sum_{m=-2}^{\infty} \sum_{n=-2}^{\infty} B_{mn}\phi_m(x)\phi_n(y), \qquad (12)$$

$$w(x, y) = \sum_{m=-2}^{\infty} \sum_{n=-2}^{\infty} C_{mn}\phi_m(x)\phi_n(y), \qquad (13)$$

while satisfying the freely supported boundary conditions [28]. The potential and kinetic energy use the respective displacement and rotation functions depending on the coefficients A_{mn}, B_{mn}, and C_{mn} to build the Lagrangian expression. This formulation is minimized by derivation with respect to the coefficients. It is summed up in matrix form as

$$(\mathbf{K} - \omega^2\mathbf{M})\mathbf{E} = 0 \qquad (14)$$

with the stiffness matrix $\mathbf{K}$, the mass matrix $\mathbf{M}$, the natural frequencies $\mathbf{f} = \omega/(2\pi)$, and the coefficient matrix $\mathbf{E}$

$$\mathbf{E} = \begin{Bmatrix} A_{-2,-2} & A_{-2,-1} & ... & A_{M,N} \\ B_{-2,-2} & B_{-2,-1} & ... & B_{M,N} \\ C_{-2,-2} & C_{-2,-1} & ... & C_{M,N} \end{Bmatrix}^T, \qquad (15)$$

with truncation order $M = 8$ and $N = 8$.

From Eq. (14), natural frequencies and eigenvectors can be computed by solving the eigenproblem.

The supports of the model are chosen as 'free', similar to the freely suspended specimens in the experiments. As input parameters to the model, the dimensions of the LVL plates (Table 4) and the timber material properties $\hat{\theta}$, i.e., elasticity moduli in longitudinal E_x and transverse direction E_y, shear moduli G_{xy}, G_{xz}, and G_{yz}, density ρ and Poisson's ratio ν_{xy} are required. Using the model (Eq. (14)), natural frequencies $\mathbf{f}_\theta = \mathbf{f}_t(\theta)$ are determined numerically and incorporated in the Bayesian inference.

However, first, a one-at-a-time sensitivity analysis [29, 30] is conducted to reduce the parameter space by identifying the most relevant input LVL material parameters for the Bayesian inference approach. Hence, it is evaluated which material properties mostly influence the seven lowest natural frequencies, which lie in the range of $f_{\theta_i} \in [0, 800]$ Hz. The Rayleigh–Ritz model uses seven material input parameters, i.e., the material properties. Each material property is varied in the range of $\hat{\theta}_i \in [0.9 \cdot \theta_{i,0}, 1.1 \cdot \theta_{i,0}]$. Here, $\hat{\theta}_0 = [E_{x,0}, E_{y,0}, G_{xy,0}, G_{xz,0}, G_{yz,0}, \nu_{xy,0}, \rho_0]^T$ denotes the initial parameter values of the timber material properties as given in Table 3.

The variation range is chosen as $\pm10\%$, since the CoV for wooden materials is approximately given as CoV ≈ 0.1 in

[25], which covers the parameter range within one standard deviation. The varied material properties are introduced in the forward model. Eigenfrequencies $\mathbf{f}_{\theta_i}$ are subsequently computed and compared to the initial results $\mathbf{f}_{\theta_0}$ obtained through the initial values θ_0. The respective modes are denoted by the number of nodal lines in the x (fiber direction) and y (transverse to the fiber) directions, e.g., (1,1), as depicted in Fig. 5. Then, the sensitivity is calculated as

$$S_i = \mathbf{\Delta}_f/\Delta_{\hat{\theta}} = (\mathbf{f}_{\hat{\theta}_i} - \mathbf{f}_{\hat{\theta}_0})/(\hat{\theta}_i - \hat{\theta}_0). \qquad (16)$$

This yields high sensitivities ($S_i \geq 0.05$) of the natural frequencies to all input material parameters $\hat{\theta}$ except for the Poisson's ratio ν_{xy} and the shear modulus G_{xz} (Fig. 5). Consequently, the most relevant material input parameters are identified as $\theta = [E_x, E_y, G_{xy}, G_{yz}, \rho]^T$ and are subsequently used for the inference of the timber material properties.

2.2.4 Prior probabilities

The initial probabilities—the priors—represent the beliefs about the uncertain parameters before measurement data are considered [26]. Based on the information given in [25], lognormal distributions $\theta_i \sim \mathcal{LN}(\mu_i, \sigma_i^2)$ are assigned for the elasticity moduli, E_x and E_y, and for the shear moduli, G_{xy} and G_{yz}, and a normal distribution $\rho \sim \mathcal{N}(\mu_\rho, \sigma_\rho^2)$ is assigned for the density ρ. μ_i denotes the location parameter in the lognormal distributions and the mean value for the normal distribution. σ_i represents the standard deviation in both cases. In [25], information on the CoV is also given as CoV$_\rho = 0.1$ and CoV$_{\text{moduli}} = 0.13$ leading to standard deviations of $\sigma_\rho = 0.1 \cdot \rho_0$ and $\sigma_i = 0.13$. By means of the prior probabilities, prior predictive checks are performed [31]. Samples for the material values are drawn from the prior probabilities for a specific set of μ_i and σ_i, inserted into the forward model, and the seven lowest natural frequencies $\mathbf{f}_\theta$ are determined. Then, the measured natural frequencies $\mathbf{f}_{\text{exp},t}$ are plotted together with the calculated natural frequencies $\mathbf{f}_\theta$. If the measured ones lie within the range spanned by the calculated values, the parameters of the prior probabilities indicate physically meaningful results for the natural frequencies. Nevertheless, for this set of standard deviations of the priors, the prior predictive checks showed measured frequencies lying outside the range of calculated values. Hence, a larger CoV$_{\text{moduli}} = 0.25$ than proposed for the moduli in [25] is chosen. The chosen value stems from the CoV given in [25] for the bending strength, since the moduli are related to bending strength. For this selected configuration

$$E_x \sim \mathcal{LN}(\ln(E_{x,0}), 0.25^2), \qquad (17)$$
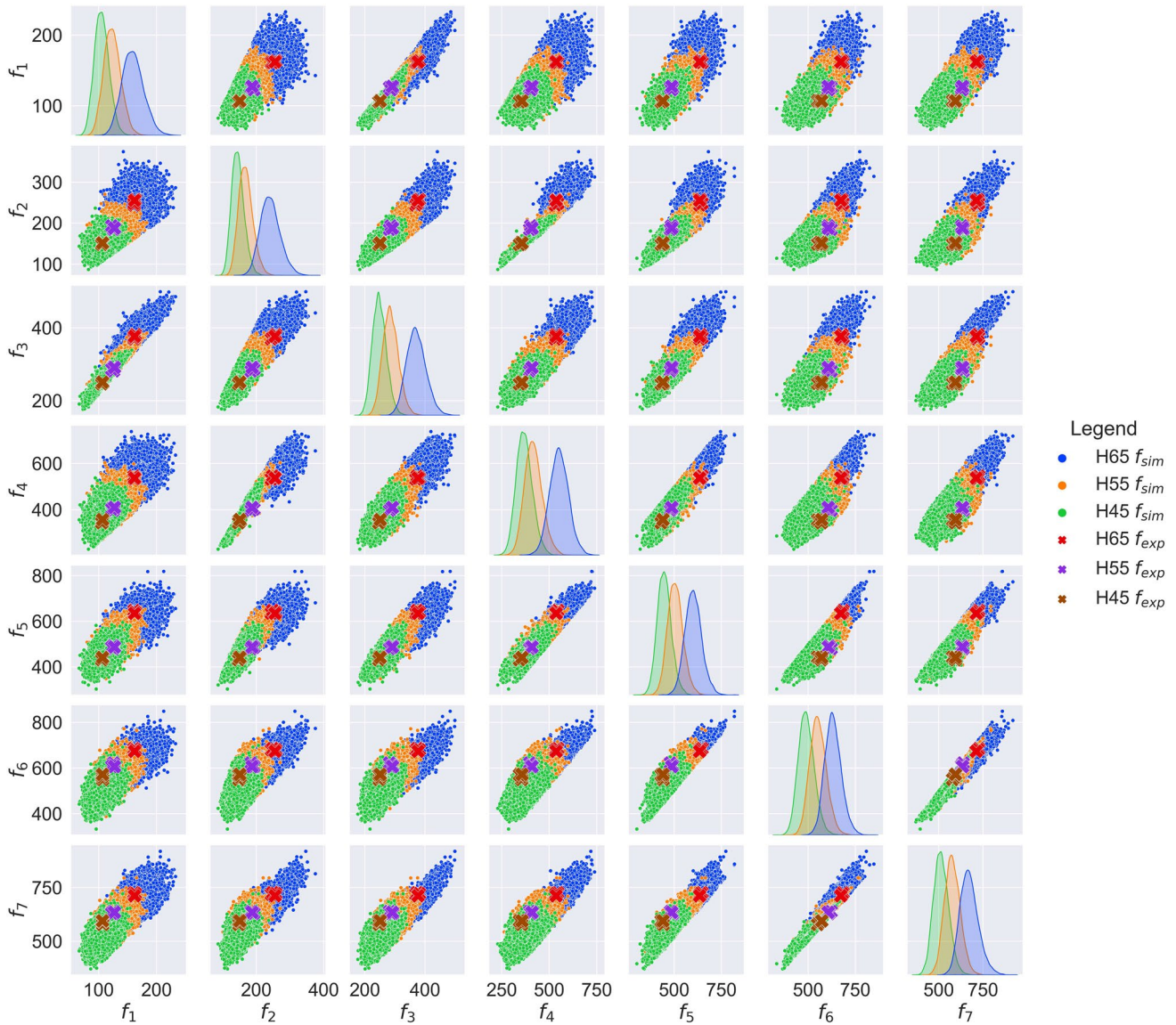
Fig. 6 Prior predictive checks: the numerically $\mathbf{f}_{\text{fem},t}$ and experimentally $\mathbf{f}_{\text{exp},t}$ determined natural frequencies are plotted using contrasting colors for the sake of comparison

$$E_y \sim \mathcal{LN}(\ln(E_{y,0}), 0.25^2), \tag{18}$$

$$G_{xy} \sim \mathcal{LN}(\ln(G_{xy,0}), 0.25^2), \tag{19}$$

$$G_{yz} \sim \mathcal{LN}(\ln(G_{yz,0}), 0.25^2), \tag{20}$$

$$\rho \sim \mathcal{N}(\rho_0, (0.10 \cdot \rho_0)^2), \tag{21}$$

the prior predictive check results are shown in Fig. 6.

All measured eigenfrequencies $\mathbf{f}_{\text{exp},t}$ lie within the range of the numerically evaluated eigenfrequencies $\mathbf{f}_\theta$. Hence, the above priors are assigned.

2.2.5 Posterior distribution

Finally, methods are needed that explore the posterior probabilities. In this context, Markov Chain Monte Carlo Sampling methods are often used, since an analytical solution only exists in rare cases, e.g., if conjugacy is present. The sampling utilizes the forward model (Sect. 2.2.3), which must be computed for each likelihood evaluation during sampling [26].

This study uses the so-called Sequential Monte Carlo sampler within the Python package PyMC [32] to infer the posterior probabilities of the uncertain material parameters θ. This algorithm is advantageous for multimodal posterior probabilities. Unlike usual Markov

Chains, the sampler is less susceptible to getting stuck in local minima, which is overcome by applying the idea of tempering [33].

The identified probability densities are subsequently available as inputs for the probabilistic analysis of the hybrid building element together with the uncertain joint stiffness values.

2.3 Uncertain joint inputs

For the modal analysis of the hybrid structure, stiffness properties for the fastener model (Fig. 3 on the right) are required. The linear spring element is applied to connect DOFs in the x- and y-direction with the stiffness k_{hor} and in the z-direction with the stiffness k_{ver}. Since different fastener types, i.e., nails[3] and screws,[4] are used for the upper and lower joint due to manufacturing reasons, different stiffness values are applied for the upper, $k_{ver,u}$ and $k_{hor,u}$, and lower, $k_{ver,l}$ and $k_{hor,l}$, joints.

Ibrahim and Pettit [34] provide an extensive overview of uncertainties in bolted joints and other fasteners. The authors point out that deterministic response evaluations could lead to unnecessarily conservative system designs, emphasizing the need to consider parameter uncertainties in jointed structures. Consequently, the joints' stiffness values are assigned to be uncertain inputs in this study.

Various studies state coefficients of variation CoV for the stiffness in joints. The identified CoV in the literature ranges from 5% [35] to 25% [36]. Subsequently, CoV = 25% is chosen for the normally distributed probabilities of the joints' stiffness. However, the joints' stiffness values are not known in advance. Hence, an MAP estimation [26, 37] approximates the mean value of the joints' stiffness. The MAP estimation is used instead of a full Bayesian inference, since the necessary large number of evaluations of the hybrid structure's FE model would require too high computational effort. MAP estimation is performed using the equations of Sect. 2.2 while replacing the forward model of the LVL plates with the FE simulation of the hybrid structure. Furthermore, the measurement data of the LVL plates are substituted by the results from the experiments on the hybrid specimen described in Sect. 2.1.1. Finally, the MAP estimation leads to the stiffness values in Table 5.

The identified values lie within a reasonable range with values given by [38], i.e., axial and shear stiffness properties of approximately 50 MPa for a beam structure jointed by M10 bolts and nuts.

2.4 Probabilistic analysis of the hybrid steel–timber building element

Utilizing the identified uncertain inputs, numerical probabilistic analysis for the modal properties of the hybrid steel–timber structure is performed to assess the influence of input uncertainties of the prediction tool. Parameter uncertainties are considered by assuming probability distributions for the inputs [26] and performing an MC simulation [39]. Here, random samples are drawn to compute the natural frequencies of the hybrid element numerically (see, e.g., [39]). Utilizing the MC method, target statistics, i.e., mean values, standard deviations, and percentiles of natural frequencies of the hybrid structure, are estimated by a set of generated realizations computed based on the samples. Latin hypercube sampling (LHS) reduces the realizations necessary for reasonable results by evenly spreading the samples over the entire sampling space [40]. In [11], LHS for MC simulations is investigated for a wooden floor model. The authors concluded that LHS using $n_{LHS} = 40$ sampling steps led to converged results for four sampled parameters. This indicates that if the number of samples n_{LHS} is chosen equal to ten times the dimension d of the parameters $n_{LHS} = 10 \cdot d$, satisfying results can be achieved. The probabilistic prediction tool used in this study is based on the model of Sect. 2.1.2 to determine the influence of model parameter uncertainties on the modal properties of the building element. Thus input uncertainties, i.e., for the LVL material properties (Sect. 2.2), E_x, E_y, G_{xy}, G_{yz} and ρ, and for the joint stiffness values, $k_{ver,u}$, $k_{ver,l}$, $k_{hor,u}$, and k_{horl} (Sect. 2.1.2), are propagated through the simulation model to the resulting natural frequencies $\mathbf{f}_{FE}$ of the hybrid steel–timber test sample.

3 Results

As uncertain LVL material properties are required for the probabilistic analysis of the hybrid steel–timber element, results concerning the Bayesian inference of the LVL's material parameters are presented first. Second, the outcomes of the probabilistic analysis of the hybrid steel–timber element are displayed.

3.1 Stochastic estimates of the material properties of the LVL

The posterior probabilities of the LVL's material properties result from the Bayesian approach (Sect. 2.2) using a Sequential Monte Carlo Sampler with seven chains, including 500 samples each. The outcome is described by the mean values $\hat{\mu}_{\theta_i}$ and the standard deviations $\hat{\sigma}_{\theta_i}$. The mean values are compared to the material parameters

Table 5 Mean values of stiffness of upper (u) and lower (l) joints in vertical (ver) and horizontal (hor) directions

$k_{\text{hor,l}}$ [N/m]	$k_{\text{hor,u}}$ [N/m]	$k_{\text{ver,l}}$ [N/m]	$k_{\text{ver,u}}$ [N/m]
$8.96 \cdot 10^6$	$8.41 \cdot 10^6$	$9.60 \cdot 10^6$	$8.86 \cdot 10^6$

provided by the manufacturer (Table 3) through the deviation of the resulting mean and the provided property $a = 1 - \hat{\mu}_{\theta_i}/\theta_{i,0}$. These results as well as the $\hat{\text{CoV}} = \hat{\sigma}_{\theta_i}/\hat{\mu}_{\theta_i}$ are listed in Table 6. Deviations above $\pm 10\%$ are marked in bold letters.

The difference between inferred and provided material properties lies above 5% for all parameters, often even above 10%, which represents a significant difference emphasizing the relevance of the Bayesian inference. Moreover, the identified posterior probabilities become slightly narrower than the priors for E_x, E_y, G_{xy}, and ρ, which is shown by the smaller $\hat{\text{CoV}}$ (Table 6) of these material parameters compared to the priors' CoV for the density $\text{CoV}_\rho = 0.10$ and for all other material parameters $\text{CoV}_{\theta_i} = 0.25$. The prior and posterior probabilities of all material parameters are plotted together in Fig. 7 to check the identified properties. Here, the narrower posterior probabilities are also visible. Furthermore, for all properties, the prior and posterior probabilities overlap.

Moreover, model validation is performed concerning LVL plate natural frequencies using the forward model (Sect. 2.2.3) and experimentally determined natural frequencies $\mathbf{f}_{\exp,t}$ of the LVL components. For this purpose, natural frequencies of the LVL panels, i.e., $H45i$, $H55i$, and $H65i$, are calculated numerically using an MC simulation (Sect. 2.4), LHS, and 6000 samples for the material properties drawn from the posterior distribution. The computed values f_i are presented in Fig. 8 as box plots together with the experimentally identified values $f_{\exp,t,i}$.

All measured eigenfrequencies lie within the whiskers spanned by the sampled eigenfrequencies or even within the first-to-third quartile values. Hence, the inferred material properties, together with the forward model, represent the LVL material properly.

3.2 Probabilistic modal analysis of hybrid steel–timber structure

The material properties in terms of mean and standard deviation identified before (Table 6) are used in this section, together with the parameters for the joint stiffness (Table 5), in a stochastic analysis of the hybrid steel–timber building element. Nine parameters are assigned to be uncertain and are consequently sampled from their distribution by LHS: E_x, E_y, G_{xy}, G_{yz}, ρ, $k_{\text{hor,l}}$, $k_{\text{hor,u}}$, $k_{\text{ver,l}}$, and $k_{\text{ver,u}}$. Using ten times the dimension of the parameters, the number of samples yields as $n_{\text{LHS}} = 90$. However, to verify the convergence of the results, additional samples are computed, and the results of $n_{\text{LHS}} = 110$ and $n_{\text{LHS}} = 90$ are compared. The comparison is made for the first structural eigenfrequency of the FE model at approximately $f_{\text{FE,hyb}} = 59.4\,\text{Hz}$. The following differences between the two cases are calculated:

- Deviation for mean value: $(1 - f_{\mu,110}/f_{\mu,90}) \cdot 100 = -0.1\%$.
- Deviation for standard deviation: $(1 - f_{\sigma,110}/f_{\sigma,90}) \cdot 100 = -2.8\%$.
- Deviation for 5th percentile: $(1 - f_{5\%,110}/f_{5\%,90}) \cdot 100 = -0.0\%$.
- Deviation for 95th percentile: $(1 - f_{95\%,110}/f_{95\%,90}) \cdot 100 = -0.2\%$.

Hence, the deviations lie below 1% for all evaluated stochastic parameters except for the standard deviation, which lies below 3%. This is assumed to be suitable as it is done similarly in [11, 41].

Table 7 shows the mean values f_μ, standard deviations f_σ, 5th $f_{\text{P}=(0.05)}$, and 95th percentile $f_{\text{P}=(0.95)}$ of the MC simulated results $f_{\text{LHS,hyb}}$ sampled by LHS with $n_{\text{LHS}} = 90$ together with the measured $f_{\exp,\text{hyb}}$ and simulated eigenfrequencies f_{hyb,θ_0} using the initial material properties θ_0 (Table 3) and the joint stiffness values from Table 5. The mean values of $f_{\text{LHS,hyb}}$ differ from f_{hyb,θ_0} due to the deviating material properties identified by Bayesian inference. The identified modes, (1,1), (2,0), (2,1), (3,0), and (0,2), are named similarly to the LVL plates in Fig. 5. For a visual illustration, the plots of Fig. 5 can be considered, since the mode shapes are just scaled to a larger geometry for the hybrid structure.
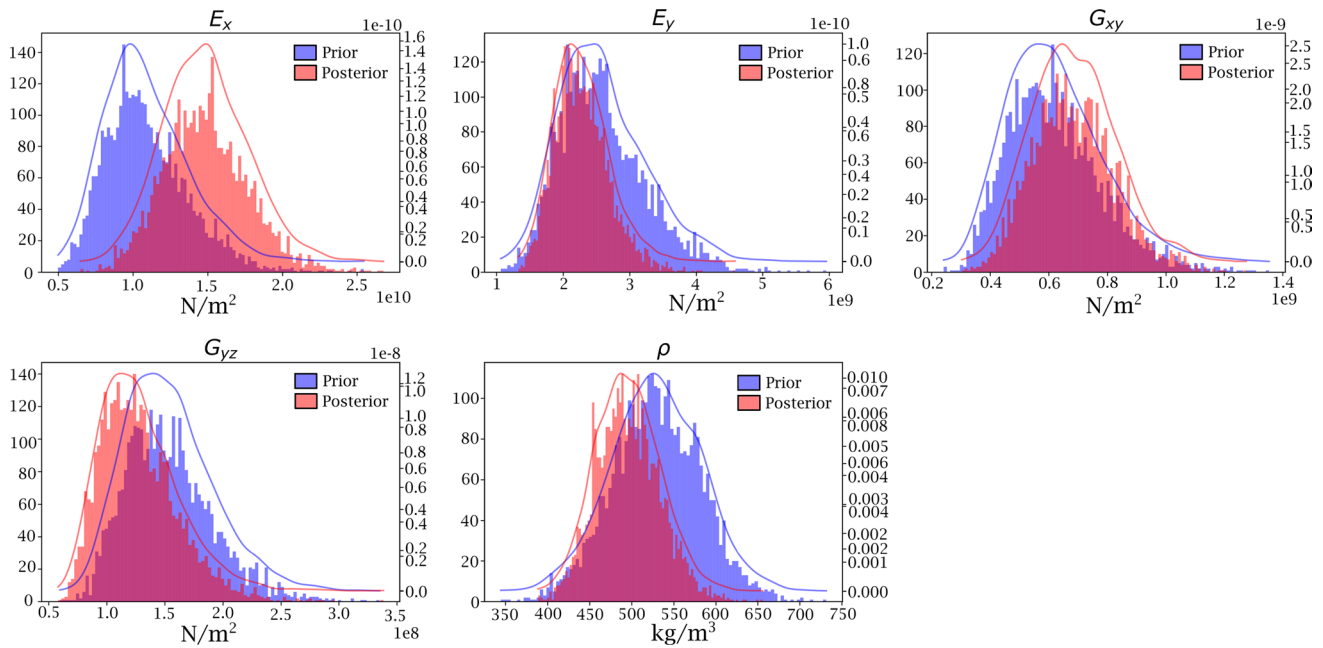
Table 6 Mean values $\hat{\mu}_{\theta_i}$, the $\hat{\text{CoV}}$, the manufacturer's data $\theta_{i,0}$, and the deviation a are listed. Deviations above $\pm 10\%$ are marked in bold letters

	$\hat{\mu}_{\theta_i}$	$\hat{\text{CoV}}$	a	θ_0
$E_x/10^{10}\,\text{N/m}^2$	1.49	0.19	**− 0.41**	1.06
$E_y/10^9\,\text{N/m}^2$	2.27	0.18	0.09	2.50
$G_{xy}/10^8\,\text{N/m}^2$	6.86	0.21	**− 0.14**	6.00
$\rho\,\text{kg/m}^3$	496	0.08	0.06	530
$G_{yz}/10^8\,\text{N/m}^2$	1.28	0.26	**0.15**	1.50

Fig. 7 Probability densities of the inferred material properties—priors (blue) and posteriors averaged for all chains (rose)

However, it has to be noted that the fiber direction of the LVL panels is oriented along its shorter edge, whereas for the hybrid panels, the fiber direction follows the long side of the panel. Hence, for the hybrid structure, the first bending mode occurs along this long side, whereas for the LVL plates, it occurs along the transversal direction. In the case of the first mode, $(1,1)$, the mean value of $f_{\mu,\text{LHS,hyb},(1,1)}$ is close to the measured eigenfrequency $f_{\text{exp,hyb},(1,1)} = 57.1\,\text{Hz}$. Hence, the calculated difference equals

$$\Delta_{\mu,\text{LHS},(1,1)-\exp,(1,1)} = 2.3\,\text{Hz}. \tag{22}$$

Moreover, the identified CoV for the MC simulations' mean and standard deviation range between 0.4% and 2.86%.

If the 5th and 95th percentiles are examined, which is state of the art in the building sector [42], the difference between the respective percentile values

$$\Delta_{5^{th}-95^{th}} = f_{\text{LHS,P}=(0.95)} - f_{\text{LHS,P}=(0.05)} \tag{23}$$

ranges from 1.2 Hz for mode $(3,0)$ to 7.0 Hz for mode $(2,0)$ (Table 7).

In Fig. 9, the probability density function estimated from the samples of the first natural frequency for mode $(1,1)$ is visualized together with the measured frequencies, and the 5th and 95th percentile values. Although the measured natural frequency does not perfectly match the point of maximum probability of the probability density function, it is still covered by the percentile values, showing an adequate prediction of the FE model concerning the lowest natural frequency of the hybrid element. However, the remaining

measured natural frequencies $f_{\text{exp,hyb}}$ (Table 7) do not lie within the percentile values computed by the MC simulation. One possible reason for the deviations in the modes $(2,0)$, $(3,0)$, and $(2,1)$ is the assumption of an ideal geometry of the steel core in the FE model. In the ideal configuration, stiffness is gained via the trapezoidal slopes of the steel core. However, since these are most likely not ideally positioned in the test specimen, a stiffer structure is obtained in the simulation than in the measurement. This is reflected in the higher natural frequencies. In the case of mode $(0,2)$, pre-deformations and residual stresses of the steel core could stiffen the test specimen as a result of the manufacturing process. Since no pre-deformations and residual stresses are considered in the model, the model behaves less stiffly than in the measurement.

4 Discussion

The statistical estimates of the LVL material properties are used in the forward model to compute the natural frequencies of LVL plates. The computed values comply well with the measured eigenfrequencies for equivalent LVL plates, which indicates physically meaningful inferred material properties. Furthermore, the inferred posterior distributions are narrower than the priors, which implies less uncertainty of the material parameters once the measurement data are taken into account.
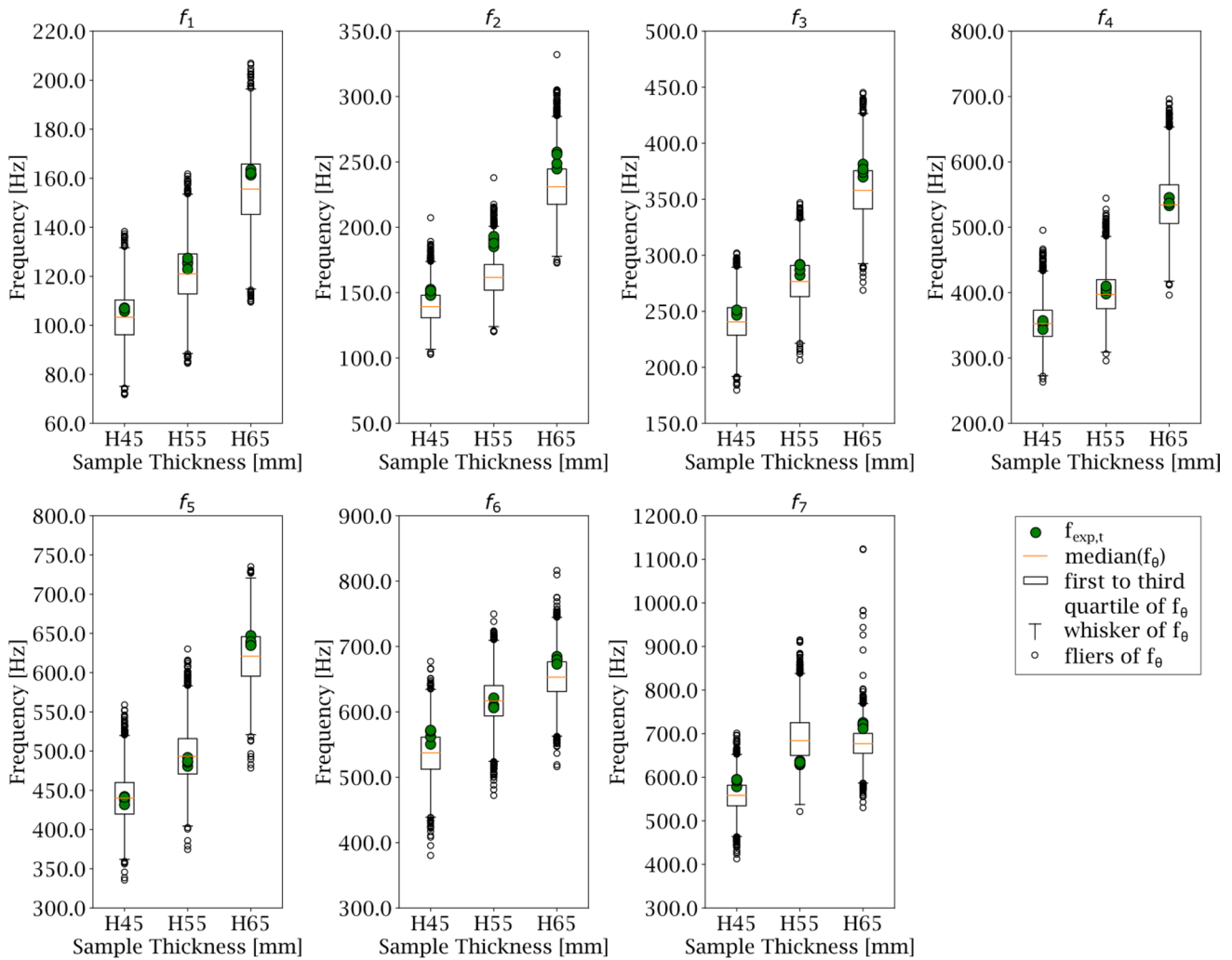
Fig. 8 Box plots of simulated eigenfrequencies of LVL plates using inferred material properties compared to experimentally determined eigenfrequencies (green markers)

The MC simulation of the hybrid steel–timber building element leads to converged results for 90 Latin Hypercube samples. The resulting statistical estimates of the natural frequencies show deviations of 5–7 Hz for some of the 5th and 95th percentiles, which represents a significant difference and, hence, should be addressed for a proper design of a structure. Moreover, the deviation of the sampled mean values for the natural frequencies differs from the computed frequencies using the initial material properties provided by the manufacturer, which emphasizes the need for material parameter identification.

The first measured eigenfrequency for mode (1,1) lies within the range spanned by the simulated eigenfrequencies, which is essential since the first eigenfrequency of a floor is relevant for a design in terms of serviceability related to vibration, e.g., in the European timber design standard [43]. Still, the MC simulation results do not cover the other experimentally identified natural frequencies. Further investigations might lead to deeper insight, e.g., considering frequency-dependent material and joint parameters or residual stresses in the hybrid element. Furthermore, an approach using Bayesian inference not only for the wooden material properties but also for the joint parameters might lead to better results. However, a faster model is required for this. Possible approaches could be surrogate models or model order reduction.

Moreover, it should be noted that, currently, no strength-related characteristics are included in the investigations. Static test series and further studies concerning, e.g., load-carrying capacity could be analyzed in future studies but are out of the scope of the current work.

Table 7 Mean values μ, standard deviation σ, 5th percentile $f_{P=(0.05)}$, and 95th percentile $f_{P=(0.95)}$ of eigenfrequencies $f_{\text{LHS,hyb}}$, ranges between 5th and 95th percentile values $\Delta_{5^{th}-95^{th}}$, measured $f_{\text{exp,hyb}}$ and initially simulated eigenfrequencies f_{hyb,θ_0} are listed

f_i [Hz] for mode	$f_{\text{LHS,hyb}}$ [Hz]				$\Delta_{5^{th}-95^{th}}$ [Hz]	f_{hyb,θ_0} [Hz]	$f_{\text{exp,hyb}}$ [Hz]
	μ	σ	$P=(0.05)$	$P=(0.95)$			
(1,1)	59.4	1.7	56.8	62.5	5.7	52.1	57.1
(2,0)	83.6	2.3	80.1	87.1	7.0	77.2	70.9
(2,1)	105.3	0.8	103.3	106.2	3.0	95.4	76.4
(3,0)	108.4	1.4	105.6	110.1	4.5	99.7	88.3
(0,2)	99.5	0.4	98.9	100.1	1.2	102.3	113.9
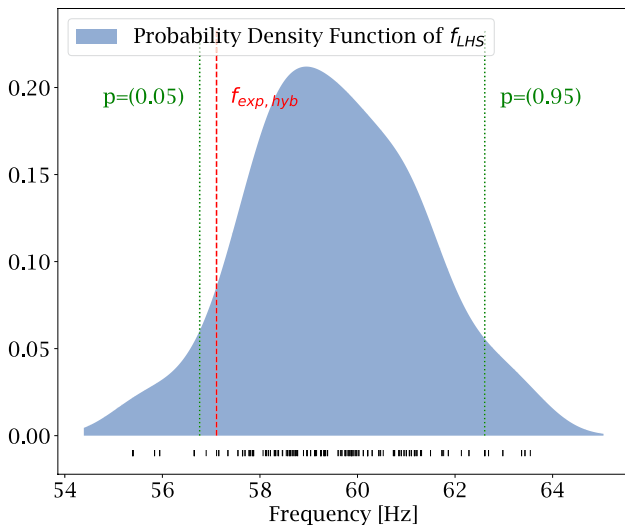
Fig. 9 Probability density function estimated by $f_{\text{LHS,hyb},(1,1)}$, measured frequencies $f_{\text{exp,hyb},(1,1)}$, and percentiles $P=(0.05)$ and $P=(0.95)$

5 Conclusions

In summary, this research article leverages Bayesian inference and Monte Carlo simulation to address uncertainty in the modal properties of a hybrid steel–timber building element. The primary goal of the research is to facilitate more efficient building designs by shifting from traditional conservative safety factors to an approach that accounts for data uncertainty. The hybrid building element under investigation features a structure comprising a trapezoidal steel web and laminated veneer lumber flanges. Given the inherent variability in timber materials, Bayesian inference is employed to derive probability distributions representing the timber's material properties, thereby providing a realistic representation of uncertainty. The key findings are itemized as follows:

- The posterior probabilities obtained through Bayesian inference reveal narrower probability distributions than the prior knowledge, denoting a reduction in uncertainty regarding the timber's material properties.
- The research uncovers an unexpected and substantial deviation of inferred mean values from manufacturer-provided data, emphasizing the importance of accounting for real-world variability in structural design.

The inferred material properties, together with uncertain joint parameters, are utilized in a Monte Carlo simulation. Mean values of joint properties are estimated using maximum a posteriori estimation, and the coefficient of variation is assigned based on literature data. Employing Latin hypercube sampling and a finite element model, a probabilistic analysis of the hybrid building element is performed. Here, the following outcomes are observed:

- The 5th and 95th percentiles of the structure's natural frequencies resulting from the Monte Carlo simulation span a range of up to 7 Hz for the natural frequency at 83.6 Hz. This range emphasizes the significant variability inherent in the structural response and underlines the critical necessity of considering uncertainty in the design of building elements.
- The first measured natural frequency for mode (1,1) falls within the range spanned by the simulated eigenfrequencies, which is crucial for designing a floor with consideration for vibration-related serviceability. However, it is observed that the other measured eigenfrequencies do not align with the range of eigenfrequencies calculated by the Monte Carlo simulation, suggesting the need for further investigations.

These findings collectively contribute to advancing the field of structural engineering, emphasizing the significance of probabilistic modeling and uncertainty quantification in optimizing building designs for enhanced efficiency. Future research avenues could involve extending Bayesian inference to incorporate joint parameters and exploring alternative fastener models to refine our understanding of hybrid element behavior.

Appendix

The Lagrangian for the orthotropic Mindlin plates is computed as [28]

$$L = T - U \tag{24}$$

with the strain energy U and the kinetic energy T. The strain energy is calculated as

$$
\begin{aligned}
U = \iint_A \Bigg\{ & D_{11}\left(\frac{\partial \psi_x}{\partial x}\right)^2 + D_{22}\left(\frac{\partial \psi_y}{\partial y}\right)^2 \\
& + (\mu_{xy}D_{11} + \mu_{yx}D_{22})\frac{\partial \psi_x}{\partial x}\frac{\partial \psi_y}{\partial y} \\
& + D_{xy}\left(\frac{\partial \psi_x}{\partial y} + \frac{\partial \psi_y}{\partial x}\right)^2 + \kappa G_{xz}h\left(\psi_x + \frac{\partial w}{\partial x}\right)^2 \\
& + \kappa G_{yz}h\left(\frac{\partial w}{\partial y}\right)^2 \Bigg\}\mathrm{d}x\mathrm{d}y
\end{aligned}
\tag{25}
$$

with the flexural rigidities of the plate

$$D_{11} = \frac{E_x h^3}{12(1 - \nu_{xy}\nu_{yx})}, \tag{26}$$

$$D_{12} = \frac{\nu_{xy}E_x h^3}{12(1 - \nu_{xy}\nu_{yx})}, \tag{27}$$

$$D_{21} = \frac{\nu_{yx}E_y h^3}{12(1 - \nu_{xy}\nu_{yx})}, \tag{28}$$

$$D_{22} = \frac{E_y h^3}{12(1 - \nu_{xy}\nu_{yx}^2)}, \tag{29}$$

$$D_{xy} = \frac{G_{xy}h^3}{12}. \tag{30}$$

Moreover, the total kinetic energy is given as

$$T = \frac{\rho h \omega^2}{2}\int_0^l \int_0^b [w^2 + h^2(\psi_x^2 + \psi_y^2)/12]\mathrm{d}x\mathrm{d}y. \tag{31}$$

Data availability Some or all data, models, or codes that support the findings of this study are available from the corresponding author upon reasonable request.

Declarations

Competing interests Bettina Chocholaty was financially supported by the German Federal Ministry of Food and Agriculture through the Fachagentur Nachwachsende Rohstoffe e.V. (FNR) (grant number 22009817). All authors declare that they have no conflicts of interest.

Ethical statement No experiments on animals and humans are conducted in this article. There are no human subjects in this study and informed consent is not applicable. Furthermore, critical data, such as personal information, are not analyzed.

References

1. Cheraghi-Shirazi N, Crews K, Malek S. Review of Vibration Assessment Methods for Steel-Timber Composite Floors. Buildings. 2022;12(12):2061. https://doi.org/10.3390/buildings12122061.
2. Hassanieh A, Chiniforush AA, Valipour HR, Bradford MA. Vibration behaviour of steel-timber composite floors, part (2): evaluation of human-induced vibrations. J Constr Steel Res. 2019;158:156–70. https://doi.org/10.1016/j.jcsr.2019.03.026.
3. Technical Committee ISO/TC 98/SC 2. ISO 10137:2007(E) - Bases for design of structures - Serviceability of buildings and walkways against vibrations; 2007.
4. Technical Committee ISO/TC 43/SC 2. EN ISO 10140-3 - Acoustics - Laboratory measurement of sound insulation of building elements - Part 3: Measurements of impact sound insulation; 2021. https://doi.org/10.31030/3237068.
5. Chocholaty B, Roozen NB, Maeder M, Marburg S. Vibroacoustic response of steel-timber composite elements. Eng Struct. 2022;271: 114911. https://doi.org/10.1016/j.engstruct.2022.114911.
6. Chiniforush AA, Alamdari MM, Dackermann U, Valipour HR, Akbarnezhad A. Vibration behaviour of steel-timber composite floors, part (1): Experimental & numerical investigation. J Constr Steel Res. 2019;161:244–57. https://doi.org/10.1016/j.jcsr.2019.07.007.
7. Soize C. A comprehensive overview of a non-parametric probabilistic approach of model uncertainties for predictive models in structural dynamics. J Sound Vib. 2005;288(3):623–52. https://doi.org/10.1016/j.jsv.2005.07.009.
8. Brake MR. The mechanics of jointed structures. Cham: Springer; 2016.

9. Gant F, Rouch P, Champaney L. Updating of uncertain joint models using the Lack-of-Knowledge theory. Computers & Structures. 2013;128:128–35. https://doi.org/10.1016/j.compstruc.2013.06.013.

10. Qian C, Ménard S, Bard D, Negreira J. Development of a vibroacoustic stochastic finite element prediction tool for a CLT floor. Appl Sci. 2019;9(6):1106. https://doi.org/10.3390/app9061106.

11. Persson P, Flodén O. Effect of material parameter variability on vibroacoustic response in wood floors. Appl Acoust. 2019;146:38–49. https://doi.org/10.1016/j.apacoust.2018.10.034.

12. Sepahvand K, Marburg S. Identification of composite uncertain material parameters from experimental modal data. Probab Eng Mech. 2014;37:148–53. https://doi.org/10.1016/j.probengmech.2014.06.008.

13. Sepahvand K, Marburg S, Hardtke HJ. Stochastic free vibration of orthotropic plates using generalized polynomial chaos expansion. J Sound Vib. 2012;331(1):167–79. https://doi.org/10.1016/j.jsv.2011.08.012.

14. Gogu C, Haftka R, Le Riche R, Molimard J, Vautrin A, Sankar B. Bayesian statistical identification of orthotropic elastic constants accounting for measurement and modeling errors. In: 50th AIAA/ASME/ASCE/AHS/ASC Structures, Structural Dynamics, and Materials Conference 17th AIAA/ASME/AHS Adaptive Structures Conference 11th AIAA No; 2009. p. 2258. https://doi.org/10.2514/6.2009-2258.

15. Daghia F, de Miranda S, Ubertini F, Viola E. Estimation of elastic constants of thick laminated plates within a Bayesian framework. Compos Struct. 2007;80(3):461–73. https://doi.org/10.1016/j.compstruct.2006.06.030.

16. Melzerová L, Janda T, Šejnoha M, Šejnoha J. FEM models of glued laminated timber beams enhanced by Bayesian updating of elastic moduli. International Journal of Civil and Environmental Engineering. 2015;9(5):692–8.

17. Schneider F, Papaioannou I, Straub D, Winter C, Müller G. Bayesian parameter updating in linear structural dynamics with frequency transformed data using rational surrogate models. Mech Syst Signal Process. 2022;166: 108407. https://doi.org/10.1016/j.ymssp.2021.108407.

18. Ewins DJ. Modal Testing - Theory, Practice and Application. New York: John Wiley & Sons; 2009.

19. ANSYS, Inc . Ansys Engineering Simulation Software; 2019.R1. Available from: https://www.ansys.com/.

20. Shen Z, Liu X, Zang C, Hu S. Bayesian Uncertainty Identification of Model Parameters for the Jointed Structures with Nonlinearity. Shock and Vibration. 2021;2021. https://doi.org/10.1155/2021/2638995.

21. Langer P, Maeder M, Guist C, Krause M, Marburg S. More than six elements per wavelength: The practical use of structural finite element models and their accuracy in comparison with experimental results. J Comput Acoust. 2017;25(04):1750025. https://doi.org/10.1142/s0218396x17500254.

22. Ballast DK. Handbook of construction tolerances. John Wiley & Sons; 2007.

23. Andrej A. Schneider: Bautabellen für Ingenieure. vol. 21. Bundesanzeiger Verlag; 2014. https://doi.org/10.1002/best.201190039.

24. STEICO SE. Konstruktionsheft von STEICO zu LVL/Furnierschichtholz; 2020. Accessed: 2021-01-19. Available from: https://www.steico.com/de/downloads/dokumente/produkte-allgemeines.

25. Faber M, Vrouwenvelder T. JCSS PROBABILISTIC MODEL CODE - Part III: Resistance Models; 2006. Accessed: 2023-02-02. https://www.jcss-lc.org/jcss-probabilistic-model-code/.

26. Gelman A. Bayesian Data Analysis. 3rd ed. Chapman and Hall/CRC; 2013.

27. Xiang N. Model-based Bayesian analysis in acoustics-A tutorial. The Journal of the Acoustical Society of America. 2020;148(2):1101–20. https://doi.org/10.1121/10.0001731.

28. Shi D, Zhuang Z, Zhang T. Free vibration analysis of orthotropic rectangular Mindlin plates with general elastic boundary conditions. In: INTER-NOISE and NOISE-CON Congress and Conference Proceedings. vol. 249. Institute of Noise Control Engineering; 2014. p. 1477–1485.

29. Mottershead JE, Link M, Friswell MI, Schedlinski C. Model updating. Handbook of Experimental Structural Dynamics. 2020;p. 1–53.

30. Basaglia BM, Li J, Shrestha R, Crews K. Response prediction to walking-induced vibrations of a long-span timber floor. J Struct Eng. 2021;147(2):04020326. https://doi.org/10.1061/(asce)st.1943-541x.0002888.

31. Wesner JS, Pomeranz JP. Choosing priors in Bayesian ecological models by simulating from the prior predictive distribution. Ecosphere. 2021;12(9): e03739. https://doi.org/10.1101/2020.12.10.419713.

32. Salvatier J, Wiecki TV, Fonnesbeck C. Probabilistic programming in Python using PyMC3. PeerJ Computer Science. 2016;2: e55. https://doi.org/10.7717/peerj-cs.55.

33. Martin O. Bayesian Analysis with Python: Introduction to statistical modeling and probabilistic programming using PyMC3 and ArviZ. Packt Publishing Ltd; 2018.

34. Ibrahim R, Pettit C. Uncertainties and dynamic problems of bolted joints and other fasteners. J Sound Vib. 2005;279(3–5):857–936. https://doi.org/10.1016/j.jsv.2003.11.064.

35. Gangadharan SN, Nikolaidis E, Haftka RT. Probabilistic system identification of two flexible joint models. AIAA J. 1991;29(8):1319–26. https://doi.org/10.2514/6.1990-1144.

36. Segalman DJ, Gregory DL, Starr MJ, Resor BR, Jew MD, Lauffer JP, et al. Handbook on dynamics of jointed structures. Sandia National Laboratories, Albuquerque. 2009;.

37. Gauvain JL, Lee CH. Maximum a posteriori estimation for multivariate Gaussian mixture observations of Markov chains. IEEE transactions on speech and audio processing. 1994;2(2):291–8. https://doi.org/10.1109/89.279278.

38. Shah MA, Yunus M, Rani MA, Omar R, Mora A. Stochastic model updating of bolt-jointed structure for structural dynamics applications. International Journal of Automotive and Mechanical Engineering. 2021;18(2):8760–71. https://doi.org/10.15282/ijame.18.2.2021.14.0670.

39. Kroese DP, Taimre T, Botev ZI. Handbook of monte carlo methods. John Wiley & Sons; 2013.

40. Olsson AM, Sandberg GE. Latin hypercube sampling for stochastic finite element analysis. J Eng Mech. 2002;128(1):121–5. https://doi.org/10.1061/(asce)0733-9399(2002)128:1(121).

41. Luegmair M, Schmid JD. Challenges in vibroacoustic vehicle body simulation including uncertainties. SAE Technical Paper; 2020.

42. Technical Committee CEN/TC 250. DIN EN 1990:2021-10 - Eurocode: Basis of structural design - German Version; 2021.

43. Technical Committee CEN/TC 250. Eurocode 5: Design of timber structures, Part 1-1: General - Common rules and rules for buildings [Standard]; 2010.

A.3 Paper C

Vibration and impact sound properties of hybrid steel-timber floor structures

Bettina Chocholaty, Nicolaas Bernardus Roozen, Karl-Alexander Hoppe, Marcus Maeder, Steffen Marburg

TECHNICAL **&** **A**PPLIED **A**RTICLE

OPEN **∂** **A**CCESS

Vibration and impact sound properties of hybrid steel-timber floor structures

Bettina Chocholaty[1],[*] (ID), Nicolaas Bernardus Roozen[2],[1] (ID), Karl-Alexander Hoppe[1] (ID), Marcus Maeder[1] (ID), and Steffen Marburg[1] (ID)

[1] Chair of Vibroacoustics of Vehicles and Machines, Department of Engineering Physics and Computation, TUM School of Engineering and Design, Technical University of Munich, Boltzmannstr. 15, 85748 Garching n. Munich, Germany

[2] Laboratory of Soft Matter and Biophysics, Katholieke Universiteit Leuven, Celestijnenlaan 200D, 3001 Leuven, Belgium

Abstract – Lightweight floor structures, such as timber or hybrid timber floors, face challenges associated with excessive vibrations and elevated levels of low-frequency impact sound. Especially here, accurate prediction of a floor's vibration and acoustic behavior is essential. However, typical laboratory testing of building elements is costly and time-consuming. To reduce costs, in this study, adapted simulations are carried out on two types of hybrid steel-timber floor structures to evaluate vibrations and impact sound. The hybrid elements are made of laminated veneer lumber as the top and bottom layers and a trapezoidal steel component as the web. Vibration measurements are used in combination with Bayesian optimization to efficiently calibrate Finite Element models, which are subsequently utilized to quantify and validate the floor structures regarding vibrations and impact sound. The two types of cross-sections, i.e., closed and open, are investigated and compared. The impact sound pressure level computations reveal promising results in predicting the behavior of the hybrid structures. However, further countermeasures are required to fulfill vibration serviceability requirements.

Keywords: Hybrid steel-timber floor, Vibrations, Impact sound, Laminated veneer lumber

1 Introduction

With the growing significance of carbon neutrality and environmental sustainability, the construction industry is actively developing sustainable solutions. Research on sustainable construction has recently expanded beyond conventional materials to encompass hybrid structures that incorporate timber in conjunction with steel [1–3], and concrete [4, 5]. These hybrid building elements have led to a range of investigations involving aspects such as vibration characteristics [1, 2], economic viability, environmental sustainability [3], and safety performance [6]. One notable area of concern in these modern hybrid structures, particularly in the context of extended spans and slender designs for lightweight floors such as wood and hybrid wood floors, evolves around their susceptibility to low resonance frequencies and annoying vibrations, which can potentially cause discomfort among occupants [7, 8]. Consequently, a significant challenge in the context of large-span timber floors lies in the exceedance of allowable vibration limits, thus making vibration serviceability a paramount criterion for design [9].

As an example, research by Hassan et al. [10] illustrates that in terms of deformations, Cross-Laminated Timber slabs with spans of 7 m and relatively modest thickness can be accommodated. However, issues arise as natural frequencies dip below 8 Hz for spans of approximately 4.5 m [10]. In such scenarios, composite or hybrid timber structures emerge as potential solutions. Perković et al. [11], for instance, determined a natural frequency of approximately 10 Hz for a hybrid concrete-timber floor with a 7-m span.

Furthermore, lightweight structures like timber or hybrid timber floors often encounter challenges with impact sound insulation [12]. Typically, building standards and regulations rely on laboratory testing for assessing the suitability of floor structures. However, these laboratory tests, especially those concerning impact sound insulation, are time-consuming and costly [13, 14] and are conducted in certified testing facilities. In the context of vibrational characteristics, either calculations or certified measurements are imperative [15]. Therefore, when adequately executed, simulations have emerged as an appealing alternative to laboratory tests.

Simulation-based engineering design often employs numerical models such as those based on the Finite Element

*Corresponding author: bettina.chocholaty@tum.de

Method (FEM), a tool extensively used by engineers across various disciplines. In practice, there tends to be a discrepancy between FEM predictions and actual test results, attributed to model form errors and approximation errors, both considered types of epistemic uncertainty [16]. To minimize the discrepancy between simulations and measurements, model parameters are iteratively adjusted, a procedure referred to as model updating. This iterative process reduces approximation errors and enhances both the reliability and accuracy of the model. The procedure involves the identification of model parameters by minimizing a problem-specific objective function [17]. Various approaches have been proposed for this purpose, whereas the approach of Bayesian optimization, in particular, offers a means to minimize the need for extensive model evaluations [18]. Its efficiency results from employing Gaussian process regression and an acquisition function for an iterative search of optimal model parameters [19].

Furthermore, recognizing the challenges presented by vibroacoustic properties of hybrid steel-timber floors, recent research [2, 20, 21] has explored innovative floor elements. In [2], the analysis focuses on a structure comprising a wooden plate combined with an H-shaped steel beam, primarily evaluating its vibration serviceability. In [20], a modular hybrid steel-timber floor constructed by Cross Laminated Timber and a U-shaped steel beam is studied experimentally. Meanwhile, [21] delves into the vibrational behavior of a hybrid steel-timber structure featuring top and bottom laminated veneer lumber (LVL) plates and a trapezoidal steel web floor element in between, with a particular emphasis on the influence of joints on overall vibroacoustics.

However, despite these valuable contributions, there remains a need for a comprehensive assessment of the acoustic properties of hybrid timber-steel structures, which are relevant for the applicability of the building elements in practice. Moreover, the structure examined in [21] has yet to be subjected to an investigation regarding its vibration serviceability. This study addresses this gap by studying both vibration serviceability and impact sound levels of the hybrid floors presented in [21]. To achieve this objective, the applied approach involves the calibration of a Finite Element model (FE model) using Bayesian optimization techniques [22]. The Bayesian optimization framework is chosen since it requires fewer model evaluations for a minimization than commonly used approaches by applying Gaussian process regression [18]. The calibration process is based on data derived from experimental vibration analysis, which allows the identification of critical parameters associated with the joints within these hybrid structures. Subsequently, using the calibrated simulation model, vibration limits and impact sound criteria are evaluated, providing valuable insights into the applicability and performance of these innovative floor elements. As a result, this research offers a comprehensive numerical exploration of the vibroacoustic behavior of a novel LVL-trapezoidal steel floor design. These findings, in turn, offer initial assessments for the prospective integration of these building components into sustainable construction practices.

2 Hybrid steel-timber floor structures

This study numerically analyzes hybrid structures composed of LVL and trapezoidal steel frames. In detail, it is constructed by top and bottom LVL plates with a trapezoidal steel core in between. The structural components are connected by fasteners whose stiffness values are unknown in advance. The numerical analysis is conducted using FEM. First, a calibration of the unknown joint parameters p is performed utilizing numerically determined natural frequencies as well as mode shapes and results from experimental modal analyses on small-scale test specimens, i.e., $S1^*$ and $S2^*$. Subsequently, the updated joint parameters $p_{n_{it}}$ are used in an FE simulation to analyze large-scale floor specimens, i.e., $S1$ and $S2$, regarding vibration dose values (VDV) and impact sound pressure levels. The impact sound pressure level simulations use a numerically implemented tapping machine load. The overall workflow is visualized in Figure 1.

## 2.1 Description of investigated structures and simulation models

Two configurations are investigated: a closed ($S1$) and an open ($S2$) cross-section. Snippets of the test specimens are visualized in Figure 2 together with their geometric properties, which are also listed in Table 1.

According to ISO 10140-5 [23], the recommended size of a floor structure, which is to be analyzed concerning impact sound, is given as 10–20 m^2, and the shorter edge should be greater than 2.3 m. Hence, the dimensions of 3.6 m × 2.8 m are chosen for the hybrid floors (Tab. 1). However, due to the testing facility's limited spatial capacities, it has been impossible to carry out vibration measurements on the entire floor structures as given in Table 1. Hence, smaller specimens are used for the model validation and calibration, i.e., a closed $S1^*$ and an open cross-section $S2^*$.

The main difference between the open and closed cross-sections lies in the design of the lower timber plate, which is either a continuous wooden panel for closed cross-sections or made of several separate panels for open configurations. Based on preliminary structural investigations, it has been determined that the upper screw connection may be too weak in terms of load-carrying capacity and that nails would be beneficial for the upper joint. However, as the nail connection can only be made from the steel side, the open variant has been designed. The respective mounting direction of the fasteners can also be seen in Figure 2. Obviously, the different geometry, fasteners, and materials used for both types of cross-sections influence the dynamic behavior, e.g., the modal properties, of the investigated systems, which is why the two types are subsequently compared concerning VDV and impact sound insulation.

In the case of the closed form, both LVL plates are built of the material *BauBuche*[1] *Type Q* (*BB-Q*). For the open

---

[1] Hardwood LVL by Pollmeier Massivholz GmbH & Co.KG, D-99831 Amt Creuzburg, Germany.
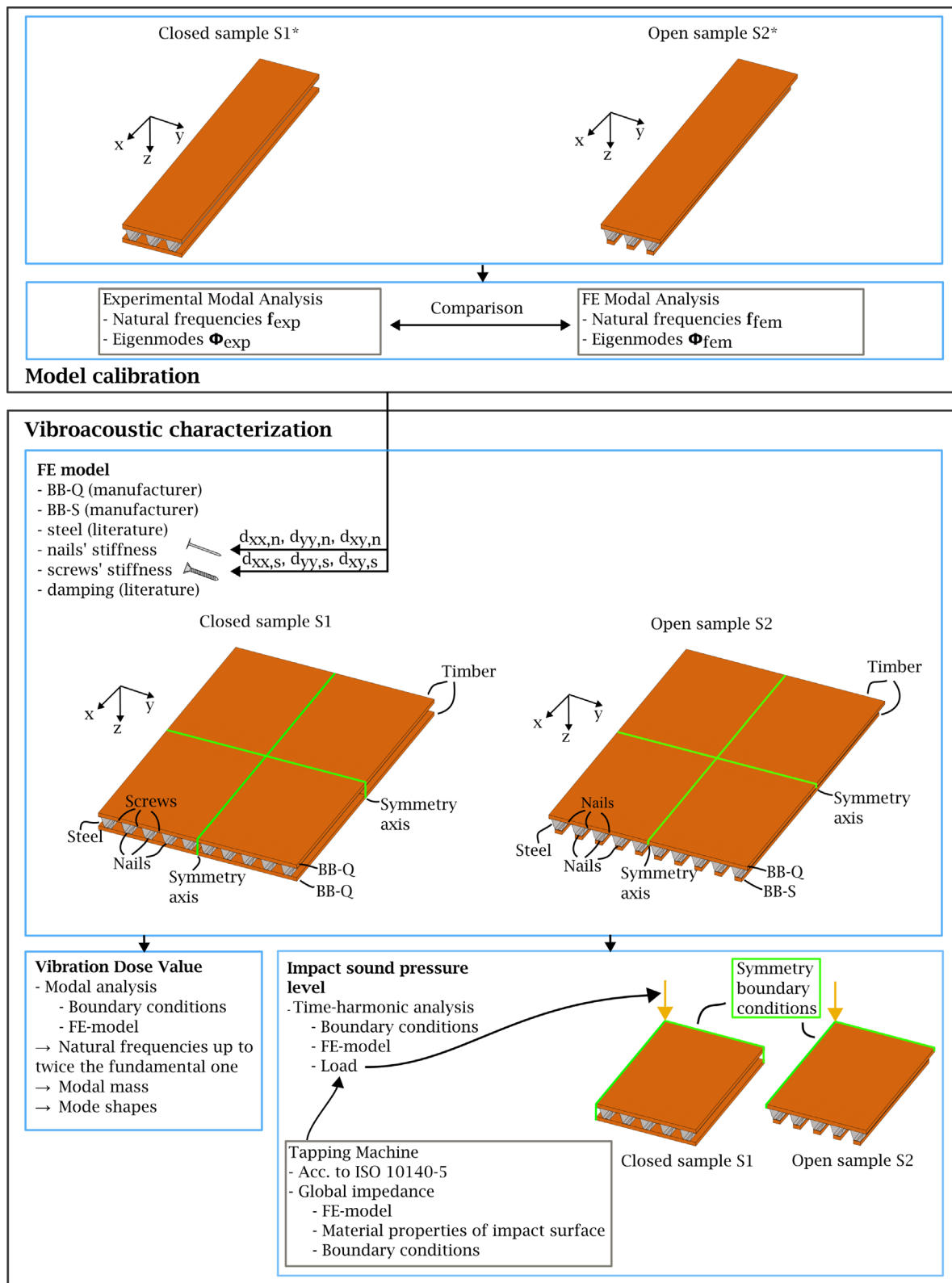
Figure 1. Overall workflow of the study: calibration of unknown model parameters p is performed utilizing numerically determined natural frequencies as well as mode shapes and results from experimental modal analyses on the small-scale test specimens, $S1^*$ and $S2^*$. The updated parameters $p_{n_{it}}$ are used in a subsequent Finite Element simulation to analyze the large-scale floor specimens, $S1$ and $S2$, regarding vibration dose values and impact sound pressure levels. The impact sound pressure level simulations use a numerically implemented tapping machine load.
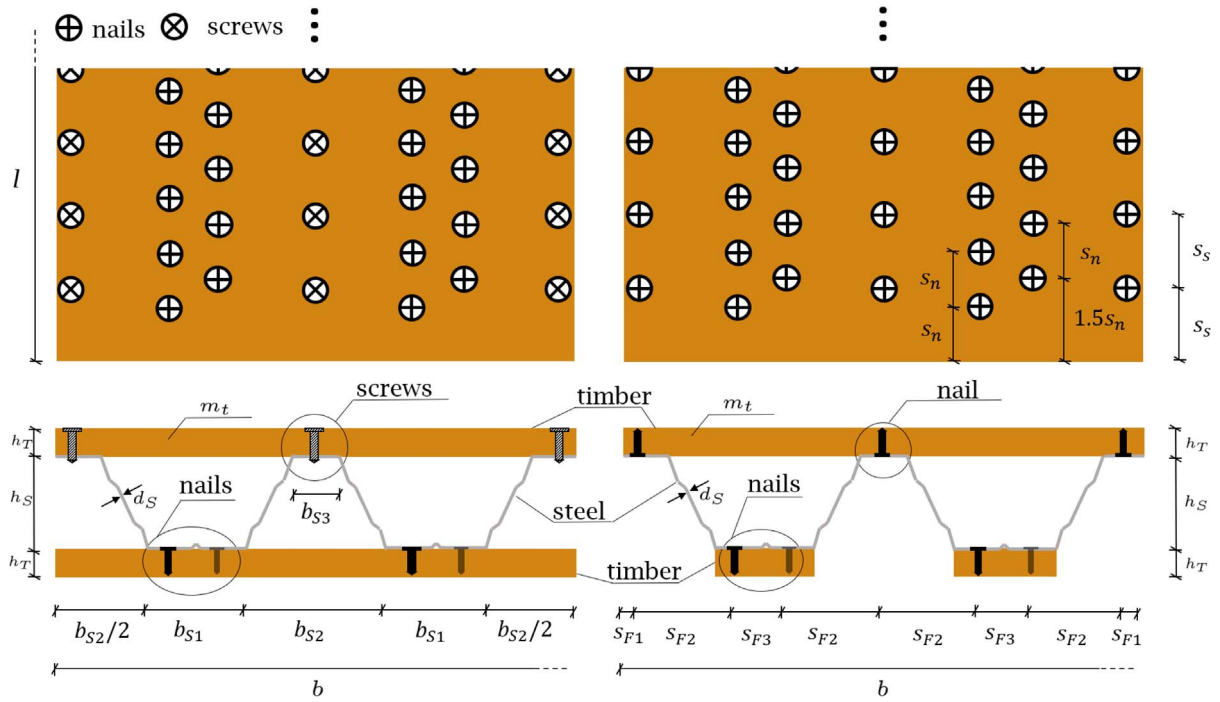
Figure 2. Snippets of closed (left, $S1$) and open (right, $S2$) hybrid LVL and trapezoidal steel elements. The lower timber plate is built of a continuous lower wooden panel for closed cross-sections and made of several separate panels for open configurations. The respective geometrical parameters are given in Table 1.

Table 1. Specimens $S1$ (closed) and $S2$ (open): the geometric parameters are defined in Figure 2. All geometric quantities are given in [m].

Sample	$S1$	$S2$
Cross-section type c_T	Closed	Open
Material of LVL plates m_T	BB-Q	BB-Q & BB-S
Length l	3.60	3.60
Width b	2.80	2.80
Thickness of LVL plates h_T	0.040	0.040
Thickness of steel plates d_S	$0.75 \cdot 10^{-3}$	$1.50 \cdot 10^{-3}$
Height of steel core h_S	0.155	0.155
Width steel b_{S1}	0.110	0.110
Width steel b_{S2}	0.170	0.170
Width steel b_{S3}	0.040	0.040
Longitudinal upper spacing s_s	0.120	0.120
Longitudinal lower spacing s_n	0.090	0.090
Transversal fastener position s_{F1}	0.010	0.010
Transversal fastener position s_{F2}	0.103	0.103
Transversal fastener position s_{F3}	0.050	0.050

Table 2. Material properties of LVL and steel provided by the manufacturer and literature [24, 25].

Material	E_x [N/m^2]	E_y [N/m^2]	G_{xy} [N/m^2]	v_{xy} [−]	ρ [kg/m^3]
BB-Q	1.28×10^{10}	2.00×10^{9}	8.20×10^{8}	0.04	800
BB-S	1.68×10^{10}	4.70×10^{8}	7.60×10^{8}	0.04	800
Steel	2.10×10^{11}	$2.10 \times 10^{11} = E_x$	8.10×10^{10}	0.3	7850
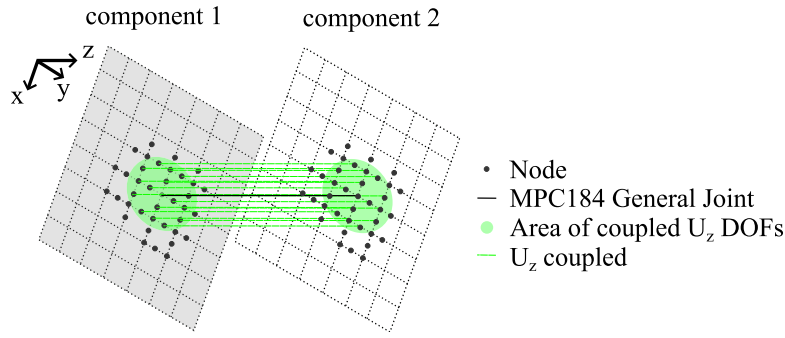
Figure 3. Fastener model: an MPC184 general joint element (represented by a black line) using a stiffness matrix between nodes related to fasteners on the substructures (grids). Coincident nodes at the interface of steel and timber are coupled related to the z-displacement (green lines) within an area surrounding the fastener (green circle).

cross-section, the upper plate is also made of *BB-Q* whereas the lower one is made of *BauBuche Type S* (*BB-S*) [24]. The respective material properties provided by the manufacturer [24] or taken from literature [25] are given in Table 2. The numerical studies use the commercial FE software *ANSYS* [26]. For the FE model, the structural components are represented by quadratic shell elements (SHELL281) with the provided orthotropic material characteristics for the timber parts and isotropic material properties for the steel sheets. Both specimen cross-section types use a trapezoidal core using steel with a nominal yield strength of $f_{y,k} = 320$ N/mm^2. However, the thickness of the steel core differs for the open, $d_S = 1.5$ mm, and closed, $d_S = 0.75$ mm, configuration. Furthermore, comparing the open and closed cross-sections, the fastener type varies due to the manufacturing process of the building elements. For the open configuration, nails[2] join the steel plates with the upper and the lower LVL plate. In the closed case, nails are only applied to join the lower LVL plate to the steel core. The upper LVL plate is attached through screws[3]. The respective positions of the fasteners are visualized in Figure 2.

For all fasteners, the ANSYS element type "MPC184 general joint" is utilized. These elements allow specifying a stiffness matrix with 21 entries:

$$
d_{\text{joint}} = \begin{bmatrix}
d_{11} & d_{12} & d_{13} & d_{14} & d_{15} & d_{16} \\
 & d_{22} & d_{23} & d_{24} & d_{25} & d_{26} \\
 & & d_{33} & d_{34} & d_{35} & d_{36} \\
 & & & d_{44} & d_{45} & d_{46} \\
 & \text{sym.} & & & d_{55} & d_{56} \\
 & & & & & d_{66}
\end{bmatrix}. \qquad (1)
$$

Here, the indices "1", "2", and "3" denote displacements in the x-, y-, and z-direction, respectively. Moreover, the indices "4", "5", and "6" refer to rotational degrees of freedom (DOFs) around the x-, y- and z-axis, respectively. The coordinate directions are visualized in Figure 1. A preliminary analysis conducted as part of this work revealed only three stiffness parameters, i.e., $d_{11} = d_{xx}$, $d_{22} = d_{yy}$, and $d_{12} = d_{xy}$,

---

[2] Unpublished prototype.
[3] Thin sheet metal screws 6.0 × 90 by Reisser-Schraubentechnik GmbH, D-74653 Ingelfingen-Criesbach, Germany.

that significantly influence the vibrational behavior of the structure. Hence, all other entries of the fasteners' stiffness matrix are set to zero.

The concept for the fastener model is depicted in Figure 3. In addition to the general joint elements, coupling constraints for the displacement in the z-direction are applied to closely located nodes at the interface of steel and timber surrounding the joints. The surrounding of the joints means within a radius of 0.022 m. This radius is determined through an empirical evaluation of the parameter space and leads to the best match of simulation and experimental results with the fixed value. In this surrounding area, nodes that are coincident within a certain tolerance behave as infinitely stiff coupled related to the displacement in z-direction. The tolerance is set just large enough to cover the distance between steel and timber components. This way, pairs of steel and timber component nodes are coupled concerning their displacement in z-direction.

Since the open cross-sections only use nails, denoted by the index "n", the same joint stiffness parameters are assumed for the upper (u) and lower (l) joints $d_{ij,l} = d_{ij,u} = d_{ij,n}$. For the case of closed configurations, different joint parameters for upper and lower connections are set, i.e., $d_{ij,u} = d_{ij,s}$ and $d_{ij,l} = d_{ij,n}$, where the index "s" refers to properties related to screws. As the fastener models' parameters are initially unknown, they constitute the unknown model parameters p, identified using model calibration and vibration measurements in the first analysis step.

The FE model uses a mesh size of $l_{\text{ele},t} \approx 0.015$ m for the timber components and of $l_{\text{ele},s} \approx 0.013$ m for the steel core. In [27], six to eight quadratic elements per wavelength have led to an acceptable error in eigenfrequencies compared to a converged solution. Hence, the bending wavelengths λ [28] are computed using the respective material properties of Table 2. The comparison of the sixth of the timber's bending wavelength $\lambda/6$ with the mesh size shows that the finite element size of the timber components is valid up to 10000 Hz, which is sufficient for the current studies. In the case of the steel parts, the used mesh size accounts for six to eight quadratic elements per wavelength in the low-frequency range. However, the mesh size is only valid up to 1300 Hz, for $S1$ with a steel thickness of $d_S = 0.75$ mm, and up to 2400 Hz, for $S2$ with a steel thickness
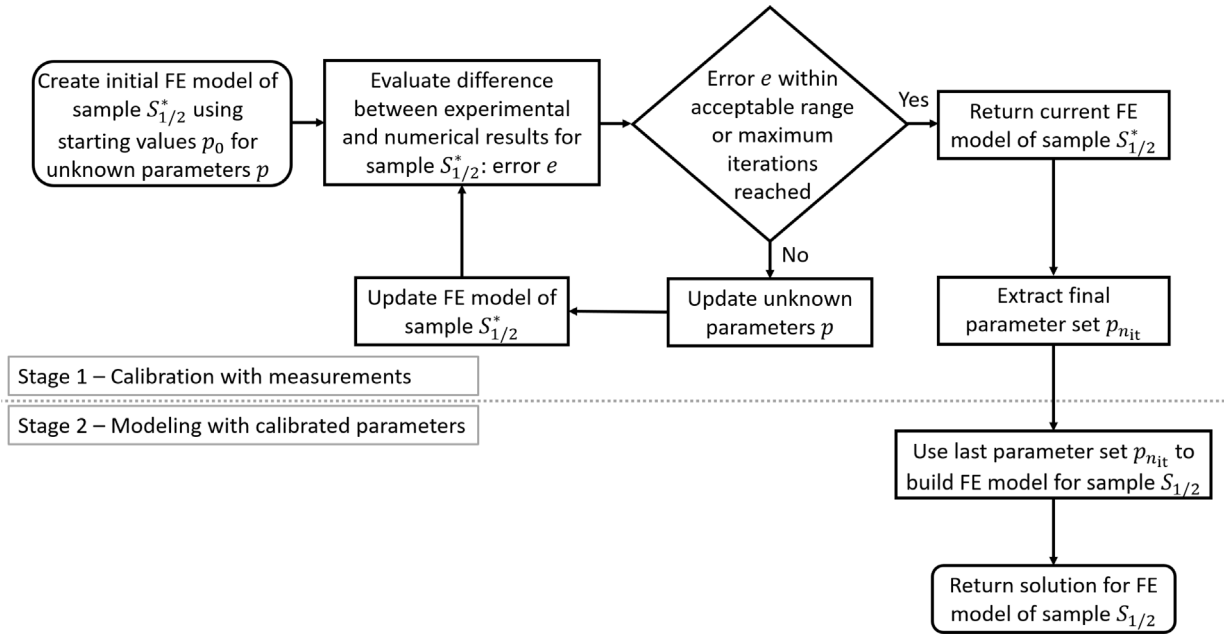
Figure 4. Flowchart of the model calibration: An FE model of the respective measured sample $S1^*$ or $S2^*$ is calibrated by iteratively adapting the unknown parameters p and computing an error e using the numerical and experimental results.

of $d_S = 1.5$ mm. Due to the limited computational resources, it becomes impossible to reduce the mesh size further. The current model for the vibroacoustic evaluation already uses approximately 0.9 million DOFs. Hence, the simulations are performed until the specified maximum frequency for the respective cases.

2.2 Model calibration

For the model calibration, the closed and open samples $S1^*$ and $S2^*$ are used. The in-plane dimensions of the test specimens are changed to 3.50 m x 0.84 m due to the limited spatial capacities of the testing facilities. All other properties remain as specified for the large-scale samples in Table 1.

2.2.1 Numerical approach

The FE model of the respective sample $S1^*$ or $S2^*$ is calibrated by iteratively adapting the model parameters p, i.e., the joint stiffnesses values of the nails $d_{ij,n}$ and the screws $d_{ij,s}$, and computing an error e using the numerical and experimental results. An overview of the model calibration workflow is visualized in Figure 4.

Six parameters in the FE model calibration are unknown at the beginning:

$$p = [d_{11,s}, d_{12,s}, d_{22,s}, d_{11,n}, d_{12,n}, d_{22,n}]. \qquad (2)$$

The closed specimen uses all six of them, whereas the open specimen utilizes only the three parameters related to nails, i.e., $d_{ij,n}$. First, the calibration of the nails' parameters is conducted using the data of the open specimen. Subsequently, those resulting nail parameters are used in the model of the closed specimen. Second, the screws' parame-

ters are calibrated utilizing the model and the measurement data of the closed specimen.

The free boundary conditions and the load position are adopted in the model in correspondence with measurement setups. Furthermore, a frequency resolution of $\Delta f = 1.0$ Hz is applied in the frequency range of interest $f_{low} \in [10, 312.5]$ Hz, which covers the measured frequency range.

2.2.2 Experimental approach

Vibration measurements are performed on the two test samples $S1^*$ and $S2^*$ to identify modal properties through experimental modal analysis [29]. Therefore, a pseudo-random excitation is applied to the specimens by means of a B&K[4] modal exciter type 4284 connected to the test samples utilizing a stinger at one point on the specimen. Heavy-duty slings are used to suspend the test samples in the measurement setup (Fig. 5) to simulate free boundary conditions in the FE model.

A force transducer (B&K Force Transducer Deltatron Type 8230) measures the force applied to the specimens. Moreover, a scanning Laser Doppler Vibrometer PSV-500[5] (LDV) records the surface velocity on the specimen's side opposite the force application position on a distributed grid of scan points. The measured force and velocity data are combined to compute the frequency response function. A Fast Fourier Transformation transforms the recorded time data to the frequency domain. The resulting spectra are averaged over 25 measurements for each scan point in the complex plane. Furthermore, the signals are adapted using a rectangular window. The sampling rate

---

[4] Hottinger Brüel & Kjær GmbH, D-64293 Darmstadt, Germany.
[5] Polytec GmbH, D-76337 Waldbronn, Germany.

Figure 5. Scan setup using heavy-duty slings for suspension with Laser Doppler Vibrometer (LDV) (a) and shaker (b).
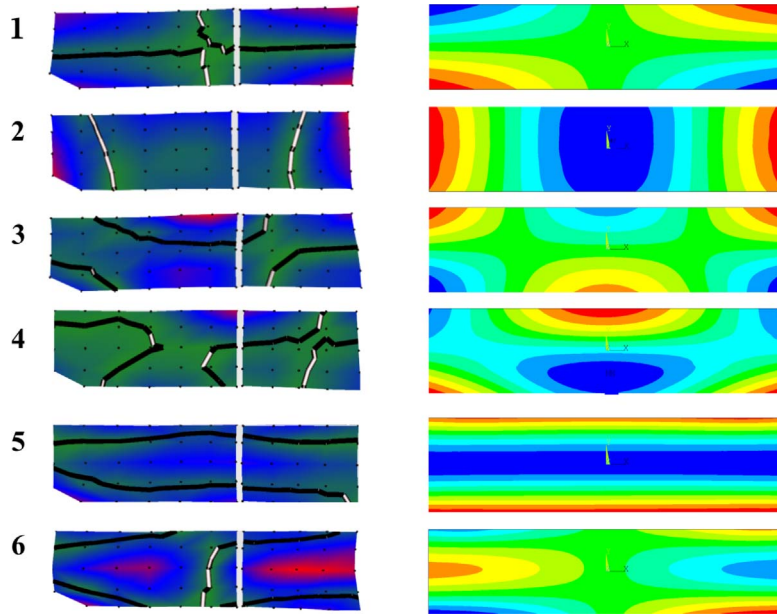
Figure 6. Mode shapes for the sample $S1^*$: experimentally determined (left) and numerically simulated (right) after model calibration.

$f_{\text{smp}} \approx 781$ Hz and the frequency resolution of $\Delta f \approx 390$ mHz are applied. All data acquisition tasks utilize the Polytec software. Further details on the measurements are given in [21].

After performing experimental modal analyses, the experimentally determined modes visualized in Figure 6 for the closed specimen $S1^*$ and in Figure 7 for the open specimen $S2^*$ are used to calibrate the model.

2.2.3 Parameter optimization

The respective stiffness values of fasteners are calibrated using experimental modal analysis data and the FE modal analysis results of the samples $S1^*$ and $S2^*$. A multi-objective model updating [30] is used, which considers a frequency error e_1 and a mode shape error e_2:
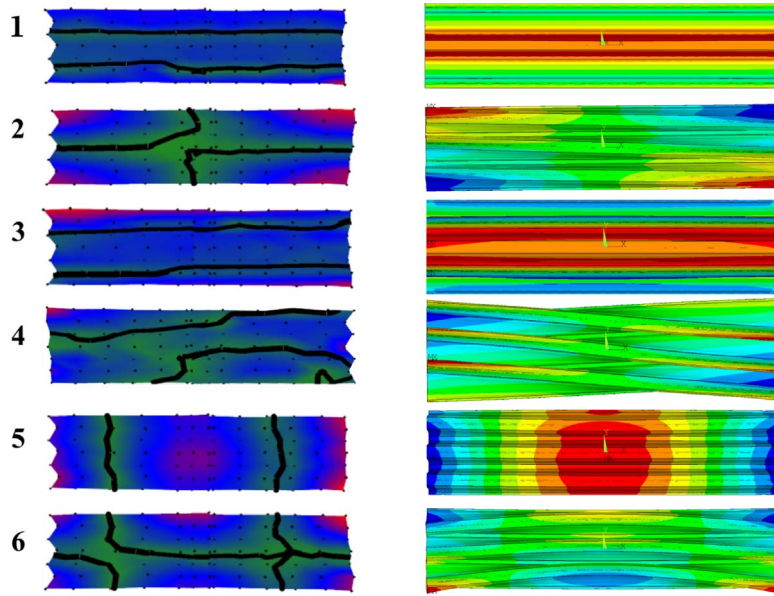
$$\min \ e(p) = \min(e_1(p) \& e_2(p)), \qquad (3)$$

$$e_1(p) = \sum_{m=1}^{N_m} (e_{r,m})^2 = \sum_{m=1}^{N_m} \left(\left| \frac{f_{\text{exp},m} - f_{\text{fem},m}}{f_{\text{exp},m}} \right| \right)^2, \qquad (4)$$

$$e_2(p) = \sum_{m=1}^{N_m} \left(\frac{1 - \text{MAC}_m}{\text{MAC}_m} \right)^2, \qquad (5)$$

where f_{exp} and f_{fem} are the experimentally and numerically determined natural frequencies, respectively, and MAC_m is the modal assurance criterion of the mode shapes computed, as described in [31]:

$$\text{MAC}_m = \frac{(\Phi_{\text{exp},m} \Phi_{\text{fem},m})^2}{(\Phi_{\text{exp},m}^T \Phi_{\text{exp},m})(\Phi_{\text{fem},m}^T \Phi_{\text{fem},m})}. \qquad (6)$$

Figure 7. Mode shapes for the sample $S2^*$: experimentally determined (left) and numerically simulated (right) after model calibration.

(a)   (b)
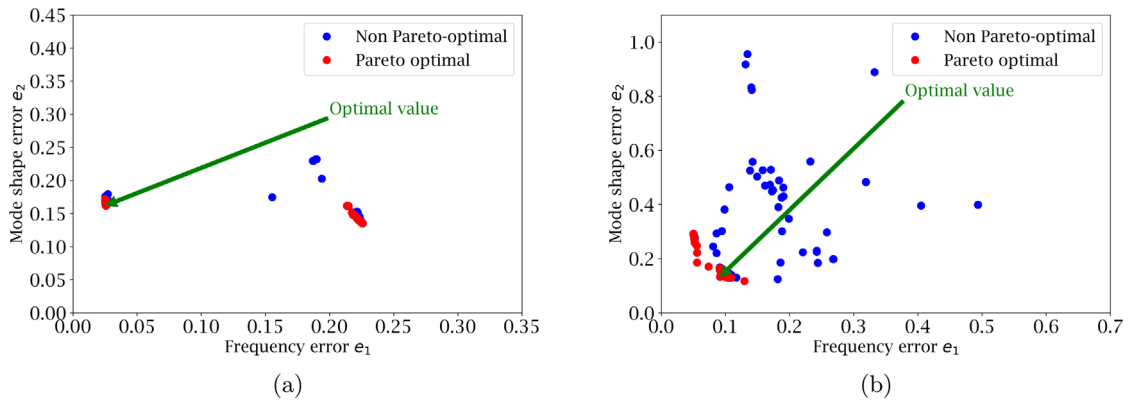
Figure 8. Pareto optimal front of the multi-objective optimization for the closed $S1^*$ (a) and open $S2^*$ (b) specimen.

Here, N_m equals the number of eigenfrequencies and modes considered in the optimization and is assigned as $N_m = 6$ as six modes per specimen, i.e., $S1^*$ and $S2^*$, are taken into account. A multi-objective optimization is chosen instead of a single-objective optimization to circumvent the choice of weightings of the errors e_1 and e_2. The optimization goal is to identify the best solution in the Pareto optimal front [32]. Hence, based on the evaluations of the objective functions of equations (4) and (5), the Pareto optimal front, $e = (e_1(p), e_2(p))$, is computed. For conflicting objectives, a singular optimal solution does not exist. Instead, there is a collection of alternative solutions referred to as Pareto optimal solutions. These solutions are optimal because no other solutions within the parameter space surpass them when considering all objectives [33]. Thus, a criterion is established to determine the most suitable solution at the Pareto optimal front by summing both errors for each point on the Pareto optimal front (Fig. 8) and taking the set of

parameters, which leads to the smallest sum of errors as the best solution:

$$e = \min(\mathbf{e}_1(p) + \mathbf{e}_2(p)). \tag{7}$$

As an optimization method, Bayesian Optimization is utilized due to its benefits explained hereafter. First, regarding the number of function evaluations needed, Bayesian optimization is a highly efficient method. Furthermore, it performs well even when the objective function contains multiple local maxima. The method can integrate prior beliefs concerning the problem, which aids in guiding the sampling process and balancing the exploration and exploitation of the search space. As it relies on Bayes' theorem, the prior knowledge embodies our initial beliefs concerning the range of potential objective functions. Despite the unknown nature of the cost function, it is justifiable to assume that there is prior knowledge about specific properties, such as smoothness, which renders certain objective

Table 3. Numerically f_{fem} and experimentally f_{exp} determined natural frequencies [Hz], relative frequency error $e_{r,m} = |(f_{\text{exp},S1/2^*,m} - f_{\text{fem},S1/2^*,m})/f_{\text{exp},S1/2^*,m}|$ and MAC before and after the automatic model calibration: $m \in [1, 6]$ for $S1^*$ and $S2^*$.

$S1^*$		Before			After		
m	$f_{\text{exp,m}}$	$f_{\text{fem},m}$	$e_{r,m}$	MAC_m	$f_{\text{fem},m}$	$e_{r,m}$	MAC_m
1	48.3	54.3	0.12	0.98	50.8	0.05	0.98
2	76.6	81.3	0.06	0.81	71.6	0.07	0.84
3	78.7	95.8	0.22	0.77	88.0	0.12	0.74
4	90.4	90.0	0.00	0.51	90.3	0.00	0.77
5	102.1	100.7	0.01	0.81	100.5	0.02	0.80
6	114.5	136.7	0.19	0.78	106.9	0.07	0.67
$S2^*$		Before			After		
m	$f_{\text{exp,m}}$	$f_{\text{fem},m}$	$e_{r,m}$	MAC_m	$f_{\text{fem},m}$	$e_{r,m}$	MAC_m
1	40.0	42.7	0.07	0.90	42.7	0.07	0.90
2	49.0	51.3	0.05	0.98	49.6	0.01	0.98
3	68.1	80.2	0.18	0.92	80.1	0.18	0.92
4	77.1	96.6	0.25	0.61	94.3	0.22	0.61
5	86.9	88.6	0.02	0.97	85.1	0.02	0.97
6	105.1	100.6	0.04	0.95	97.3	0.07	0.95

Table 4. Initial p_0 and calibrated $p_{n_{\text{it}}}$ parameters for the closed $S1^*$ and open $S2^*$ specimen: u and l denote the upper and lower joint, respectively. All values in the table refer to the properties of nails except for the entries marked by †, which refers to screw parameters.

	$S1^*$		$S2^*$	
	p_0	$p_{n_{\text{it}}}$	p_0	$p_{n_{\text{it}}}$
$d_{11,u}$	2.5e7†	9.6e6†	2.5e7	5.0e7
$d_{12,u}$	5.0e7†	9.2e5†	5.0e7	1.0e5
$d_{22,u}$	2.5e6†	1.5e8†	2.5e6	5.0e7
$d_{11,l}$	5.0e7	5.0e7	2.5e7	5.0e7
$d_{12,l}$	1.0e5	1.0e5	5.0e7	1.0e5
$d_{22,l}$	5.0e7	5.0e7	2.5e6	5.0e7

functions more credible than others. As observations are accumulated, the prior distribution and the likelihood function are merged, leading to updated beliefs in the posterior distribution. For efficient sampling, Bayesian optimization employs an acquisition function to find appropriate sampling locations. This decision inherently involves a trade-off between exploration (in areas where the objective function is highly uncertain) and exploitation (sampling values where the objective function is anticipated to be high) [34]. Due to its goal to minimize the number of objective function evaluations and, thus, to reduce the computational effort, Bayesian Optimization is applied in this study.

Since the parameters for the fasteners are initially unknown, a manual search is performed first by picking and testing reasonable values. Using the best choice for the joints' stiffness values $d_{ij,s}$ and $d_{ij,n}$ of the manual search, an already acceptable match is achieved, as is visible in the columns denoted by "before" in Table 3. The label "before" is assigned since these results are computed utilizing manually found parameter values. The label "after" refers to results calculated with the parameters found by the Bayesian optimization.

The initial joints' parameters, as identified by the manual search, are given in Table 4 denoted by p_0. The properties $p_{n_{\text{it}}}$ in Table 4 refer to the values found by the automatic model calibration performed using Bayesian optimization.

The optimization, i.e., the automatic model calibration, utilizes the manually found parameters as guiding values for the bounds specified in the calibration procedure. Narrow, i.e., $\pm 25\%\ p_0$, and broader, i.e., $-90\%/+1000\%\ p_0$, bounds are applied to thoroughly search the parameter space. Subsequently, the pairs of errors at the Pareto front are found, and the pair of those data points with the least sum, i.e., $e = \min(\mathbf{e}_1(p) + \mathbf{e}_2(p))$ is chosen as the best solution. The respective results of the parameter search are visualized in Figure 8, together with the Pareto optimal front for both specimens.

From the optimization computations, the parameters labeled as $p_{n_{\text{it}}}$ in Table 4 and, thus, the natural frequencies and MAC values denoted by "after" of Table 3 result.

Figure 8 shows that two groups of error combinations are formed for the test specimen $S1^*$, while there is only one for $S2^*$. For $S1^*$, one group of model solutions results in a smaller frequency error with almost equal mode error compared to the other group. Hence, a better solution is found for the group with the smaller frequency error. This aspect can also be observed in Table 3. The relative frequency error before the automatic model calibration lies above 10% for modes 1, 3, and 6, which is strongly reduced to errors below 10%, i.e., $e_{r,m} \in [0.02, 0.07]$, for all modes except the third, where it lies slightly above, i.e., $e_{r,3} = 0.12$. This improvement in frequency error comes with the price of reduced MAC values for modes 3, 5, and 6, i.e., $\text{MAC}_m \in [0.74, 0.80]$. However, the relative reduction of MAC values before and after the automatic updating lies below 0.03 for modes 3 and 5 and is only exceeded for mode 6 with a MAC value reduction of 0.08. Generally, the MAC values for specimen $S1^*$ are not as good as for the open specimen $S2^*$. Only the MAC for the first mode lies above 0.90. For modes 2 and 5, the MAC values are still above 0.80, but the values are even lower for modes 3, 4, and 6. The reason for this behavior is presumably the shape of the modes. As visualized in Figure 6, only mode 1 shows a nice and clear behavior. Modes 2–6 are either challenging to identify, non-symmetric, or both. This circumstance could stem from manufacturing inaccuracies, e.g., slight relative rotations of the components, which lead to a non-symmetric built-up, pre-stress, and pre-deformation. Furthermore, sample $S1^*$ uses a steel sheet of thickness $d_s = 0.75$ mm as opposed to $d_s = 1.5$ mm for $S2^*$, leading to individual parts of the steel frame vibrating locally, which influences the global structural behavior. Moreover, the modes are challenging to identify in the experiments, e.g., due to closely spaced modes. Consequently, due to the overall improved agreement between numerical and experimental results, the updated parameters $p_{n_{\text{it}}}$ are deemed acceptable.

For $S2^*$, in Figure 8b, only one group of model solutions exists, and the Pareto front is discernible. The Pareto criterion assesses whether a state improves by changing one target value without deteriorating another. The Pareto front shows the values that represent the best compromise. Here, no solution with a smaller frequency error could be found without causing an increase in the mode error. Due to this behavior, only a slight improvement of frequency and mode error is achieved for $S2^*$ as can be seen in Table 3: only the natural frequencies $f_{S2^*,2}$ and $f_{S2^*,4}$ become slightly closer to the experimentally determined natural frequencies. However, simultaneously, the match for $f_{S2^*,6}$ becomes slightly worse, and the MAC values do not increase. In particular, the fourth mode, which appears to be less clear than the others (Fig. 7), shows some discrepancy with the simulation results regarding natural frequency. This mode also shows a MAC of only 0.61, presumably due to the complexity of the mode shape. Moreover, the natural frequencies of the first and third modes, i.e., the bending modes in the lateral (y-) direction, are somewhat apart from the numerical results. However, a better match is challenging to obtain since, for an advantageous adaptation of the joint parameters, the other natural frequencies deviate more from their experimental counterparts. Still, all MAC values lie above 0.90 except for mode 4 due to a complex mode shape. Furthermore, except for the second lateral bending mode 3 and the unclear mode 4, the relative frequency error lies below 10%, which is satisfying. Hence, also for the open cross-section, the calibrated parameters $p_{n_{it}}$ are assumed to be suitable for the simulations related to the vibroacoustic validation, which is described in the following section.

The updated values of the fasteners are calibrated for natural frequencies up to approximately 115 Hz and are thus adaptable for the VDV calculations, which consider modes around and below this frequency. However, it should be noted that frequencies of up to 1.3 kHz and 2.4 kHz are examined in the context of impact sound tests. Therefore, uncertainty is added to the model by assuming that the joint stiffnesses from the updating procedure are suitable for these impact sound computations.

2.3 Model for vibroacoustic validation

FE analyses are performed to validate the vibration serviceability and impact sound characteristics of the hybrid steel-timber structures, as measurements are often time-consuming and costly [13, 14]. Here, the floor structures $S1$ and $S2$ (Tab. 1) without additional components, such as floating floors or walls located on the edges of the floors, are considered in the simulations. Even though these assumptions result in discrepancies between the predicted and presumably observed behavior of in-situ floors, the FE models are assumed to provide a first estimate of the applicability of the proposed hybrid floors.

The parameters $p_{n_{it}}$ (Tab. 4), i.e., the joint parameters identified by calibration, are utilized for these FE models. Given the profound influence of boundary conditions on structural vibration and sound radiation in the

low-frequency regime, and in light of the unavailability of measurements for samples $S1$ and $S2$ in a built-in configuration, the investigations focus on the two extreme scenarios regarding boundary conditions: namely, clamped ("c") and free ("f"). In the clamped configuration, all degrees of freedom are constrained along the outer edges of the floor structure, whereas in the free boundary condition scenario, none are restrained. Furthermore, to increase computational efficiency and manage system matrices with respect to memory resources and disk space, symmetry boundary conditions are employed in the FE model. This approach involves discretizing and solving only one-quarter of the floor element, assuming that the remaining three-quarters can be derived through symmetry principles. The respective boundary conditions are applied along the cutting planes of the quartered floor structure. The load for impact sound computations is located in the center of the structure, which is the point of symmetry in x- and y-directions (see Fig. 1 for the definition of the coordinate system). This excitation force only excites symmetric modes in both the x- and y-directions. Therefore, applying only symmetric boundary conditions is theoretically sufficient, and no additional antisymmetric boundaries need to be considered in the response analysis.

As the VDV calculation is based on the load case of a person crossing the floor, all kinds of modes are excited and thus need to be considered. Therefore, for the computation of the VDV, symmetric, antisymmetric, and all possible combinations of support conditions are applied in the simulation to incorporate both antisymmetric and symmetric mode shapes.

The implementation of the antisymmetric and symmetric boundary conditions is performed by imposing constraints on nodes, respectively DOFs, in the planes of symmetry or antisymmetry. Hence, the following DOFs are constrained:

- For symmetry conditions
  - In the plane with the normal in x-direction: displacements in x-direction, rotations around the y-axis, rotations around the z-axis.
  - In the plane with the normal in y-direction: displacements in y-direction, rotations around the x-axis, rotations around the z-axis.

- For antisymmetric conditions
  - In the plane with the normal in x-direction: displacements in y- and z-direction, rotations around the x-axis.
  - In the plane with the normal in y-direction: displacements in x- and z-direction, rotations around the y-axis.

Furthermore, the global impedance for the impact load computation taken from the respective FE model is scaled due to symmetry considerations [35].

In contrast, the "c" and "f" boundary conditions are implemented along the outer edges as previously described. Hence, four cases are investigated:
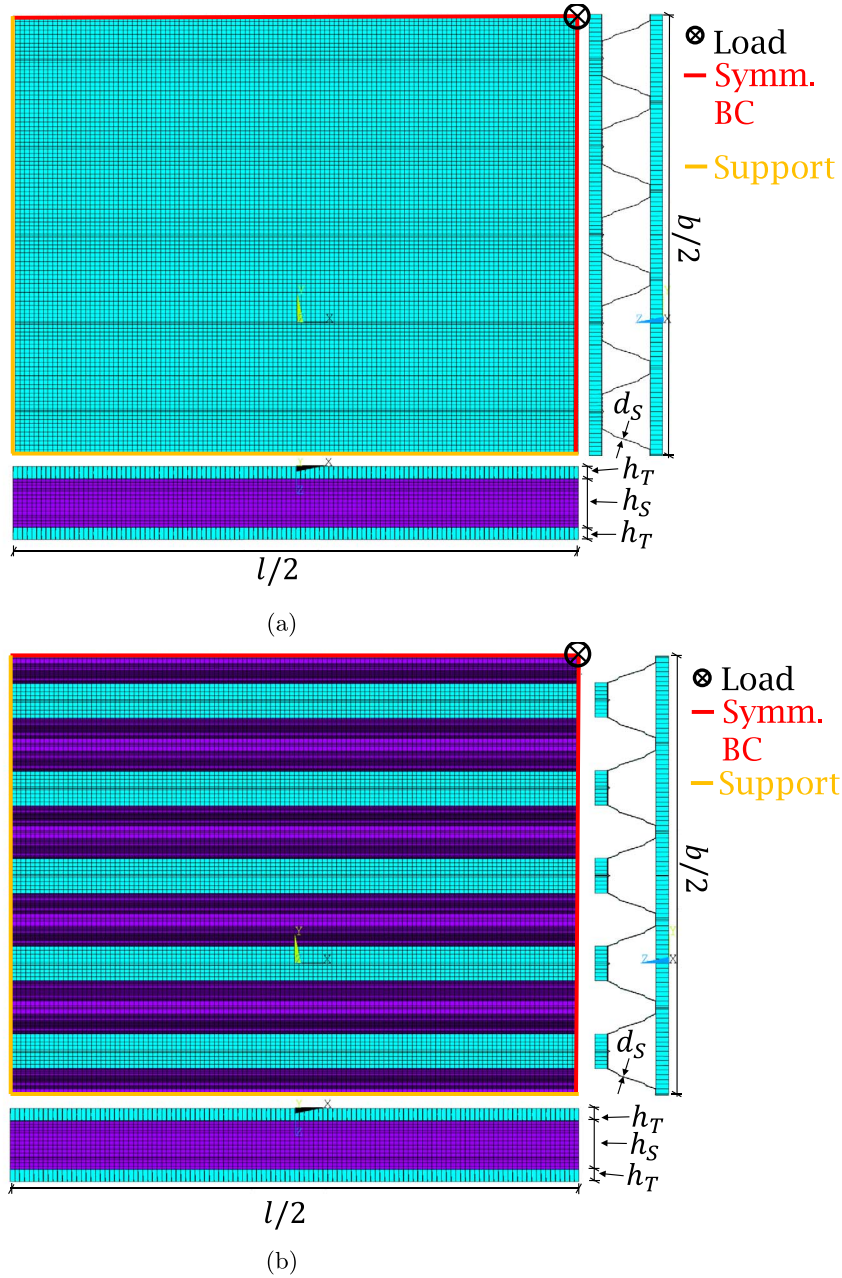
Figure 9. FE model of closed sample $S1$ (a) and open sample $S2$ (b): bottom view and side views. Steel is colored purple, and timber parts are cyan. The element thickness is visually scaled to represent the thickness of the respective component.

- Closed cross-section, clamped boundary condition: $S1,c$;
- Closed cross-section, free boundary condition: $S1,f$;
- Open cross-section, clamped boundary condition: $S2,c$;
- Open cross-section, free boundary condition: $S2,f$.

The FE models of the analyzed one-quarter of the floor structures are visualized in Figure 9.

A structural modal damping ratio of 1% is chosen according to the recommendation of the European timber standard [36]. The damping identified for the test specimens $S1^*$ and $S2^*$ is deemed inappropriate for the FE-model

of the floor structures, i.e., $S1$ and $S2$, since boundary conditions significantly influence the damping of a structure [37] as well as the overall built-up. Furthermore, no structural vibration tests have been possible on large-scale floor structures in a built-in situation. The chosen damping ratio is applied as a structural loss factor $\eta_s = 0.01 \times 2$ in the FE-model for the whole analyzed frequency ranges $f_{\text{impact},S1} \in [10, 1300]$ Hz and $f_{\text{impact},S2} \in [10, 2400]$ Hz. Here, uncertainty is introduced in the simulation model since the damping value proposed by Eurocode 5 [36] applies to low frequencies related to vibrations. A timber joist floor investigated by Wang et al. [38] showed an approximate structural loss factor of 0.02 up to 2500 Hz. Although

Algorithm 3.1. Impulsive response calculation procedure

1: Compute modes and eigenfrequencies f_m up to twice the fundamental frequency f_1

2: Calculate effective footfall impulse $I_{\text{eff},m} = 54 \cdot \dfrac{f_w^{1.43}}{f_m^{1.30}}$ with the maximum walking frequency $f_w = 1.8$ Hz and the considered eigenfrequencies f_m

3: Compute peak velocity in each mode m: $\hat{v}_m = \Phi_{e,m}\Phi_{r,m}I_{\text{eff},m}/\hat{m}_m$ with $\Phi_{e,m}$ the value of the mode shape m at the excitation position, $\Phi_{r,m}$ the value of the mode shape m at the receiving position, $\hat{m}_m$ the modal mass of mode m

4: From this, calculate the velocity response in each mode over the period of one footfall T with ζ as the modal damping ratio: $v_m(t) = \hat{v}_m \exp\left(-2\pi f_m \zeta t\right)\sin\left(2\pi f_m t\right)$ with the modal velocity magnitude $\hat{v}_m$

5: Compute total response to each footfall $v(t) = \sum_{m=1}^{N} v_m(t) \cdot w_m$ with a weighting w_m taken from [42] as suggested in [41]

6: For a time-harmonic analysis, the total response to each footfall can be converted to accelerations by computing the acceleration magnitude from the velocity magnitude as $\hat{a} = (-i\omega)\hat{v}$

7: From the resulting acceleration time history, root-mean-square (RMS) response evaluated over one footfall $a_{\text{RMS}} = \sqrt{\dfrac{1}{T}\int_0^T a(t)^2 \mathrm{dt}}$

---

this work deals with a pure timber instead of a hybrid steel-timber floor, the chosen loss factor of 0.02 is deemed acceptable as a first estimate, as currently, no investigations exist on the impact sound behavior of hybrid steel-timber floors such as the presently studied ones.

3 Vibroacoustic criteria

The updated and adapted FE model is used in the following sections to evaluate the floor structures, $S1$ and $S2$, concerning the vibration serviceability and impact sound insulation.

3.1 Vibration serviceability

A recent review on steel-timber composite floors [39] states AISC Design 11 [40] and CCIP-016 [41] as currently the most adequate references concerning vibrations of hybrid steel-timber systems. According to [41], the regulations described in the document apply to structures made of plenty of construction materials with walking excitation. For floor structures with natural frequencies above 4 Hz, the impulsive response calculation procedure is adopted as shown in Algorithm 3.1.

The response factor can be calculated utilizing the acceleration time history from Algorithm 3.1, which is related to continuous vibration. Nevertheless, a continuous vibration is seldom the case. Consequently, the concept of VDV proposed in [40] is used to estimate the acceptability of intermittent vibration:

$$VDV = \left(\int_0^T a^4(t)\mathrm{dt}\right)^{1/4} = 0.68 a_{\text{w,rms}}(n_{\text{day/night}}T_{\text{single}})^{1/4} \quad (8)$$

with $a_{w,\text{rms}}$ the RMS-acceleration response from Algorithm 3.1, $n_{\text{day}} = 32$, $n_{\text{night}} = 16$ and the time it takes to cross the floor

$$T_{\text{single}} = \frac{d_{\text{floor}}}{v_{\text{step}}} = \frac{\sqrt{(l^2 + b^2)}}{(1.67 f_w^2 - 4.83 f_w + 4.50)}. \quad (9)$$

Consequently, FE modal analysis is adopted to identify the fundamental frequency f_1, the natural frequencies f_m of

modes up to twice the fundamental frequency, and the corresponding modal masses $\hat{m}_m$ of these modes. The modal damping ratios are taken as 1%, as recommended by [36].

3.2 Impact sound

The standard ISO 10140-5 [23] specifies procedures to measure impact sound properties. Here, the tapping machine is described as excitation for impact sound measurements. A numerical version of the tapping machine is used in this work. The procedure to compute the loading that is applied to the FE model is described in the following.

Brunskog et al. [43] provide a method to calculate the discrete frequency spectrum of the impact loading due to a standard tapping machine. The floor is described by a general frequency-dependent driving-point impedance Z_{dp}. The hammer impact force $f_0(\mathrm{t}) = F_0\delta(t)$ is applied to the structure. This yields the frequency-dependent force $f_0(\omega) = F_0$ by a Fourier transform which varies between $2M_0v_0$ and M_0v_0 for an elastic and plastic impact where $v_0 = 0.886$ m/s is the initial hammer velocity and $M_0 = 0.5$ kg equals the weight of a hammer. Here, the geometric mean $\sqrt{2}M_0v_0$ is considered [44]. The spectrum of the continuing impact is given as

$$f_1'(\omega) = \frac{f_0}{1 + i\omega M_0/Z_{\text{dp}}}. \quad (10)$$

Then, an inverse Fourier transform computes the corresponding force in time $f_1'(t)$. The time of the zero crossing $t_{\text{cut}} = \{\min t | t > 0, f_1'(t) = 0\}$ is found and the force spectrum $F_1(\omega)$ is computed by a Fourier transform. Finally the Fourier series components $F_n = F_1(nf_h)f_h$ with $f_h = 1/T_h$ and $T_h = 0.5$ s for each of the five hammers are applied to the floor structure at the respective frequencies [43]. An exemplary plot of the tapping machine load over frequency is given in Figure 10.

Furthermore, the driving-point impedance of the floor is computed from the local Z_L and global impedance Z_G as follows [38]:

$$Z_{\text{dp}} = \frac{Z_G(\omega)Z_L(\omega)}{Z_G(\omega) + Z_L(\omega)}. \quad (11)$$
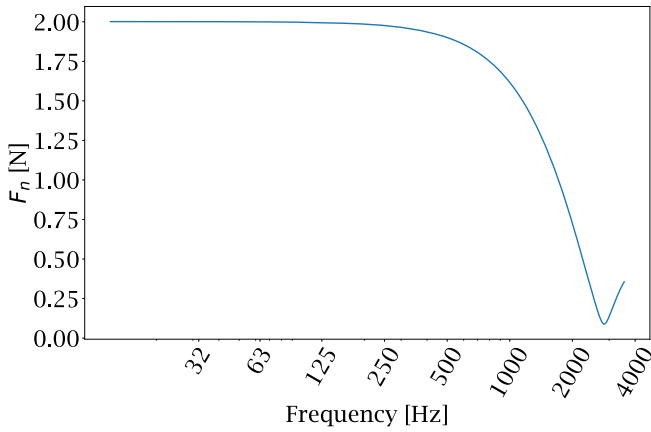
Figure 10. Example plot of load F_n against frequency.

The global impedance

$$Z_{\mathrm{G}}(\omega) = \frac{-iD_{jj}(\omega)}{\omega} \qquad (12)$$

is found using the dynamic stiffness of the floor

$$D_{jj}(\omega) = -\omega^2 M_{jj} + K_{jj}(1 + ig) \qquad (13)$$

taken from the FE model at the DOF j of the impact with M_{jj} and K_{jj} as mass and stiffness matrix entries and a material damping coefficient $g = 0.0084$ for the upper timber plate, which is derived from vibration measurements of the LVL plates.

The local impedance is analytically approximated [38]:

$$Z_L(\omega) = \frac{2Er_h}{i\omega(1 + v)(1 - v)} . \qquad (14)$$

with r_h the hammer radius, the Poisson's ratio $v = \sqrt{v_{xy} \cdot v_{yx}}$, and the elasticity modulus $E = \sqrt{E_x \cdot E_y}$ of the respective material.

The computed force is used in the desired frequency range of f_{impact} as excitation on the structure in a time-harmonic analysis. The considered frequency range differs between open and closed cross- sections due to requirements concerning finite element sizes. Hence, $f_{\mathrm{impact},S1} \in [10, 1300]$ Hz and $f_{\mathrm{impact},S2} \in [10, 2400]$ Hz are applied as frequency ranges in the simulations. The resolution of $\Delta f = 2$ Hz for the impact sound calculations results from the repetition frequency of the hammers of the tapping machine. To determine impact sound characteristics, the sound power P is computed from the surface velocity of the lower surfaces of the samples, i.e., timber panels and radiating steel surfaces, using the Rayleigh integral [45, 46]. The sound power level is calculated from the computed sound power P as

$$L_{\mathrm{W}} = 10\log_{10}(P/10^{-12}). \qquad (15)$$

Moreover, third-octave band data is calculated from the equidistant frequency data.

Since the goal is to compare normalized sound pressure levels for the hybrid steel- timber floors, sound power levels

L_W are converted to sound pressure levels L_p according to the following relation from [47]:

$$L_p = L_W - \left\{ 10 \log \left(\frac{A}{A_0} \right) + 4.34 \frac{A}{S} + 10 \log \left(1 + \frac{Sc}{8Vf} \right) \right.$$
$$\left. + C_1 + C_2 - 6 \right\} \qquad (16)$$

where the equivalent absorption surface A of the room equals

$$A = \frac{55.26V}{cT_{60}} \, [\mathrm{m}^2]. \qquad (17)$$

A reverberation time of $T_{60} = 0.45$ s is considered, as specified in [48] for the respective room volume $V = l \cdot b \cdot h_{\mathrm{room}} = 24.3$ m^3 where the room height is assigned to be $h_{\mathrm{room}} = 2.4$ m and length l and width b are taken from Table 1. Moreover, the reference surface $A_0 = 1$ m^2 and the sound wave velocity $c = 343$ m/s are specified. The overall surface of the room is computed as $S = l \cdot b \cdot h_{\mathrm{room}} \cdot 2 + b \cdot h_{\mathrm{room}} \cdot 2 = 51.1$ m^2. Furthermore, the center frequency of third-octaves f [Hz] and the correction terms

$$C_1 = -10 \log \left(\frac{p_s}{p_{s,0}} \right) + 5 \log \left[\frac{273.15 + \theta}{\theta_0} \right], \qquad (18)$$

as well as

$$C_2 = -10 \log \left(\frac{p_s}{p_{s,0}} \right) + 15 \log \left[\frac{273.15 + \theta}{\theta_1} \right], \qquad (19)$$

are required for equation (16). The calculation of the correction terms in equations (18) and (19) uses the static air pressure $p_s = 95$ kPa for an altitude of 500 m, the reference static air pressure $p_{s,0} = 101.325$ kPa, the air temperature $\theta = 293.2$ K (=20°), $\theta_0 = 314$ K and $\theta_1 = 296$ K. Subsequently, the following relation from [23] is applied

$$L_n = L_p + 10 \log \left(\frac{A}{10 \, \mathrm{m}^2} \right) \qquad (20)$$

to compute the normalized impact sound pressure.

4 Results

In this section, the findings related to vibration serviceability and impact sound properties of the samples denoted as S1 and S2 are presented. The boundary conditions play a significant role in influencing the structural vibration and sound radiation in the low-frequency range. Unfortunately, measurements in a built-in situation have not been feasible. Thus, a comparative analysis is conducted between two extreme cases with different boundary conditions, namely, clamped ("c") and free ("f").

4.1 Vibration serviceability properties

The VDV is a critical metric for evaluating the potential for adverse comments in residential buildings, as prescribed

Table 5. VDV ranges for the probability of adverse comments

Place and time	Low probability [ms$^{-1.75}$]	Adverse comments possible [ms$^{-1.75}$]	Adverse comments probable [ms$^{-1.75}$]
Residential buildings day	0.2–0.4	0.4–0.8	0.8–1.6
Residential buildings night	0.1–0.2	0.2–0.4	0.4–0.8

Table 6. Fundamental frequencies $f_{1,j}$ [Hz], modes for the VDV evaluation $f_{m,j}$ [Hz], and modal masses $\hat{m}_{m,j}$ of the samples $j \in [S1,f; S1,c; S2,f; S2,c]$.

Sample j	$f_{1,j}$ [Hz]	$f_{m,j}$ [Hz]	$m_{m,j}$ [kg]
$S1,c$	49.81	{49.81; 56.82; 70.06; 89.54}	{0.28; 0.11; 0.04,0.03}
$S1,f$	17.75	{17.75; 22.45; 34.18}	{0.69; 0.34; 0.21}
$S2,c$	63.42	{63.42; 66.96; 74.34; 84.20; 88.19; 88.99; 90.23; 92.47; {92.50; 107.6; 108.73; 110.2; 112.73; 112.80; 116.78}	{1.93; 0.43; 0.18; 0.11; 0.10; 0.10; 0.07; 0.08; {0.09; 0.06; 0.05; 0.06; 0.06; 0.42; 0.14}
$S2,f$	5.29	{5.29}	{14.97}

by the British Standard BS 6472-1 [42]. The respective limit values for the VDV are given in Table 5, which are compared with the VDV calculated for all samples $j \in [S1,f; S1,c; S2,f; S2,c]$ using Algorithm 3.1 and equation (8). This computation involves determining fundamental frequencies $f_{1,j}$, modes to be considered $f_{m,j}$, and modal masses $\hat{m}_{m,j}$ through FE modeling. The results for the different sample configurations are presented in Table 6.

Upon evaluating the VDV for the test specimens, as shown in Table 7, several observations emerge. Firstly, it is evident that $S2,c$ exhibits a higher number of modes within the specified frequency range $\Delta f_{S2,c} \in [0, 2 \cdot f_{1,S2,c}]$, primarily due to its relatively high fundamental frequency $f_{1,S2,c}$ and the presence of numerous localized modes originating within the steel frame, which is not as pronounced in $S1$. Secondly, $S2,f$ has a relatively low fundamental natural frequency $f_{1,S2,f}$, necessitating consideration of only the fundamental mode within the observed range of $\Delta f_{S2,f} \in [0,2 \cdot f_{1,S2,f}] = [0, 10.58]$ Hz.

In terms of day and night VDV, samples $S1,c$, $S1,f$, and $S2,c$ exhibit similar values, around 0.57. Notably, $S2,f$ stands as an outlier, with a VDV reaching up to 1.67, indicating problematic vibrational behavior. The other samples fall within the "adverse comments possible" range, while $S2,f$ exceeds this threshold and falls into the category of "adverse comments probable". However, the behavior of a built-in floor structure, which presumably lies between the extreme boundary conditions of free and clamped, yields VDV values that also fall within a range between "possible" and "probable" adverse comments.

As specified in Algorithm 3.1, the structural response depends on the damping ratio, which has been fixed using normative specifications. Hence, uncertainty related to the damping remains and should be kept in mind when interpreting the results.

4.2 Impact sound properties

The results of impact sound pressure levels are examined from two perspectives: the influence of different

Table 7. VDV during the day VDV$_{d,j}$ [ms$^{-1.75}$] and VDV during the night VDV$_{n,j}$ [ms$^{-1.75}$] of the samples $j \in [S1,f; S1,c; S2,f; S2,c]$.

Sample j	VDV$_{d,j}$ [ms$^{-1.75}$]	VDV$_{n,j}$ [ms$^{-1.75}$]
S1,c	0.65	0.55
S1,f	0.57	0.46
S2,c	0.57	0.48
S2,f	1.67	1.41

boundary conditions, i.e., free "f" and clamped "c", and the effect of the two distinct cross-section types, i.e., open and closed. The comparison of the impact sound results under the different boundary conditions "f" and "c" is depicted in Figure 11.

Two insights can be gained from these plots. Firstly, as anticipated, the impact of boundary conditions is most pronounced in the lower frequency range, up to 80 Hz for $S1$ and up to 500 Hz for $S2$. Secondly, the impact of boundary conditions is more substantial for the closed specimen $S1$ compared to the open one $S2$ up to 100 Hz. This discrepancy arises because, in the clamped case, all edges of the lower timber panel are fixed for $S1$, whereas for $S2$, only the edges at the longitudinal ends of the lower timber panel are fixed, resulting in a greater influence of boundary conditions in the low-frequency range for $S1$.

Furthermore, a comparison of the different cross-section types, open and closed, under both boundary conditions is presented in Figure 12.

Both cross-section types exhibit similar quantitative behavior, with $S1$ displaying slightly higher sound pressure levels in some third octaves, specifically about 5 dB higher than $S2$. This observation suggests that $S2$ radiates slightly less sound than $S1$. Qualitatively, the two configurations share similar curve shapes, but slight shifts in characteristics are observed in frequency due to their different structural setups. For instance, under clamped support conditions, both specimens initially exhibit a low sound pressure level at lower frequencies, at approximately
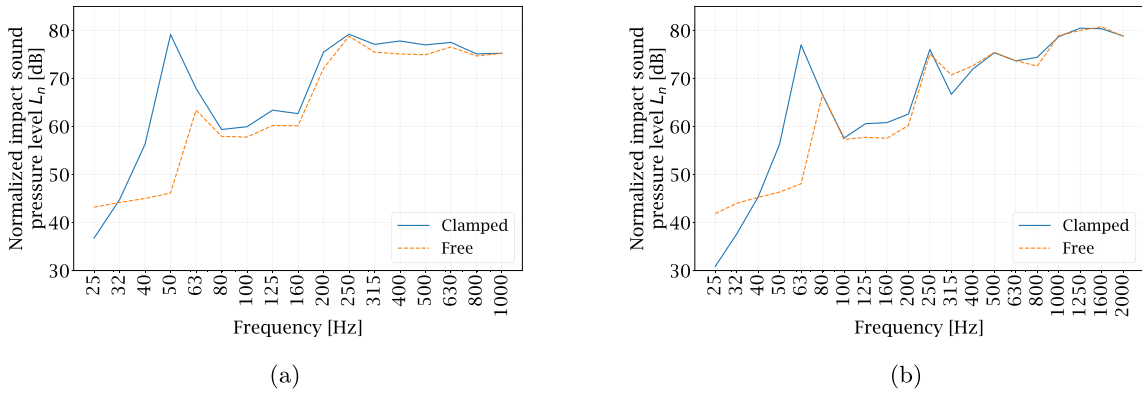
Figure 11. Normalized impact sound pressure of samples $S1$ (a) and $S2$ (b) for the cases "f" and "c" for third-octave bands.
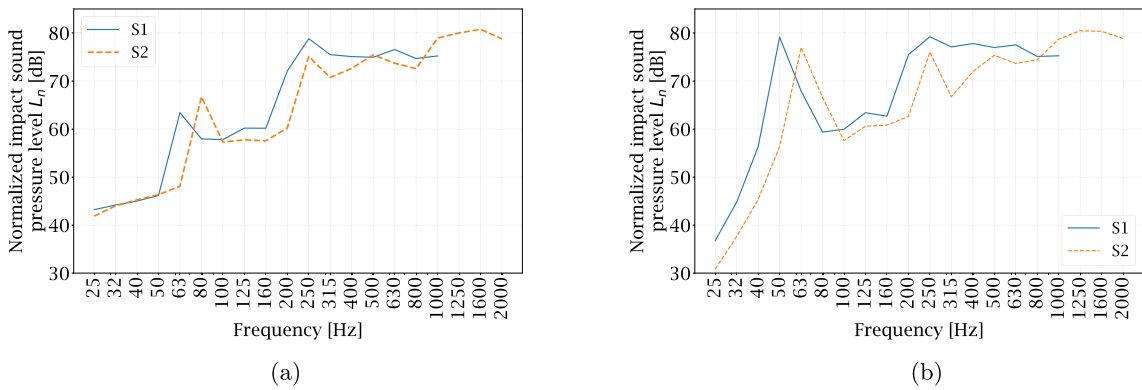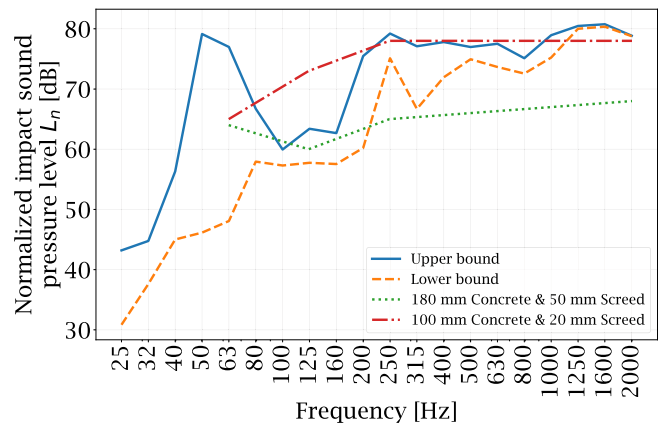

Figure 12. Comparison of the sound pressure levels of the samples $S1$ (closed) and $S2$ (open) for the cases "f" (a) and "c" (b) for third-octave bands.

30 Hz. Subsequently, a distinct peak is shown at roughly 50 Hz for $S1$ and approximately 63 Hz for $S2$. Notably, the peak for $S2$ shifts to the adjacent third-octave band due to the resonant behavior of the structure. Furthermore, qualitative disparities become evident in the clamped support scenario within the frequency range of 160–800 Hz, where $S2$ demonstrates more fluctuations in sound pressure levels than $S1$.

To provide context for the impact sound behavior of the hybrid steel-timber floors, the impact sound pressure level values from Table B.2 of ISO 12354-2 [49] for concrete floors (100 mm and 180 mm thick) with a bonded screed layer (20 mm and 50 mm thick) are included for comparison in Figure 13. The lower and upper bounds of sound pressure levels for the hybrid steel-timber floors are established, offering a range of in-situ behavior. This means that in every third-octave band, the minimum value of the four sound pressure levels, i.e., $S1$,f, $S1$,c, $S2$,f and $S2$, c, is identified and taken as a value for the lower bound and vice versa for the upper bound.

In the low-frequency range up to 200 Hz, the lower and upper bounds cover values similar to those of concrete floors. In the mid-frequency range, up to around 1000 Hz, the hybrid floors' sound pressure levels fall between the two concrete floors. Beyond 1000 Hz, the hybrid floors exhibit sound pressure levels higher than the concrete floors,

Figure 13. Comparison of the upper and lower bounds of the sound pressure levels computed for the hybrid floor samples $S1$ and $S2$ with the values for a 100 mm thick concrete floor with a 20 mm thick bonded screed and a 180 mm thick concrete floor with a 50 mm thick bonded screed provided in [40]. Results are given in third-octave bands for the upper and lower bounds and in octaves for the concrete floors.

with a decreasing trend at 2000 Hz. This indicates that the levels may approach those of concrete floors at higher frequencies. However, this could not be definitively verified

due to the limited computational resources and, hence, limited observed frequency ranges. Additionally, it should be noted that the damping and joint stiffness values are chosen based on assumptions explained in previous sections. Thus, the interpretation of the results is subject to the respective modeling choices. In conclusion, the hybrid floors demonstrate behavior similar to concrete floors. However, influences of additional structural components of a built-in situation, e.g., floating floors, are not considered in this study. Hence, a more realistic setting in a building might give more insight into the comparison of the floor types.

5 Discussion

In the present study, the FE models of the hybrid floor structures rely on parameters derived from the calibration of FE models of smaller specimens. It is worth noting that this step assumes the transferability of these parameters, a presumption that should be validated through future large-scale tests. Moreover, the construction of all models, both for small- and large-scale specimens, is based upon certain assumptions. These assumptions cover factors such as the appropriateness of the realization of free boundaries in the measurements and the suitability of the employed joint and structural model. The results indicate that the structural behavior has been reasonably approximated.

The assessment of vibration serviceability, as evaluated by the VDV, emphasizes concerns related to potential resident annoyance. Observably, none of the examined cases exhibit a low probability of adverse comments. One potential remedy for enhancing the performance of these floor structures involves increasing the distributed mass of the floor. However, such a mass increase necessitates accurate adjustment, as it concurrently affects the natural frequency of the floor – a factor of substantial significance for vibration serviceability as a too-low fundamental frequency may pose a challenge. Additionally, another potential strategy for mitigating the issue of high VDV involves increasing inherent damping. Investigating the damping characteristics in greater detail may provide valuable insights for effectively addressing this concern.

Regarding impact sound pressure levels, as expected, the influence of boundary conditions is most pronounced in the lower frequency range. Furthermore, the open and closed cross-sections display quite similar behavior, thus making the open setup only slightly more convenient for practical applications. When the performance of the hybrid structures is compared with commonly used concrete floors with bonded screed, it becomes evident that a similar level of performance can be achieved. Still, it is to be noted that a built-in situation in buildings differs from the tested setting as usually floating floors or soft coverings are applied to further reduce impact sound noise. This step is commonly performed after the floor installation for both concrete and hybrid steel-timber floors. Compared to the concrete floors, the hybrid floors might be considered beneficial in terms of weight and sustainability.

6 Conclusions

In conclusion, this investigation explores novel hybrid steel-timber floor elements, primarily focusing on their vibration serviceability and impact sound performance. Leveraging Finite Element analysis techniques, this study provides a comprehensive examination of the behavior of these innovative building components in terms of vibroacoustics. First, the Finite Element model is validated by aligning it with experimental data on natural frequencies and modes and determining joint stiffness values. This calibrated model serves as the basis for the in-depth analysis of vibration serviceability. This analysis expressed through vibration dose values, offers an initial insight into the real-world performance of these hybrid floor elements. Additionally, this study numerically explores the hybrid steel-timber floors' impact sound insulation properties, an aspect that has received limited attention in previous research. The outcomes presented herein reveal that the proposed building elements exhibit comparable behavior to that of conventional concrete ceilings, thus making the application of hybrid steel-timber floors feasible for future construction projects. The assumptions related to the structural damping and the applicability of the joint stiffness parameters at higher frequencies must be kept in mind, and further investigations in this regard are still required. Moreover, analyses in a realistic setting utilizing additional structural components, e.g., floating floors, will lead to more detailed insights into the impact sound insulation. It is worth noting that while the resultant vibration amplitudes, as quantified by vibration dose values, mostly fall within the range of possible adverse comments, there remain possibilities to further investigate the damping behavior of large-scale floor structures, which might support their broader adoption in construction practices. Laboratory tests on large-scale floor structures might further be used to validate the impact force applied to the FE model using an ISO tapping machine.

Conflict of interest

Author declared no conflict of interests.

Data availability statement

Data are available on request from the authors.

Author contribution statement

Bettina Chocholaty: Conceptualization, Methodology, Software, Data Curation, Validation, Formal Analysis, Visualization, Writing – original draft, Writing – review & editing. *Nicolaas Bernardus Roozen*: Conceptualization, Methodology, Writing – review, Supervision. *Karl-Alexander Hoppe*: Methodology, Writing - review & editing. *Marcus Maeder*: Writing – review, Supervision. *Steffen Marburg*: Funding acquisition, Resources, Supervision, Writing – review.

References

1. A. Chiniforush, M.M. Alamdari, U. Dackermann, H. Valipour, A. Akbarnezhad: Vibration behaviour of steel-timber composite floors, part (1): experimental & numerical investigation. Journal of Constructional Steel Research 161 (2019) 244–257.

2. A. Hassanieh, A.A. Chiniforush, H.R. Valipour, M.A. Bradford: Vibration behaviour of steel-timber composite floors, part (2): evaluation of human-induced vibrations. Journal of Constructional Steel Research 158 (2019) 156–170.

3. M. Fujita, J. Sakai, H. Oda, M. Iwata: Building system for a composite steel-timber structure. Steel Construction 7 (2014) 183–187.

4. A.T. Balasbaneh, W. Sher, D. Yeoh, K. Koushfar: LCA & LCC analysis of hybrid glued laminated timber–concrete composite floor slab system. Journal of Building Engineering 49 (2022) 104005.

5. W. Zhu, H. Yang, W. Liu, B. Shi, Z. Ling, H. Tao: Experimental investigation on innovative connections for timber–concrete composite systems. Construction and Building Materials 207 (2019) 345–356.

6. A. Hassanieh, H. Valipour, M. Bradford: Experimental and numerical study of steel-timber composite (STC) beams. Journal of Constructional Steel Research 122 (2016) 367–378.

7. J. Negreira, A. Trollé, K. Jarnerö, L.-G. Sjökvist, D. Bard: Psycho-vibratory evaluation of timber floors – towards the determination of design indicators of vibration acceptability and vibration annoyance. Journal of Sound and Vibration 340 (2015) 383–408.

8. J. Weckendorf, G. Hafeez, G. Doudak, I. Smith: Floor vibration serviceability problems in wood light-frame buildings. Journal of Performance of Constructed Facilities 28 (2014) A4014003.

9. A. Pavic: Results of IStructE 2015 survey of practitioners on vibration serviceability. In: Proceedings of the SECED 2019 Conference: Earthquake Risk and Engineering towards a Resilient Word, London, UK, 9–10 September, 2019.

10. O.A. Hassan, F. Öberg, E. Gezelius: Cross-laminated timber flooring and concrete slab flooring: a comparative study of structural design, economic and environmental consequences. Journal of Building Engineering 26 (2019) 100881.

11. N. Perković, V. Rajčić, J. Barbalić: Analytical and numerical verification of vibration design in timber concrete composite floors, Forests 12 (2021) 707.

12. N.-G. Vardaxis, D. Bard Hagberg, J. Dahlström: Evaluating laboratory measurements for sound insulation of cross-laminated timber (CLT) floors: configurations in lightweight buildings. Applied Sciences 12 (2022) 7642.

13. F.G. Branco, L. Godinho: On the use of lightweight mortars for the minimization of impact sound transmission. Construction and Building Materials 45 (2013) 184–191.

14. L. Godinho, R. Masgalos, A. Pereira, F. Branco: On the use of a small-sized acoustic chamber for the analysis of impact sound reduction by floor coverings. Noise Control Engineering Journal 58 (2010) 658–668.

15. Technical Committee ISO/TC 98: ISO 10137 – Bases for design of structures – Serviceability of buildings and walkways against vibrations, International Organization for Standardization, Geneva, Switzerland, 2007.

16. B. Szabó, I. Babuška: Finite Element Analysis: Method, Verification and Validation. John Wiley & Sons, 2021.

17. J.E. Mottershead, M. Link, M.I. Friswell, C. Schedlinski: Model Updating. In: R. Allemang, P. Avitabile, Eds. Handbook of experimental structural dynamics. Springer, New York, NY, 2021, pp. 1–53.

18. B. Shahriari, K. Swersky, Z. Wang, R.P. Adams, N. De Freitas: Taking the human out of the loop: A review of bayesian optimization. Proceedings of the IEEE 104 (2015) 148–175.

19. S. Tao, A. Van Beek, D.W. Apley, W. Chen: Multi-model bayesian optimization for simulation-based design. Journal of Mechanical Design 143 (2021) 111701.

20. D. Owolabi, C. Loss, J. Zhou: Vibration properties and serviceability performance of a modular cross-laminated timber-steel composite floor system. Journal of Structural Engineering 149 (2023) 04023171.

21. B. Chocholaty, N.B. Roozen, M. Maeder, S. Marburg: Vibroacoustic response of steel–timber composite elements. Engineering Structures 271 (2022) 114911.

22. F. Nogueira: Bayesian Optimization: Open source constrained global optimization tool for Python, 2014. Available at https://github.com/fmfn/BayesianOptimization.

23. Technical Committee ISO/TC 43: DIN EN ISO 10140–5 – Acoustics – Laboratory measurement of sound insulation of building elements – Part 5: Requirements for test facilities and equipment, European Committee for Standardization, Brussels, Belgium, 2021.

24. Pollmeier Massivholz GmbH & Co.KG: Leistungserklärung einer Platte in Baubuche.2018. Available at https://www.pollmeier.com/de/produkte/ueber-baubuche/baubuche-platte (accessed: 2022-01-19).

25. A. Andrej: Schneider: Bautabellen für Ingenieure, vol. 21. Bundesanzeiger Verlag, 2014.

26. ANSYS, Inc.: Ansys engineering simulation software, 2019. Available at https://www.ansys.com/.

27. P. Langer, M. Maeder, C. Guist, M. Krause, S. Marburg: More than six elements per wavelength: The practical use of structural finite element models and their accuracy in comparison with experimental results. Journal of Computational Acoustics 25 (2017) 1750025.

28. L. Cremer, M. Heckl: Abstrahlung von Körperschall. In: L. Cremer, M. Heckl, Körperschall. Springer, 1996, pp. 459–545. https://doi.org/10.1007/978-3-662-08182-2.

29. D.J. Ewins: Modal testing – theory, practice and application. John Wiley & Sons, New York, 2009.

30. S. Ereiz, I. Duvnjak, J.F. Jiménez-Alonso: Review of finite element model updating methods for structural applications. Structures 41 (2022) 684–723.

31. R.J. Allemang: The modal assurance criterion – twenty years of use and abuse. Sound and vibration 37 (2003) 14–23.

32. O. Cuate, O. Schütze: Pareto explorer for finding the knee for many objective optimization problems. Mathematics 8 (2020) 1651.

33. K. Christodoulou, E. Ntotsios, C. Papadimitriou, P. Panetsos: Structural model updating and prediction variability using pareto optimal models. Computer Methods in Applied Mechanics and Engineering 198 (2008) 138–149.

34. E. Brochu, V.M. Cora, N. De Freitas: A tutorial on bayesian optimization of expensive cost functions, with application to active user modeling and hierarchical reinforcement learning. 2010. Preprint available at https://arxiv.org/abs/1012.2599.

35. C.Q. Howard, B.S. Cazzolato: Acoustic Analyses using MATLAB® and ANSYS®. CRC Press, 2014.

36. Technical Committee CEN/TC 250: DIN EN 1995 1–1 – Eurocode 5: Design of timber structures, Part 1–1: General – Common rules and rules for buildings, European Committee for Standardization, Brussels, Belgium, 2010.

37. C. Geweth, S. Baydoun, F. Saati, K. Sepahvand, S. Marburg: Effect of boundary conditions in the experimental determination of structural damping. Mechanical Systems and Signal Processing 146 (2021) 107052.

38. P. Wang, C. Van Hoorickx, G. Lombaert, E. Reynders: Numerical prediction and experimental validation of impact sound radiation by timber joist floors. Applied Acoustics 162 (2020) 107182.

39. N. Cheraghi-Shirazi, K. Crews, S. Malek: Review of vibration assessment methods for steel-timber composite floors. Buildings 12 (2022) 2061.

40. T. Murray, D. Allen, E. Ungar, D. Davis: Vibrations of steel-framed structural systems due to human activity: AISC design guide 11. American Institute of Steel Construction, USA, 2016.

41. M.R. Willford, P. Young: A design guide for footfall induced vibration of structures. Concrete Society for the Concrete Centre London, London, UK, 2006.

42. Committee GME/21: BS 6472–1 – Guide to evaluation of human exposure to vibration in buildings – part 1: vibration sources other than blasting, 2008. https://doi.org/10.3403/19971044U.

43. J. Brunskog, P. Hammer: The interaction between the ISO tapping machine and lightweight floors. Acta Acustica united with Acustica 89 (2003) 296–308.

44. J. Lietzén, J. Miettinen, M. Kylliäinen, S. Pajunen: Impact force excitation generated by an ISO tapping machine on wooden floors. Applied Acoustics 175 (2021) 107821.

45. D. Fritze, S. Marburg, H.-J. Hardtke: Estimation of radiated sound power: a case study on common approximation methods. Acta Acustica united with Acustica 95 (2009) 833–842.

46. F. Fahy: Sound and structural vibration: radiation, transmission and response, Academic Press, London and Orlando, FL, 1985.

47. Technical Committee CEN/TC 211: DIN EN ISO 3741 – Acoustics – determination of sound power levels and sound energy levels of noise sources using sound pressure – Precision methods for reverberation test rooms, 2011. https://doi.org/10.31030/1642422.

48. Subcommittee NA 001-02-03-03 UA: DIN 18041 – Acoustic quality in rooms – Specifications and instructions for the room acoustic design, 2016. https://doi.org/10.31030/2395845.

49. Technical Committee CEN/TC 126: DIN EN ISO 12354-2 – Building acoustics – estimation of acoustic performance of buildings from the performance of elements – part 2: impact sound insulation between rooms, 2017. https: //doi.org/10.31030/2625099.